CHARACTERIZATION OF DENSE SUSPENSIONS USING FREQUENCY DOMAIN PHOTON MIGRATION

A Dissertation

by

YINGQING HUANG

Submitted to the Office of Graduate Studies of
Texas A&M University
in partial fulfillment of the requirements for the degree of

DOCTOR OF PHILOSOPHY

May 2004

Major Subject: Chemical Engineering

CHARACTERIZATION OF DENSE SUSPENSIONS USING FREQUENCY DOMAIN PHOTON MIGRATION

A Dissertation

by

YINGQING HUANG

Submitted to the Office of Graduate Studies of
Texas A&M University
in partial fulfillment of the requirements for the degree of

DOCTOR OF PHILOSOPHY

Approved as to style and content by:

Eva M. Sevick-Muraca (Chair of Committee)	Sam Mannan (Member)
Daniel F. Shantz (Member)	Henry F. Taylor (Member)

Kenneth R. Hall
(Head of Department)

May 2004

Major Subject: Chemical Engineering

ABSTRACT

Characterization of Dense Suspensions Using Frequency Domain Photon Migration.

(May 2004)

Yingqing Huang, B.S., Tsinghua University;

M.S., University of Missouri-Rolla

Chair of Advisory Committee: Dr. Eva M. Sevick-Muraca

Interparticle interactions determine the microstructure, stability, rheology, and optical properties of concentrated colloidal suspensions involved in paint, paper, cosmetic, and pharmaceutical industries, etc.

Frequency domain photon migration (FDPM) involves modeling the photon transport in a multiple scattering medium as a diffusion process in order to simultaneously determine isotropic scattering and absorption coefficients from measured amplitude attenuation and phase shift of the propagating photon density wave.

Using FDPM, we investigated the impact of electrostatic interaction upon the optical properties and structure of dense charged suspensions. We demonstrated that electrostatic interactions among charged polystyrene latex may significantly affect the light scattering properties and structure of dense suspensions at low ionic strength (<0.06 mM NaCl equivalent) by actual FDPM measurement. We showed that the structure factor models addressing electrostatic interaction can be used to describe the microstructure of charged suspensions and quenched scattering due to electrostatics, and demonstrated that FDPM has the potential to be a novel structure and surface charge

probe for dense suspensions. We also showed that the FDPM measured isotropic scattering coefficients may respond to the change in effective particle surface charge, and displayed the potential of using FDPM for probing particle surface charge in concentrated suspensions.

We presented that the interference approximation implies a linear relationship between the absorption coefficient and volume fraction of suspension. We illustrated that FDPM measured absorption coefficient varies linearly with suspension volume fraction and affirmed the interference approximation from a perspective of light absorption. The validation of the interference approximation enables us to develop the methodology for estimating absorption efficiencies and imaginary refractive indices for both particles and suspending fluid simultaneously using FDPM. We further demonstrated a novel application of FDPM measured absorption coefficients in determining pigment absorption spectra, and displayed the potential of using FDPM as a novel analytical tool in pigment and paint industry.

DEDICATION

To My Grandparents

whose memory, as seeds of love and sources of care, endures

ACKNOWLEDGEMENTS

I could not have reached this momentous point in my life without having received tremendous assistance from others. I would like to thank my advisor, Dr. Eva Sevick-Muraca, whose guidance and encouragement significantly impacted my approach to research and the content of this dissertation. I would like to thank my committee, Dr. Henry Taylor, Dr. Sam Mannan, and Dr. Daniel Shantz, whose suggestions have also impacted the content of this dissertation. I would like to thank my colleagues, Dr. Ranadhir Roy, Dr. Daniel Hawrysz, Dr. Jounwang Lee, Dr. Zhigang Sun, Dr. Alan Thompson, Dr. Michael Gurfinkel, Dr. Anuradha Godavarty, Eddy Kuwana, Jessica Houston, Amit Joshi, Tianshu Pan, John Rasmussen, Sarabjyot Singh Dali, Feng Liang, and Sharney Torrance, whose assistance has also contributed to the content of this dissertation. I especially would like thank Dali for his careful proof of the writing. I would like to thank National Science Foundation, which primarily funded this research. Finally, I would like to thank my parents, Daolin Huang and Daqing She; my brother and his wife, Dr. Zheng Huang and Xinxin Zhang; my closest friends, Dr. Jinsong Zhao, Dr. Hongkun Liang, Dr. Zhaohui Yang, Lauren Zhang, Lingfeng Yuang, Dr.Timmy Bao, Yiming Ding, Xin Liu and his wife Hongyang Wang, Feng Qing and his wife Xin Li, Frank Wang and his wife Huiyan Zhang, Yanjun and her husband Tao Yu, Li Zhu and her husband Yueqiang Gui, Yuhua Qiao and her husband Jinchao Yang. I would also thank other friends, whose name I cannot fully list here. I would especially express my thanks to my significant other, Jie Lin. Through calm and turbulent times, these people have nurtured my growth as a scholar and accompanied my life in Texas.

TABLE OF CONTENTS

Page

CHAPTER Page

CHAPTER Page

CHAPTER Page

CHAPTER Page

LIST OF FIGURES

Page

Page

Page

Page

Page

Page

Page

Page

Page

Page

Page

LIST OF TABLES

Page

Page

Page

CHAPTER I

INTRODUCTION

I.1. Motivation

Concentrated colloidal suspensions are widely involved in many manufacturing processes involving chemical, environmental, pharmaceutical, paints, pigments, and semiconductor industries. The performance of such a product depends on colloidal stability and rheology, which are mediated by particle interactions, which determine correlated particle spatial arrangement (or microstructure) of the suspension. In dilute suspensions, where particles are located spatially far apart (with particle volume fractions typically less than 1%), particle interactions can be neglected, and particles can move and occupy space randomly. In concentrated suspensions, particles compete with each other for space, and particle interactions generate favorable particle spatial arrangements, which are referred to as correlated particle positions or microstructure (Figure I.1).

Particle size distribution and microstructure also impact optical properties of a suspension, which are critical to inks, pigments, paints, etc. Finally, the development of nanoparticle crystals,[1] chemical sensors,[2, 3] and photonic materials require the controlled order of nanoparticles at varying length scales. An understanding of the physics that govern particle interactions and microstructure is needed in order to advance these new emerging fields.[4]

This dissertation follows the style of *Journal of the Optical Society of America A*.

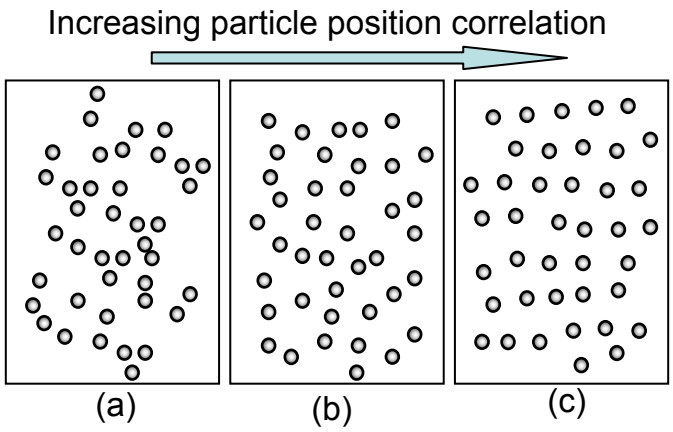

Figure I.1 Particle interactions generate favorable spatial arrangements for all particles, and will cause particle position correlation (or called microstructure).

Since correlated particle positions impact the optical properties of suspensions, it is possible to infer microstructure and interaction parameters from the optical properties of these suspensions.

The optical technique known as frequency domain photon migration (FDPM) has emerged as a new optical technique for bio-medical applications, providing an accurate and reliable measurement of tissue isotropic scattering and absorption coefficients. In addition, researchers at the Photon Migration Laboratories demonstrated its strong potential for characterizing concentrated suspensions.[5-8] Briefly, this technique consists of monitoring the "time dependence" of light propagation in multiple scattering media, which enables simultaneous determination of scattering and absorption optical properties. In dense suspensions, the interference approximation relates the measured scattering properties to correlated particle positions. In this and other works, FDPM measurement of light scattering properties has been used to infer microstructure as well as particle size of concentrated suspensions. Typically, these works have assumed

correlated particle position arose predominantly from volume exclusion effects,[9-13] i.e. particles are unable to occupy the same volume.

However, particles are usually charged, and the interparticle electrostatic repulsive interactions, which are sometimes critical to the stability of the suspension, can be of significant industrial importance. Though a quantitative understanding of the electrostatic interaction (ESI) among charged particles is imperative to formulate dense colloidal products, the impact of electrostatic interactions on particle position correlation is only qualitatively understood.

I.2. Goal of research

Goal #1. This dissertation seeks to explore the application of FDPM to probe elusive yet important electrostatic interactions in concentrated suspensions, and to verify two important electrostatic interaction models (introduced in Chapter III).

The interference approximation, which ascribes the measured scattering properties to the interference of light scattered by particle "structure," has been widely used to address light scattering properties of suspension.

Goal #2. The second goal of this research seeks to affirm the interference approximation from the perspective of light absorption in addition to light scattering measurement.

Previously, characterizations of concentrated suspensions were limited to the measured light scattering properties without utilizing light absorption information. Capable of simultaneously determining scattering and absorption properties of suspensions independently, FDPM offers an opportunity to examine the interference

approximation from the perspective of particle light absorption, in addition to the particle light scattering. The third goal of this dissertation seeks to validate the use of FDPM to characterize optical and physical properties of suspending fluid and suspended particles.

The following specific aims of this work are:

1. to examine suitable data analysis methods for extracting scattering and absorption information from FDPM measurement in dense suspension;
2. to compare two structure factor models addressing ESI by comparing model predicted isotropic scattering coefficients with experimental values measured using FDPM;
3. to investigate the effect of ionic strength on the ESI and on the microstructure, as measured by FDPM;
4. to investigate the sensitivity of FDPM to the changes in effective surface charge, as measured by FDPM;
5. to determine light absorption efficiencies of suspended particles and solvent of concentrated suspensions, and to validate the applicability of interference approximation; and
6. to validate FDPM for characterizing particle absorption efficiency.

I.3. Organization of the thesis

The physical background of light scattering and ensemble methods for characterizing concentrated suspensions will be introduced in Chapter II; Chapter III will briefly introduce particle interaction potential models and colloidal structure theories.

The background of time-dependent light propagation in dense suspensions is presented in Chapter IV, and Chapter V will cover the details of FDPM data analysis methods and FDPM instrumentation.

In Chapter VI, we will compare two structure factor models addressing particle repulsive electrostatic interactions, which depend upon the ionic strength of suspending fluid and the effective surface charges of suspended particles. The investigation of the impact of ionic strength on light scattering and colloidal structure will be presented in Chapters VII and VIII respectively. As a supplement to Chapters VII and VIII, Chapter IX will address the impact of the effective surface charge on the optical properties of a suspension, and will explore the possibility of probing mean surface charge of suspended particles using FDPM.

The work presented in Chapters VII through IX is based on FDPM measurements of isotropic scattering coefficients at two wavelengths for a single kind of polystyrene latex. Chapter X will extend FDPM measurements of isotropic scattering coefficients for two different kinds of polystyrene lattices at 7 different wavelengths, and the multiple wavelength measurements of isotropic scattering coefficients will be used to regress parameters regarding particle size distribution and effective surface charges.

Though FDPM can determine light absorption and scattering properties of a multiple scattering medium simultaneously, the application of FDPM in characterizing particle suspensions so far relies primarily on scattering measurements. Utilizing FDPM-measured absorption coefficients, Chapter XI will examine the interference approximation used in Chapters VII through X from the perspective of light absorption and will demonstrate a linear relationship between the light absorption efficiency and the particle volume fraction of a suspension. Chapter XII will present the validation of using FDPM for characterizing light absorption spectra of pigment particles, demonstrating a new FDPM application of industrial importance.

The work in this thesis will be summarized in Chapter XIII, and significant conclusion will be reviewed.

Organization of this dissertation is provided in Figure I.2.

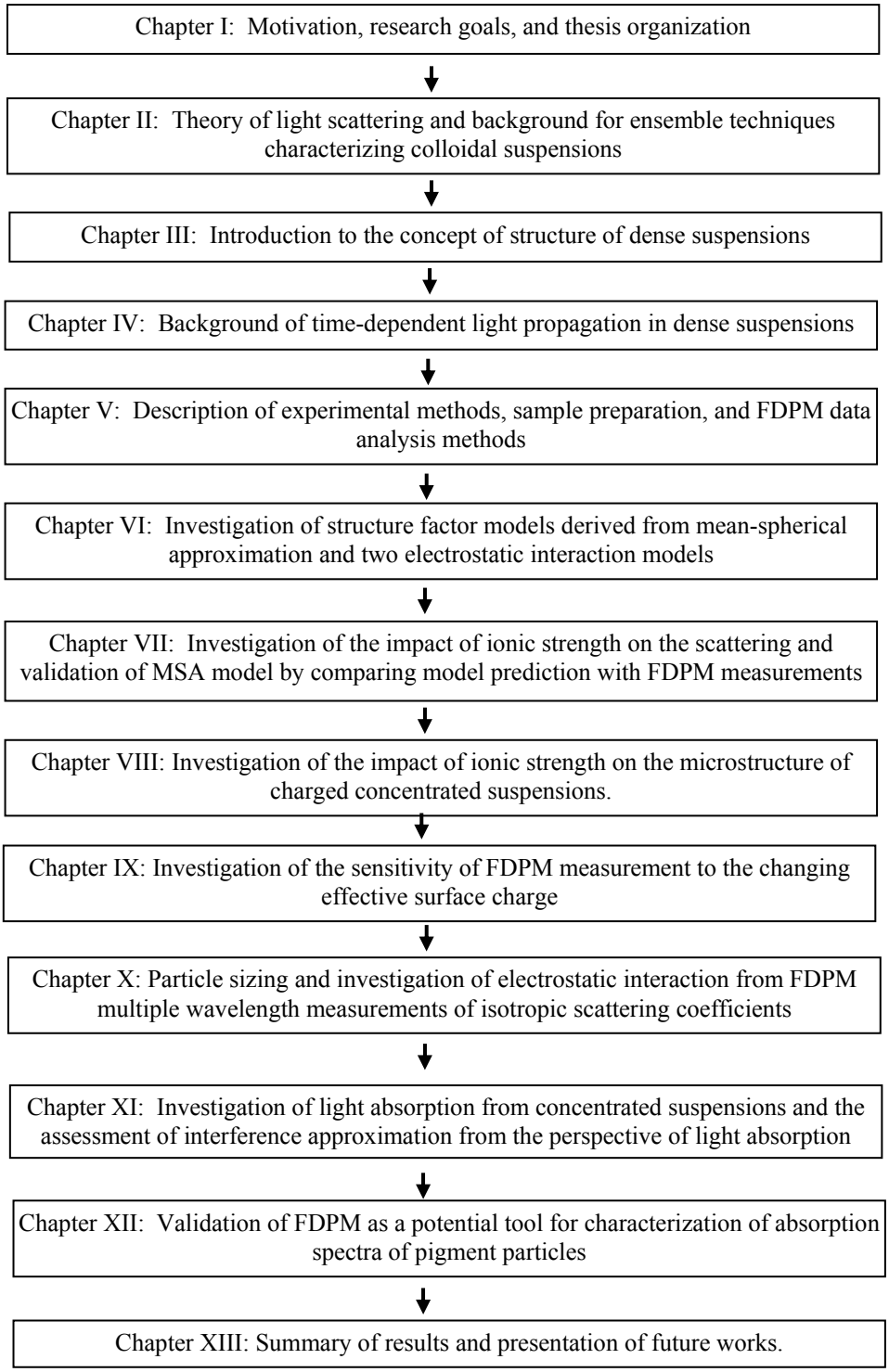

Figure I.2 The organization of thesis.

CHAPTER II

BACKGROUND OF LIGHT SCATTERING

II.1. Physics of light scattering

Light scatters when it encounters a particle of refractive index that differs from its surroundings. The light scattered outward away from the particle only changes the direction of the light, while the inward scattering toward the particle center causes particle light absorption. The intensity distribution of outward scattering, $I(\theta)$, (shown in Figure II.1) depends on the wavelength, the refractive indices of both the particle and the surrounding fluid, as well as particle size and geometry.

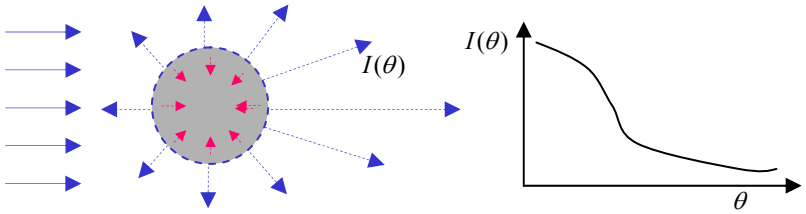

Figure II.1 Angle-dependent light scattering intensity depends on wavelength, the refractive indices of the particle and its surroundings, as well as the particle size and geometry. The angle dependent scattering intensity, I(θ), of a particle within a uniform incident electric magnetic field can be determined from Mie's solution of the Maxwell equation.[14]

II.1.1. Mie theory

Mie solved Maxwell equations governing particle light scattering from an incident planar wave by expanding incident and scattering electromagnetic fields in terms of spherical harmonics and determining the coefficient for each harmonic term

using the boundary conditions of continuous transient electric and orthogonal magnetic fields at the particle-solvent interface.[14] The angle dependent scattering intensity, *I(θ)*, of a particle within a uniform incident electric magnetic field can be determined from Mie's solution of Maxwell equations. Upon using the Mie theory, the scattering cross section, C_{sca}, which indicates scattering power of a particle, can be calculated by integrating angle-dependent scattering intensity over all directions:

$$C_{sca} = (\frac{\pi\sigma}{2})^2 \int_0^{\theta} q_{scat}(\theta, \sigma, m, \lambda) \sin(\theta) d\theta \qquad \text{(II.1)}$$

where σ is the radius of the particle; λ is the wavelength; θ is the scattering angle; and *m* is the relative refractive index of particle to the surroundings. The angle dependent scattering efficiency, $q_{scat}(\theta, \sigma, m, \lambda)$, is predicted from Mie theory and the information of particle size, relative refractive index, *m*, and wavelength λ. The interesting natural phenomena of light scattering from particles has been detailed in the monograph of van der Hulst.[15] The computer algorithm of Mie's theory provided by Bohren and Huffman[14] is used in this work. The scattering efficiency, Q_{sca}, is defined as the ratio of effective scattering cross section to the projected area of particle in the direction of incident light. For a spherical particle, the scattering efficiency can be calculated from:

$$Q_{sca} = \frac{4C_{sca}}{\pi\sigma^2} \qquad \text{(II.2)}$$

The total extinction efficiency of a particle, C_{ext}, can be calculated from the forward scattering theory, which states that the total extinction power of a particle is

proportional to the real part of the complex amplitude of the scattered light in the forward direction, $S_1(0)$. The term of $S_1(0)$ can be calculated from Mie theory:

$$C_{ext} = Q_{ext} \cdot \pi\sigma^2 = \frac{\lambda^2}{\pi} \mathrm{Re}(S_1(0)) \tag{II.3}$$

A subtraction of scattering cross section, C_{sca}, from total extinction cross section, C_{ext}, leads to absorption cross section, C_{abs}:

$$C_{abs} = Q_{abs} \cdot \pi\sigma^2 = C_{ext} - C_{sca} \tag{II.4}$$

Therefore, the particle light absorption can be fully determined from the particle scattering pattern.

From Mie theory, one can also evaluate average cosine of scattering, $\overline{\cos\theta}$, by inserting $\cos\theta$ into the integrand of Eqn (II.1) and integrating over scattering angle:[14]

$$(1-g) \cdot Q_{sca} = \overline{\cos\theta} \cdot Q_{sca} = (\frac{\lambda}{2\pi a})^2 \int_0^{\theta} q_{sca}(\theta) \sin\theta \cos\theta d\theta \tag{II.5}$$

The scattering anisotropy is defined as $g = (1 - \overline{\cos\theta})$, and indicates the balance of light scattered in the forward and backward directions. The scattering anisotropy, g, vanishes at isotropic scattering, where the scattered light is evenly distributed over all scattering directions.

The angle-dependent scattering amplitude, $q_{scat}(\theta, \sigma, m, \lambda)$, for an individual particle is predicted from Mie's solution and can be used to infer scattering and absorption of colloidal suspensions. For the case of a uniform incident light field, particle size can be determined from the angular scattering intensity distribution with *a*

priori information of refractive indices of particles and surrounding medium by solving an inverse problem of Eqn (II.1). This is "done" with *single* scattering in *dilute* solutions, and is the basis for the laser diffraction measurements, which will be reviewed in the following section.

II.2. Light scattering from particles in suspensions

Depending upon the particle size distribution (PSD), particle concentration, refractive indices of particles and solvent, as well as particle spatial arrangement, the propagation of light in ensemble suspensions can be classified in several ways. Depending upon the times of scattering events when light passes through a suspension, the propagation of light can involve either *single* scattering or *multiple* scattering. Depending upon the relation between particle's scattering efficiencies with their positions, the scattering can be either *dependent* or *independent*. In addition, while a technique is classified as *dynamic* light scattering if it analyzes the time-correlation of the intensity of the scattered light, a *static* techniques investigates the time-averaged scattering intensity itself. The following subsections will introduce ensemble light scattering techniques within each category.

II.2.1. Single scattering and multiple scattering

II.2.1.1 Single scattering

In either a dilute suspension or a thin slab of concentrated suspension, radiation penetrating through a suspension may be scattered at most once. Alternatively, one can state that a photon passing through a suspension can at most be scattered by a single particle. This phenomenon, shown in Figure II.2a is called "single scattering."

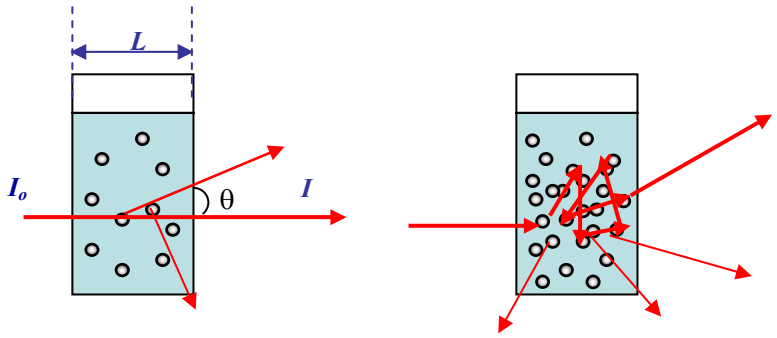

(a) Single scattering (b) Multiple scattering

Figure II.2 Single scattering and multiple scattering of suspensions.

The scattering coefficient, μ_s, which represents the effective scattering cross section per unit volume, is usually used to indicate the light scattering efficiencies of suspensions. The scattering coefficient, μ_s, has a dimension of inverse length, can be equivalently interpreted as the probability for light to be scattered when passing a unit length within a scattering medium. In a dilute suspension, μ_s, increases linearly with particle concentration and with the scattering efficiencies of particles:

$$\mu_s = \sum_i \rho_i C_{sca,i} \tag{II.6}$$

where ρ_i is the number density for the particle with extinction cross section $C_{sca,i.}$.

Both suspending solvent and suspended particles in a suspension can absorb light, and the light absorption coefficient, μ_a, represents the probability of light being absorbed as it passes a unit length within the suspension., The summation of scattering coefficient and absorption coefficient is termed total extinction coefficient, which specifies the efficiency of a medium to diminish geometrically propagated light.

If the total extinction efficiency is represented by Σ_t, light diminishes exponentially with the optical path length, L, when passing through a single scattering suspension as:

$$I = I_o e^{-\Sigma_t L} \tag{II.7}$$

II.2.1.2 Multiple scattering

Multiple scattering occurs when radiation is scattered multiple times before it escapes from an opaque medium. Milk is a typical example of multiply light scattering medium, in which visible light passing through it is multiply scattered. A dilute suspension can singly scatter or multiply scatter light depending on the distance that light travels through it or the number of experienced scattering events. When light travels for a sufficiently long distance, a dilute suspension can multiply scatter light, since the chance of light scattering increases as the distance light travels increases. The distance light travels through a multiple scattering medium is not a simple relation of the geometry of the sample holder and the distance between incident and detecting points, as shown in Figure II.2b. The extinction of light passing through a multiple scattering suspension can not be described using Eqn (II.7). However, the propagation of light in a multiply scattering medium can be modeled as a diffusion process, which will be introduced in Chapter IV.

In addition to the scattering coefficient, μ_s, the isotropic scattering coefficient, defined as, $\mu_s' = (1-g)\mu_s$, is more often used to describe scattering properties of a multiple scattering tissues or suspensions. The isotropic scattering indicates the

probability of incident light into a suspension being randomly directed due to scattering when traveling a unit path length.

For a dilute suspension, both the scattering coefficient, μ_s, and the isotropic scattering coefficient, $\mu_s^{'}$, are proportional to the particle number density, ρ:

$$\mu_s \propto \rho \int_0^{\theta} q_{sca}(\theta) \sin\theta d\theta \tag{II.8}$$

$$\mu_s^{'} = (1-g)\mu_s = \rho \int_0^{\theta} q_{sca}(\theta) \sin\theta (1-\cos\theta) d\theta \tag{II.9}$$

However, for a concentrated suspension, the above two relations may not be correct. The scattering coefficient fails to increase linearly with the particle concentration, and *dependent* scattering occurs. The *dependent* scattering and *independent* scattering will be introduced in the next subsection.

II.2.2. Independent and dependent light scattering

Depending upon whether a particle in suspension has the same effective scattering efficiency as it has when isolated, (or alternatively depending upon if Eqn (II.6) holds,) the particle scattering can be classified as either independent scattering or dependent scattering.

II.2.2.1 Independent scattering

When particles in a dilute suspension are widely separated, they can move randomly without generating correlation in their spatial positions.

When light is incident on a suspension, each particle is immersed in both the primary electromagnetic field of incident light and secondary fields of scattered light

from other particles. When the particle separation distances are large, the secondarily scattered field from other particles (shown as dashed arcs in Figure II.3) is negligible in comparison to the original incident light (shown as solid parallel lines in Figure II.3). In this case, independent scattering occurs. Independent scattering usually occurs when the distance between particles is greater than the wavelength of light that is scattered.

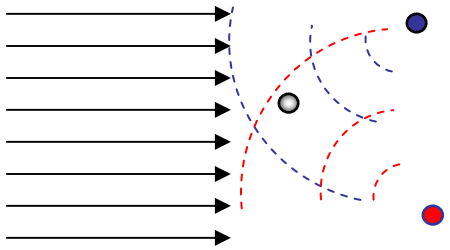

Figure II.3 When particles are far from each other, the secondarily scattered field from other particles, (shown as dashed arcs) is negligible in comparison to the original incident light (showed as solid parallel lines).

II.2.2.2 Dependent scattering

Due to the increased number of particles and the closer particle spacing within concentrated suspensions, the secondary scattered field from neighboring particles may no longer be negligible. Therefore, the scattered field from a particle also depends on the particles nearby, and scattering is termed "dependent." Since the positions of the neighboring particles are spatially correlated, the secondary scattered fields from closest neighboring particles may be partially coherent. Consequently, particle scattering efficiencies in concentrated suspensions also depend on correlated particle positions arising from particle interactions.[16] Numerical solution of the governing Maxwell

equations shows that the far field scattering pattern due to a few closely packed particles depends upon the particle orientation and particle separation.[17, 18] Typically, dependent scattering occurs when the average distance between particles are less than or comparable with the wavelength.

II.2.2.3 Interference approximation

Concentrated suspensions involving dependent scattering are not unusual, and understanding the physics of dependent scattering is of critical commercial application, such as color prediction in the formulation of paints.

Rigorous treatment by solving the governing Maxwell equations for the optical properties of suspensions is difficult. While Xu and coworkers[19] recently generalized the Mie's solution and calculated the scattering field of an agglomerate of ordered particles using harmonic expansion methods, their methodology cannot be extended to a dense suspension containing an enormous number of particles undergoing Brownian motion. Approximation methods are typically used to address the dependent scattering with the correlated particle positions.

The interference approximation (IA) has been introduced to address dependent scattering of dense suspensions. The IA, which ascribes hindered scattering power to the interference effects of light scattered from different particles[20-22] assumes:

1. the incident field on a particle is not impacted by its neighbors;
2. particle scattering is not affected by its neighbors in the near-field, or particles scatter independently;

3. the scattered fields from different particles interfere in the far field depending upon particle position correlation, as indicated in Figure II.4.

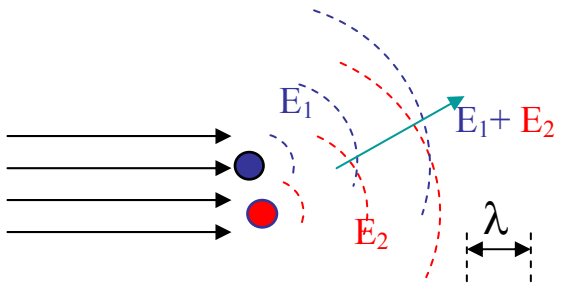

Figure II.4 Interference ascribes dependent scattering to the interference of scattering fields (E_1 and E_2) from closely positioned particles. The symbol of λ indicates the wavelength of the incident light.

According to the IA, particles in dilute suspensions are randomly positioned and scattered electric fields from different particles are not phase-correlated. Therefore interference effects can be neglected. However, with increasing particle concentrations, the correlated particle positions result in phase correlation of the scattered light and generate interference effects or dependent scattering.

If valid, IA predicts that correlated particle positions will not impact particle absorption efficiencies. In this dissertation, the validity of IA will be investigated from a new perspective of light absorption as well as light scattering.

II.2.3. Static light and dynamic light scattering

Depending on whether the angle dependence of time-averaged scattering intensity or time correlation of the intensity of scattered light is detected and analyzed, the instrumentation can be classified as static or dynamic light scattering.

II.2.3.1 Static light scattering

Characterization of suspensions using the static scattering techniques is theoretically well understood. Static light scattering techniques detect time-averaged light scattering intensity as a function of scattering angle as shown in Figure II.5.

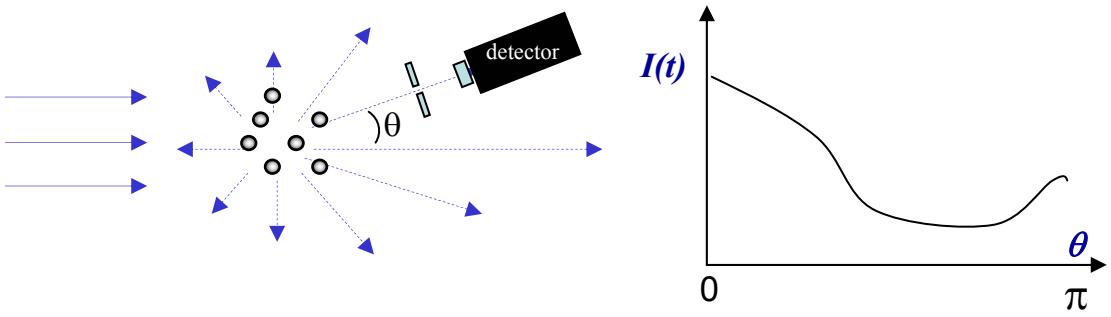

Figure II.5 Static light scattering techniques detect time-averaged light scattering intensity as a function of scattering angle, as in the ensemble techniques of angular light scattering described below in the next subsection.

The scattering pattern (or intensity distribution of the scattered light) of a single particle within a planar incident field depends on the particle size, particle shape, wavelength, and refractive index. Therefore it is possible to infer the size and shape information of particles in a dilute suspension from the scattering pattern measured in the far field by using appropriate scattering theory, which predicts angle dependent scattering intensity. Information regarding microstructure can be inferred from the angle

dependent interference effects, which can be determined by comparing detected scattering pattern in dense suspensions with independent scattering pattern in a dilute suspension, which can be measured in dilute suspension or predicted using appropriate scattering theory. The principle of static light scattering is illustrated in Figure II.6. The curve of $S(\theta)$ describes the interference effects, and is called structure factor. The structure factor theory will be introduced in Chapter III.

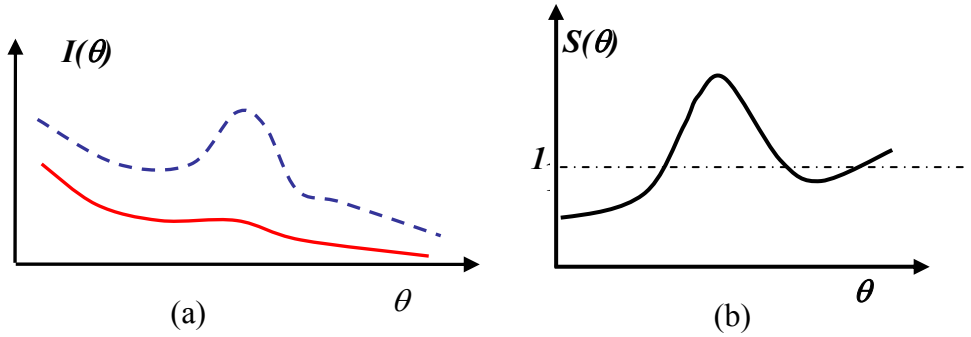

Figure II.6 (a) The scattering intensity distributions of dependent scattering (dashed line) and independent scattering (continuous line). (b)The angle dependent interference effects, which can be determined by comparing detected scattering pattern in dense suspensions with the independent scattering pattern measured in dilute suspension or predicted using appropriate scattering theory.

Static angle light scattering techniques (SALS),[23-26] small angle neutron scattering (SANS),[23, 27-34] and small angle x-ray scattering (SAXS)[35-37] techniques are all based on static scattering. These small angle scattering techniques earn their names from the fact that they detect intensity of scattered radiation at small scattering angles (typically < 10°). X-ray and neutron have higher energies, and can pass through concentrated suspensions without significant multiple scattering effects. However, X-

ray scattering needs an expensive monochromatic synchrotron source, and neutron scattering requires a nuclear reactor for a radiation source. The high cost and difficulty in implementing these expensive radiation sources prevent x-ray and neutron scattering techniques to be applied in general laboratories and industrial environments.

Static light scattering techniques can be applied in the multiple scattering suspensions, and techniques depend upon measuring multiply scattered light in a static manner as be introduced later in this section. It is noted that correlation between the scattering intensity and the scattering angles are lost in multiply scattering medium.

Due to the relatively low energy associated with photons in comparison to x-ray and neutron, static light scattering techniques require either sufficiently dilute samples to eliminate the multiple scattering effects or suitable refractive index matching, which involves adding higher refractive agents to adjust the solvent refractive index towards that of the particles in order to decrease the particle scattering efficiency. Since the added index matching agents change original solvent conditions and may subsequently change the interaction and microstructure of suspensions, refractive index matching is not feasible for characterizing many colloidal systems of commercial applications.

II.2.3.2 Dynamic light scattering

Static light scattering (SLS) techniques can obtain particle size information or microstructure from measured time-averaged scattering intensity. In contrast to SLS, dynamic light scattering (DLS) investigates the time-correlation of intensity fluctuations of singly scattered light, as shown in Figure II.7. DLS is briefly highlighted here as an example of ensemble dynamic measurements.

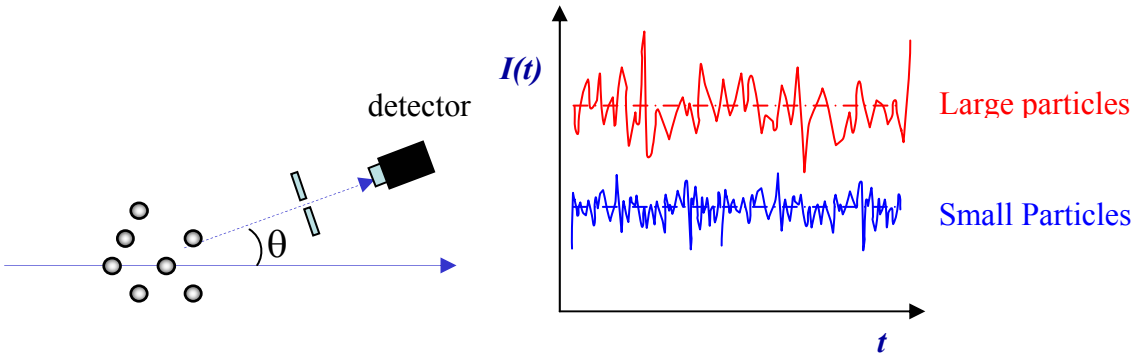

Figure II.7 Dynamic light scattering (DLS) measures the decay of intensity fluctuations of singly scattered light and relates it to the Brownian motion of the scattering particles through the Stokes-Einstein equation. Larger particles have smaller mobility and light scattered from large particles varies slowly, while small particles move rapidly and the scattered light varies at a greater frequency.

The time-correlation in the scattered intensity, which can probe how fast the measured intensity fluctuates with time, can be related to the mobility of particles under Brownian motion via Stokes-Einstein equation.[38, 39] The principle of dynamic light scattering will be presented in next section. Generally, larger particles have smaller mobility and light scattered from large particles fluctuates slowly (Figure II.7), while small particles move more rapidly, and the light scattered from small particles fluctuates at a higher frequency.

Similar to the static light scattering, dynamic light scattering cannot be applied to multiple scattering suspensions. In a multiple scattering suspension, the measured temporal correlation of scattering intensity can no longer be related to the mobility of single particles. The technique that measures the temporal correlation of multiply scattered light will be introduced in the next section.

II.3. Ensemble based optical characterization methods

II.3.1. Turbidity measurement

Turbidity statically measures the transmission extinction of light, and is typically used to characterize single scattering suspensions. Turbidity measurements can be considered as a special case of the static light scattering, where only the scattering intensity in the forward direction is measured.

If the light extinction due to particle absorption is negligible in contrast to light extinction due to particle scattering, one can use classical scattering theories to set up the inverse problem in order to determine the particle size distribution.

$$-\frac{1}{L}\ln\frac{I(\lambda)}{I_o(\lambda)} = \mu_s(\lambda) = \int_0^\infty \frac{3Q_{sca}(x,m,\lambda)}{2x}\phi_v f_v(x)dx \qquad \text{(II.10)}$$

where $I_o(\lambda)$ and $I(\lambda)$ are the intensities of light passing through a reference cell that contains only suspending solvent and light passing through the sample cell containing the suspension under testing respective; L is the optical path length from the sample cells; ϕ_v is the particle volume fraction within a suspension; f_v(x) is the volume-based particle size distribution function for particles with diameter x with $\int_0^\infty f_v(x)dx = 1$; m is the relative refractive index of particles to the solvent; and $Q_{sca}(x,m,\lambda)$ again is the scattering efficiency for particle of diameter x suspended in the solvent at wavelength λ.

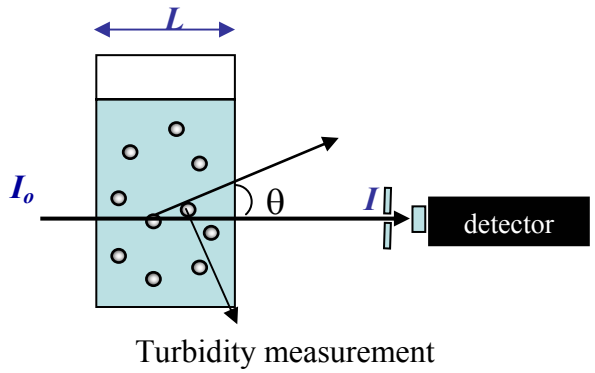

Figure II.8 Turbidity measurement determines the extinction of light passing in the forward direction.

In turbidity measurements, the concentration of particles must be accurately determined independently to obtain particle size information, and reference samples are required to cancel the light absorption from solvent and light reflection from the sample cell. The principle set up is shown in Figure II.8.

Since turbidity measurement assumes single scattering, it is theoretically not suitable to characterize concentrated suspensions that multiply scatter light. Even though turbidity measurements have been extended to include samples with moderate multiple scattering, the light signal scattered back into the optical path prohibits its appropriate application to strongly multiply scattering suspensions.

II.3.2. Dynamic light scattering

In DLS, the temporal correlation of scattering intensity, rather than the absolute scattering intensity as a function of time, *I(t)*, is directly measured as is illustrated in Figure II.9.

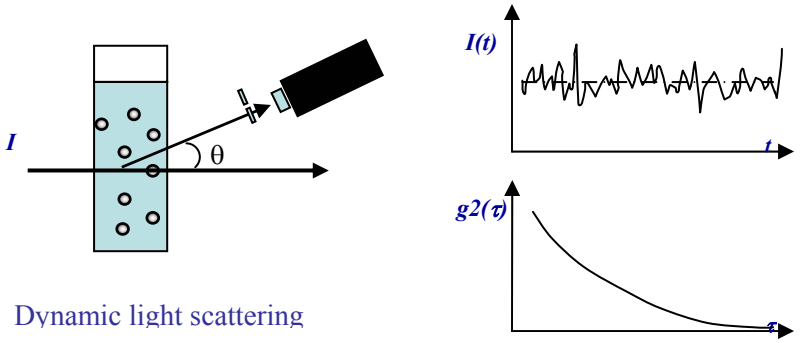

Figure II.9 Dynamic light scattering measures the decay of fluctuations of singly scattered light and relates it to the Brownian motion of the scattering particle in order to obtain an effective particle size.

The intensity temporal autocorrelation function, $g^{(2)}(\tau)$, which is related to the particle size, can be determined from the intensity fluctuation from the relation, $g^{(2)}(\tau)$:

$$g^{(2)}(\tau) =< I(0)I(\tau)/I(0)^2 >$$

where τ is called correlation delay time. When the correlation delay time approaches infinity, $g^{(2)}(\tau)$ tends to an asymptotic limit of $g^{(2)}(\infty) = 1$, stating the intensity of the scattered light is not correlated if the time interval between scattering events is long enough.

The first order temporal electric correlation function, defined as $g^{(1)}(\tau) =< E(0)E(\tau)/E^2 >$, addresses the temporal fluctuation in electric field of the scattered light. The first order temporal electric correlation function, $g^{(1)}(\tau)$, can be calculated from the intensity autocorrelation function $g^{(2)}(\tau)$ via the relation:[39]

$$g^{(2)}(\tau) = 1 + \beta \mid g^{(1)}(\tau) \mid^2 \qquad \text{(II.11)}$$

where β is defined as $g^{(2)}(0)-1$ and is independent of particle concentration. For dilute monodisperse suspensions, the first order electric correlation autocorrelation function, $g^{(1)}(\tau)$, for the scattered light is related to particle diffusion coefficient D_p by: [25,26]

$$g^{(1)}(\tau) = \exp(-q^2 D_p \tau) \tag{II.12}$$

where $q = \frac{4\pi n_l}{\lambda}\sin\frac{\theta}{2}$, is the scattering wave vector; and n_l is the refractive index of solvent. The particle diffusion coefficient, D_p, for a spherical particle of diameter σ is given by the Stokes-Einstein Equation:

$$D_p = \frac{k_B T}{3\pi\eta\sigma} \tag{II.13}$$

where k_B is the Boltzmann's constant; T is temperature, and η is the viscosity of the solution. Upon determining and regressing $g^{(1)}(\tau)$ as a function of temporal delay time τ against Eqn (II.12) from dynamically measured intensity of the scattered light, one determine the value of the particle diffusion coefficient, D_p. The particle diameter can then be subsequently determined by applying Stokes-Einstein Equation.

For polydisperse suspensions, $g^{(1)}(\tau)$ can be written in a form of integral:

$$g^{(1)}(\tau) = \int_0^\infty f(x)\cdot w(x,q)\cdot \exp(-q^2\cdot D_p(x)\cdot\tau)dx \tag{II.14}$$

where *f(x)* is the particle size distribution for dilute a suspension. The term of $w(x,q)$ is a weight factor addressing relative scattering efficiency for particles of diameter x at the

scattering vector q, and can be predicted from Mie theory. Obtaining particle size distribution requires solving the inverse problem of Eqn (II.14). In dynamic light scattering techniques, the determination of *f(x)* usually needs a assumed shape of particle size distribution, such as Gaussian distribution, lognormal distribution, etc. The weight factor, $w(x,q)$, is frequently assigned the value of unity in many applications in order to simplify the inverse problem.

Dynamic light scattering techniques, also termed photon correlation spectroscopy (PCS), quasi-elastic light scattering (QELS), are primarily used for measuring particle sizes in the range of 10 nm ~10 μm. Dynamic light scattering has became a standard method for characterizing particle size in dilute suspensions (at volume fractions usually < 0.1 %).

As described previously, DLS is not suitable for particle sizing in multiple scattering suspensions, while multiple scattering events invalidate Eqn (II.14). Cross correlation techniques and two color dynamic light scattering techniques, which extract singly scattered light from multiply scattered light, have been used to study opaque suspensions.[40, 41] Nonetheless, these adaptations still cannot be used in strong multiply scattering regions due to the vanishingly small singly scattered light component in the presence of overwhelming multiple scattering signal.

Before we introduce the optical techniques that obtain particle size information from dynamic time correlation of multiply scattered light, the angle-dependent scattering techniques will be introduced.

II.3.3. Angular light scattering (diffraction)

In contrast to turbidity measurements in which light extinction is measured in the forward direction as a function of wavelengths, angular light scattering or diffraction measurements assess the intensity of scattered monochromatic light as a function of scattering angle. The angle-dependent scattering intensity is analyzed and compared with predicted values for particles in order to determine particle size distribution. Since angular light scattering usually uses highly-collimated light from lasers, it is frequently termed laser diffraction. Typically, commercial angular light scattering instruments are usually limited to a single wavelength, or a few wavelengths. Certainly, the measurements of angle-dependent scattering intensity can be extended to multiple wavelengths.

For a monodisperse suspension, the detected light at a scattering angle, θ, is proportional to the angular dependent scattering intensity for a particle, $q_{sca}(\sigma, m, \lambda, \theta)$, which can be predicted from Mie theory or other approximated theories:

$$\frac{I(\lambda,\theta)}{I_o} \propto q_{sca}(\sigma, m, \lambda, \theta) \tag{II.15}$$

where *m* is the ratio of relative refractive index of particles to that of their surroundings.

For a polydisperse suspension, the angle-dependent scattering efficiency, $q_{sca}^{j}(m, \lambda, \theta)$, detected at a detector *j* is related to the particle size number distribution, f(x), the total particle number density ρ, and relative refractive index m by the expression:

$$q_{sca}^{j}(m,\lambda,\theta) \propto \int_{\Delta\theta}\int_{x_i}^{x_f} \rho f(x) q_{sca}(\sigma,m,\lambda,\theta) dx d\theta \qquad \text{(II.16)}$$

where $\Delta\theta$ is the differential scattering angle and depends on the size and the orientation of detecting window for detector *j*. Typically, photon detectors are assigned on a solid state ring with sample cell located at the center with detecting window normal to the sample cell as shown in Figure II.10. Angular scattering intensity is typically detected at 32-64 different angles to ensure enough resolution in measured intensity distributions. Eqn (II.15) or (II.16) constitutes the inverse problem to be solved in order to obtain particle size distribution or refractive index by fitting the experimental measured angle-dependent scattering intensity against model prediction.

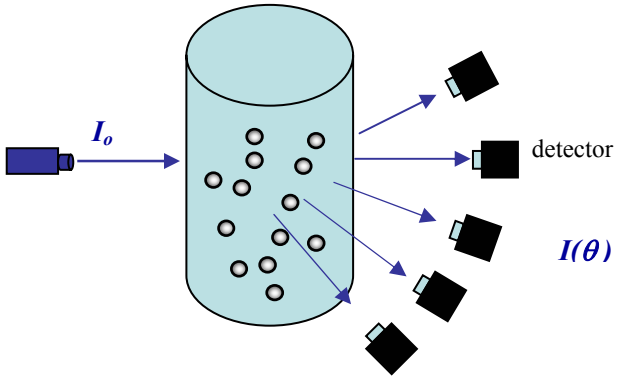

Figure II.10 Angular diffraction measurements assess angle dependent scattering intensity of monochromatic light at multiple scattering angles in order to determine the particle size distribution of a suspension.

Both Eqns (II.15) and (II.16) assume that the suspension is dilute enough to ensure single and independent scattering. Hence the angular scattering or diffraction measurement cannot accurately characterize suspensions that multiply scatter light. For dilute suspensions, diffraction measurements can provide accurate size distributions for

dilute suspensions with diameters in a range from 0.05 μm to 3000 μm, the widest dynamic range of any commercially available method. The diffraction measurements of scattered light have also been used to measure particle size distributions of aerosols, particles or liquid droplets suspended in air.

II.3.4. Diffuse wave spectroscopy (DWS)

As introduced previously, DLS measures temp-correlation of singly scattered light from dilute suspensions. There is time-correlation in multiply scattered light, and the degree of the correlation depends upon the distance between the points of incident illumination and collection as well as the optical properties of a suspension. While DLS measures the time-correlation of the *singly* scattered light intensity, DWS measures the intensity time-correlation of *multiply* scattered light at varying distances away from the light source without requiring dilution of a suspension (Figure II.11). [42-53]

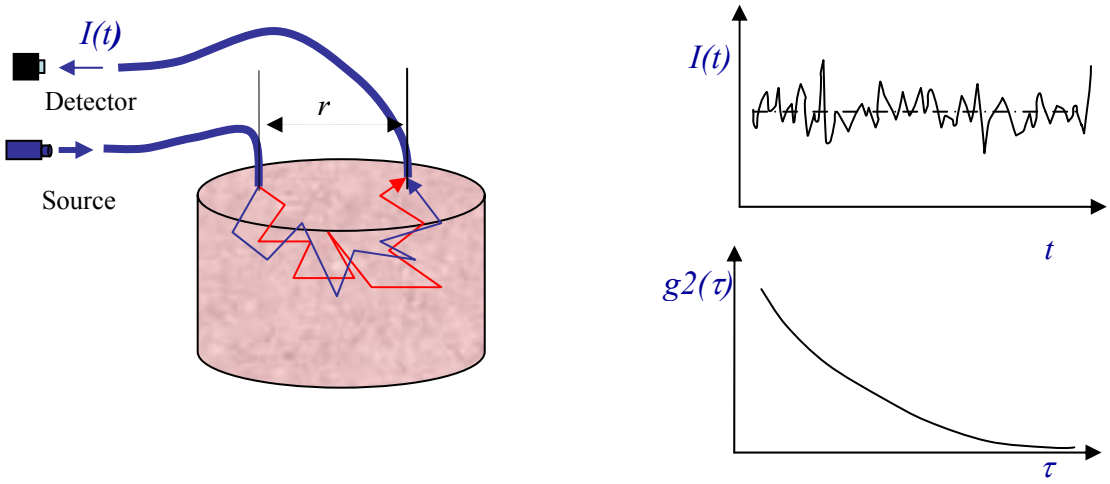

Figure II.11 Diffuse wave spectroscopy (DWS) measures the time correlation in the fluctuation of multiply scattered light detected at known distances away from the light source.

In the DWS, the propagation of light in a multiply scattering medium can be treated as diffusion process that will be introduced in Chapter IV. In a multiply scattering medium, light traveling from the light source to the detector may follow many different paths, *s*, as shown in Figure II.11. Consequently, the temporal electric field correlation function must account for all possible paths, *s*, of detected light propagating in a multiple scattering suspension. For a monodisperse suspension, where particles scatter light independently, the electric field correlation function can be calculated from an expression including an integral over the path length *s*:

$$g^{(1)}(\tau) \propto \int_0^\infty P(s) \exp\left(\left[\left(\frac{2\pi n_l}{\lambda}\right)^2 D_p \tau \frac{s}{l^*} \right] ds \right. \qquad \text{(II.17)}$$

where $l^* = 1 \Big/ (\mu_s' + \mu_a)$ is the transport mean free path length; and *P(s)* is the distribution function of path lengths as light propagates from a source to a detector; n_l is the refractive index of suspending fluid for light of free space wavelength, λ; and D_p is again particle diffusion coefficient. The path distribution function P(s) can be directly determined by measuring the pulse widening of pico-second or femto-second pulse of incident light (Figure II.12). In addition, it may also be obtained from a diffusion analysis of light propagating in multiple scattering medium, which will be introduced in the Chapter IV.

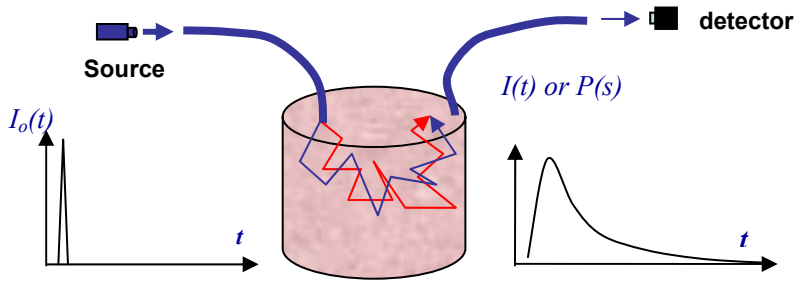

Figure II.12 The distribution of paths, P(s), described can be experimentally determined by measuring I(t) at a detector position following an pico- or femto- second light impulse at a source point.

Herein, both the isotropic mean free scattering length l^* (the inverse isotropic scattering coefficient), and path distribution function P(s) are sensitive to the light scattering properties of suspensions, which depend upon particle size distribution, particle concentration, and particle interactions within the suspension. Obtaining the particle diffusion coefficient, D_p, from the intensity autocorrelation function requires independent measurement of the optical properties, or *P(s)*, μ_s' , and μ_a, of suspensions.[46, 47, 50]

For a dilute monodisperse suspension, the particle diffusion coefficient, D_p can be related to the particle diameter, σ, through Einstein-Stokes equation (II.13). For non-interacting polydisperse suspensions, the measured effective diffusion coefficient $D_{p,eff}$ is averaged over all particles, and is related to the particle number distribution f(x) by:

$$D_{p,eff} = \int_0^\infty \frac{f(x)}{l^*(x)} D_p(x)dx \Big/ \int_0^\infty \frac{f(x)}{l^*(x)} dx \qquad \text{(II.18)}$$

where $l^*(x)$ is the scattering length for a suspension with particles of diameter x, and indicates scattering power of particle of different sizes.[54] Eqn (II.18) composes an inverse problem to be solved for particle size distribution.[54]

For interacting suspensions, the measured diffusion coefficient can not be related to the particle diameter via the Einstein-Stokes equation (II.13). It not only depends on the particle size, but also depends on the particle density-density response function, which addresses the response in particle positions at the time, $t+\Delta t$, with respect to the particle position at a previous time t.[55] The density-density response function is also termed dynamic structure factor, and depends on the particle volume fraction, particle size distribution, and particle interaction potentials. The time-averaged position correlation function, or called radial distribution function (RDF), is related to the static structure factor. RDF and static structure factor will be introduced in the next chapter.

For a interacting suspension, the measured effective particle diffusion coefficient $D_{p,eff}$ is a complicated function of the viscosity of suspending liquid, and dynamic structure factor: $D_{p,eff} = f(\eta, f(x), \text{dynamic structure factor})$.

The determination of particle size distribution has not been successful due to complexity in correlating to $D_{p,eff}$. Horne and coworkers even state that the DWS can not be used to determine the spread of particle size distribution in a dense interacting suspension.[51]

Though DWS has not been able to obtain particle size of interacting suspensions, it is extremely sensitive to the relative changes in particle interactions and dynamic properties.[50, 52, 56, 57]

Particle sizing using DWS needs the independent information of optical path distribution function, *P(s)*, in additional to the scattering and absorption properties of a colloidal suspension. Techniques, such as diffuse reflectance spectroscopy and frequency domain photon migration, only need the scattering information of *P(s)* in order to determine particle size distribution, and will be introduced in the following.

II.3.5. Diffuse reflectance spectroscopy

Diffuse reflectance spectroscopy (DRS) and diffuse transmission spectroscopy (DTS) have been developed in order to extend static light scattering techniques to characterize multiple scattering suspensions. DRS measures diffusely reflected multiply scattered light, while DTS monitors light traveling across a volume of multiply scattering volume (shown in Figure II.13).

The portion of diffusely reflected light (diffuse reflectance) and the portion of diffusely transmitted light (diffuse transmittance) both depend upon the absorption coefficient μ_a and isotropic scattering coefficient, μ_s' of the medium. These two wavelength dependent parameters govern the light propagation in multiple scattering media, where light propagation can be modeled via photon diffusion theory (introduced in Chapter IV). [58, 59]

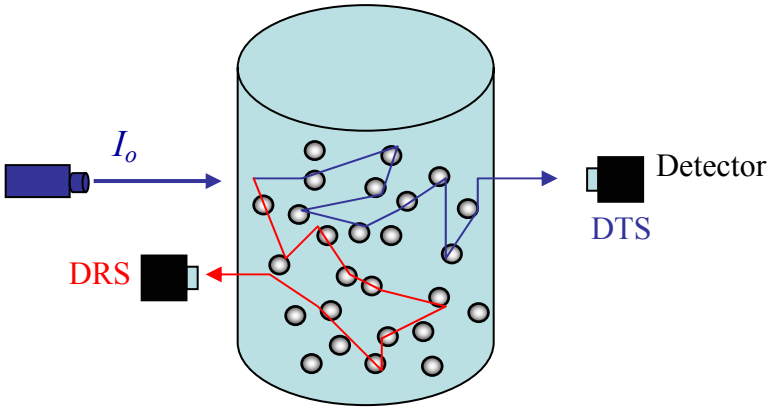

Figure II.13 DRS depend upon monitoring the portion of diffusely reflected light of an incident source located on the same plane as the detector, while the diffuse transmittance measures the portion of light transmitted across a source to reach a detector.

The diffuse reflectance at a point detector located distance r from a point source, I(r), can be the estimated from the solution of optical diffusion equation with proper boundary conditions. For a semi-infinite medium, the intensity of the diffusely reflected light can be related to the optical properties of suspensions through:

$$I(r) \propto \frac{\exp(-\sqrt{3\mu_a(\mu_a+\mu_s')}r}{2\pi r^2}\left[\sqrt{3\mu_a(\mu_a+\mu_s')}+1/r\right] \qquad \text{(II.19)}$$

From the measured intensity of diffusely reflected light as a function of source-detector separation distance, *r*, one can obtain the information of absorption μ_a and μ_s'.

It is possible to solve the following integral equation as an inverse problem to obtain the particle size distribution f(x) or even volume fraction, from multiple wavelength measurements of isotropic scattering coefficients, μ_s':

$$\mu_s'(\lambda) = \frac{3\phi_v}{2}\int_0^\infty \frac{Q_{sca}(\lambda,x)(1-g(x,\lambda))f(x)}{x}dx \qquad \text{(II.20)}$$

where ϕ_v is the volume fraction. The scattering anisotropy g(x, λ) can be computed from the classic scattering theory, as introduced in the first section of this chapter.

Since the two optical properties appearing in Eqn (II.19) are combined as the product of $3\mu_a(\mu_a + \mu_s')$, it is difficult to extract the absorption and isotropic scattering coefficients independently of one another. In order to solve the inverse problem of Eqn (II.20) for the particle size distribution, *f(x)*, empirical correlation or auxiliary measurement is required to determine μ_s' in order to apply DWS or DTS.

It requires the accurate determination of isotropic scattering coefficients separated from absorption coefficients for robust characterization of multiply scattering suspensions. Frequency-domain photon migration (FDPM) introduced in the following subsection is one of techniques capable of determining separated isotropic scattering and absorption coefficients separately and accurately.

Similar expressions can be found for diffuse transmittance measurements, and will not be provided here.[60]

II.3.6. Frequency domain photon migration

Frequency domain photon migration (FDPM) illustrated in Figure II.14 depends on measuring "time-of-flight" light propagation to extract isotropic scattering coefficients independent from absorption coefficients for a multiply scattering suspension. FDPM requires launching a "photon density wave," whose intensity is modulated to vary sinusoidally with time, and measures the phase shift (PS) and amplitude attenuation of the propagating photon density wave relative to the incident light. Upon modeling the propagation of the incident "photon density wave" using a

diffusion analysis,[58, 59] the measurements of phase shift and amplitude as a function of modulation frequency or source-detector separation distance can be fitted to a first principles model to obtain the absorption, μ_a and isotropic scattering coefficient, μ_s', independently.[61]

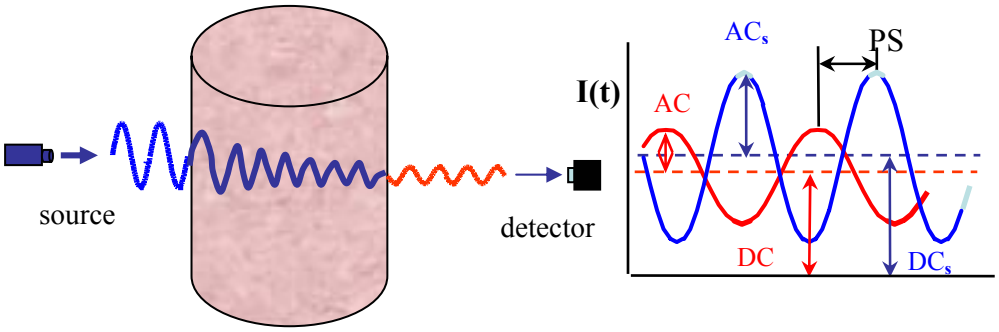

Figure II.14 Frequency domain photon migration measures the phase shift (PS) and amplitude attenuation (AC) of the propagating photon density wave in a multiple scattering medium to determine the isotropic scattering and absorption coefficients.

FDPM actually determines the propagation characteristics of light in a multiple scattering medium, rather than the absolute intensity of the scattered light, so no external calibration or sample reference is required. From FDPM measured isotropic scattering coefficient as a function of wavelength, one can solve the inverse problem of Eqn (II.20) to obtain the particle size distribution *f(x)* and volume fraction of a independent multiply scattering suspensions from multiple wavelength measurements of isotropic scattering coefficients.

From multiple wavelength measurements at varying modulation frequencies between 30-100 MHz, members of Photon Migration Labs (in Texas A&M) have

demonstrated the ability to obtain the particle size distribution for polystyrene latex and titanium dioxide dispersions (with volume fraction > 1%).[5, 10-12, 62, 63] The effective mean particle size obtained from FDPM compares favorably to those obtained from the DLS measurement.

It is noted that Eqn (II.20) is only suitable to describe the light scattering from dilute suspensions, where particles scatter independently. Light scattering from suspensions with dependent scattering will be treated in Chapter III.

Using a non-invasive "photon density wave" and remote detection of the light signal via fiber optics, FDPM can be used to characterize hazardous particle streams on-line.

The classification of light scattering techniques for characterizing colloidal suspensions are summarized in the following table. It is noted that the classification cannot be considered rigorous. Instruments that combines both static and dynamic scattering have been developed.

Table II.1 Classification of light scattering techniques

	Single Scattering	Moderate Multiple Scattering	Multiple Scattering
Static	SALS, SAXS, SANS	Turbidity	DRS, DTS, FDPM
Dynamic	DLS	Cross-Correlation, Two Color Light Scattering	DWS

II.4. Acoustic and electroacoustic

Acoustics[64-74] and electro-acoustics[67, 68, 70, 71, 74-84] have been developed to characterize interactions and particle size of dense suspensions. The extinction and scattering of acoustic waves traveling across a suspension are responsive to particle size distribution, particle volume fraction, as well as particle interaction of the suspension. Therefore, the measurements of propagation characteristics of acoustic waves may provide information of the suspensions. The physics of characterizing suspensions using acoustics or electroacoustics will be briefly summarized in this section.

II.4.1. Acoustic techniques

Acoustic techniques measure intensity attenuation and propagation speed of a sound wave as a function of modulation frequency in order to obtain particle size distributions and volume fraction of colloidal suspensions.

The acoustic wave, or pressure wave, propagating in a suspension can dissipate through following mechanisms:[85]

1. Viscous (hydrodynamic) mechanism

   The dissipation of acoustic wave via viscous mechanism results from the "shear wave" generated by the suspended particles oscillating in the suspending solvent. The density difference between the particle and solvent causes the relative movement between particles and solvent near the particle surface and generates a shear wave, which dissipates acoustic energy through shear friction.

2. Thermal mechanism

The thermal mechanism caused by the temperature gradient aroused near the particle surface. This thermal extinction of acoustic wave can be explained by the thermal dynamic relations between pressure and temperature for both particles and the solvent.

3. Scattering mechanism

   Scattering of acoustic wave is analogous to the scattering of light. Acoustic scattering changes direction of propagating acoustic wave and does not dissipate its kinetic energy.

4. Structure mechanism

   Structure extinction arises from the particle position correlation due to the particle interactions. Depending upon the frequency of propagating acoustic wave and the correlation length in the particle positions, the structure in a dense suspension may either increase or decrease the dissipation of acoustic wave.

5. Intrinsic loss

   The intrinsic loss refers to the dissipative loss of acoustic wave due to thermal motion of molecules of the wave carrier. The intrinsic loss in a solid phase is negligible in comparison to that in a liquid phase.

6. Electrokinetic mechanism

   The oscillation of a charged particle in a suspension generates an alternative electric field, which extracts energy from the acoustic wave. The

electrokinetic loss refers to the energy conversion from mechanical energy to electromagnetic energy.

In comparison to the mechanism of light extinction, the extinction of acoustic wave is much more involved. However, the methodologies of instrumentation for acoustic spectroscopy and frequency domain photon migration (FDPM) are similar. Both acoustic approaches and FDPM depend upon measuring attenuation and phase shift of propagating wave in a suspension.

In acoustics, the propagation (including the reflection and scattering) characteristics of a low intensity sonic wave is measured while it transverses a suspension from a vibrator driven by a RF generator to a sound detector, which converts sound wave to a RF signal for data acquisition as shown in Figure II.15.

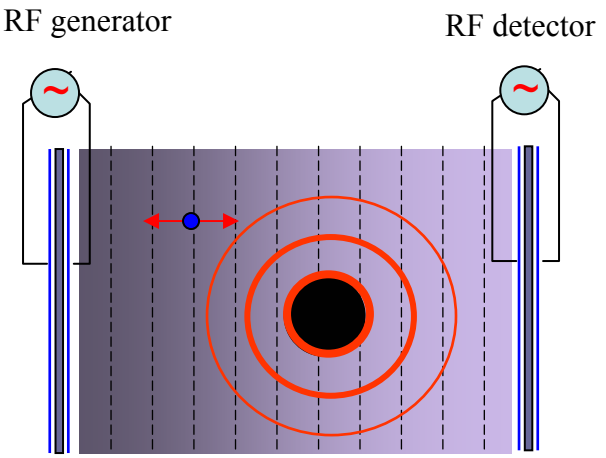

Figure II.15 Acoustic techniques detect the propagation (including the reflection and scattering) of low intensity sound waves transiting a suspension between a vibrator driven by a RF generator and sound detector, which converts the sound wave to a RF signal.

II.4.1.1 Attenuation spectroscopy

When particle sizes are comparable to or larger than the wavelength of the acoustic wave, the transmitted intensity of ultrasound wave $I(\omega)$ at frequency ω after passing a sample cell with path length, L, can be related to the acoustic extinction coefficient $K(\omega)$ by:

$$I(\omega) = I_o(\omega)e^{-LK(\omega)} \tag{II.21}$$

where $I_o(\omega)$ is the intensity of the incident ultrasonic wave. Eqn (II.21) is in the same form of Eqn (II.7) that describes light scattering in a single scattering medium. Eqn (II.21) suggests that acoustic techniques based on the Eqn (II.21) can not be applied to a multiple scattering system. For a singly scattering medium, the extinction coefficient can be related to particle area concentration ϕ_A, and the particle ultrasonic extinction efficiency $\alpha(\omega,x)$ by:

$$K(\omega) = \phi_A \int_0^\infty \alpha(\omega, x) f_A(x) dx \tag{II.22}$$

where f_A is the particle area density distribution. Upon replacing $K(\omega)$ in Eqn (II.21) with Eqn (II.22), Equation (II.21) takes a similar form to Eqn (II.8), which describes light extinction in the turbidity measurements.

The extinction of an acoustic wave introduced previously is much more involved than that of light wave. First principles models have been created to predict $\alpha(\omega,x)$ from material properties of the suspensions.[64] The analytical models for $\alpha(\omega,x)$ have been developed by O'Brien,[76] Dukhin and Goetz, and have been summarized in the monograph by Dukhin and Goetz.[85] These models not only require structure

information to address the structure loss, but also need numerous other material properties to address the viscous, thermal, and intrinsic loss as well as scattering loss. The details of these acoustic loss models will not be provided here.

With a model addressing particle ultrasonic extinction efficiencies, $\alpha(\omega,x)$, particle size distribution can be obtained from measured acoustic attenuation spectrum by solving an inverse problem of Eqn (II.22) from measured ultrasonic extinction coefficient $K(\omega)$ as a function of frequency.

II.4.1.2 Acoustic velocity spectroscopy

When a sonic wave travels through a suspension, the suspended particles will move along with the oscillating sonic wave with a phase lag, and exert a drag force that tends to slow down the traveling sonic wave. At low ultrasonic frequencies, the suspended particles will move in phase with oscillating acoustic pressure wave, and the reflection and scattering of propagating sound waves do not depend on the particle size. The transmission and reflection of a sound wave in such a suspension depend upon the mismatch between the acoustical impedances for the suspending fluid and the suspended particles. The acoustical impedance is defined as the complex ratio of pressure to the velocity, and is a material property related to the density and compressibility of materials. Due to the presence of the particles, the velocity of low frequency acoustic wave under propagation is reduced to an extent depending upon the particle concentrations. Upon measuring the speed of the acoustic wave in the suspension, the particle concentration can be inferred.

Upon combining acoustic attenuation spectroscopy and velocity spectroscopy, both the particle distribution and particle concentration can be determined from acoustic measurement of attenuation and speed of propagating sound wave as a function of frequency.

Generally, prediction of sound propagation using first principles model requires determination of many properties of particles and solvents.[86] These properties are listed in the following table.

Table II.2 Properties that affect the ultrasound probation in a colloidal suspension. Adopted from reference.[85]

	Suspending fluid	Suspended particles
Density	Yes	Yes
Compressibility	Yes	Yes
Isobaric heat capacity	Yes	Yes
Thermal conductivity	Yes	Yes
Thermal expansion coefficient	Yes	Yes
Shear viscosity	Yes	No

Determination of these properties need additional measurements, which limits the application of acoustic techniques.

II.4.2. Electro-acoustic techniques

Electroacoustic techniques include electro acoustic sonic amplitude (ESA) and Chemical vibration potential (CVP) (or ultrasonic vibration potential (UVP)). ESA measures the phase lag and amplitude of the pressure wave generated by motion of charged particles driven by an oscillating electromagnetic filed. CVP[67, 85, 87-90] measures the electric signal generated from the oscillation of charged particles driven by acoustic wave at varying frequencies.

II.4.2.1 Electroacoustic sonic amplitude

Electrokinetic sonic amplitude (ESA) measurement depends on the generation of a sound wave due to the oscillation of charged particles in the imposed electrical field. An external oscillating electric field causes the vibration of the charged particles in the suspension.

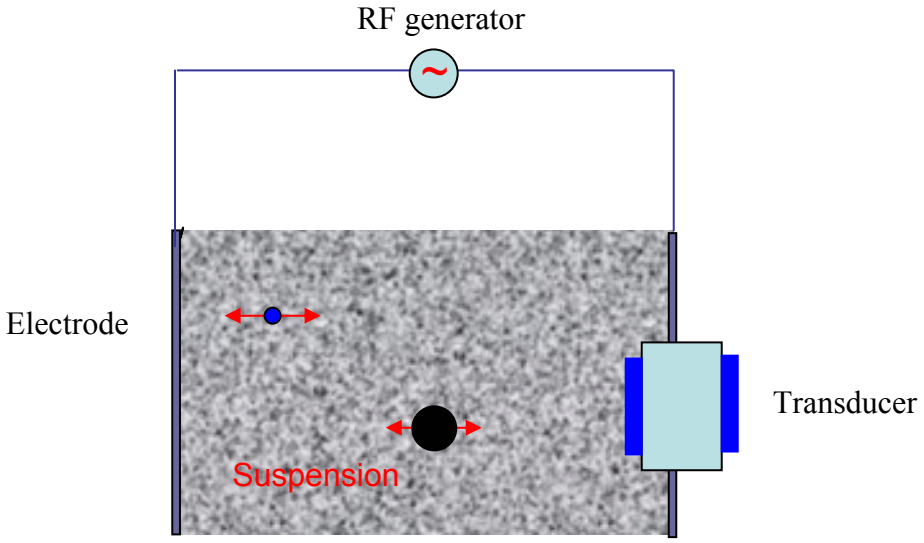

Figure II.16 An external oscillating electric field causes the vibration of the charged particles in the suspensions. The movement of particles generates a sound wave which propagates to a receiver for detection.

The movement of particles generates a sound wave which propagates to a receiver for detection (shown in Figure II.16). The application of ESA for characterizing dense suspensions has been summarized by Hunter[81, 91], Dukhin and Goetz.[85]

In order to drive suspended particles to move and generate sonic wave, the imposed electrophoretic forces must overcome inertial force of particles and drag force exerted on particles by solvent. The intensity of generated sonic wave and its phase lag with respect to the driving external electric field depend on the particle mobility, μ_D. Particle mobility, μ_D in ESA measurements can be predicted by: [85]

$$\mu_D = \frac{ESA(\omega)\rho_l}{A(\omega)F(Z_T, Z_s)\phi_v(\rho_p - \rho_l)} \tag{II.23}$$

where ESA(ω) is normalized by the applied external electrical field; A(ω) is an instrument parameter, and can be determined by suitable calibration; $F(Z_T, Z_s)$ is a function that depends upon the impedance of transducer, Z_T, and the suspension under testing, d; ρ_l and ρ_p are the density of the suspending solvent and particle respectively.

In CVP measurements, a similar relation to Eqn (II.23) exists, and particle mobility, μ_D can be predicted by: [85]

$$\mu_D = \frac{CVI(\omega)\rho_l}{A(\omega)F(Z_T, Z_s)\phi_v(\rho_p - \rho_l)} \tag{II.24}$$

where $CVI(\omega)$ measurement is normalized by the pressure gradient, which generates the CVI.

From either the ESA or CVI analysis of the measured magnitude and phase lag of the generated acoustic or electric wave, one can determine particle dynamic mobility,

μ_D. The particle mobility, μ_D, depends upon particle sizes and zeta potential of the particles, where zeta potential is defined as the potential at the particle shear plane surrounding particles. Within the shear plane, the counter ions attach on a particle and move with the particle in Brownian motion, and counter ions outside the shear plane may have relative movement with respect to the particle.

At higher modulation frequencies, and the determined average dynamic mobility, $< \mu_D(\omega) >$, as a function of acoustic frequency, can be related to the mass based particle size distribution $f_m(x)$ by:

$$< \mu_D(\omega) >= \int_0^\infty \mu_D(\omega, x) f_m(x) dx \qquad \text{(II.25)}$$

where $\mu_D(\omega, x)$ is the mobility for particles of diameter x at the acoustic frequency, ω.

The particle mobility $\mu_D(\omega, x)$ is also proportional to the zeta potential of particles, and also depends on the particle pair-wise interaction potentials (introduced in the next chapter) and particle volume fraction. Models that relate particle mobility to particle size, volume fraction and zeta potentials have been summarized in the monograph by Dukhin and Goetz. [85]

Upon measuring average dynamic mobility, $< \mu_D(\omega) >$, as a function of modulation frequency, particle size distribution or zeta potential can be determined from solving a Fredholm inverse problem composed by Eqn (II.25). The relation between zeta potential and mobility will be introduced in Chapter III.

Like acoustics, an electro-acoustic technique also requires several material properties for the suspended particle and suspending fluids (shown in the Table II.3).

The accuracy of electroacoustics strongly depends on the accuracy and precision of data for these material properties. In emulsions, the compressibility of particles depends upon the size and surfactant concentration, which makes the problem even more complicated.

Table II.3 Material properties required in electro-acoustic measurement. Adopted from reference [85]

	Suspending fluid	Suspended particles
Density	Yes	Yes
Compressibility	Yes	Yes
Isobaric heat capacity	Yes	Yes
Thermal conductivity	Yes	Yes
Thermal expansion coefficient	Yes	Yes
Shear viscosity	Yes	No
Permittivity	Yes	No
Electrical conductivity	Yes	No

Commercial acoustics and electro-acoustic instrumentation are currently available. To increase the robustness of the characterization and the measurement range of the instrumentation, both acoustic measurements and electro-acoustic measurements are combined in one instrumentation setup.

Although ESA or CVP measurements have been used to characterize dense suspensions, values representing zeta potentials obtained from ESA or CVP

measurements differ from those measured using standard electrophoresis measurement.[75,92]

Unlike optical "ensemble" techniques, acoustic and electro-acoustic approaches are not affected by optical properties of the suspensions, and they are especially suitable to estimate the particle size and volume fraction for strongly absorbing dispersions, such as pigments and paints suspensions, which can not be determined by techniques such as DTS and FDPM. However, the optical properties for pigments and paints have to be determined through optical ways. The characterization of optical properties for pigments in industry will be briefly introduced in the following section.

II.5. Pigments characterization in industry

The design of product appearance is an important industrial practice for pigment and paint industries. The absorption and scattering properties of pigment and paint particles determine the appearance of coated layer and are critical to the color prediction and color matching in formulating paints and cosmetics. The color of the coatings is decided by the light absorption of pigments, and the gloss depends on the light scattering of the pigments. Light absorption efficiency is extremely critical to the color matching and color prediction in the printing and hair dyes. Currently, color matching is still based on *phenomenological* theories, which are not based on first principles. The Kubelka-Munk (K-M) theory[93] is the most widely used phenomenological theory to describe pigments optical properties of pigments in industry and will be introduced in the following section.

II.5.1. Kubelka-Munk theory

In Kubelka-Munk theory, a coating layer is modeled as a heterogeneous phase, where the particle size distribution, particle concentration, and refractive indices for both particles and inter-particle materials are not considered in order to predicting the optical properties of the coating layer. Therefore K-M theory is *phenomenological* and not based on first principles. The K-M theory assigns the multiply scattered light propagating in a coating layer in one of two categories, diffuse forward propagating light L^+, and diffuse backward propagating light, as shown in Figure II.17

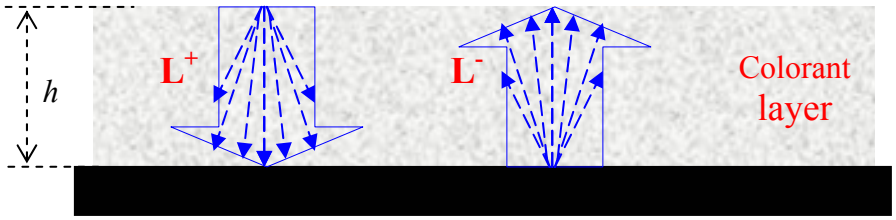

Figure II.17 Diffuse forward propagating light flux and diffuse backward propagating light flux in Kubelka-Munk (K-M) theory.

In K-M theory, the optical properties of the coating layer are represented by two parameters: scattering coefficient S (1/cm) and absorption coefficient K (1/cm). The K-M scattering coefficient, K is defined as light extinction when travels a unit length in a coating layer due to absorption only, and the K-M scattering coefficient, S, is defined as light extinction when travels a unit length due to scattering only:

$$K = \left(\frac{1}{L}\frac{dL}{dz}\right)_{abs} \tag{II.26}$$

$$S = \left(\frac{1}{L}\frac{dL}{dz}\right)_{sca} \tag{II.27}$$

Since a multiply scattering medium in K-M theory is considered as a continuous phase, absorption and scattering coefficients, K and S, can not be related to the physical properties of pigment particles and inter-particle medium. The values of K and S which are characteristics of a coating layer must be determined experimentally.

II.5.2. Measurements of K and S

The classical method for measuring K and S requires the knowledge of the diffuse reflectance from two layers of the same coating dispersion: one layer has the thickness of *h* (shown in Figure II.17) and is coated on a substrate with the diffuse reflectance R_o^*; another layer is thick enough to be considered as infinite and has the diffuse reflectance of R_∞^*.[94] The surface diffuse reflectance for these two layers, R^* and R_∞^* is then measured for the determination of the values for *K* and *S* for the coating dispersion.

Two auxiliary parameters of *a* and *b* can be evaluated from the diffuse reflectance of coating layer with "infinite" thickness, R_∞^* by:

$$a = \frac{1}{2}\left(\frac{1}{R_\infty^*} + R_\infty^*\right) \tag{II.28}$$

$$b = a - R_\infty^* = \frac{1}{2}\left(\frac{1}{R_\infty^*} - R_\infty^*\right) \tag{II.29}$$

The values of *K* and *S* can then be determined from solving the following equations:

$$S = \frac{1}{bh}\coth^{-1}\left(\frac{1 - a(R^* + R_o^*) + R^* R_o^*}{b(R^* + R_o^*)}\right) \tag{II.30}$$

$$K = S(a - 1) \tag{II.31}$$

A second method to determine K and S is through the measurements of the surface reflectance R_b^*, and R_w^* for two coating layers, which have the equal thickness of h, and cover standard black and standard white substrates with diffuse reflectance of R_{ob}^* and R_{ow}^* respectively. Then the parameters, a and b, can be determined from:

$$a = \frac{(1 + R_w^* R_{ow}^*)(R_b^* - R_{ob}^*) + (1 + R_b^* R_{ob}^*)(R_{ow}^* - R_w^*)}{2(R_b^* R_{ow}^* - R_w^* R_{ob}^*)} \tag{II.32}$$

$$b = \sqrt{a^2 - 1} \tag{II.33}$$

Then the values for K and S can be determined from Eqns (II.30) and (II.31) straight forwardly. The standard black and white substrates are typically made of ceramics and are commercially available.

The measurements of K and S as a function of wavelength can be used to represent the optical properties of a coating layer, and can also used to represent the optical properties of pigments.

II.5.3. Characterization of pigments in industry

In order to characterize the optical properties of pigment particles, the pigment particles must be first mixed into a multiply scattering dispersion with other additives to form a mixture. The dispersion used to dilute the pigments is thus frequently termed "dispersing vehicle." Then the mixture is coated either on different standard substrates or on same substrates but with different thickness, depending on the chosen method (introduced previously). The diffuse reflectance is then measured after coating layers are dried in order to determine K-M absorption and scattering coefficients, K and S, from Eqns (II.30) and (II.31) as a function of wavelength (as shown in Figure II.18).[94]

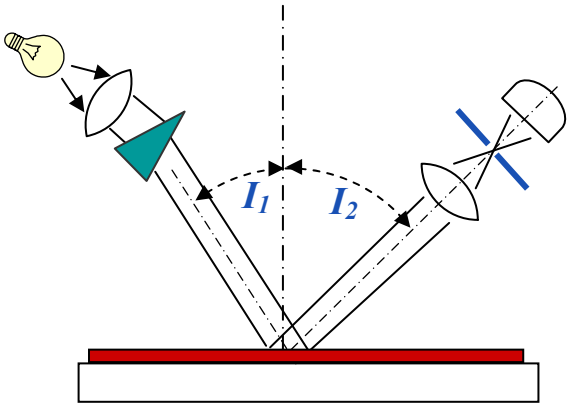

Figure II.18 Determination of the K-M scattering and absorption coefficients requires first dispersing the testing pigments in an agreed-upon suspension called the vehicle, and then coating the suspensions on a standard substrate at two different thicknesses or on two different standard substrates with same thickness.

The above measurements as a function of wavelength need to be repeated with different concentration of testing pigments. The differential contributions to the $K(\lambda)$ and $S(\lambda)$ from pigments at different concentrations can be considered as characteristics to represent the absorption and scattering efficiencies of the testing pigments.

Since the measured properties for a pigment differs from lab to lab, a third common reference is usually needed for comparing pigments. This time and capital consuming process does not employ first-principle properties to guide R&D and industrial practice, and industry urgently requires new methods capable of characterizing absolute physical properties and the first principle theory for color prediction and quality assurance.

Due to difficulties in characterizing accurate optical properties of pigments and a limited understanding of light interaction within a coated layer, the physics behind the overtone and gloss has not been quantitatively understood. Currently, industry requires

the representation of pigment properties using first principles models to enable more accurate color prediction and color matching.

CHAPTER III

STRUCTURE OF DENSE SUSPENSIONS

This chapter presents the physics and chemical engineering principles pertinent to the research described in the subsequent chapters. In the second section of Chapter II, we have introduced dependent scattering where the particle effective scattering efficiency depends upon correlated particle positions. Description of dependent scattering using interference approximation requires knowledge of correlated particle positions (or termed structure) arising from particle interactions. This chapter will introduce background of colloidal structure theory and an approach for predicting light scattering from colloidal structure associated with interference approximation. Topics of discussion include:

1. introduction of particle interactions in suspensions;
2. introduction of liquid theory describing microstructure of suspensions; and
3. introduction of the use of interference approximation to address light scattering of concentrated suspensions.

The most frequently used pair-wise particle interaction potential models will be introduced first before presenting structure factor model based on O-Z integral equation.

III.1. Particle interaction potential models

The particle interactions in a colloidal suspension are complicated functions of many factors, including particle size distribution, particle surface charges, particle concentration, and solvent conditions, etc. Theoretical modeling of correlated particle

positions demands approximate particle interaction models. Some of these particle interaction models are summarized in the following section.

III.1.1. Hard sphere interactions

The simplest interaction is the hard sphere interactions, which only account for the volume exclusion effects and prohibit spatial overlapping of particles. The hard sphere interaction potential, $u_{ij}(r)$, between particles of diameters σ_i and σ_j can be presented as:

$$u_{ij}(r) = \begin{cases} \infty & r \le \sigma_{ij} = \dfrac{1}{2}(\sigma_i + \sigma_j) \\ 0 & r > \sigma_{ij} \end{cases} \qquad \text{(III.1)}$$

Wherein the potential energy is infinitely great for $r < \sigma_{ij}$, (thus preventing the occurrence of volume overlapping of particles), and particles feel no attractive or repulsive forces when they are separated by $r > \sigma_{ij}$. Particles in this model are considered as rigid hard spheres, and Eqn (III.1) is termed as the hard sphere interaction potential.

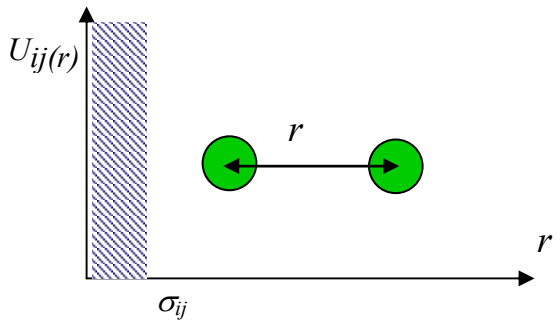

Figure III.1 Hard-sphere interaction potential of particle with diameter σ in a monodisperse suspension as a function of particle separation distance r.

Hard sphere interactions are dominant in dispersions of weakly charged, rigid spherical particles. Figure III.1 illustrates the hard sphere interaction.

The hard sphere interaction model has been widely applied in understanding the microstructure of concentrated suspensions.[95-101] The hard sphere interactions that are extended to include a short range attractive force (Figure III.2), are called attractive hard sphere interactions, and are used to mimic attractive force along with the steric repulsive force.[28, 102-105]

The attractive hard sphere interactions are useful in studying the interactions among clustering particles, such as cell particles or particles with adsorbed or grafted short polymer chains. The simplest model approximates attractive interaction as a constant when particle separation distance is within a small range, $\sigma_{ij}<r<\sigma_{ij}+d$:

$$u_{ij}(r) = \begin{cases} \infty & r \le \sigma_{ij} \\ u_o & \sigma_{ij} < r \le \sigma_{ij} + d \\ 0 & r > \sigma_{ij} + d \end{cases} \qquad \text{(III.2)}$$

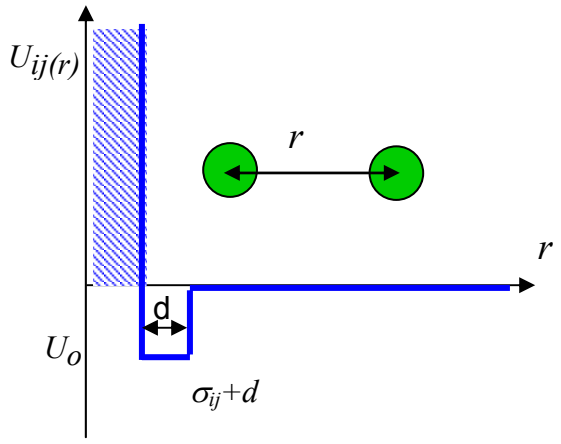

Figure III.2 Attractive hard sphere interaction between two particles.

III.1.2. Electrostatic interaction

In reality, all particles in a suspension are charged due to: 1) surface ionizable groups; 2) adsorption of ions from the solvent; and 3) imperfect crystalline structure, which results in holes and free electrons.[4, 106, 107] Even though volume exclusion interactions usually dominate in concentrated suspensions, the electrostatic interaction (ESI) in dense suspensions are critical for many industrial applications, such as stability of suspensions, emulsion polymerization, and crystallization of nano-particles.[4]

III.1.2.1 Primary model (PM) interactions

The interactions among charged suspensions can be represented by including a long range electrostatic interaction in addition to the volume exclusion effects (Figure III.3). The primary electrostatic interaction model describes the interactions among charged colloidal particles as direct Coulombic interactions in addition to the volume exclusion effects: [106, 107]

$$u_{ij}(r) = \begin{cases} \infty & r \le \sigma_{ij} \\ {e_o}^2 z_i z_j / (4\pi\varepsilon_r \varepsilon_o r) & r > \sigma_{ij} \end{cases} \qquad \text{(III.3)}$$

where e_o is the charge for a electron; ε_0 is the electric permittivity of vacuum; and ε_r is the dielectric constant of suspending fluid. The terms, z_i and z_j, are the charges in the unit of electron charge for the particle of size σ_i and σ_j respectively.

The charge neutrality in the PM model is enforced by setting $\sum_i \rho_i z_i = 0$, where ρ_i is the number density of the component *i* in the colloidal mixture.

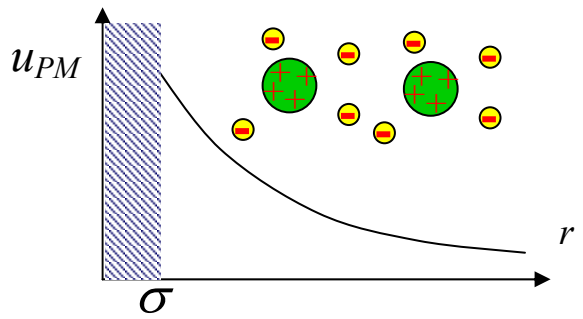

Figure III.3 Electrostatic interaction potential in the primary model as a function of particle separation distance between two charged colloidal particles (large circles). The counter ions are presented as small circles.

In the primary model, each kind of counter ions species is also considered as a component in the suspension, and charged colloidal particles are sometimes called macro ions. The PM model states that the presence of the counter ions will not impact the direct interaction among charged particles.

III.1.2.2 Hard Sphere Yukawa (HSY) interaction

Upon considering the screening effects, which are neglected in the PM model, the effective pair-wise interaction potential among charged particles in a monodisperse suspension can be described using hard sphere Yukawa (HSY) model:[108]

$$u(r) = \begin{cases} \infty & r < \sigma \\ e_o^{\,2} z_{eff}^{\,2} < \sigma > \exp(-\kappa(r-\sigma))/(4\pi\varepsilon_r\varepsilon_o r) & r > \sigma \end{cases} \qquad \text{(III.4)}$$

The parameter σ is the particle diameter; z_{eff} is the effective particle surface charge; and κ is the inverse Debye screening length defined by:

$$\kappa^2 = \frac{4\pi e_o^2}{\varepsilon_r k_B T} \sum_i n_i z_i^{\,2} \qquad \text{(III.5)}$$

where k_B is the Boltzmann constant, and T is the absolute temperature. Here n_i is the molar concentration of micro ion species i with valance z_i. The effective surface charge may not be equal to the charge located on the particle surface. The effective surface charge can be estimated from zeta potential, which refers to the electrostatic potential at the particle shear plane, and will be introduced in the Chapter V. In HSY, a charged particle is surrounded by a cloud of counter ion layer, whose thickness is characterized by, κ^{-1}. The Debye screen length decreases with increasing ionic strength at a given surface charge. The charged particles repulsively interact through volume exclusion and double layer overlapping, wherein the charge neutrality is not maintained. The hard sphere Yukawa interaction model is illustrated in Figure III.4. The HSY interaction model for monodisperse suspension is also usually termed as one component model (OCM).[109]

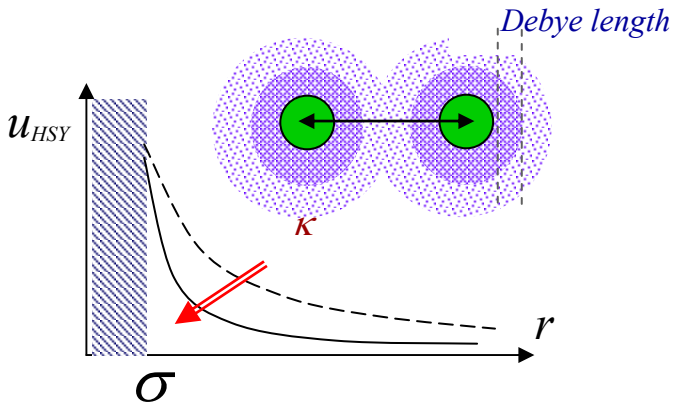

Figure III.4 Hard sphere Yukawa interaction potential as a function of particle separation distance. The charged particles repulsively interact through volume exclusion and double layer overlapping, wherein the charge neutrality is not maintained.

III.1.3. DLVO interaction potential

The van der Waals attractive force between small particles can usually be neglected. The effects of van der Waals attraction between large particles may become significant. The Derjaguin-Landau-Verwey-Overbeek (DLVO) potential considers both electrostatic repulsion force and attractive dispersion force among particles.

Figure III.5 illustrates the general DLVO interaction potential. The DLVO interaction action potential between two similar suspended particles is presented as:[110]

$$U_T = -\frac{A_H}{12}\left(\frac{1}{\xi^2+2\xi}+\frac{1}{\xi^2+2\xi+1}+2\ln\frac{\xi^2+2\xi}{\xi^2+2\xi+1}\right)+8\sigma\varepsilon_r\varepsilon_o\left(\frac{kT}{\nu e_o}\right)^2\eta^2 e^{-\kappa h} \quad \text{(III.6)}$$

where A_H is the Hamaker constant, which depends on the material properties of the particles and suspending fluid, indicating the strength of attractive force; h is the boundary-to-boundary separation distance of particles; ξ is a dimensionless ratio of h to the diameter particles; the parameter η is defined by $\eta = \tanh(\nu e_o \varphi_o / 4kT)$; φ_o is electric potential at the particle surface, with the position at infinite distance from particle as the reference; and ν is the valance of the counter ions. DLVO has been used to qualitatively predict the stability of the colloidal suspensions. The generalized DLVO potential is illustrated in Figure III.5.

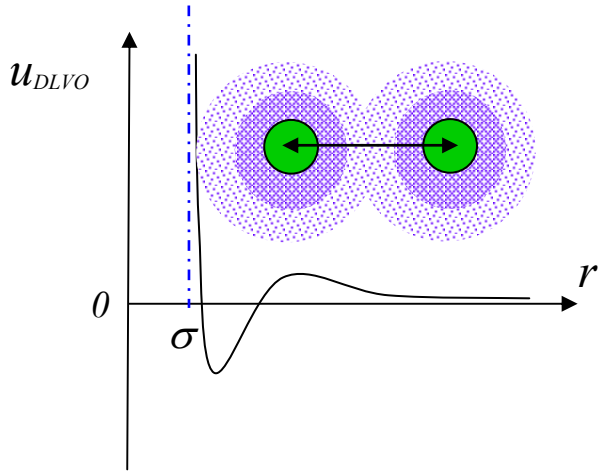

Figure III.5 A general DLVO interaction potential between two charged particles as a function of separation distance r.

Depending on the relative magnitude of van der Waals forces and repulsive electrostatic forces, the minimum and secondary maximum shown in Figure III.5 may not exist, where the first maximum usually refers to the infinite potential at the overlapped condition.

When large polymer molecules are added into the colloidal suspensions, the depletion force resulting from added polymer due to either entropic or enthalpy effects will also mediate the particle interactions.[4] The addition of polymer molecules has long been used to stabilize the particle suspensions. The depletion interaction will not be addressed here for brevity, but has been studied extensively using FDPM by Shinde and coworkers.[6]

The introduced particle interactions can affect the optical properties of suspensions by generating particle position correlation, or termed as structure. The effects of electrostatic interactions described either in HSY model (Eqn (III.1)) or PM model (Eqn (III.3)) can be used to predict colloidal structure describable via a structure

factor model. The structure factor models derived from Ornstein-Zernike (O-Z) integral equation approach will be introduced in the following section.

III.2. Static structure factor

Particles in concentrated suspensions are not randomly orientated, and the ordering in particle spatial arrangement forms the colloidal "structure" arising from the particle interaction potentials presented above. Figure I.1 in the first chapter illustrates the ordering of particles in the 2-D. The structure of a suspension is typically expressed by the radial distribution function, g(r) (Figure III.6).[55]

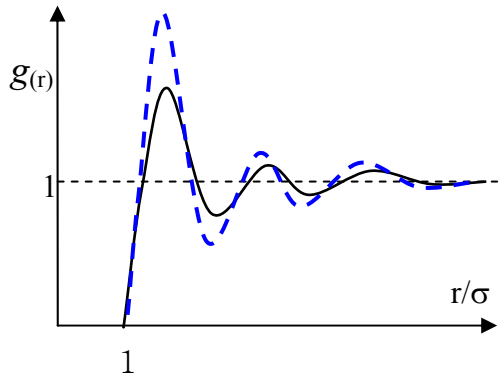

Figure III.6 Radial distribution function represents the possibility of finding another particle at the distance r with respect to the particle with diameter σ. Generally, the higher the oscillating amplitude in the g(r) curve, the more ordering exists in the particle spatial correlation in general.

A radial distribution function (RDF), or pair correlation function (PCF), $g_{ij}(r)$, which describes the possibility of finding a particle of component *i* at center to center distance *r* with regard to another particle of component *j*, can portray correlated particle positions between these two components. Typically, the higher the oscillating amplitude

in the g(r) curve (Figure III.6), the more ordering exists in the particle spatial correlation. If the value of the PCF $g_{ij}(r) = 1$, it means there is no favorable relative arrangement among positions of component *i* and component *j*, and their relative positions are completely random.

A radial distribution function, or pair correlation function, $g_{ij}(r)$, can portray correlated particle positions between components *i* and *j*, but cannot be readily combined with interference approximation to address dependent scattering arising from the correlated particle positions. The Fourier transform of the RDF results in the static structure factor S(q) function shown in Figure III.7, where *q* is the scattering vector. The structure factor S(q) describes the resonance spatial frequencies and is a direct measure of the local ordering of colloidal particles.[55]

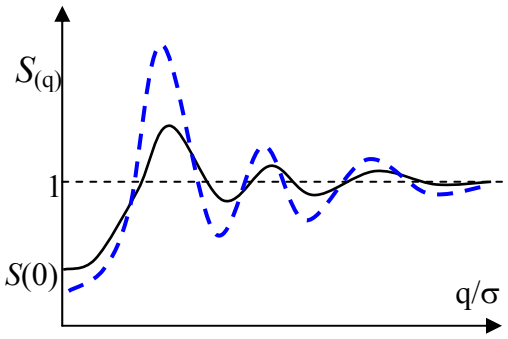

Figure III.7 Static structure factor S(q) versus dimensionless scattering vector q/σ, where σ is the particle diameter. Generally, the higher the oscillating amplitude in the S(q) curve, the more ordering exists in the particle spatial correlation in general.

For a monodisperse suspension, the static structure factor at zero scattering vector, S(0) is related to the isothermal compressibility χ_T, by:[111]

$$S(0) = \rho k_B T \chi_T \tag{III.7}$$

where ρ is the particle number density; k_B is the Boltzmann constant and T is the temperature in Kelvin.

The static structure factor can be experimentally measured from small angle light, neutron, or x-ray scattering, where the angle-dependent intensity of light scattered by a suspension at a small angle is detected after transiting a concentrated suspension. The small path length must be sufficiently small and refractive index matching is frequently used in order to quench multiple scattering. It is also possible to predict structural factor from particle interaction position models using first principles model. The next section will introduce predicting structure factor through Orstein-Zernike integral equation.

III.3. Structure factor theory

III.3.1. Ornstein-Zernike integral equation

Statistical mechanics theory,[55] which predicts the thermodynamic properties of the liquid, has been incorporated to describe correlated particle spatial arrangement in a concentrated suspension.[20] The correlated particle positions are typically represented by pair correlation function (PCF), $g_{ij}(r)$, or called radial distribution function (RDF). The pair correlation function (PCF), $g_{ij}(r)$ predicts the possibility of finding a particle of species *i* at distance r with respect to a particle of species *j*. In addition, the absolute value of total correlation function, defined as $h_{ij}(r) = g_{ij}(r) - 1$, equivalently indicates the ordering of colloidal suspensions. These correlation functions can be theoretically predicted upon solving the Ornstein and Zernike integral equation:[55]

$$h_{ij}(r) = c_{ij}(r) + \sum_{l} \rho_l \int c_{ij}(r')h_{lj}(|r - r'|)dr' \qquad \text{(III.8)}$$

Where c_{ij}(r) is called the direct correlation function between particle components i and j, which arises from direct particle interaction; ρ_l is the number density of particles of species l. The O-Z equation states that total interaction between two particles is equal to the summation of the direct interaction between them and the indirect interaction through all surrounding particles, as illustrated by the Figure III.8.

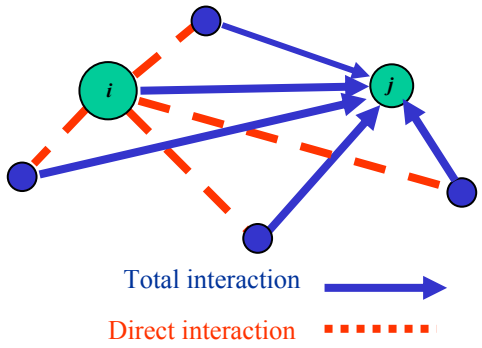

Figure III.8 Interaction of particles among a colloidal suspension: O-Z equation states that total interaction between two particles is equal to the summation of the direct interaction between them and the indirect interaction through all surrounding particles.

The O-Z equation for a monodisperse suspension can be simply written as:

$$h(r) = c(r) + \rho \int h(|r - r'|)c(r')dr' \qquad \text{(III.9)}$$

Including the relation between h_{ij}(r) and g_{ij}(r), O-Z equation (III.9) is not self-closed, and an additional closure relation is needed to make it a closed set. From diagrammatic expansion of interactions, one can obtain another relation among h(r), c(r), and u(r), called bridge relation:

$$h(r) - c(r) - \ln(h(r) + 1) = \beta \cdot u(r) - B(r) \tag{III.10}$$

Nonetheless, the bridge relation of Eqn (III.10) introduces another new function, $B(r)$, called bridge function whose exact form is not available. Therefore, an approximated bridge function, or an equivalent approximated relationship among three unknown functions h_{ij}(r), c_{ij}(r), g_{ij}(r) is needed to close the O-Z equation. This function is described below in Section III.3.2.

The Fourier transform of general O-Z equation of Eqn (III.9) can be presented in a matrix form in Fourier space:

$$[I + H(q)][I - C(q)] = I \tag{III.11}$$

where $q = \frac{4\pi}{\lambda} \sin\frac{\theta}{2}$ is the scattering vector; I is the identity matrix and $H(q)$, and $C(q)$ are the matrices with the elements respectively of:

$$H_{ij}(q) = (\rho_i \rho_j)^{1/2} h_{ij}(q) \tag{III.12}$$

$$C_{ij}(q) = (\rho_i \rho_j)^{1/2} c_{ij}(q) \tag{III.13}$$

where $h_{ij}(q)$ and $c_{ij}(q)$ are the 3-D Fourier transform of direct correlation function, $h_{ij}(r)$, and total correlation function, $c_{ij}(r)$, respectively. The partial static structure factor $S_{ij}(q)$ can be related to $h_{ij}(q)$ by :

$$S_{ij}(q) = \delta_{ii} + (\rho_i \rho_j)^{1/2} h_{ij}(q) \tag{III.14}$$

Therefore, once the direct correlation function, $h_{ij}(r)$, or the total correlation function, $c_{ij}(r)$ can be obtained from the solution of O-Z equation, the structure factor can be determined from Eqn (III.14).

A single structure factor is not sufficient to portray the microstructure of a polydisperse suspension, in which two or more different particle components of different sizes or charge are present. The partial structure factor $S_{ij}(q)$ indicates the averaged interference effects of light scattered from the component i and component j at wave vector q. A partial structure factor $S_{ij}(q)$ can only describe the spatial correlation of between components i and component j, and a matrix of partial structure factors is needed to completely depict the microstructure of colloidal mixture.

In diluted suspensions (volume fractions < 1%), particles scatter light independently, and $S_{ij}(q)$ reduces to identity. For a monodisperse system, $S_{ij}(q)$ simply reduces to a single structure factor function S(q).

Given an approximate closure relationship and a model describing particle interactions, the O-Z equation provides a way (shown in Figure III.9) of predicting the structure of concentrated suspensions through the structure factor.

As shown in Figure III.9, a particle interaction potential model is combined with a approximated closure model discussed below in order to close O-Z equation and make it solvable.

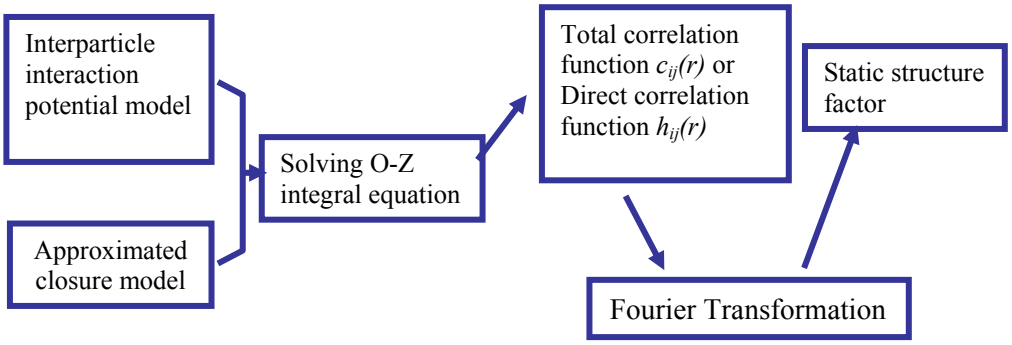

Figure III.9 Methodology of predicting structure factor from the solution of O-Z integral equation with a particle interaction model and an approximated closure relation.

Upon solving O-Z equation analytically or numerically, one can obtain the total correlation function $c_{ij}(r)$ or the direct correlation function $h_{ij}(r)$, whose Fourier transforms can be used to determine static structure factor via Eqn (III.14).

In the next subsection, the most popular closure relations to the O-Z equation will be summarized.

III.3.2. Introduction to the closure relations of the O-Z equation

The four most investigated closures are mean spherical approximation (MSA), Percus-Yevick (PY), Hyperneted Chain (HNC), and Rogers-Young (RY) relations.

III.3.2.1 Hypernetted-chain closure

The Hypernetted-chain (HNC) relation closes the O-Z equation by assuming that the bridge function takes following relation:

$$g_{ij} = \exp[-\beta u_{ij}(r) + h_{ij}(r) - c_{ij}(r)] \qquad \text{(III.15)}$$

This closure is effective for electrostatic interactions, including long-ranged Coulombic interaction, or screened-Coulombic interactions, especially at moderate charges and low volume fraction.[112-115] However, analytical solution to the O-Z equation

with this closure has not been found. Obtaining the structure information relies on the corresponding numerical solutions.

III.3.2.2 Percus-Yevick closure

The Percus-Yevick (PY) approximation closes the O-Z equation with the following relation:

$$c_{ij}(r) = \exp[-\beta u_{ij}(r) + \gamma_{ij}(r)] - \gamma_{ij}(r) - 1 \qquad \text{(III.16)}$$

where $\gamma_{ij}(r) = h_{ij}(r) - c_{ij}(r)$. With PY closure and hard sphere interactions, the O-Z equation has analytical solutions to monodisperse suspensions as well as to suspension mixtures. The PY approximation can be simplified from Taylor series expansion of the exponential term in Eqn (III.15) and neglecting the second and higher order terms. The PY approximation is also frequently expressed equivalently as:

$$g_{ij} = \exp[-\beta u_{ij}(r)] \cdot [h_{ij}(r) - c_{ij}(r)] \qquad \text{(III.17)}$$

The PY approximation provides a good description of structure for short range interactions, and are used extensively due to the availability of an analytical solution to the OZ equation for hard sphere systems [116, 117] and sticky hard-sphere systems.[102, 118]

III.3.2.3 Rogers-Young closure

To adapt the accuracies of the PY approximation at short ranged interactions, and the HNC approximation at long range electrostatic interactions simultaneously, the Rogers-Young closure[119] combined the HNC and PY approximations by using a mixing function, which interpolates both HNC and PY approximations. The Rogers-Young (RY) closure is given by:

$$g_{ij}(r) = \exp[-\beta u_{ij}(r)] \cdot \{1 + \{\exp[(h_{ij}(r) - c_{ij}(r))f(r)] - 1\} / f(r)\} \qquad \text{(III.18)}$$

where parameter α in the mixing function of $f(r) = 1 - \exp(\alpha \cdot r)$ is determined by requiring the isothermal compressibility obtained from the Virial equation and from the solution of the O-Z equation to match in order to achieve thermodynamic consistency. Unfortunately, the analytical solution of the O-Z equation with RY closure has not been found and a numerical solution is required.

III.3.2.4 Mean spherical approximation closure

The mean spherical approximation (MSA) simply assumes a linear relation between the direct correlation function, $c_{ij}(r)$, and the effective interparticle potentials, $u_{ij}(r)$ when particle are out of direct contact:

$$\begin{cases} h_{ij}(r) = -1 & r < \sigma_{ij} = (\sigma_i + \sigma_j)/2 \\ c_{ij}(r) = -\dfrac{u_{ij}(r)}{k_B T} & r > \sigma_{ij} \end{cases} \qquad \text{(III.19)}$$

where $u_{ij}(r)$ is the effective pair-wise interaction potential between particles of species *i* and *j* at the center-to-center distance, *r*. The first relation in Eqn (III.19) shows that $h_{ij}(r) = -1$ at $r < \sigma_{ij}$, is equivalent to $g_{ij}(r) = 0$, indicating hard sphere effects that prohibit space overlapping of particles. The second relation indicates the approximated asymptotic relation between c_{ij}(r) and pair-wise particle interaction potential $u_{ij}(r)$ at $r > \sigma_{ij}$.

Hayter and Penfold presented a structure factor model based on the analytical solution of the one component O-Z equation with hard sphere Yukawa potential based on Blum's solution.[120, 121] Recently, Herrera *et al.*[122] presented a simpler version of structure factor model for one component system. Also, Ginoza *et al.*[122-125]and Gazzillo

et al.[126] later each presented a structure factor model independently for the hard sphere Yukawa mixtures.

When dealing with dilute particle suspensions of strong ESI, the MSA predicts an unphysical negative $g(r)$ when $r < \sigma$. Hansen and Hayter addressed the negative RDF [73] by rescaling the particles physical diameter to a larger effective diameter σ_{eff}, which satisfies $g(\sigma_{eff}) = 1$. The new model is called rescaled mean sphere model (RMSA). Ruiz-Estrada *et al* extended this type of rescaling treatment to the multiple component systems.[127]

Using MSA closure, Hirioke[128, 129] derived the explicit expression for direct correlation function, c_{ij}(r), from the solution of the O-Z equation provided by Blum *et al.* [120, 121, 130] with primary electrostatic interaction model.

Other closures, including soft mean-spherical approximation have also been reported in literature,[55] but to our best knowledge, their analytical solutions are not available yet. A review regarding these closures can be found elsewhere.[131]

Upon solving O-Z equation from a given interaction potential model associated with a suitable closure relation, the structure factor can be determined and be used to address dependent scattering of concentrated suspensions.

III.4. Light scattering from suspensions

Light scattering efficiencies of closely positioned particles (with interparticle distances less than the wavelength of the incident light) depend on particle relation

orientation, no matter if particles exist in a concentrated suspension or form an isolated particle assembly.[16-18]

The amplitude distribution of the scattered light field varies with the correlated particle positions. If a scattering system consists only of a few closely position particles, it is possible to solve the governing Maxwell equation to obtain the scattering characteristics of these particles.[17, 18] A concentrated suspension usually contains billions of particles per c.c. It is difficult if not impossible to solve the Maxwell equations governing light scattering from enormous number of suspended particles under thermal motion. Practically, various approximations associated with a structure model addressing dependent scattering are usually used to predict scattering properties of these suspensions.

Interference approximation (IA)[20,26,132] is the most frequently used method and can be easily applied to predict light scattering properties of concentrated suspension.

III.4.1. Interference approximation

Interference approximation comprises the following assumptions: 1) correlated particle positions do not change the scattering pattern of individual particles or equivalently the secondary field is negligible in comparison to the incident field; 2) the changed particle scattering power results from the interference of light scattered from different particles at the far field; 3) the average interference effects of light can be described by a structure factor function.

Assuming the secondary field is negligible in comparison to the incident field, the microstructures in a suspension would not change the scattering pattern of the

individual particles. Therefore, IA implies that the microstructure in a suspension will not impact the particle absorption efficiency, which is inward scattering efficiency (Figure III.10).

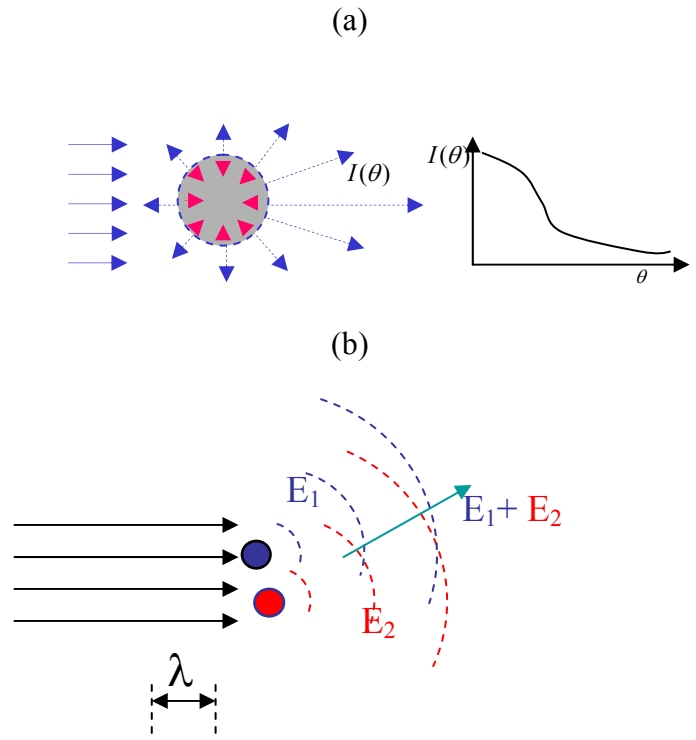

Figure III.10 Interference approximation assumes each individual particle scatters independently and ascribes quenched scattering efficiency to the interference of scattering fields (E_1 and E_2) from closely positioned particles. The interference effects are describable through a structure factor function.

Other approximations include quasi-crystalline approximation (QCA)[133, 134] and hole approximation (a special case of QCA) can also be used to calculated scattering properties of particle systems. In contrast to the IA which neglects the secondary fields scattered from the neighboring particles, QCA approximation considers that particles scatter original incident light as well as the secondary light scattered from its neighboring particles.

Similar to IA, QCA also assumes that the scattered fields from different particles interfere in the far field. With the consideration the secondarily scattered field, QCA is theoretically more rigorous than IA and has the potential to provide scattering properties of a suspension more accurately than IA. However, QCA requires numerically solving a reduced set of coupled Maxwell equations in order to obtain scattering characteristics of suspended particles. The description of physics underlying QCA will be provided in Appendix A, and will not be included here.

Since IA can provide comparable accuracy with QCA over a wide range[21, 22] it will be used throughout the work of this thesis. The prediction of isotropic scattering coefficient using interference approximation will be introduced in following subsection.

III.4.2. Light scattering in concentrated colloidal suspension

The scattering intensity resulting from a planar incident wave upon an ensemble of structured particles, $I(q)$, can be predicted by applying the interference approximation:[135, 136]

$$I(q) = \sum_i \sum_j F_{ij}(q, \sigma_{i,} \sigma_j)(\rho_i \rho_j)^{1/2} S_{ij}(q) \qquad \text{(III.20)}$$

where ρ_i and ρ_j are the number densities of particle of of size $\sigma_{i,}$ and σ_j; $S_{ij}(q)$ is the partial structure factor addressing the interference of the light scattered from particle component *i and j* at the scattering wave vector *q*. $F_{ij}(q, \sigma_{i,} \sigma_j)$ is the binary form factor between the spherical particles at wave vector, q, and can be calculated by:[87]

$$F_{ij} = \mathrm{Re}(f_{1,i} f_{1,j}^{*} + f_{2,i} f_{2,j}^{*}) \qquad \text{(III.21)}$$

where $f_{1,i}$ and $f_{2,i}$ are the scattering amplitudes into two orthogonal polarization states from a particle with size $\sigma_{i,}$ and can be calculated using Mie scattering theory. $f_{1,j}^{*}$ and

$f_{2,j}^{*}$ are the complex conjugates of $f_{1,i}$ and $f_{2,i}$ respectively. For a monodisperse system, the form factor F_{ii} can be simply calculated by:

$$F = | f_1 |^2 + | f_2 |^2 \tag{III.22}$$

It is noted that the calculation of the binary form factor with different sizes using Mie theory of light scattering is not the same as that for X-ray or neutron scattering. Because the wavelengths of X-ray or neutrons are much longer than the effective sizes of the scattering nuclei and electrons, Rayleigh-Gans-Debye (RGD) approximation can be appropriately used. The scattering amplitudes are real for x-ray and neutron scattering, and the binary form factor can be approximated using the geometrical average of form factors for each individual particle species:

$$F_{ij} = [F_1(q) \cdot F_2(q)]^{1/2} \tag{III.23}$$

However, Mie scattering theory should be employed in this study because the wavelengths used in our experiments are in same order of magnitude to the particle sizes. In Mie theory, the scattering amplitudes are complex, so Eqn (III.21) should be used to calculate binary form factor for particles in a multi-component mixture. At the particle size of 143 nm and wavelength in the near infrared region, the approximated Eqn (III.23) can be used to calculate binary form factor without causing significant difference in the calculated isotropic scattering coefficients. However, to minimize error, the rigorous Eqn (III.21) is used to calculate binary form factor throughout this thesis.

With the scattering intensity calculated from Eqn (III.20), isotropic scattering coefficient of suspensions, μ'_s, can be theoretically predicted by the following equation:

$$\mu'_s = \frac{\pi}{(2n_m\pi/\lambda)^2}\int_0^{\pi} I(q)\sin\theta(1-\cos\theta)d\theta \qquad \text{(III. 24)}$$

here, n_m is the refractive index of the medium, and ϕ is the volume fraction of suspended particles. For a monodisperse suspension, the isotropic scattering coefficient can be calculated from:[6]

$$\mu_s'(\lambda) = \frac{6\phi_v}{(2\pi m/\lambda)^2\sigma^3}\int_0^{\pi} F(q)\cdot S(q)\cdot \sin\theta\cdot(1-\cos\theta)d\theta \qquad \text{(III.25)}$$

The above equation can be used to verify the structure factor model by comparing model predicted and experimentally measured scattering coefficients.

CHAPTER IV

BACKGROUND: TIME-DEPENDENT LIGHT PROPAGATION IN DENSE SUSPENSIONS

Time-dependent techniques detect the temporal response of scattered light intensity with regard to the light source whose intensity varies with time. In time-dependent techniques, the *kinetics* of the light propagation is detected. In contrary to the time-dependent techniques, the continuous-wave or intensity based techniques detect time averaged intensity of light at varying detector positions.

IV.1. Frequency domain photon migration measures

Depending on how the intensity of light source is modulated, time-dependent optical techniques usually belong to one of two categories, namely time domain or frequency domain. In time domain, the light source typically emits short light pulses from femto-seconds to pico-seconds in width, and time-dependent intensity of light is detected at some distance away from the light source. The delay and distortion of detected light pulse is used to investigate the optical properties of the medium (Figure IV.1a). In time domain approaches, expensive high speed electronics instruments are required in order to measure the temporal response of intensity change in the range of pico seconds. In frequency domain approaches, the intensity of light source is sinusoidally modulated at varying frequencies, and the demodulation and relative phase shift of propagating light are detected with respect to the incident light (Figure IV.1b). In frequency domain approaches, an instrument[137] to detect the phase shift of

propagating photon density wave is required. Time-domain and frequency domain measurement can be inter-converted using the Fourier transformation.

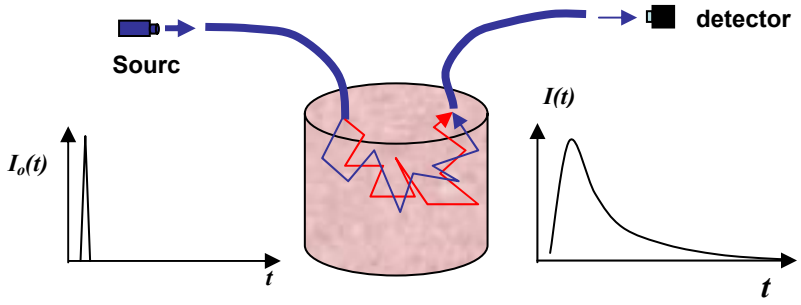

a. time domain

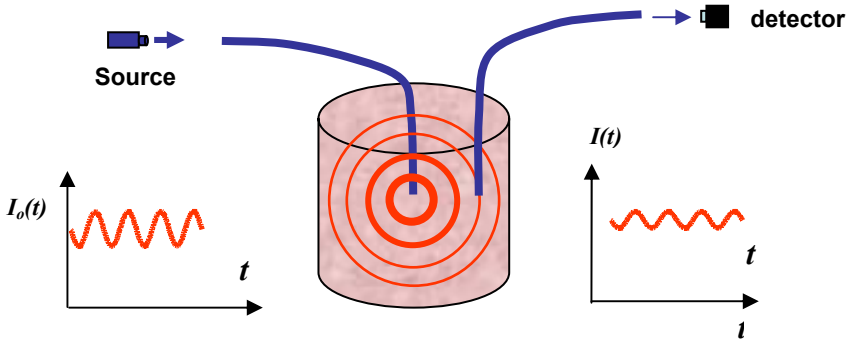

b. frequency domain

Figure IV.1 Time domain and frequency domain measurements of light propagation in a multiple scattering medium.

IV.2. Time-dependent radiative transport equation in dense suspensions

Diffusion theory has long been used to describe the propagation of neutrons in a nuclear reactor, where neutron transportation in a multiple scattering medium can be considered as "random walk" and be modeled as a diffusion process. The scheme used

to describe neutron propagation can also be extended to addressing light propagation in a multiple scattering suspension.[59, 138, 139]

IV.2.1. Derivation of radiative transport equation

We start the derivation of photon diffusion equation from the balance of energy carried by the light passing through a non-reentry control volume, from which light escaped cannot re-enter without being scattered back by particles outside the control volume (Figure IV.2).

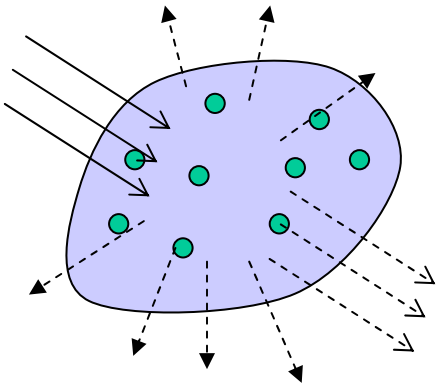

Figure IV.2 Extinction of radiance in random none-reentry control volume in a colloidal suspension.

We further assume that the amount of scatters and absorbers within the boundary can be negligible, and that particles scatter with their characteristic scattering cross section and scattering phase function, which describes intensity distribution of scattered light in different scattering directions.

Radiance, $\varphi(r,\hat{\Omega},t)$, is defined as the rate of energy flow per unit area at position *r* and time *t* per unit solid angle, Ω, with the direction represented by the unit vector, $\hat{\Omega}$. Radiance $\varphi(r,\hat{\Omega},t)$ is a scalar property, whose corresponding vector property with direction in unit vector, $\hat{\Omega}$, is called angular (or specific) current density, $\vec{j}(r,\hat{\Omega},t) = \varphi(r,\hat{\Omega},t)\hat{\Omega}$. The integral of radiance over all solid angle, is termed flux or fluence rate:

$$\phi(r,t) = \int_{4\pi} \varphi(r,\hat{\Omega},t)d\Omega \qquad \text{(IV.1)}$$

From the definition of radiance, $\varphi(r,\hat{\Omega},t)/c$, is the energy density carried by the radiance, where *c* is the speed of light in the medium. Therefore, the total energy carried by radiance $\varphi(r,\hat{\Omega},t)$ in a medium with volume *V* can be obtained by a volume integral as $\int_V \varphi(r,\hat{\Omega},t)dV/c$. The time rate of change in energy in the control volume carried by $\varphi(r,\hat{\Omega},t)$ can be calculated from the energy balance considering rate of energy gain and rate of energy loss:

$$\frac{\partial}{\partial t}[\int_V \varphi(r,\hat{\Omega},t)dV]/c d\hat{\Omega} = gain - loss \qquad \text{(IV.2)}$$

The energy carried by radiance $\varphi(r,\hat{\Omega},t)$ in a particle suspension of volume *V* can diminish upon being:

1) absorbed by the suspending fluids;

2) scattered away from original traveling direction $\hat{\Omega}$ by scatterers inside the volume;

3) absorbed by suspended particles; and

4) upon flowing out of the control volume through the surface.

The energy in volume V carried by radiance $\varphi(r,\hat{\Omega},t)$ can gain from:

1) any radiation source within the volume; $s(r,\hat{\Omega},t)$;

2) collection of light scattered into by the scatterers in the control volume; and

3) radiance flowing into the volume through the surface.

The absorption loss in a homogeneous fluid is proportional to the radiance, $\varphi(r,\hat{\Omega},t)$ and the absorption efficiency of the fluid, α, which can be related to its imaginary refractive index, n_l" and the wavelength, λ, by

$$\alpha = \frac{4\pi \cdot n_l''}{\lambda} \tag{IV.3}$$

In a suspension of total volume V, radiance absorption from suspending fluid is: $\int_V \varphi(r,\hat{\Omega},t)\cdot(1-\phi_v)\cdot\alpha\cdot dV$, where ϕ_v is the volume fraction of the particles in the suspension. The factor of (1- ϕ_v) is inserted into the integrand to exclude the volume occupied by the particles. Likewise, the absorption loss of radiance due to the suspended particles can be described as $\int_V \varphi(r,\hat{\Omega},t)\cdot\phi_v\cdot\mu_{a,p}\cdot dV$, where $\mu_{a,p}$ represents volume based absorption efficiency of particles. For nanoparticles, $\mu_{a,p}$ may not equal to the corresponding bulk property of same material, but can be related to the Mie theory predicted absorption cross section by: $\mu_{a,p} = \frac{1}{\phi_v}\sum_i \rho_i C_{abs,i}$, where ρ_i is the number

density and $C_{abs,i}$ is absorption cross section of suspended particle species, *i*. The absorption coefficient of the suspension can be calculated by combining the absorption from the particles and suspending fluid:

$$\mu_a = \phi_v \cdot \mu_{a,p} + (1-\phi_v) \cdot \alpha \,. \tag{IV.4}$$

The scattering loss in the control volume is $\int_V \varphi(r,\hat{\Omega},t) \cdot \mu_s \cdot dV$, where μ_s is the scattering coefficient. The scattering coefficient of suspension is proportional to the density and effective particle scattering cross section: $\mu_s = \sum_i \rho_i C_{sca,i}$.

The radiance loss due to the particle scattering and absorption of suspended particles and suspending fluid can be summed up as:

$$\int_V \varphi(r,\hat{\Omega},t) \cdot (\mu_s + (1-\phi_v) \cdot \alpha + \phi_v \cdot \mu_{a,p}) \cdot dV = \int_V \varphi(r,\hat{\Omega},t) \cdot \Sigma_t \cdot dV \tag{IV.5}$$

where total extinction coefficient Σ_t indicates the total extinction power of a suspension due to both absorption and scattering loss of radiance by the suspension :

$$\Sigma_t = \mu_s + \mu_a = \mu_s + (1-\phi_v) \cdot \alpha + \varepsilon \cdot \mu_{a,p} \tag{IV.6}$$

Let us first start with the radiance source in addressing radiance gain mechanisms in propagation. The radiance gain generated by the radiation source within the control volume, $s(r,\hat{\Omega},t)$, can be simply represented by a volume integral, $\int_V s(r,\hat{\Omega},t)dV$.

The second gain mechanism, radiation scattering collection, can be calculated by integrating $\varphi(r,\hat{\Omega}',t)$ weighted by the scattering phase function $P(\hat{\Omega}' \to \hat{\Omega})$ over all

scattering directions $\hat{\Omega}'$: $\int_V [\int_{4\pi} \varphi(r,\hat{\hat{\Omega}}',t)\cdot\mu_s\cdot P(\hat{\Omega}'\to\hat{\Omega})\cdot d\hat{\Omega}']dV$, where phase function $P(\hat{\Omega}'\to\hat{\Omega})$ describing normalized scattering intensity distribution satisfies:

$$1=\int_{4\pi} P(\Omega\to\Omega')\cdot d\Omega' \tag{IV.7}$$

The radiance flowing into the control volume can be written as an area integral of $-\int_{S^+}\varphi(r,\hat{\Omega},t)\hat{\Omega}\cdot\vec{S}ds=-\int_{S^+}\vec{j}(r,\hat{\Omega},t)\Omega\cdot\vec{S}ds$, where S^+, is the surface of the control volume accepting incident radiance and $\vec{S}$ is the surface normal vector pointing outward. Correspondingly, the radiance streaming out can be written as $-\int_{S^-}\varphi(r,\hat{\Omega},t)\cdot\hat{\Omega}\cdot\vec{S}ds=\int_{S^-}\vec{j}(r,\hat{\Omega},t)\cdot\vec{S}ds$, where S^-, is the surface from which radiation leaves the volume. The stream term, which includes radiation flowing into and out the control volume, forms a completed surface integral, which can be transferred into a volume integral by applying Gauss's theory:

$$\int_{S^+}\vec{j}(r,\hat{\Omega},t)\cdot d\vec{S}+\int_{S^-}\vec{j}(r,\hat{\Omega},t)\cdot d\vec{S}=\oint_S\vec{j}(r,\hat{\Omega},t)\cdot\vec{S}ds=\int_V(\nabla\cdot\vec{j})dV \tag{IV.8}$$

Upon expanding radiance gain and radiance loss mechanism with their mathematic expression details, Eqn (IV.2) becomes:

$$\frac{\partial}{\partial t}[\int_V\varphi(r,\hat{\Omega},t)dV]/c=[\int_V\frac{\partial\varphi(r,\hat{\Omega},t)}{c\partial t}dV]=\int_V\varphi(r,\hat{\Omega},t)\Sigma_t dV+ \quad -$$

$$\int_{4\pi}\varphi(r',\Omega',t)\cdot\mu_s\cdot P(\Omega'\to\Omega')\cdot d\Omega'+\int_V s(r,\hat{\Omega},t)dV-\int_V\nabla\cdot\vec{j}dV \tag{IV.9}$$

Since Eqn (IV.9) holds at an arbitrary non-reentry volume, the integrand at left hand side must equal to that at the right hand side:

$$\frac{\partial}{\partial t}\varphi(r,\hat{\Omega},r)/c+\nabla.\vec{j}+\Sigma_t\varphi=\int_{4\pi}\varphi(r',\Omega',t)\cdot\mu_s\cdot P(\Omega'\to\Omega')\cdot d\Omega'+s(r,\hat{\Omega},t) \quad \text{(IV.10)}$$

Eqn (IV.10) is often called radiative transport equation (RTE).

IV.2.2. Diffusion approximation of photon propagation

Eqn (IV.10) contains radiance $\varphi(r,\hat{\Omega},t)$ as a function of solid angle, which is seldom a variable of direct experimental interest. One can integrate Eqn (IV.10) over all solid angle to remove the angular dependence. The energy change term, medium extinction term, stream term, and source term can be integrated respectively as:

$$\int_{4\pi}\frac{\partial}{c\partial t}\varphi(r,\hat{\Omega},t)d\Omega=\frac{\partial}{c\partial t}(\int_{4\pi}\varphi(r,\hat{\Omega},t)d\Omega)=\frac{\partial\phi(r,t)}{c\cdot\partial t}$$

$$\int_{4\pi}\varphi(r,\hat{\Omega},t)\Sigma_t d\Omega=\Sigma_t\phi(r,t)$$

$$\int_{4\pi}\nabla\cdot\vec{j}\cdot d\Omega=\nabla.(\int_{4\pi}\vec{j}\cdot d\Omega)=\nabla.\vec{J}$$

$$\int_{4\pi}s(r,\hat{\Omega},t)d\Omega=S_r(r,t)$$

The integration of the scattering collection term can be modified by changing the order of integration to be $\mu_s\cdot\int_{4\pi}\varphi(r',\hat{\Omega}',t)\cdot(\int_{4\pi}P(\hat{\Omega}'\to\hat{\Omega})\cdot d\Omega')d\Omega$, which can be further reduced as $\mu_s\cdot\phi$ by applying normalization properties of phase function shown in Eqn

(IV.7) and the definition of flux rate: $\int_{4\pi} \varphi(r',\hat{\Omega}',t)\cdot d\Omega' = \phi$. After collecting terms, we can obtain the so called radiation continuity equation as:

$$\frac{\partial}{\partial t}\phi(r,t)/c + \nabla\cdot\vec{J}(r,t) + \mu_a\phi(r,t) = S_r(r,t) \qquad \text{(IV.11)}$$

This equation does not contain angular dependent radiance $\varphi(r,\hat{\Omega},t)$, but it introduces two new terms of current density $\vec{J}(r,t)$ and flux rate $\phi(r,t)$. Solving Eqn (IV.11) still needs either detailed information of the angular dependence of radiance $\varphi(r,\hat{\Omega},t)$ or an approximated relation between current density, $\vec{J}(r,t)$, and flux rate, $\phi(r,t)$. At the conditions of 1) linear scattering anisotropy, where radiance is linear with the solid angle, and 2) slow rate of change in current density $\vec{J}(r,t)$, the diffusion approximation relates flux rate $\phi(r,t)$, and current density $\vec{J}(r,t)$ by:

$$\vec{J}(r,t) = -D\nabla\phi(r,t) \qquad \text{(IV.12)}$$

Analogous to the Fick's law of diffusion, *D* in Eqn (IV.10) is correspondingly called photon diffusion coefficient, and the approximated relation between current density $\vec{J}(r,t)$ and flux rate $\phi(r,t)$ is called diffusion approximation.

IV.3. Diffusion approximation of photon migration

In this section, the derivation of the diffusion approximation from the two assumptions is summarized.

By multiplying RTE of Eqn (IV.10) with unit vector $\hat{\Omega}$ representing the scattering direction and integrating over solid angle Ω, we can obtain:

$$\frac{\partial}{\partial t}\vec{J}(r,t)/c+\nabla.\int_{4\pi}\hat{\Omega}\hat{\Omega}\varphi(r,\hat{\Omega},t)d\Omega+(\Sigma_t-g\mu_s)\phi(r,t)=\vec{S}_1(r,t) \qquad \text{(IV.13)}$$

where the integration of rate of energy change, source term, and medium extinction terms, in Eqn (IV.10) are respectively:

$$\int_{4\pi}\frac{\partial}{c\partial t}\hat{\Omega}\varphi(r,\hat{\Omega},t)d\Omega=\frac{\partial}{c\partial t}(\int_{4\pi}\varphi(r,\hat{\Omega},t)\hat{\Omega}d\Omega)=\frac{\partial\vec{J}}{c\cdot\partial t}$$

$$\int_{4\pi}\hat{\Omega}\varphi(r,\hat{\Omega},t)\Sigma_t d\Omega=\Sigma_t\vec{J}$$

$$\int_{4\pi}\hat{\Omega}\cdot s(r,\hat{\Omega},t)d\Omega=\vec{S}_1(r,t)$$

The integration of scattering cross section term can be simplified by first switching the order of integration and inserting $(\hat{\Omega}'\cdot\hat{\Omega}')=1$ into the integrand:

$$\Sigma_s\cdot\int_{4\pi}(\int_{4\pi}\hat{\Omega}\cdot\varphi(r',\hat{\Omega}',t)\cdot P(\hat{\Omega}'\to\hat{\Omega})\cdot d\Omega')d\Omega$$

$$=\int_{4\pi}[\int_{4\pi}\hat{\Omega}\cdot(\hat{\Omega}'\cdot\hat{\Omega}')\varphi(r',\hat{\Omega}',t)\cdot\mu_s\cdot P(\hat{\Omega}'\to\hat{\Omega})\cdot d\Omega]d\Omega'$$

Since the scattering phase function of $P(\hat{\Omega}'\to\hat{\Omega})$ only depends on the relative orientation of original propagating direction vectors $\hat{\Omega}'$ and scattered direction $\hat{\Omega}$, it can be written as a function of scattering angle, $P(\mu_o)$, where $\hat{\Omega}'\cdot\hat{\Omega}=\mu_o$ is the cosine of scattering angle. Then the scattering collection term equals to: $\mu_s\cdot\int_{4\pi}\varphi(r',\hat{\Omega}',t)\cdot[\int_{-1}^{1}\mu_o P(\mu_o)d\mu_o]d\hat{\Omega}'$, which can further be simplified as $\Sigma_s\cdot g\cdot\phi$, where $\int_{-1}^{1}\mu_o P(\mu_o)d\mu_o=g$ is the scattering anisotropy. The integration of the stream term

in Eqn (IV.10) contains a second order tensor, $\hat{\Omega}\hat{\Omega}$, and it cannot be further reduced without the information on the angular dependence $\varphi(r,\hat{\Omega},t)$.

$$\int_{4\pi}\hat{\Omega}(\hat{\Omega}\nabla\cdot\varphi)d\Omega = \nabla.\int_{4\pi}\hat{\Omega}\hat{\Omega}\cdot\varphi(r,\hat{\Omega},t)d\Omega \qquad \text{(IV.14)}$$

When radiance is only weakly dependent on the solid angle, or linear scattering anisotropy assumption holds, $\varphi(r,\hat{\Omega},t)$ can be approximated as a linear function of solid angle:

$$\varphi(r,\hat{\Omega},t) = A(r,t) + \vec{B}(r,t)\cdot\hat{\Omega} \qquad \text{(IV.15)}$$

where the scalar $A(r,t)$ and vector $B(r,t)$ can be determined by applying Eqn (IV.15) in the definitions for the flux rate $\phi(r,t)$ and current density $\vec{J}(r,t)$ respectively to obtain:

$$\phi(r,t) = \int_{4\pi}\phi(r,\hat{\Omega},t)d\Omega = A(r,t)\int_{4\pi}d\Omega + \vec{B}(r,t)\cdot\int_{4\pi}\hat{\Omega}d\Omega \qquad \text{(IV.16)}$$

$$\vec{J}(r,t) = \int_{4\pi}\phi(r,\hat{\Omega},t)\hat{\Omega}d\Omega = A(r,t)\int_{4\pi}\hat{\Omega}d\Omega + \vec{B}(r,t)\cdot\int_{4\pi}(\hat{\Omega}\cdot\hat{\Omega})d\Omega \qquad \text{(IV.17)}$$

By applying $\int_{4\pi}d\hat{\Omega} = 4\pi$, $\int_{4\pi}\hat{\Omega}d\Omega = 0$; and $\int_{4\pi}(\hat{\Omega}\cdot\hat{\Omega})d\Omega = \frac{4\pi}{3}$ in the two equations above. One can obtain $A(r,t)$ and $B(r,t)$ as:

$$A(r,t) = \frac{1}{4\pi}\phi(r,t) \qquad \text{(IV.18)}$$

$$\vec{B}(r,t) = \frac{3}{4\pi}\vec{J}(r,t) \qquad \text{(IV.19)}$$

Therefore, with the assumption of linear anisotropy, radiance can be equivalently written as:

$$\varphi(r,\hat{\Omega},t)=\frac{1}{4\pi}\phi(r,t)+\frac{3}{4\pi}\vec{J}(r,t)\cdot\hat{\Omega} \qquad \text{(IV.20)}$$

If we insert linear anisotropy approximation shown in Eqn (IV.20) above into Eqn (IV.14), we can obtain: $\nabla.\int_{4\pi}\hat{\Omega}\hat{\Omega}\cdot\varphi(r,\hat{\Omega},t)d\Omega=\nabla.\int_{4\pi}\hat{\Omega}\hat{\Omega}\cdot(\frac{1}{4\pi}\phi(r,t)+\frac{3}{4\pi}\vec{J}(r,t)\cdot\hat{\Omega})d\Omega$, which can then be simplified to $\frac{1}{3}(\nabla.\phi)$ by applying $\int_{4\pi}\hat{\Omega}\hat{\Omega}\hat{\Omega}d\Omega=0$. Subsequently, Eqn (IV.13) can than be simplified to be:

$$\frac{\partial}{\partial t}\vec{J}(\vec{r},t)/c+\frac{1}{3}\nabla.\phi+(\Sigma_t-g\mu_s)\vec{J}(\vec{r},t)=\vec{S}_1(\vec{r},t) \qquad \text{(IV.21)}$$

where $\Sigma_{tr}=\Sigma_t-g\mu_s=\mu_a+(1-g)\mu_s$ is usually called macroscopic transport cross section, or inverse transport mean free path, and $\mu_s'=(1-g)\mu_s$ is also called isotropic scattering coefficient, or reduced scattering coefficient.

The linear approximation of Eqn (IV.20) is also usually called P_1 approximation, since the Eqn (IV.20) can also be derived from series expansion of phase function using first two Legendre polynomials: $P_0(\mu_o)=1$ and $P_1(\mu_o)=\mu_o$:

$$P(\mu_o)=\frac{1}{4\pi}(1+3g\mu_o) \qquad \text{(IV.22)}$$

Likewise, the P_2 approximation or higher order approximations can also be obtained in a similar manner.

If the first term in Eqn (IV.21) representing rate of change in the current density is much smaller in comparison with other terms, such that $\frac{\partial\vec{J}(\vec{r},t)}{\vec{J}(\vec{r},t)\partial t}<<c\Sigma_{tr}$, it can be

neglected. Physically this means time rate of change in current density is much smaller than interaction frequency of radiation with the medium, and quasi-stationary approximation usually holds. This approximation usually satisfies when the modulation frequency is less then GHz. If there is no source presented in the control volume, Eqn (IV.21) can then be reduced to obtained the diffusion approximation shown previously as Eqn (IV.12), where $D = \frac{1}{3\Sigma_{tr}}$ is the diffusion coefficient.

Upon using diffusion approximation, we have derived so called photon diffusion equation, or one speed radiation diffusion equation for radiance balance:

$$\frac{\partial}{\partial t}\phi(\vec{r},t)/c - \frac{\nabla^2.\phi(\vec{r},t)}{3(\mu_a - \mu_s')} + \mu_a\phi(\vec{r},t) = S(\vec{r},t) \qquad \text{(IV.23)}$$

The photon diffusion approximation above can be Fourier-transformed from time domain into frequency domain as:

$$D\nabla^2\phi_{AC}(r,\omega) - [\mu_a - \frac{i\omega}{c}]\phi_{AC}(r,\omega) = S_r(r,\omega) \qquad \text{(IV.24)}$$

In infinite media with a single point source located in the coordinate origin, photon density $U(r,t) = \phi(r,t)/(c \cdot h\nu)$ at position *r* and time *t* can be obtained from the solution of above frequency domain diffusion equation:

$$\begin{aligned}\phi = {} & \frac{S_{DC}\exp(-\mu_{eff}r)}{4\pi Dcr} + \frac{S_{AC}}{4\pi Dcr}\exp\{-r(\frac{c^2\mu_a{}^2+\omega^2}{c^2D^2})^{1/4}\cos[\frac{1}{2}\tan^{-1}(\frac{\omega}{c\mu_a})]\} \\ & \times\exp\{i\cdot r\cdot(\frac{c^2\mu_a{}^2+\omega^2}{c^2D^2})^{1/4}\sin[\frac{1}{2}\tan^{-1}(\frac{\omega}{c\mu_a})] - i\cdot(\omega t+\phi_o)\}\end{aligned} \qquad \text{(IV.25)}$$

where $\mu_{eff} = (\mu_a/D)^{1/2}$; S_{DC}, S_{AC}, and ϕ_o are the average intensity, modulation amplitude and initial phase associated with point optical source.

In Eqn (IV.25), the optical source is assumed to be isotropic, emitting PDW uniformly in all directions. In reality, most light emitted from the source fiber optic travels in the forward direction. After experiencing a certain number of scattering events in a multiple scattering medium, light will propagate in a random direction and the light source can be deemed as isotropic. It is shown that after light travels 10 times the isotropic transport mean free path (defined as $1/(\mu_a + \mu_s')$), it will propagate in a random direction.[59,140, 141] Therefore, a fiber optic can be considered as an isotropic source if received light is observed at a point located 10 times of transport mean free path away.

The analytical solution of Eqn (IV.24) for a semi-infinite boundary condition and other boundary conditions have also been derived, and are presented elsewhere.[142, 143]

IV.4. Light absorption in dense suspensions and interference approximation

Interference approximation states that particle scatters light independently, and scattered light from different particles interferes in the far field. Particles scatter with an effective scattering cross section, which depends on correlated particle positions.

Under the statement of the interference approximation, correlated particle positions do not change the incident electromagnetic field in the near field, so the particle absorption efficiency, which corresponds to the electromagnetic wave scattered inwardly toward particle center, should remain the same.

Therefore, the interference approximation implies that the absorption coefficient of a suspension varies linearly with its particle volume concentration:

$$\mu_a = (1-\phi_v)\cdot\alpha + \phi_v \cdot \mu_{a,p} \qquad \text{(IV.26)}$$

CHAPTER V

METHODS AND MATERIALS

V.1. Physics of frequency domain photon migration instrumentation

V.1.1. Physics

Frequency domain photon migration (FDPM) [144, 145] has been demonstrated to be an effective probe of structure in opaque colloidal suspensions.[6-8, 11] The typical FDPM setup used in measuring optical properties of a colloidal system has been detailed by Richter and Sevick.[145,146]

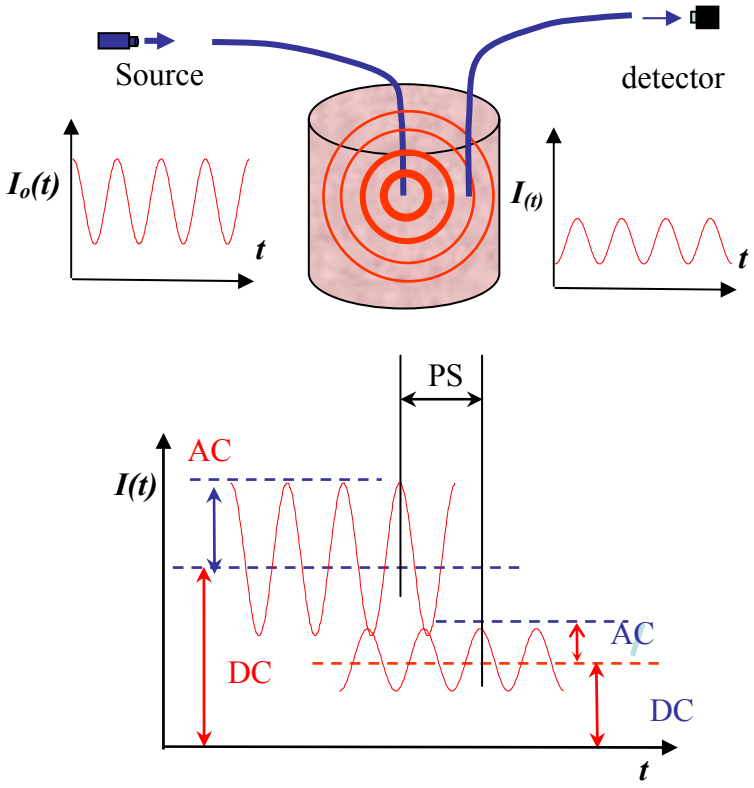

Figure V.1 FDPM depends upon launching a photon density wave (PDW) via a fiber optic into a colloidal suspension and detecting phase shift and intensity attenuation as a function of source-detector separation distance at varying frequencies.

Briefly, FDPM depends upon launching a *photon density wave* (PDW) via a fiber optic into a colloidal suspension. The average intensity (*DC*) and amplitude (*AC*) of the photon density wave attenuates and its phase shifts as the wave propagates away from the source. The PDW propagating through the medium is collected by another fiber optic at a point located at known distances away from the source. The measurements of DC, AC and phase shift (PS) measured as a function of modulation frequency, ω, and source-detector separation distance can be used to extract optical properties using a diffusion analysis of photon transport. In the following, the data analysis of FDPM will be introduced after introducing FDPM instrumentation.

V.1.2. FDPM instrumentation

A typical schematic of point-illumination and point-detection FDPM instrumentation setup are illustrated in Figure V.2.

Frequency domain photon migration requires a light source that generates the photon density wave modulated at the RF frequency range typically around 100 MHz. In this work, the intensity attenuation and phase shift of the propagating photon density wave are detected using heterodyning and referencing techniques to determine isotropic scattering and absorption coefficients through a diffusion analysis (introduced in the subsection of FDPM data analysis).

In the following, we will provide description of FDPM instrumentation in the following order:

1) Generation of incident photon density wave;

2) Introduction of heterodyning technique for detecting phase shift of photon density wave;

3) Introduction of referencing and relative measurement which enable calibration-free FDPM operation

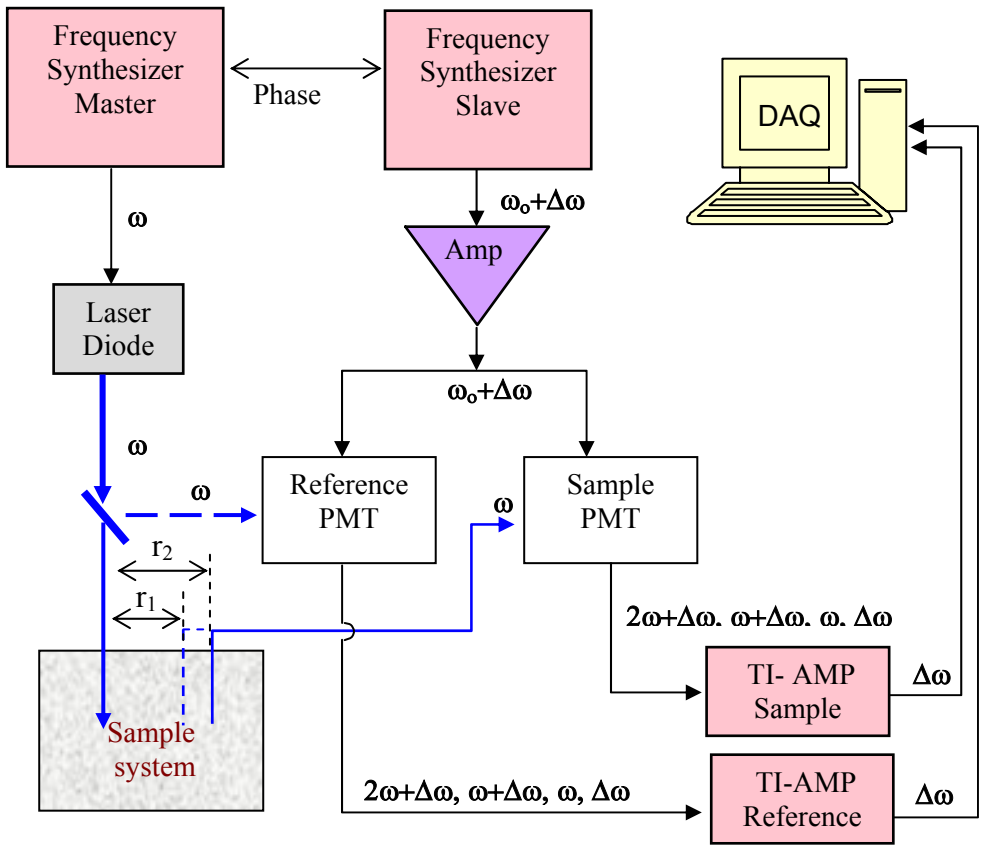

Figure V.2 Schematic of point-illumination and point-detection FDPM instrumentation set up, where the directly modulated laser diode is used as the light source.

V.1.2.1 Generation of incident photon density wave

There are a total of seven wavelengths used to conduct FDPM measurements in the work of this thesis. The four red or near infrared wavelengths, (828, 785, 687, and

650 nm,) are provided from laser diodes (Thorlabs, CA). The wavelengths of 568, 514, and 483 nm are provided from Argon-Krypton gas discharge laser (643 R-AR-A01, Melles- Griot Laser Group, Carlsbad, CA), since the laser diodes at these wavelengths were not available.

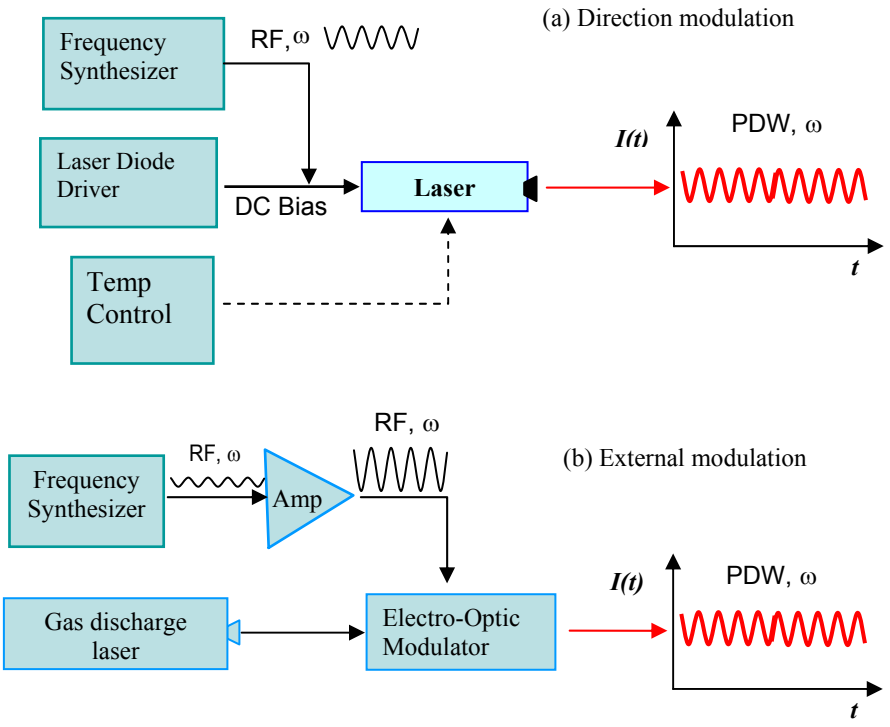

Figure V.3 Generation of the incident photon density wave: (a) direction modulation by superimposing a RF signal on the laser diode DC bias current; (b) external modulation by passing continuous wave light through an external electro-optic modulator.

The photon density waves at these wavelengths are generated in two ways. The intensity of light emitted from laser diode is modulated by directly superimposing an amplified RF signal at the desired modulation frequency over the direct driving current (Figure V.3a). The direct modulation requires the response of light source to be fast

enough to respond to the RF signal in the linear response region of laser diode, where the intensity of emitted light is proportional to the driving current. With laser diodes as light source, a DC bias is adjusted to ensure a laser diode works in its linear region and to control its modulation depth, defined as the amplitude (AC) to the average intensity (DC) of the photon density wave.

The gas-discharge laser cannot respond fast enough and does not respond linearly with an RF driving current; therefore it can not be directly modulated. Hence, an external electro-optic modulator (Model:350-160, Conoptics, CT) was used to modulate continuous wave light emitted from the laser (Figure V.3b). A typical electro-optical modulator contains a crystal, whose refractive index changes with the superimposed RF signal. A polarized light traveling through the crystal experiences a modulated refractive index. Upon passing through a polarizer after going through the crystal, the intensity of light may be controlled sinusoidally with the superimposed RF signal. Since the external modulator usually needs relative high voltage, a high gain amplifier (> 40 dbm) is usually required to increase RF signal generated by the frequency synthesizer.

In this work, the photon density wave provided by the directly modulated laser diode was more stable than that obtained from external modulation of light emitted from gas discharge laser.

V.1.2.2 Heterodyning techniques

Although light can be modulated by a RF to have a frequency at the order of 100 MHz and a photon multiplier tube (PMT) can convert the photon density wave into RF

signal of same frequency, the converted RF signals cannot be directly acquired by a general data acquisition (DAQ) board (DAQCard-A1-16E-6, National Instruments, Austin, TX), which has at most a maximum scanning rate of 10 M scan/s/channel.

Heterodyning techniques embed the information at the RF modulation frequency, ω, into a manageable heterodyned frequency,$\Delta\omega$, by mixing it with another signal of frequency $\omega+\Delta\omega$ at the photomultiplier tube (PMT). The photon multiplier tube thus acts as a signal mixer (Figure V.4).

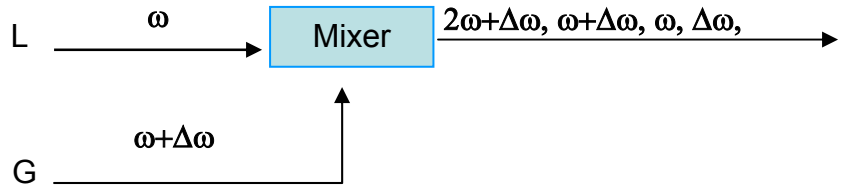

Figure V.4 Schematic of heterodyned mixer for detection of the amplitude (AC) and phase angle.

The output signal from a PMT (shown in Figure V.4) is the product of two input signals: the intensity of detected light signal L, and the magnification gain control signal G. The term, L, with the amplitude L_{AC} represents the intensity of photon density wave, which is modulated at frequency ω and experiences a phase shift of θ as it propagates from the light source to a position with distance r to the light source; the term of L_{DC} represents average intensity of modulated light.

$$L = L_{DC} + L_{AC}\cos(\omega t + \theta) \tag{V.1}$$

The gain modulation signal, *G*, which is generated from a phase-locked slave signal synthesizer at the modulation frequency of $\omega+\Delta\omega$, has the amplitude G_{AC} and average signal level G_{DC}:

$$G = G_{DC} + G_{AC}\cos[(\omega + \Delta\omega)t + \theta_{inst}] \tag{V.2}$$

where θ_{inst} is the phase delay associated with the instrumentation and does not originate from the propagation of photon density wave.

The output of the mixed signal output, *S,* contains high frequency (2ω+Δω, ω+Δω, ω) components and a low frequency component at the frequency of Δω:

$$\begin{aligned} S &= L \times G \\ &= L_{DC}G_{DC} + L_{DC}G_{AC}\cos[(\omega + \Delta\omega)t + \theta_{inst}] \\ &+ G_{DC}L_{AC}\cos(\omega t + \theta) + \frac{L_{AC}G_{AC}}{2}\cos(\Delta\omega t + \theta_{inst} - \theta) \\ &+ \frac{L_{AC}G_{AC}}{2}\cos[(2\omega + \Delta\omega)t + \theta_{inst}) \end{aligned} \tag{V.3}$$

The mixed signal is sent over to a trans-impedance amplifier (TI-AMP) (Model 70710, Stratford, CT), which acts as a low pass filter and blocks the high frequency component. The surviving low frequency signal contains the phase shift, θ, and intensity properties, L_{AC}, and D_{AC}, relating to the original light signals:

$$S = L_{DC}G_{DC} + \frac{L_{AC}G_{AC}}{2}\cos(\Delta\omega t + \theta_{inst} - \theta) \tag{V.4}$$

The low frequency signal, Δω, typically in the range of 100 Hz- kilohertz, can be easily detected using a general DQA board, which acquires and digitizes the low frequency signal from analog output of a trans-impedance amplifier.[147]

Heterodyning techniques allow the determination of phase and amplitude of high frequency signals through detecting the phase shift and amplitude of signals at a lower heterodyne frequency. The average intensity, $L_{DC}L_{AC}$, amplitude $\frac{L_{AC}G_{AC}}{2}$, and the phase angle $\theta_{inst} - \theta$ of the acquired signal can be determined through a fast Fourier transform (FFT) analysis. The information of light signal L_{AC}, L_{DC}, θ, are coupled with the information of the PMT modulation signal G, G_{AC}, G_{DC}, and the instrumentation information, θ_{inst}. The amplitude, average intensity, and phase shift of light signal can be extracted though referencing techniques and relative measurement of the photon density wave at two different source detector separation distances.

V.1.2.3 Referencing and relative measurement

FDPM depends upon detecting the phase shift and intensity attenuation of the photon density wave as it propagates away from the light source. Determination of θ_{inst} is not necessary, and the phase difference and intensity ratio as a function of source-detector separation distance is of direct interest. In our typical FDPM measurement, a reference channel is included to eliminate the phase shift introduced by the instrumentation, θ_{inst}.

Figure V.2 shows two signal processing channels, a sample channel and a reference channel. The modulated light beam at modulation frequency ω is split into two parts, and each part is delivered into one of the two channels. Most of light is delivered into the sample via a fiber optic, and the propagating PDW is collected by another fiber optic delivered to a sample PMT. The remaining light is sent to a reference

PMT directly (Figure V.2). A PMT in each channel mixes the accepted light signal at modulation frequency ω with RF signal generated from a phase locked slave signal generator at the frequency of ω+Δω.

The mixed signals pass the TI-AMP for each channel, and the surviving low frequency components of both channels are acquired by the DAQ computer simultaneously. The phase angles introduced by the instrument in the sample channel θ_{inst} and in the reference channel, θ_{inst}', are different and are both dependent on the modulation frequency.

Figure V.5 illustrates the scheme of referencing and relative measurements used in FDPM at two different source-detector separation distances, r_1 and r_2. At each source-detector separation distance, the relative ratio for DC and AC between the sample and the reference channels and the difference in phase between the two channels are measured and termed as referenced measurements thereafter (Figure V.5).

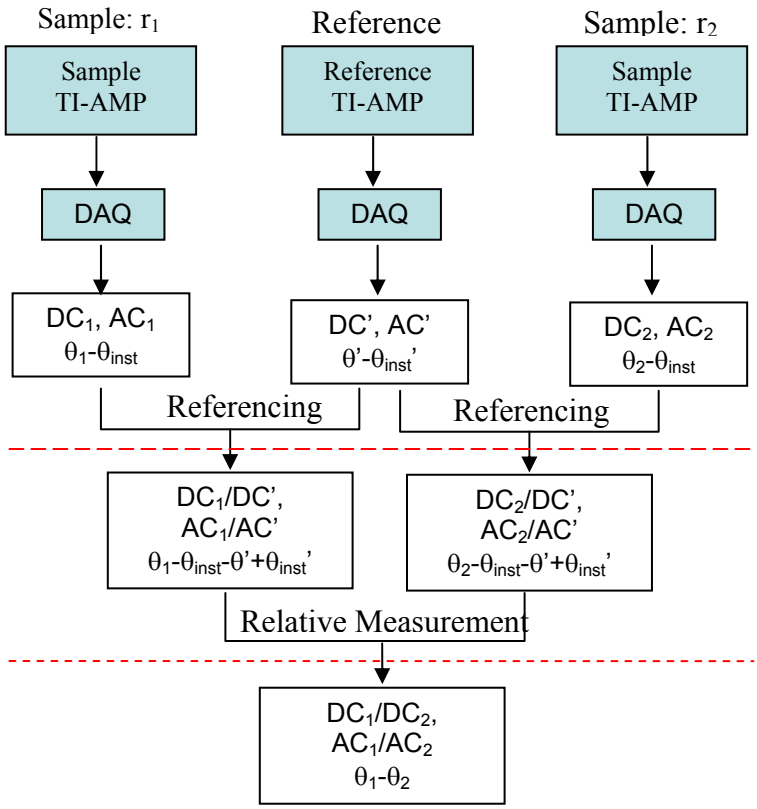

Figure V.5 Schematic of referencing and the relative distance measurement to obtain the intensity attenuation and phase delay of photon density wave propagating from r_1 to r_2.

Referencing alone just combine the measurements from both sample and reference channels at each source-detector separation distance: the referenced AC and DC measurements from the sample channel is relative to those from the reference channel by taking the ratio; the referenced PS measurements include the phase shift of the propagating PDW, θ_1 or θ_2 as well as the phase difference, (θ_{inst} - θ_{inst}' - θ') introduced by instruments.

In order to eliminate the AC and DC of the reference channel and the instrumentation-introduced phase shifts, the referenced FDPM measurements at two

different source-detector separation distances, r_1 and r_2, are compared. The relative amplitude and average, AC_1/AC_2, and DC_1/DC_2, and the relative phase difference θ_1-θ_2, at these two points r_1 and r_2 can be determined, eliminating the instrument-introduced phase shift θ_{inst} - θ_{inst}' - θ' , as well as amplitude and average intensity from reference channel *AC'*, and *DC'* (Figure V.5).

Upon taking the internal referencing and relative measurements, frequency domain photon migration does not need calibration for source intensity and instrumentation introduced phase shift. In order to keep the measurements comparable, the instrument conditions, such as gains of PMT and TI-AMP, and alignment of the light should remain unchanged when the collecting fiber is shifted from r_1 to r_2.

The relative measurement of amplitude, average intensity and phase shift at two more source-detector separation distance can be used to determine the isotropic scattering and absorption coefficients via a diffusion analysis that will be introduced in the following.

V.1.3. FDPM data analysis

The analytical solution Eqn (IV.24) of frequency domain photon diffusion equation shown as Eqn (IV.25) can be used to analyze *AC*, *DC,* and *PS* data measured at two or more source-detector separation distances. From the solution of frequency domain photon migration equation (Eqn (IV.25)), one easily identify the average intensity DC(r), amplitude AC(r), and phase angle PS(r) as a function of source-detector separation distance *r*:

$$DC(r) = \frac{S_{DC} \exp(-\mu_{eff} r)}{4\pi Dcr} \tag{V.5}$$

$$AC(r) = \frac{S_{AC}}{4\pi Dcr} \exp\{\text{-r}(\frac{\text{c}^2 {\mu_a}^2 + \omega^2}{\text{c}^2 D^2})^{1/4} \cos[\frac{1}{2}\tan^{-1}(\frac{\omega}{\text{c}\mu_\text{a}})]\} \tag{V.6}$$

$$PS(r) = r \cdot (\frac{\text{c}^2 {\mu_a}^2 + \omega^2}{\text{c}^2 D^2})^{1/4} \sin[\frac{1}{2}\tan^{-1}(\frac{\omega}{\text{c}\mu_\text{a}})] - (\omega t + \Delta\theta_{inst}) \tag{V.7}$$

where c is the speed of light in the medium; $\Delta\theta_{inst}$ is the instrumentation-introduced phase difference between sample channel and reference channel; and S_{AC}, and S_{DC} are the amplitude and average intensity associated with the source. If we select r_o as the reference measurement position, the relative values of AC, DC and PS detected at r with respect to the measurements at r_o can be calculated:

$$DC_{rel} = \frac{DC(r)}{DC(r_0)}) = \frac{r_o}{r} \exp\{-(r - r_0)[3\mu_a(\mu_a + \mu_s')]^{1/2}\} \tag{V.8}$$

$$AC_{rel} = \frac{AC(r)}{AC(r_0)}) = \frac{r_o}{r} \exp\{-(r - r_0)(\frac{\text{c}^2 {\mu_a}^2 + \omega^2}{\text{c}^2 D^2})^{1/4} \cos[\frac{1}{2}\tan^{-1}(\frac{\omega}{\text{c}\mu_\text{a}})]\} \tag{V.9}$$

$$PS_{rel} = PS(r) - PS(r_0) = (r - r_0)(\frac{\text{c}^2 {\mu_a}^2 + \omega^2}{\text{c}^2 D^2})^{1/4} \sin[\frac{1}{2}\tan^{-1}(\frac{\omega}{\text{c}\mu_\text{a}})] \tag{V.10}$$

The experimentally determined values of AC_{rel} and DC_{rel} in the left hand sides of Eqns (V.8) and (V.9) do not depend on the amplitude and average intensity of the light source. Furthermore, the relative phase in the left hand side of the Eqn (V.10) is not associated with the phase introduced by instrumentation, $\Delta\theta_{inst}$.

Upon applying any two of these three equations, we can determine the optical properties of μ_a and μ_s' from FDPM measurement at two different source-detector

separation distances, r and r_o. Usually, the data measured by FDPM are superfluous, and there is more than one way to analyze FDPM experiments of AC, DC, and PS to obtain optical properties via Eqns (V.8) through (V.10).[94,95] For example, FDPM measurements can be repeated multiple times at each modulation frequency and each source-detector separation distance in a matter of seconds due to high data acquisition rate of computer controlled devices, and one can conduct FDPM measurements at multiple distances, and multiple modulation frequencies. Based on how one obtains μ_a and μ_s' from the superfluous measurements of AC, DC, and PS, one can classify FDPM data analysis methods into one of two classes: multiple frequency or multiple distance methods.[10] Multiple frequency methods determine μ_a and μ_s' from FDPM measurements of AC, DC, and PS at two different source-detector separation distances, but at multiple frequencies in order to minimize the experimental error; and multiple distance methods determine μ_a and μ_s' from measurements of AC, DC, and PS at multiple distances but at a single modulation frequency.

V.1.3.1 Multiple frequency methods

With multiple frequency methods, one determines the measurements of AC_{rel}, DC_{rel}, and PS_{rel} as a function of modulation frequency, ω, at 2 source-detector distances, r and r_o. Parameter estimates of μ_a and μ_s' are obtained by minimizing the differences between experimental and calculated measurements of AC_{rel}, DC_{rel}, and PS_{rel}. In general the estimates of μ_a and μ_s' are determined by minimizing the error function:

$$\chi^2 = \sum_i \frac{[AC_{\exp t,i}(\omega_i) - AC_{theo,i}(\omega_i)]^2}{\sigma_{AC,i}^{\ 2}} + \sum_i \frac{[PS_{\exp t,i}(\omega_i) - PS_{theo,i}(\omega_i)]^2}{\sigma_{PS,i}^{\ 2}} + \sum_i \frac{[DC_{\exp t,i}(\omega_i) - DC_{theo,i}(\omega_i)]^2}{\sigma_{DC,i}^{\ 2}} \quad \text{(V.11)}$$

where ω_i is the modulation frequency; $AC_{\exp t,i}(\omega_i)$, $DC_{\exp t,i}(\omega_i)$,and $PS_{\exp t,i}(\omega_i)$ are the average experimental measured *relative* amplitude, *relative* average intensity; *relative* phases and, $AC_{theo,i}(\omega_i)$, $DC_{theo,i}(\omega_i)$, and $PS_{theo,i}(\omega_i)$ are the calculated values respectively; $\sigma_{AC,i}$, $\sigma_{DC,i}$, and $\sigma_{PS,i}$ are the standard deviations in the repeated measurements. For convenience, the subscription of "*rel*" is not written in Eqns (V.11) and (V.12). In this work, we repeated measurements at least 10 times, and the standard errors were within 0.5% of the corresponding measured values.

Not all of measured values for AC_{rel}, DC_{rel}, and PS_{rel} are required in order to determine the optical properties for a sample. Theoretically, any one of kind of the measurements from AC_{rel}, and PS_{rel}, is sufficient to determine μ_a and μ_s'. Certainly, any other combination of measurements from AC_{rel}, DC_{rel}, PS_{rel} can also be used in the error function. Alternatively, one can combine AC_{rel} and DC_{rel} measurements into the modulation ratio, $Mod_{rel} = AC_{rel} / DC_{rel}$, and one can minimize the error function:

$$\chi^2 = \sum_i \frac{[Mod_{\exp t,i}(\omega_i) - Mod_{theo,i}(\omega_i)]^2}{\sigma_{Mod,i}^{\ 2}} \quad \text{(V.12)}$$

Using synthetic FDPM data, Pham *et al.* [95] obtained optical properties from three different combinations: 1) *PS* only; 2) *AC* only; 3) *PS* and *AC*. They found that

simultaneous regression of synthetic *AC* and *PS* data provided the most accurate and robust way for determining μ_a and μ_s'. Fishkin *et al.* concluded from their experimental investigations that the combination of *DC* and *PS* offers comparable accuracy and precision with the combined *AC* and *PS* data.[148]

None of the relative measurements of AC_{rel}, DC_{rel}, PS_{rel} shown in the Eqns V.8 through V.10 are a linear function of μ_a and μ_s', and determination of μ_a and μ_s' using multiple frequency methods requires by minimizing the error function of Eqn (V.11) or (V.12) non-linearly. Consequently, the propagated error due to measurement deviation can not be evaluated analytically, and the unique solution to μ_a and μ_s' can not be guaranteed by the local search approaches. In addition, the nonlinear regression usually takes a longer computational time. Using the multiple distance method, these disadvantages can be avoided.

V.1.3.2 Multiple distance methods

One can also convert the Eqns (V.8) through (V.10) by taking logarithm to obtain:

$$\ln(\frac{r}{r_0} DC_{rel}) = -(r - r_0)[3\mu_a(\mu_a + \mu_s')]^{1/2} \tag{V.13}$$

$$\ln(\frac{r}{r_0} AC_{rel}) = -(r - r_0)\sqrt{\frac{3}{2}\mu_a(\mu_a + \mu_s')}(\sqrt{1 + (\frac{\omega}{c\mu_a})^2} + 1)^{1/2} \tag{V.14}$$

$$PS_{rel} = (r - r_0)\sqrt{\frac{3}{2}\mu_a(\mu_a + \mu_s')}(\sqrt{1 + (\frac{\omega}{c\mu_a})^2} - 1)^{1/2} \tag{V.15}$$

An examination of these three equations shows that the left hand sides are linear with the relative source-detector distances (r - r_o). The proportionality constants, or the slopes, can be determined from linear regressions using:

$$k_{AC} = \frac{n\sum_i \ln(\frac{r_i AC_{rel,i}}{r_o})(r_i - r_o) - (\sum_i \ln(\frac{r_i AC_{rel,i}}{r_o}))(\sum_i (r_i - r_o))}{n\sum_i (r_i - r_o)^2 - (\sum_i (r_i - r_o))^2} \tag{V.16}$$

$$k_{DC} = \frac{n\sum_i \ln(\frac{r_i DC_{rel,i}}{r_o})(r_i - r_o) - (\sum_i \ln(\frac{r_i DC_{rel,i}}{r_o}))(\sum_i (r_i - r_o))}{n\sum_i (r_i - r_o)^2 - (\sum_i (r_i - r_o))^2} \tag{V.17}$$

$$k_{PS} = \frac{n\sum_i PS_{rel,i}(r_i - r_o) - (\sum_i PS_{rel,i})(\sum_i (r_i - r_o))}{n\sum_i (r_i - r_o)^2 - (\sum_i (r_i - r_o))^2} \tag{V.18}$$

where the $AC_{rel,i,}$ $DC_{rel,i}$, and $PS_{rel,i}$ are the relative AC, DC, and PS values measured at source detector position r_i relative to that measured at the common reference position r_o. The slopes obtained from the linear regressions of the left hand sides of Eqns (V.13) through (V.15) against (r - r_o) are functions of μ_a and μ_s' only:

$$k_{DC} = -[3\mu_a(\mu_a + \mu_s')]^{1/2} \tag{V.19}$$

$$k_{AC} = -\sqrt{\frac{3}{2}\mu_a(\mu_a + \mu_s')}\left(\sqrt{1 + (\frac{\omega}{c\mu_a})^2} + 1\right)^{1/2} \tag{V.20}$$

$$k_{PS} = \sqrt{\frac{3}{2}\mu_a(\mu_a + \mu_s')}\left(\sqrt{1 + (\frac{\omega}{c\mu_a})^2} - 1\right)^{1/2} \tag{V.21}$$

If any two of three slopes from k_{DC}, k_{AC}, and k_{PS}, are known, one can simultaneously determine the numerical values for μ_a and μ_s' analytically from any

two of the three equations above. When all three slopes are used, the relation is redundant, and μ_a and μ_s' can be extracted from parameter estimation by non-linearly minimizing the error function:

$$\chi^2 = \left(\frac{k_{AC,\exp t} - k_{AC,theo}}{k_{AC,\exp t}} \right)^2 + \left(\frac{k_{DC,\exp t} - k_{DC,theo}}{k_{DC,\exp t}} \right)^2 + \left(\frac{k_{PS,\exp t} - k_{PS,theo}}{k_{PS,\exp t}} \right)^2 \qquad \text{(V.22)}$$

where $k_{AC,\exp t}$, $k_{DC,\exp t}$, and $k_{PS,\exp t}$ are slopes determined from the FDPM measurements of AC, DC, PS with respect to relative distance, $(r\text{-}r_o)$; $k_{AC,theo}$, $k_{DC,theo}$, and $k_{PS,theo}$ can be theoretically calculated from Eqns (V.19) through (V.21). Since Eqns (V.19) through (V.21) just contain two unknowns of μ_a and μ_s', an additional relation exits :

$$K = \frac{k_{AC}^{\ 2} - k_{PS}^{\ 2}}{k_{DC}^{\ 2}} = 1 \qquad \text{(V.23)}$$

where K is called criteria parameter, and can be used to check the consistency of experimental data.[10]

V.1.3.3 Combination of multiple distances and multiple frequencies methods

Due to the high efficiencies and high rate of computer controlled devices in data collection, FDPM measurements of AC, DC, and PS are redundant. Upon conducting FDPM at multiple distances and also at multiple frequencies, multiple frequency and multiple distance methods can be combined in order to give most accurate and most robust characterization of the optical properties of a sample (Figure V.6).

Figure V.6 shows two different ways to determine μ_a, and μ_s' from redundant FDPM measurements at frequency ω_1, ω_2 through ω_n, and at distance r_o, r_1, … r_m. By taking multiple frequency method first, μ_a and μ_s' can be determined from nonlinear regression of AC, DC, and PS measured at any source-detector separation distance, from r_1 through r_m with r_o as the reference.

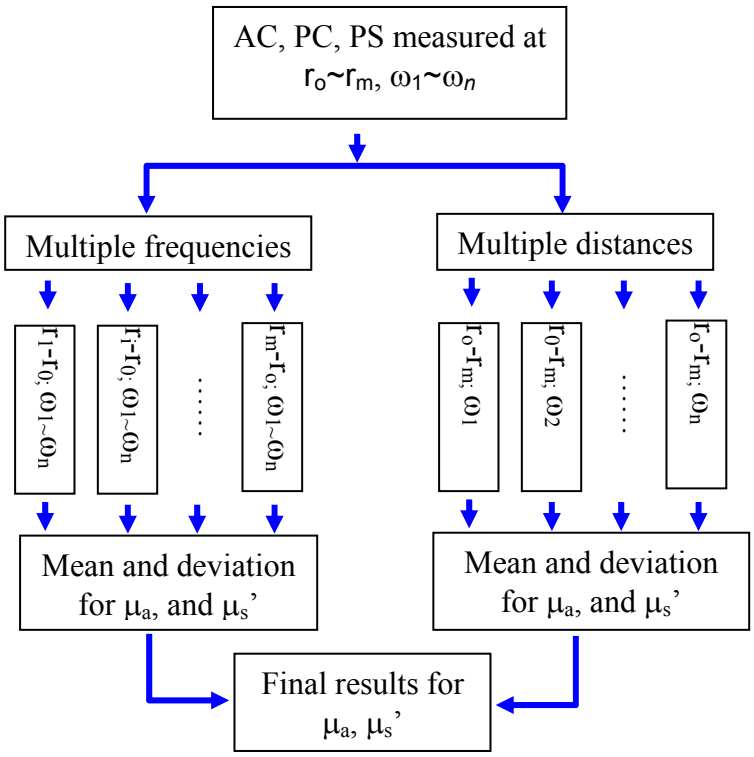

Figure V.6 FDPM data analysis using combined multiple distance and multiple frequency methods.

The values of μ_a and μ_s' determined at different source-detector separation distances are analyzed to obtain the mean values as the final results. Alternatively, one can take multiple distance analysis first by calculating μ_a and μ_s' from the regressed

slopes of DC, AC, and PS at each modulation frequencies ω_i, and then values of μ_a and μ_s' determined at all modulation frequencies can be averaged to obtain the final results.

V.1.3.4 Combination of AC, DC, and PS

Not all measurements of AC, DC, and PS are required in order to determined μ_a and μ_s'. In the multiple frequency methods, only one of them is necessary in order to determine the value of μ_a and μ_s'; in multiple distance methods, any two measurements of AC, DC, and PS are needed to generate two equations to solve for obtaining μ_a and μ_s'. Therefore, there are multiple choices to select what measurements in order to obtain μ_a and μ_s'.

Depending upon the accuracy and precision of *DC*, *AC*, and *PS* in FDPM measurements, the final numerical values of the obtained μ_a and μ_s' may be significantly different depending on the data analysis method and selected measurements for data analysis. The data analysis and experimental conditions must be optimized to ensure the validity of FDPM for determining optical properties of suspensions.

V.1.4. Optimization of FDPM measurement

In determining the optimum experimental conditions and best data analysis scheme, we conducted FDPM measurements of light scattering and absorption for a typical polystyrene latex at a wide range of frequencies ranging from 10 to 100 MHz with increments of 5 MHz, and at 11 source-detector separation distances ranging from 0.7 to 1.5 cm. From the FDPM-measured *DC*, *AC*, and *PS*, multiple distance and multiple frequency analyses are both used to extract the isotropic scattering coefficients,

which were then compared with the theoretical prediction using Percus-Yevick hard sphere model.

The mean size of the polystyrene latex was 143 nm with standard size deviation of 22 nm, which was cleaned using dialysis and conditioned to the ionic strength of 120 mM NaCl equivalent to screen the long-ranged ESI.

V.1.4.1 FDPM measurements of AC, DC, and PS

The frequency domain photon migration measurements of AC, DC, and PS at multiple source-detector separation distances and multiple modulation frequencies are illustrated in Figures V.7 through V.9 respectively.

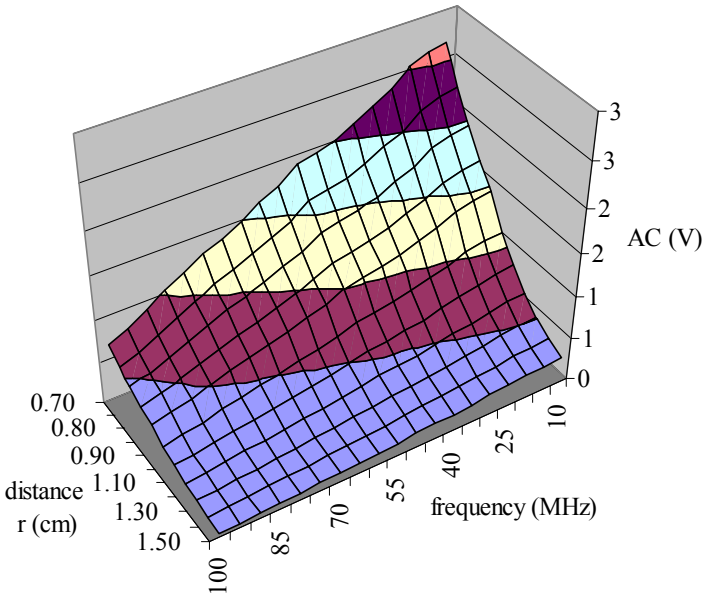

Figure V.7 FDPM measurements of AC in volts, which is proportional to the amplitude of the detected photon density wave.

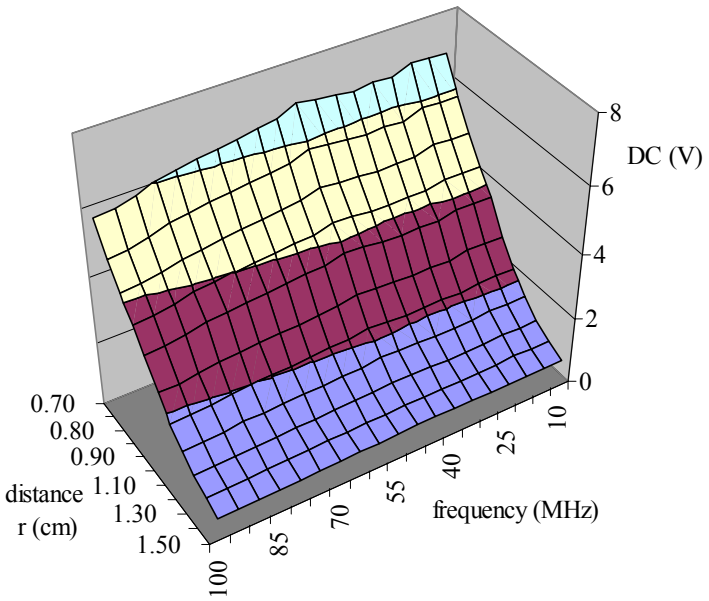

Figure V.8 FDPM of DC in volts, which is proportional to the average intensity of the detected photon density wave.

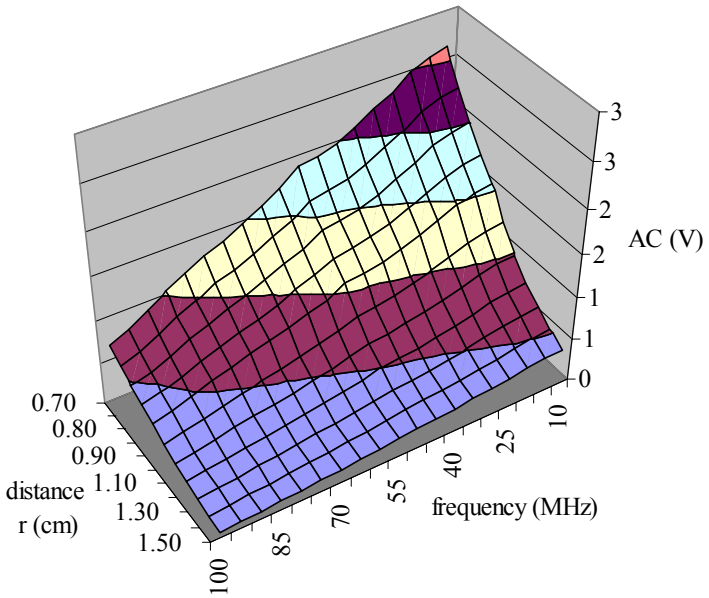

Figure V.9 FDPM measurements of relative PS in degree with regard to the reference source-detector separation distance r_o.

The standard error of the FDPM measurement of AC, DC, and PS are generally within 0.5% of the measured values, where the standard error is defined as the ratio of

standard deviation to the mean value. The standard error in AC, DC, and relative PS measurements shown in Figures V.7 through V.9 are presented in Figures V.10 through V.12 respectively.

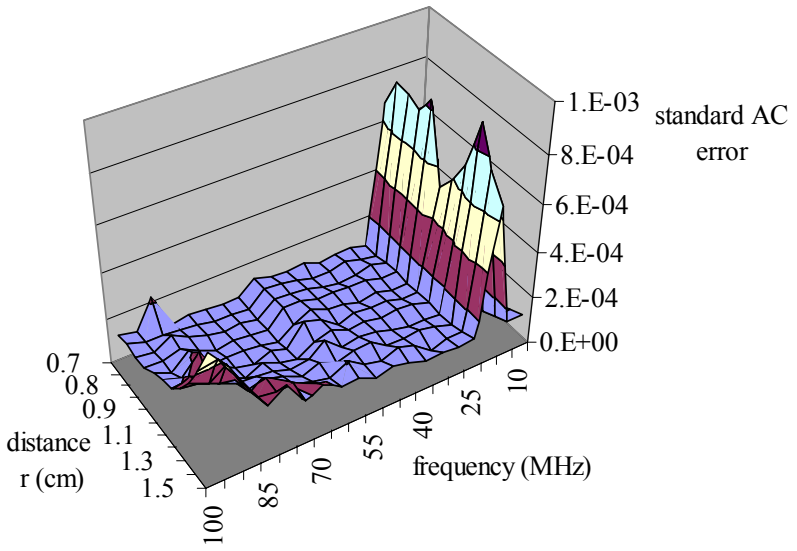

Figure V.10 Standard error for the AC measurements shown in Figure V.7.

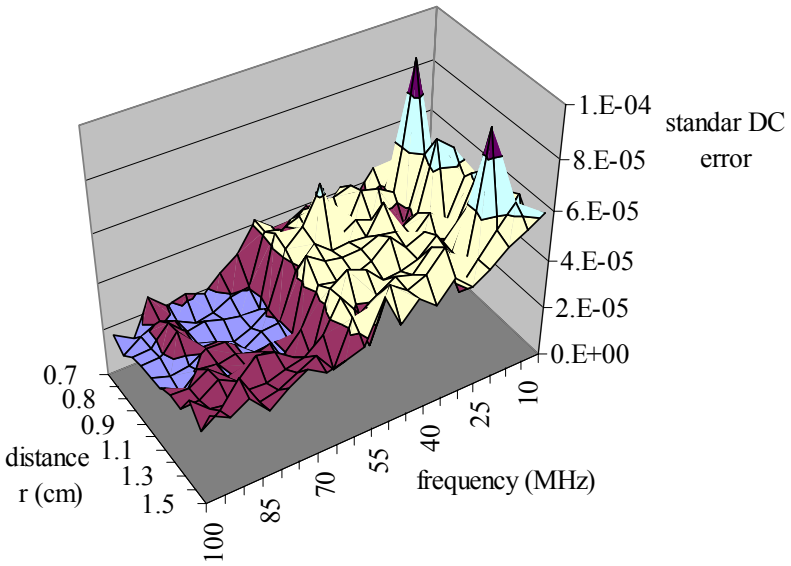

Figure V.11 Standard error for the DC measurements shown in Figure V.8.

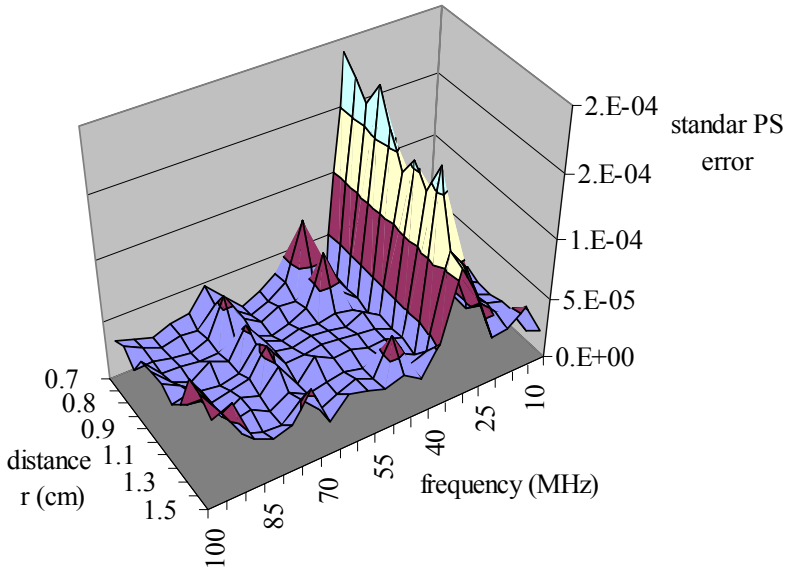

Figure V.12 Standard error for the relative phase measurements.

FDPM measured AC, DC, and PS can be used to determine optical properties via either multiple frequency methods or multiple distance methods.

V.1.4.2 Multiple frequency methods

Multiple frequency methods were first used to analyze FDPM measurements of AC, DC, and PS. There are multiple choices in selecting source-detector separation distances and selecting properties from AC, DC, and PS measurements to minimize the corresponding error function (Eqn (V.11)) for the determination of μ_a and μ_s'. We compared a total of 9 combinations of measured properties:

- *AC* only
- *PS* only
- *Mod only*
- *AC* and *DC*
- *AC* and *Mod*
- *AC* and *PS*
- *DC* and *Mod*
- *DC* and *PS*
- *AC*, *DC* and *PS*

At each possible choice listed above, the FDPM measurements at the source-detector separation distance r_o=0.7 cm were chosen to be the common reference source-detector separation distance for all the measurements conducted at all other distances. At each distance other than r_o, measurements at all modulation frequencies are included in the error function of Eqn (V.11) or (V.12) in the parameter estimation. The two

unknowns, μ_a and μ_s', are then determined by minimizing the corresponding error function using the Matlab fminsearch.m function, in which the Nelder-Mead direct search method is applied in parameter estimation.[149] Convergence of iteration was achieved when the change in the norm for the unknown optical properties and the change in the error function in the consecutive two iterations were both less than 10^{-6}. The determined isotropic scattering coefficients from varies combinations of experimental properties are shown in the Figure V.13.

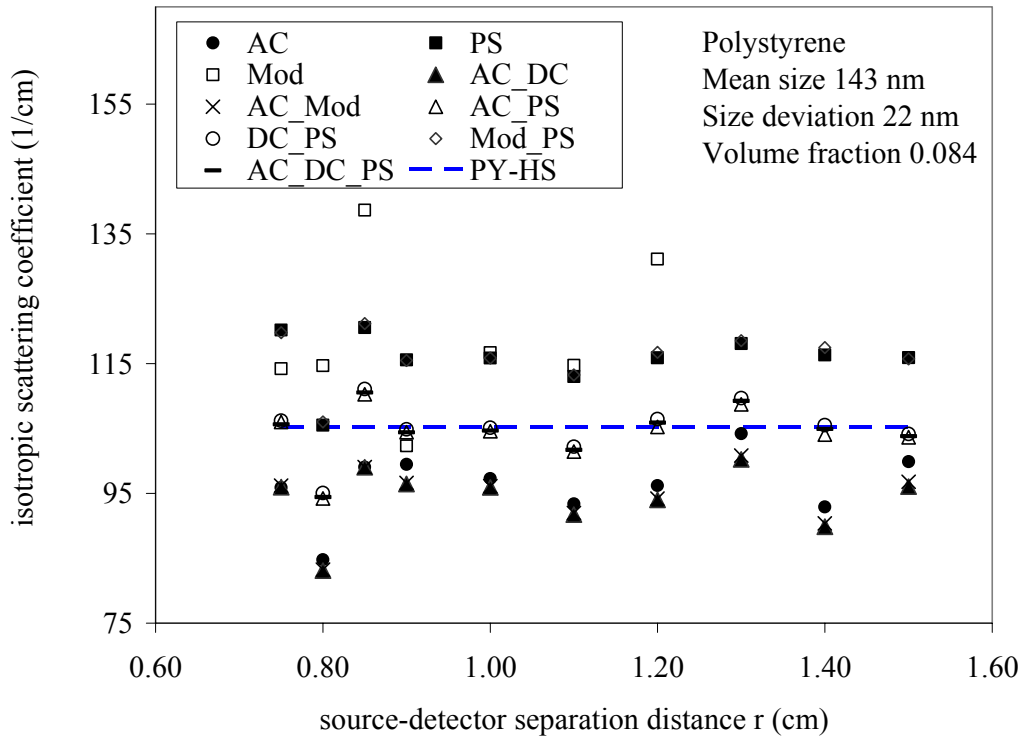

Figure V.13 Isotropic scattering coefficients calculated from PY-HS model (dashed line) and those from multiple frequency analysis (symbols) of FDPM measurements, where the r_o is selected to be 0.7 cm at source detector separation distances from 0.7 to 1.5 cm.

Figure V.13 shows that the isotropic scattering coefficients from various combinations of measurements (except from modulation (Mod) only) do not vary appreciably with the source-detector separation distance.

We noted that the minimum source-detector separation distance *r* is 7 mm, which is much greater than the minimum separation distance to ensure that the diffusion approximation is satisfied.[140, 141]

The averages and standard deviations of the isotropic scattering coefficients (shown in Figure V.13) at varying source-detector separation distances are summarized in Table V.1.

Figure V.13 shows that values of μ_s' determined from regression of modulation data alone at varying source-detector separation distance (denoted as empty square) have the largest standard deviation, about a quarter of the measured values (Table V.1)

Table V.1 The averages and standard deviations for the isotropic scattering coefficients estimated using multiple frequency methods at varying distances. The PY-HS model prediction of the isotropic scattering coefficient is 105.3 (1/cm).

	Mod	PS	AC	AC, DC	AC, Mod	AC, PS	DC, PS	Mod, PS	AC,DC, PS
Average (1/cm)	129.5	115.7	96.3	94.2	94.5	104.3	105.0	116.0	104.5
Standard error	23.0%	9.9%	-8.5%	10.5%	10.2%	-1.0%	-0.3%	10.2%	-0.7%
Standard deviation (1/cm)	20.3	4.2	5.2	5.0	5.0	4.3	4.3	4.2	4.4

Table V.1 also shows that the averaged isotropic scattering coefficients, μ_s', determined from the values of PS alone (solid squares) at all source-detector separation distances are overestimated (by about 10%) in comparison to the PY-HS model prediction, while μ_s' are underestimated if they are determined from one of these three combination of values: 1) *AC* measurements alone (solid circle); 2) both *AC* and *DC* measurements (solid triangle); and 3) both AC and Modulation ratio. The μ_s' obtained from these three selections of the intensity properties (AC, and DC) are similar, and underestimate the scattering coefficient by about 10%. The values of μ_s' obtained from the combinations of 1) AC and PS, 2) DC and PS, and 3) AC, DC, and PS measurements are systematically similar, and the relative error with respect to the PY-HS model predictions is within 1%.

Both Figure V.13 and Table V.1 show that the estimated values for μ_s' from the both measurements of modulation and PS are consistently similar with those estimated from PS measurement alone at all the source-detector separation distances. The similarity results from the fact that the modulation ratio only changes slightly as the photon density wave propagates from the light source. Therefore, a smallest error in modulation ratio arising from error in AC and DC measurements may generate a significant relative error in the measured *demodulation* of propagating photon density wave. Therefore, the demodulation in Eqn (V.11) is less weighted due to its large relative error in comparison to AC, DC, and PS measurements and including the modulation properties in the error function does not impact the error function

significantly. This may also be the reason that the μ_s' obtained from the modulation alone has the largest standard deviation. From the inspection of the relative measurement error shown in the Table V.1, the combination of the AC or/and DC with the PS gives the most accurate estimation of the isotropic scattering coefficients.

In summary, the isotropic scattering coefficients obtained from the combined measurements of AC and PS (empty triangle), DC and *PS* (open circle), as well as AC, DC, and PS (horizontal bar), are consistently similar, and match the PY-HS model prediction.

Table V.1 shows that the standard deviations obtained from a combination of PS with AC or DC are slightly less than those obtained from intensity properties only. Therefore, using PS combined with AC or DC can generate most accurate and most precise measurement of the isotropic scattering coefficients in multiple frequency analysis.

V.1.4.3 Multiple distance methods

The multiple distance analysis methods require any two equations from Eqns (V.19 through V.21) to solve for the μ_a and μ_s' analytically from the regressed slopes. Using multiple distance methods, the isotropic scattering coefficients are determined for the following combination of FDPM measurements:

- *AC* and *DC*
- *AC* and *Mod*
- *AC* and *PS*

- *DC* and *Mod*
- *DC* and *PS*
- *AC*, *DC* and *PS*

The obtained isotropic scattering coefficients are presented in the Figure V.14.

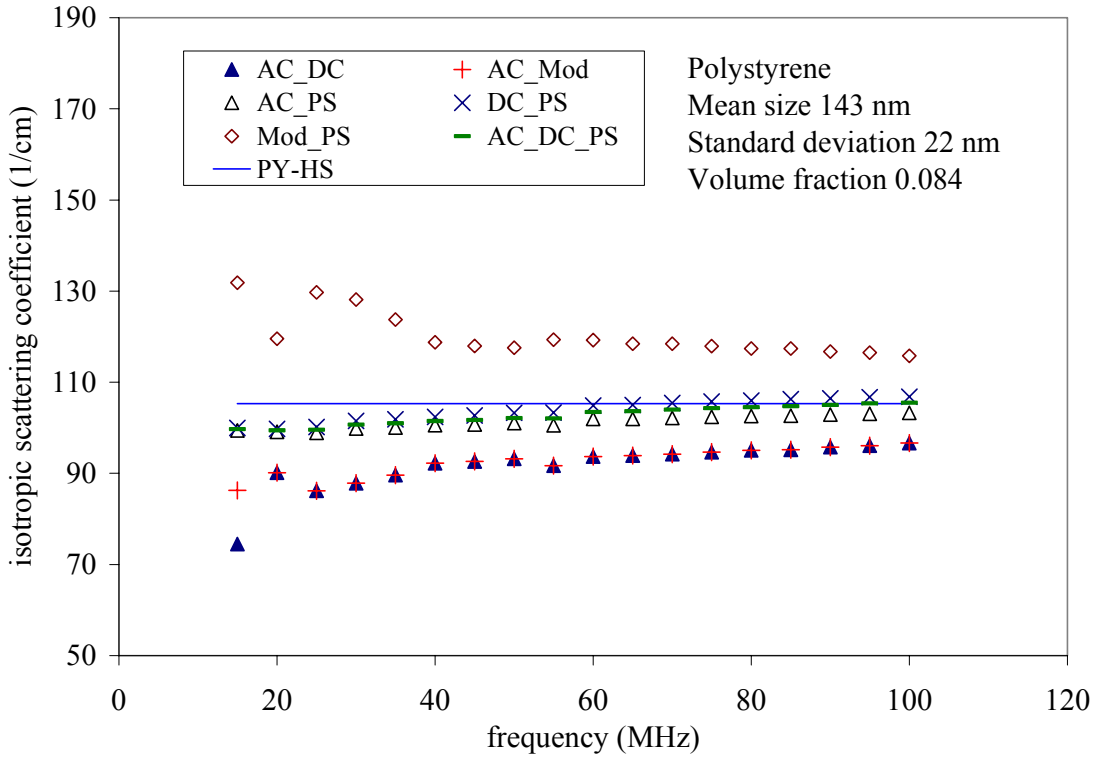

Figure V.14 Isotropic scattering coefficients obtained from monodisperse PY-HS model and those regressed using multiple distance methods at a modulation frequency range from 10 to 100 MHz with an increments of 5 MHz.

Similar to the values determined from multiple frequency methods, Figure V.14 shows that the combinations of *AC* and *PS*, *DC* and *PS*, as well as the combination of *AC*, *DC*, and *PS* give similar and consistent estimation of μ_s', which are close to the

values predicted by PY-HS model prediction. Figure V.14 also shows that data analysis using PS over predicts isotropic scattering coefficient, and an analysis using *AC* and *DC* leads to an underestimation of the isotropic scattering coefficient. This agrees with the results obtained from multiple frequency methods.

The averages and standard deviation of the isotropic scattering coefficients evaluated using multiple distance methods at varying frequencies (shown in Figure V.14) are summarized in Table V.2.

Table V.2 *The averages and standard deviation for the isotropic scattering coefficients estimated using multiple distance methods at frequencies from 10 to 100 MHz and the distance varying from 0.7 to 1.5 cm.*

	AC,DC	DC,PS	AC,PS	AC,DC, PS	AC, Mod	DC, Mod	Mod, PS
Average (1/cm)	91.4	103.6	101.2	102.5	88.8	88.6	124.3
Relative error	-13.2%	-1.6%	-3.9%	-2.6%	-15.7%	-15.9%	18.0%
Standard Deviation (1/cm)	5.9	2.4	1.4	2.0	3.2	3.2	4.7

From the Table V.2, one can identify that μ_s' determined from intensity measurements, AC, DC, or Modulation ratio, are underestimated. An examination of Figure V.14 shows that the changes in measured scattering coefficients with the increasing modulation frequency are subject to systematic error. The values of μ_s' obtained from the AC and PS, DC and PC, as well as AC, DC, and PS have the tendency

to increase with the increasing modulation frequency. The reason for the dependence of the obtained μ_s' on the modulation frequency may result from the unaccounted frequency-dependent instrument function. Figure V.14 shows that at the modulation frequencies from 50 to 100 MHz, the FDPM determined μ_s' from the AC and PS, DC and PS, and both AC, DC, and PS match the PY-HS model prediction, suggesting the frequency range from 50 to 100 MHz is more suitable to conduct FDPM measurement of isotropic scattering coefficient. We calculated the mean and deviation of the isotropic scattering coefficients evaluated using multiple distance methods at frequencies from 50 to 100 MHz, and the obtained mean, standard error in percentage, and standard deviation are presented in the Table V.3.

Table V.3 *The averages and standard deviation for the isotropic scattering coefficients estimated using multiple distance methods at frequencies from 50 to 100 MHz.*

	AC,DC	DC,PS	AC,PS	AC, DC, PS	AC, Mod	DC, Mod	Mod, PS
Average (1/cm)	94.6	94.6	102.2	94.6	105.5	117.7	104.1
Relative error	-10.2%	-10.2%	-2.9%	-10.2%	0.1%	11.8%	-1.2%
Standard Deviation (1/cm)	1.4	1.4	0.8	1.4	1.2	1.1	1.2

Table V.3 shows that at modulation frequencies between 50 and 100 MHz, isotropic scattering obtained from 1) DC and PS, 2) AC, DC, and PS, 3) AC, DC, and PS measurements give the most precise measurement of isotropic scattering coefficients.

With smallest standard error (shown in Table V.3), data analysis using AC and PS can generate an estimate of isotropic scattering with both accuracy and precision.

V.1.4.4 Summary of FDPM data analysis

The data analysis using intensity measurements of AC, DC, and modulation ratio tends to underestimate scattering data, and data analysis using PS tends to overestimate the scattering coefficients. The data analysis using a combination of *AC* or/and *DC* with *PS* in both multiple frequency methods and multiple distance methods can give accurate and consistent estimation of scattering data. The precision associated with using AC and PS, or DC and PS may result from the compromise between the overestimation from PS measurements and underestimation form the intensity measurements of AC, DC measurements.

Since multiple distance methods are based on linear regression followed by an analytical solution from the regressed slopes, the estimation error is tractable. Furthermore, isotropic scattering coefficients determined from PS combined with AC or DC measurements at the frequencies range between 50 to 100 MHz consistently match the PY-HS model prediction (shown in Figure V.13) and agree with the values determined from multiple frequency methods. The multiple distance analysis of PS and AC or DC measurement is used throughout the work presented in this thesis

Although, there is potential error associated with the assumed PY-HS prediction, the above analysis has been repeated using monodisperse polystyrene suspensions (600± 5nm) at the particle volume fraction less than 2% in order to guarantee independent scattering. These latter results also support the conclusion that multiple-

distance methods using either AC or DC with PS measurement at the modulation frequencies of 50 to 100 MHz provide the most accurate and robust evaluation of optical properties.

In this section, the suitable data analysis methods and optimum frequency range for FDPM measurements have been identified by comparing the value of isotropic scattering coefficient from PY-HS model prediction with those obtain from FDPM measurements of actual polystyrene samples. The details about sample preparation and characterization will be detailed in the next section.

V.2. Sample preparation and material characterization

The polystyrene lattices were obtained from Dow Chemical Company (Midland, MI) in concentrated water dispersions with the volume factions between 0.45~0.60. They were first dialyzed using a membrane tube (Spectra/Pro: MWCO 6-8,000, Spectrum laboratories, Inc.) in ultra-filtered-deionized water (W-20, Fisher) to remove ions and the surfactants, which had been added to stabilize the suspension. The dialyzing water was changed every 8~12 hours until the conductivity of the equilibrium dialyzing water was less than 6 ppm NaCl equivalents, as measured using a titration controller (Fisher, Accumet Model 150). The volume fractions of polystyrene lattices were measured using an evaporation method, which involves weighting samples using a 1/10000g resolution balance (Denver Instrument M-220D) before and after they were dried in an oven (Model 280A, Fisher) for 8 hr at 95°C. Weight loss due to water evaporation was used to calculate volume fraction. In order to keep the volume fraction as high as possible, 3 or 4 strips of plastic cable ties were used to bind around the

membrane tube to restrict the membrane expansion under increasing osmotic pressure associated with the dialyzing process. The dialyzed polystyrene lattices were then diluted to the desired volume fractions using final dialyzing water. 2 M sodium chloride solution (S1240, Spectrum Chemical Mfg. Corp.) was then added to adjust the suspension to desired ionic strengths. Volume fractions of samples were recalculated after the addition of NaCl solution.

V.2.1. Particle size measurements

The mean sizes of the polystyrene lattices were measured using dynamic light scattering (Zetasizer 3000HS, Malvern) after the sample was diluted in 0.1 M NaCl solution. The values were 143 nm for Dow 755 (latex A) and 226 nm for Dow 788 (latex B), as shown in Table V.4. The standard size deviation for latex A was determined by digitizing images acquired using TEM (Zeiss 10C), and analyzing the size distribution using Image Pro software (Image Pro 3.0, Cybernetics). A typical image of TEM is shown in Figure V.15.

The magnification used in the TEM measurement was about 50,000X. Three different images were taken and processed for a total number of particles > 300 in order to estimate the spread of particle sizes accurately. Since no size standard was included in the TEM measurement, and the particle size could not be directly determined from TEM with accuracy, the mean particle size was determined using dynamic light scattering (Zetasizer 3000HS, Malvern).

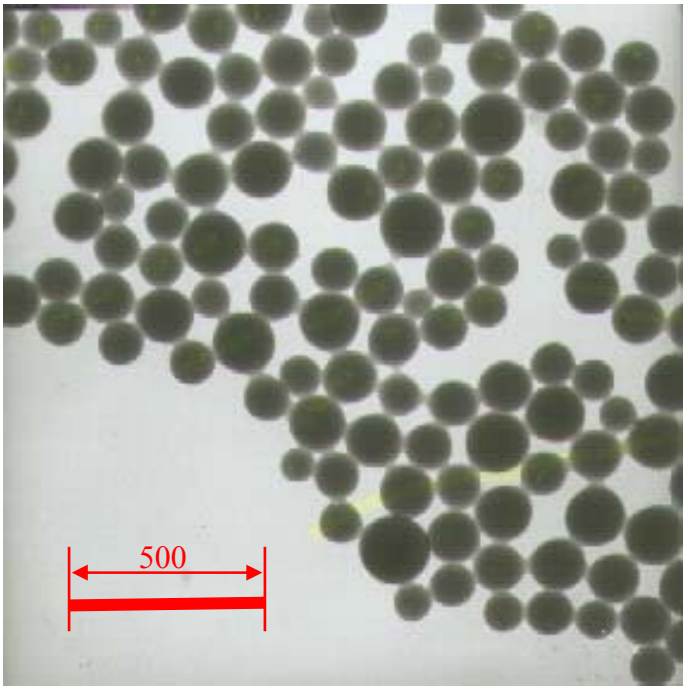

Figure V.15 TEM image of polystyrene latex B, with magnification about 50,000X.

V.2.2. Determine intrinsic particle charge using conductometric titration

The intrinsic surface charges of particles refer to the charges resulting from ionization of ionizable groups on the particle surface. The intrinsic surface charges of polystyrene were measured using the conductometric titration method after polystyrene lattices were cleaned by dialyzing and ion-exchanging processes.[150-152]

The polystyrene lattices were first dialyzed using ultra-filtered deionized- water, until the conductivity was less than 600 ppm NaCl equivalent. The dialyzed polystyrene lattices were diluted using ultra-filtered-deionized water to volume fraction about 2~5%. The dialyzed polystyrene with suitable volume fraction was then passed through ion exchange column fed with mixed ion exchange resin (AG 501-X8(D), Bio-Rad

Laboratories, CA) repeatedly until the conductivity of the polystyrene lattices reached a constant value (Figure V.16).

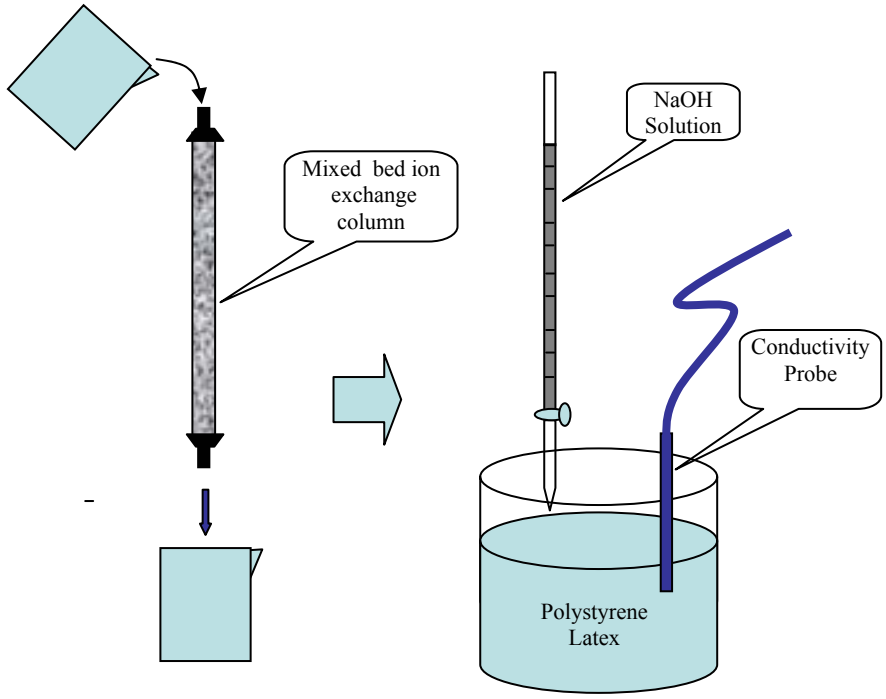

Figure V.16 Dialyzed polystyrene latex with suitable volume fraction was first passed through a mixed bed ion exchange volume, and then the conductivity is measured using a probe with addition of NaOH solution.

The ion exchanged polystyrene latex was then titrated with 100 mM NaOH with conductivity monitored by a titration controller (Fisher, Accumet Model 150). The physics behind conductometric titration is briefly introduced in the following.

After dialyzing and ion-exchange cleaning with a mixed bed ion-exchange resin, the concentration of surfactant and ions (except the H^+) are minimized, and negatively charge polystyrene particles are neutralized by positive H^+. The amount of H^+ exists in the solvent equal to the amount of total surface charges carried by the suspended

polystyrene particles. With the addition of NaOH, the added OH^- ions combine with H^+ ions to form H_2O, while Na^+ (with amount equivalent to the reacted OH-) builds up in the solvent (as shown in Figure V.17).

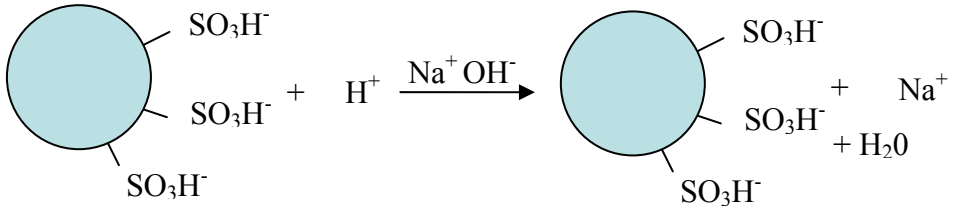

Figure V.17 Principles for the conductometric titration: with the addition of NaOH solution, the added OH^- ions combine with H^+ ions to form H_2O while Na^+ ions build up in the solution. Since the mobility of Na^+ is less than that of H^+, the conductivity of the dispersion decreases with the addition of Na^+ until H^+ in the solvent is depleted.

The conductivity of a solution is proportional to the concentration and mobility of ions. Since the mobility of Na^+ is less than that of H^+, the contribution of Na^+ to the solution conductivity is less than that of same amount of H^+. Therefore, the conductivity of the polystyrene latex decreases with the addition of Na^+ until all of H^+ existed in the solvent is depleted in the titration process. After the conductivity of the suspensions reached a minimum, continuous addition of NaOH will cause the conductivity of the suspension to increase linearly due to the excesses of added Na^+ and OH^-. A typical conductometric titration curve is illustrated in Figure V.18, where the polystyrene sample used was Dow 788 (Latex B).

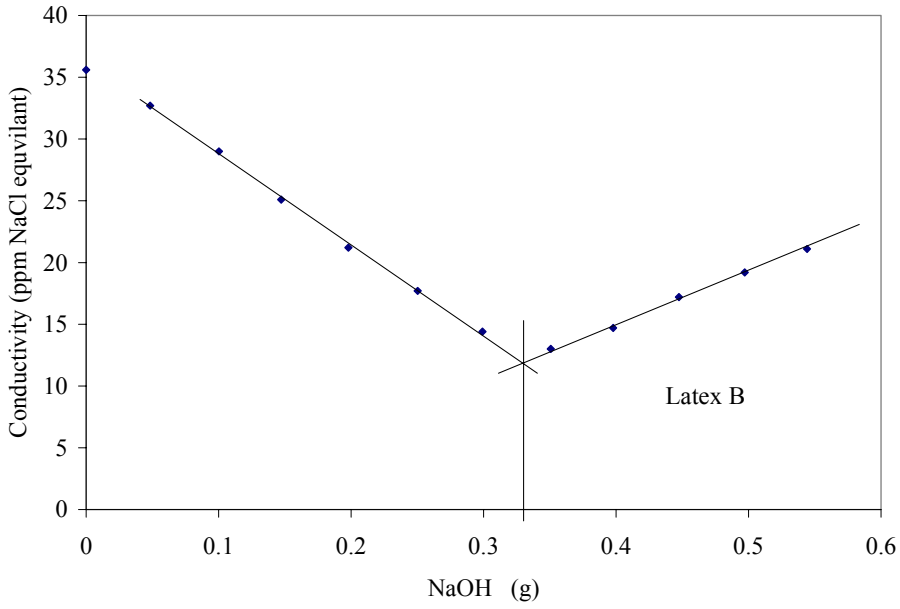

Figure V.18 Conductometric titration curve for the polystyrene latex with the mean particle size of 143 nm and standard size deviation of 22 nm at the volume fraction of 0.022 titrated using NaOH solution (0.023M).

From the amount of the NaOH added at the minimum conductivity curve, the amount of H^+ existed in the suspension before the titration can be determined. Upon assuming the total surface charges in electron charges for all latex particles in the suspension equals to the number of H^+ existing before titration, the average intrinsic particle surface charge can be calculated by dividing the total amount of Na^+ added at the minimum conductivity by the total number of latex particles in the suspension. The surface charge density can be determined by dividing average surface charge by the mean particle surface area.

The intrinsic surface charges, and the charge density obtained from the conductometric titration are also included in the Table V.4.

V.2.3. Measurement of zeta potential

Currently, we are not aware of direct methods for measuring effective surface charge or electrostatic potential at particle surface. Zeta potential, the potential at the shear plane, is frequently used to indicate electrostatic potential at the particle surfaces (Figure V.19). [107]

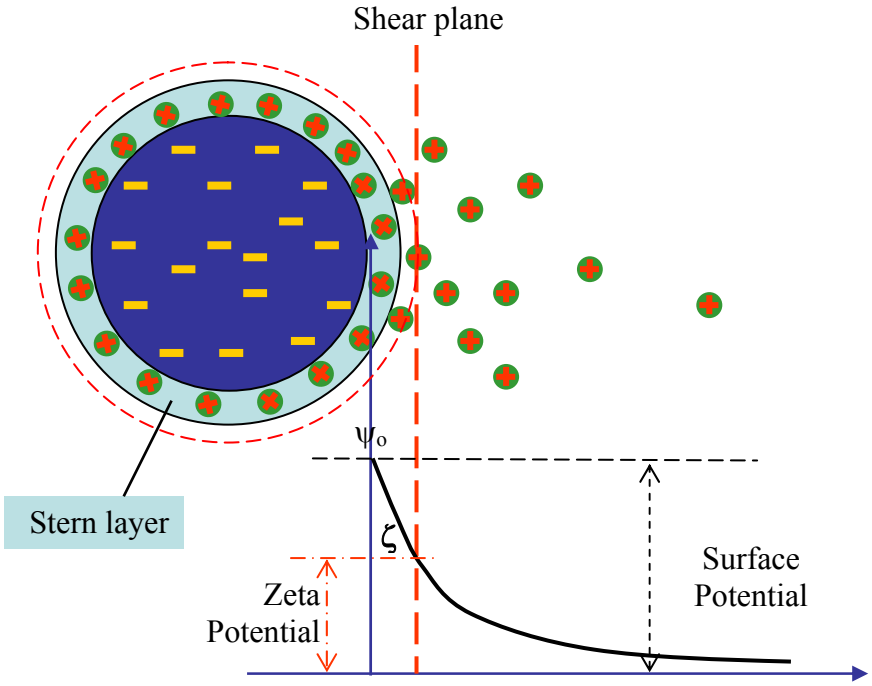

Figure V.19 Zeta potential refers to the electrostatic potential at the particle shear plane or slippery plane. Micro ions within the space between the shear plane and particle surface moves with the particle, and ions outside of shear plane can move with suspending fluid.

Zeta potentials are typically measured using electrophoretic method that measures the electrophoretic mobility of particles in a dilute suspensions (typically with particle volume fraction <0.1%). The electrophoretic mobility, U, is defined as the ratio of velocity of particle, *v*, to the external electric field, E:

$$U = \frac{v}{E} \tag{V.24}$$

The measured mobility can be related to the zeta potential, ς, through:

$$\varsigma = \frac{\eta v F}{E D_p \varepsilon_o} \tag{V.25}$$

where η and ε_o are the viscosity and electric permittivity of the solvent respectively; F is a constant depending upon ionic strength.

In the work of this thesis, the zeta potentials for the two lattices were measured using electrophoretic method (Zetasizer 3000HS, Malvern, UK) after the dialyzed polystyrene lattices were diluted in 120 mM NaCl solution. The measured Zeta potentials for both lattices are also presented in the Table V.4.

From the measured zeta potential, ζ, the effective surface charge, z_{eff}, can be estimated from the analytical solution of Poisson-Boltzmann equation numerically.[53] The Poisson-Boltzmann equation can also be solved with certain assumptions. The Smoluchowski approximation can be applied when thickness of electric double layer κ^{-1} is thin in comparison to the particle radius R, such that $\kappa R > 100$, while Debye-Hückel approximation assumes low surface potential and thick electric double layer with $\kappa R < 0.1$. The value of F in the Eqn (V.25) should be selected to be 1 at Smoluchowski approximation and selected to be 1.5 when Hückel approximation is used. Generally, the thickness of the double layer surrounding a colloidal particle is between these two extreme cases.

Table V.4 The properties of polystyrene lattices

Commercial Name	Dow 788	Dow 755
Polystyrene latex	A	B
Mean Size (nm)	143	226
Size deviation (nm)	22 (TEM)	43 (DLS)
Zeta Potential (mV)	72	48
Mean Surface Charge (e.c.)	26,000	142000
Mean Surface charge Density (mol/m^2)	6.3 E-7	1.2 E7

In Chapters III and IV, we have introduced structure factor models addressing colloidal structure and photon diffusion theory respectively. In this chapter we introduced FDPM data analysis and sample preparation and characterization methods. In the next chapters, we will compare the model predicted isotropic scattering coefficients with those determined from FDPM measurements using multiple distance methods, in order to test different structure factor models and investigate particle interactions. The next Chapter will compare the isotropic scattering coefficients predicted from two different analytical structure factor models, MSA-PM and MSA-HSY, which consider electrostatic interaction. The isotropic scattering coefficient measured using FDPM will be presented in Chapter VII.

CHAPTER VI

MSA STRUCTURE FACTOR MODELS WITH ELECTROSTATIC INTERACTIONS

VI.1. Introduction

Chapter III showed that isotropic scattering coefficients from concentrated suspensions can be predicted by combing the Mie theory for calculating the form factor with an approximate structure factor model typically obtained from solving O-Z equation. In concentrated suspensions, the correlated particle positions have strong impact on their isotropic scattering coefficients. The accuracy of estimated scattering coefficients strongly relies on the accuracy of structure factor model used.

The accuracy for a structure factor model in predicting correlated particle positions depends on both the closure relation to O-Z equation as well as the model describing particle interaction potentials. Salgi and Rajagopalan reviewed the structure factor model with an emphasis on PY-HS model.[111] Nägele reviewed investigation on structure of colloidal systems with significant electrostatic interactions.[153] The mean spherical approximation (MSA), shown as Eqn (III.19) is the most extensively used closure relation in investigating colloidal particle interactions. The electrostatic interaction among charged colloidal particles can usually be modeled by hard sphere Yukawa (HSY) or primary model (PM) interactions, which are introduced in the first section of Chapter III as Eqn (III.4) and Eqn (III.3) respectively.

With the mean spherical approximation (MSA), Hayter and Penfold[154] and later Herrera *et al.*[122] each provided a structure factor model based on the hard sphere Yukawa (HSY) interaction model for one component Yukawa system. Using primary model (PM) interaction, Hiroike[128, 129] developed an explicit expression for the direction correlation function, $c_{ij}(r)$, whose 3D Fourier transform $c_{ij}(q)$ can be used to analytically calculate the structure factor via Eqn (III.13) and Eqn (III.14).

In the following section, we investigate these three MSA structure factor models by comparing their predictions of isotropic scattering coefficients. The synthetic data were generated for monodisperse suspensions of diameter of 143 nm, and refractive indices of the particle and suspending fluid were chosen to be 1.59 and 1.33 respectively. These refractive index values correspond to the aqueous polystyrene suspensions used in the experimental work presented in the next Chapter.

VI.1.1. MSA-HSY provided by Hayter and Penfold

Hayter and Penfold[154] provided an analytical structure factor model using mean spherical approximation associated with hard sphere Yukawa interactions (MSA-HSY). The isotropic scattering coefficient predicted using Eqn (III.25) with Hayter and Penfold's structure factor model are illustrated in the Figure VI.1 as a function of wavelength, where the diameter of particles are 143 nm.

Figure VI.1 shows that the isotropic scattering coefficients predicted using Hayter and Penfold's model vary with change in surface charge *z* (electron charge) at all the 4 cases: (a) at the ionic strength of 5 mM NaCl equivalent and the volume fraction of 0.05; (b) at the ionic strength of 5 mM NaCl equivalent and the volume fraction of 0.15;

(c) at the ionic strength of 5 mM NaCl equivalent and the volume fraction of 0.32; (d) at the ionic strength of 25 mM NaCl equivalent and the volume fraction of 0.32.

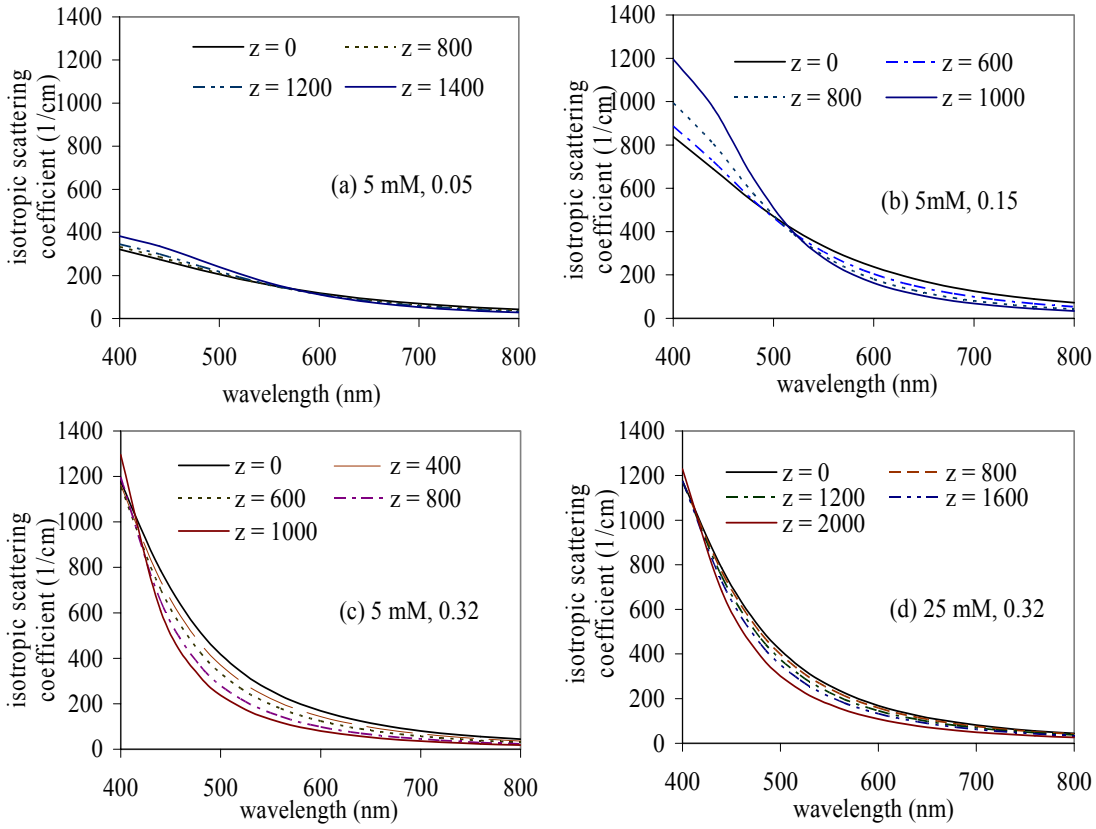

Figure VI.1 Isotropic scattering coefficient predicted by MSA-HSY model versus (Hayter and Penfold) wavelength at varying effective surface charges, z, in electron charge with (a)at the ionic strength of 5 mM NaCl equivalent and the volume fraction of 0.05; (b) at the ionic strength of 5 mM NaCl equivalent and the volume fraction of 0.15; (c) at the ionic strength of 5 mM NaCl equivalent and the volume fraction of 0.32; (d) at the ionic strength of 25 mM NaCl equivalent and the volume fraction of 0.32.

The sensitivity of changes in the predicted isotropic scattering coefficients depends upon the wavelength, ionic strength, and volume fraction. Therefore, Hayter and Penfold's structure factor model successfully predicts the change in isotropic

scattering coefficients in response to the changing ionic strength and surface charge at varying wavelength.

Figures VI.1c and VI.1d show the predicted isotropic scattering coefficients at the volume fraction of 0.32 but at different ionic strength. The predicted isotropic scattering coefficients at the ionic strength of 5 mM (Figure VI.1c) NaCl equivalent vary with a larger amplitude as the particle surface charge increase from 0 to 1000 electron charge than those at the ionic strength of 25 mM even the particle surface charge increases from 0 to 2000 electron charges (Figure VI.1d). Hayter and Penfold's model predictions of isotropic scattering predicted show a higher sensitivity to the changing surface charge at 25 mM NaCl equivalents than those at a lower ionic strength of 5 mM NaCl. Therefore this structure model reflects to some extent the screening effects due to presence of micro-ions to the long-ranged electrostatic interaction.

Our investigation verified that at the surface charge, z=0, the isotropic scattering coefficients match with the prediction using Percus-Yevick model as expected.

This structure model requires solving a polynomial equation of 4^{th} order in order to obtain a complex parameter that is needed to derive the final analytical expression for the structure factor. The correct root can only be identified after all structure factor expressions are calculated and compared. Even in most cases, only one root can generate the only physically meaningful structure factor expression; it is possible that two or more roots of the polynomial equation can lead to close but not identical structure factor expressions. In the latter case, the uniqueness of the solution cannot be guaranteed, and the structure factor cannot be easily determined with confidence.

Recently, Herrera and coworkers[122] provided another solution from MSA-HAS structure factor model that will be introduced in the next section.

VI.1.2. MSA-HSY provided by Herrera *et al.*

The structure factor model provided by Herrera *et al.* also requires solving a 4th order polynomial equation to find a parameter related to the strength of electrostatic interaction between particles. In Herrera's model, the only physically meaningful root is the only positive root and it can be easily identified by computer program. The equations used to calculate structure factor will be presented in Appendix B. With this feature, Herrera's structure factor model is much easier to apply.

Figure VI.2 illustrates the isotropic scattering coefficients predicted by Herrera *et al.* as a function of wavelength at varying surface charge z (in electron charge) for a monodisperse suspension with particle diameter of 143 nm. The predicted isotropic scattering coefficients in Figure VI.2 are plotted at four cases: (a) at the ionic strength of 5 mM NaCl equivalent and the volume fraction of 0.05; (b) at the ionic strength of 5 mM NaCl equivalent and the volume fraction of 0.15; (c) at the ionic strength of 5 mM NaCl equivalent and the volume fraction of 0.32; (d) at the ionic strength of 25 mM NaCl equivalent and the volume fraction of 0.15.

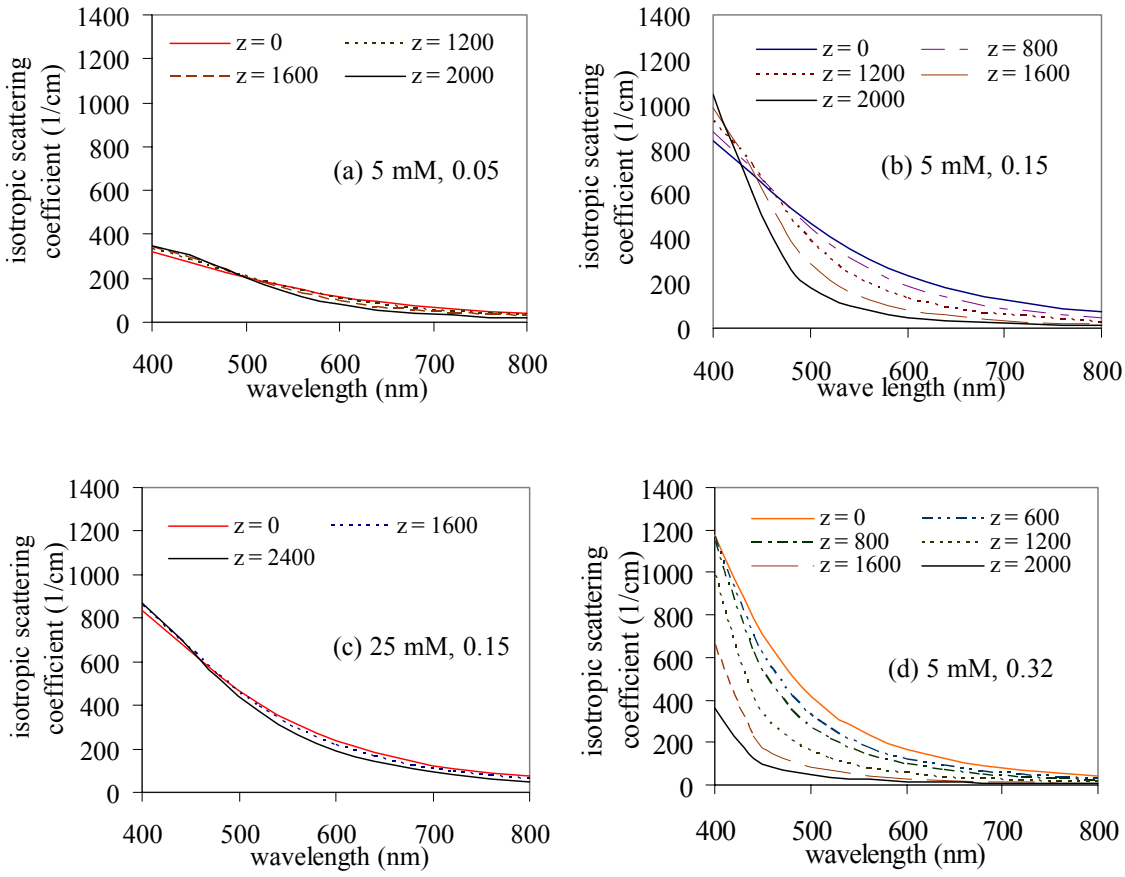

Figure VI.2 Isotropic scattering coefficient predicted by MSA-HSY model versus (Herrera et al.) wavelength at varying effective surface charges, z, in electron charge with (a)at the ionic strength of 5 mM NaCl equivalent and the volume fraction of 0.05; (b) at the ionic strength of 5 mM NaCl equivalent and the volume fraction of 0.15; (c) at the ionic strength of 25 mM NaCl equivalent and the volume fraction of 0.15; (d)at the ionic strength of 5 mM NaCl equivalent and the volume fraction of 0.32.

A comparison of Figures VI.1 and VI.2 shows that isotropic scattering coefficients predicted from these two different MSA-HSY models obtained agree qualitatively. At the ionic strength of 5 mM NaCl equivalent and volume fractions of 0.15 and 0.32, isotropic scattering coefficients predicted by Herrera's model show higher sensitivity to the surface charge than those predicted by Hayter and Penfold's model.

The difference may result from different approaches used in solving the O-Z equations: Hayter and Penfold' structure factor was derived from Baxter's factorization method;[63,64] while Herrera's solution was derived from Blum's Fourier transform approach.[68] The above comparison of the predicted isotropic scatterings indicates that two MSA-HSY structure factor models are similar but not identical in describing colloidal structure.

We affirmed that at the zero particle surface charge, $z = 0$, the prediction using Herrera's MSA model matches the prediction using PY-HS model. This is expected, since MSA relation is equivalent to the Percus-Yevick relation when particles interacts like hard spheres.

VI.1.3. MSA-PM structure factor model provided by Hiroike

Similar to HSY interaction, colloidal particles are considered as macro ions in PM interactions. There are two major difference between HSY and PM interactions: 1) particles interact through *direct* Coulombic interactions in PM, while particles interact via *screened* Coulombic interactions in HSY; and 2) while charge neutrality in HSY is not maintained, PM model Eqn (III.3) considers counter ions as components and preserves the charge neutrality of the system by requiring: $\sum_i \rho_i z_i = 0$, where ρ_i and z_i are the number density and charge for component *i* respectively.

Hiroike *et al.*[128, 129] provided an explicit expression for direct correlation function, $c_{ij}(r)$, from analytical solution of O-Z equation with primary electrostatic interaction.[120, 130] The structure factor can be obtained via Eqn (III.13) and (III.14) from the 3D Fourier transform of $c_{ij}(r)$. We calculated the isotropic scattering coefficient from Hiroike's expression of direct correlation function as a function of wavelength also

at four different conditions: (a) the ionic strength of 5 mM NaCl equivalent and the volume fraction of 0.05; (b) the ionic strength of 5 mM NaCl equivalent and volume fraction of 0.15; (c) the ionic strength of 5 mM NaCl equivalent and the volume fraction of 0.32; (d) the ionic strength of 25 mM NaCl equivalent and the volume fraction of 0.15. The calculated isotropic scattering coefficients are plotted in Figure VI.3.

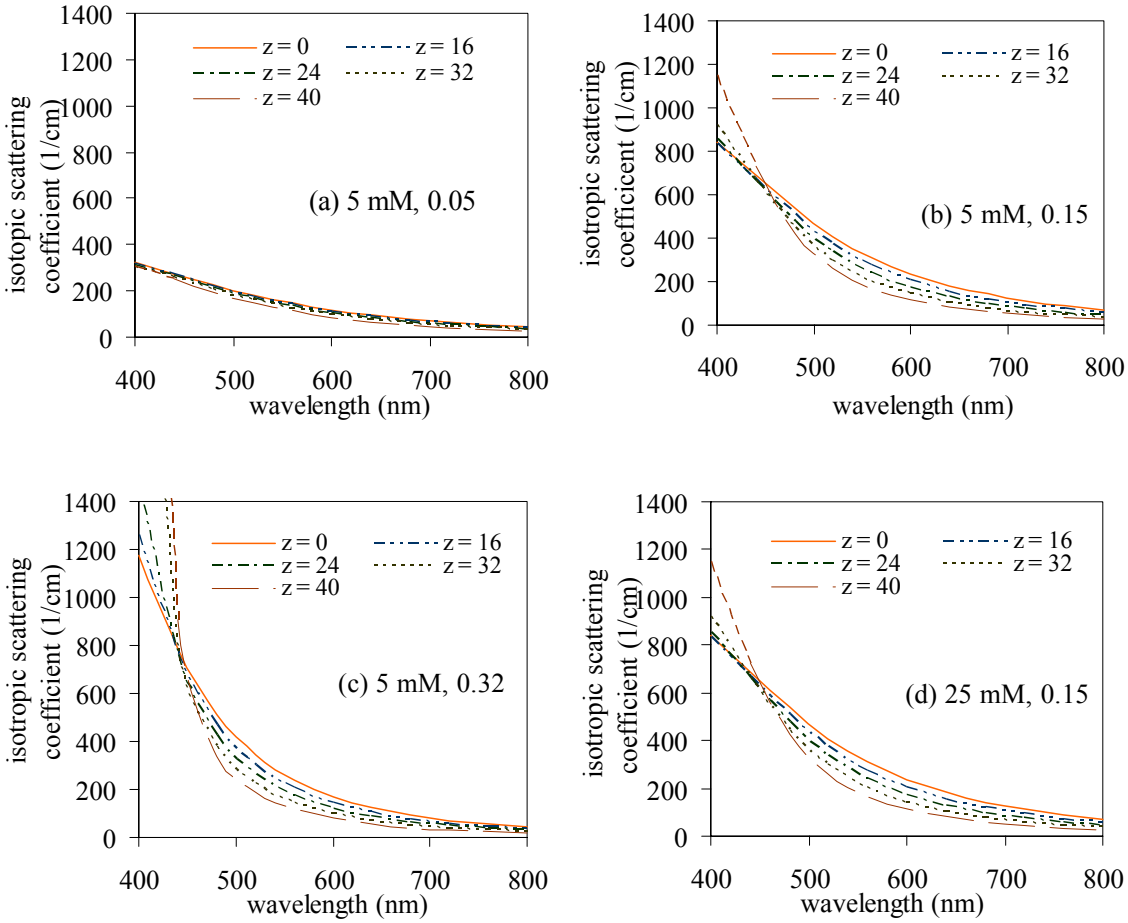

Figure VI.3 Isotropic scattering coefficient predicted by MSA-PM model versus wavelength at varying effective surface charges, z, in electron charge with (a)at the ionic strength of 5 mM NaCl equivalent and the volume fraction of 0.05; (b) at the ionic strength of 5 mM NaCl equivalent and the volume fraction of 0.15; (c)ionic strength of 5 mM NaCl equivalent and the volume fraction of 0.32; (d) at the ionic strength of 25 mM NaCl equivalent and the volume fraction of 0.15.

Figure VI.3 shows that isotropic scattering coefficients also vary with the changing surface charges. In addition, a qualitative comparison of Figure VI.3 with Figures VI.1 and VI.2 indicates the isotropic scattering coefficients predicted by HSY-PM are more sensitive to the change in surface charge *z*. For example, at the volume fraction of 0.15 and ionic strength of 5 mM NaCl equivalent, an increase in particle charge from 0 to 40 electron charge can cause a decrease of about 200 1/cm in MSA-PM predicted isotropic scattering coefficients at the wavelength of 600 nm (Figure VI.3b), while it requires the surface charge z to vary from 0 to 1000 to cause the same amount of decrease in the prediction using both MSA-HSY models (Figures VI.1 b and VI.2 b). To predict the comparable changes in isotropic scattering coefficient at some ionic strength, the effective surface charge needed using MSA-PM model is about two orders of magnitude less than those using MSA-HSY models.

In addition, there is no appreciable difference between Figure VI.3b and VI.3d, which corresponds to same volume fraction but different ionic strengths. This indicates MSA-PM model does not respond to the screening effects due the micro counter ions, and agree with the fact that PM model describes the particles interaction as direct Columbic forces. From this point of view, MSA-PM model does not adequately capture the physics of the screening effects due to the addition of micro counter ions.

VI.2. Summary

All three MSA structure factor models described above predict the change of isotropic scattering coefficient with the change in effective surface charge. The MSA-HSY model prediction reveals that the changes in isotropic scattering vary with

changing ionic strength, while the MSA-PM model prediction does not. The two MSA-HSY models shown in Figure VI.1 and Figure VI.2 were obtained from different ways and only qualitatively agree. The difference may results from different methods used in solving O-Z equation. Since Hayter and Penfold's solution cannot guarantee uniqueness, the MSA-HSY model provided by Herrera *et al.* was used in conjunction with MSA-PM model for the investigation of ESI in the following chapter describing analysis of experimental FDPM measurements.

Recently, Ginoza *et al.*[123-125] and Gazzillo *et al.*[126] provided structure factor models for a Yukawa mixture. The investigation of these models will not be included in this thesis, but will be proposed for future work.

Particle interactions cause dependent scattering and quench scattering efficiencies of particles in suspensions through mediating the structure of suspensions.[106, 107] Understanding the interaction potential among nano-particles are critical to many new applications, in material science, bio-sensor, drug delivery, and many others[1, 2,155] The simulation in this chapter shows that the predicted isotropic scattering coefficients vary with the changing particle interactions resulting from the changes in particle surface charge and ionic strength. Therefore, one may be able to infer the information on particle interaction from measured particle scattering information. Multiple scattering intrinsic to concentrated suspensions makes traditional single-scattering techniques invalid unless the cumbersome refractive index matching is accomplished.

Recently, frequency domain photon migration (FDPM) technique has been developed for accurate and precise measurements of isotropic scattering coefficients of concentration suspensions, and provides a new approach to investigate electrostatic interaction of concentrated suspensions. The FDPM measurements of isotropic scattering coefficients at varying ionic strength and volume fraction will be presented in the next chapter.

CHAPTER VII

ASSESSMENT OF ELECTROSTATIC INTERACTION IN DENSE SUSPENSIONS USING FDPM

In Chapter VI, MSA-PM and MSA-HSY (Herrera *et al.*)[122] structure factor models were examined by comparing synthetic data of isotropic scattering coefficients predicted using each of these models. The chapter will present FDPM measurements of isotropic scattering coefficients and compare them with the corresponding model predictions. The major contents are adopted from "Huang, Y.; Sun, Z.; and Sevick-Muraca. *Langmuir*, 8, 2048 (2002) Copyright [2002] American Chemical Society".

VII.1. Introduction

While prior work[7-9, 98, 99, 101] has successfully demonstrated the application of Percus-Yevick hard sphere (PY-HS) model for predicting static structure and light scattering in dense polystyrene suspensions, these studies have been limited to the structure predominantly set up by volume-exclusion effects. The ubiquitous electrostatic interactions, which are often described by primary model interactions or Yukawa interactions, depend on the effective surface charge and ionic strength of the suspending fluid. With either the PM or the HSY interaction model and MSA-closure, the solutions of Ornstein-Zernike (O-Z) can provide explicit structure factors. This enables us to compare the measured isotropic scattering coefficient from first principles model prediction upon using interference approximation introduced in Chapter III.

In this chapter, we seek to extend the time-dependent multiple scattering measurements to investigate more subtle, yet significant interactions owing to electrostatics.

VII.2. Methods of investigation

In this investigation, the isotropic scattering coefficient at varying ionic strengths and volume fractions were measured using FDPM at two wavelengths of 687 and 828 nm. The measured values of μ_s' were then regressed against model predictions using MSA-HSY and MSA-PM as a function of volume fraction, where the effective surface charge, z_{eff}, was used as the only adjustable parameter.

At each FDPM measurement, the amplitude (AC), average intensity (DC), and phase shift (PS) were detected at 6 modulation frequencies from 50 MHz to 100 MHz with increments of 10 MHz. The isotropic scattering coefficients extracted using multiple distance methods (introduced in the Chapter V) at each of these frequencies were averaged to obtain the value for the measurement. The above 6-frequency measurements are repeated for three times to obtain mean values and final standard deviation of FDPM measurements. The latex of 143 nm diameter and standard deviation (measured using TEM) of 22 nm was used as model system. Its average intrinsic surface charge was determined using conductometric titration to be 26,000 electron charges per particle, and its zeta potential (introduced in Chapter V) measured using standard electrophoresis is 72±4 mV.

In an ensemble colloidal suspension containing numerous particles, the particle size can be deemed as a continuous distribution as denoted by the continuous line in Figure VII.1. To predict dependent scattering of the polydisperse suspensions using Eqn (III.20) and (III.24), a continuous distribution must be represented by an equivalent colloidal mixture of feasible number of particle species through suitable factorization, which represents a colloidal suspension of particle continuous distribution by a mixture of a number of discrete particle components and requires that certain properties remain unchanged.

VII.2.1. Discretization of the particle size distribution

Though a normal distribution is more popular, the size distribution of particles produced from emulsion polymerization are more close to Schulz distribution in practice.[136, 153] To employ the MSA-PM model to address polydispersity, the particle size distribution (PSD) are represented as a three-component mixture, which is also shown in Figure VII.1.[156] Wherein the polydispersity, defined as the ratio of the standard deviation to the mean diameter, is chosen to be a constant.

The level of discretization is determined by requiring the equality of first six moments of both the continuous PSD and the discrete three-component mixture:

$$\int f(x) \cdot x^m dx = \sum_{i=1}^{3} n_i \cdot \sigma_i^m \qquad \text{(VII.1)}$$

where m indicates the order of moments, from 0 to 6; the particle size distribution $f(x)$ was selected as Schulz distribution; n_i and σ_i are the number fraction and particle size of the discretized equivalent mixture. The number fraction, n_i, and particle diameter, σ_i can

be determined from solving a set of equations (Eqn (VII.1) with *m* varying from 0 to 5) numerically. The result of the factorization of the latex used is presented in Table VII.1.

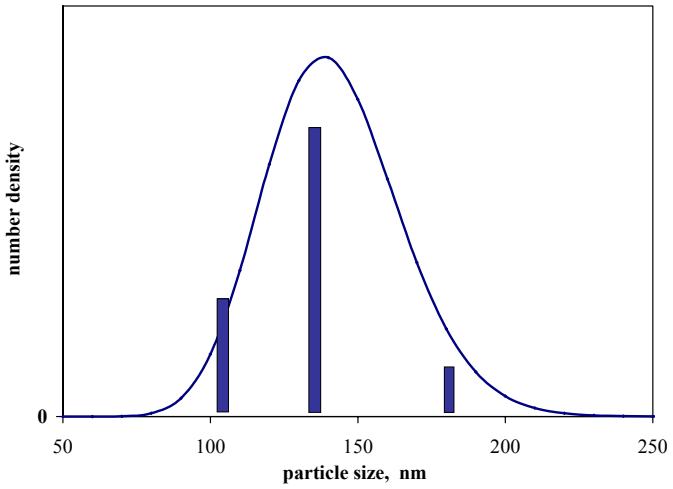

Figure VII.1 Number density size distribution for the three-component discretization (solid bars), which has the same mean diameter and standard deviation with continuous Schulz distribution (lines) with mean size determined by DLS and deviation determined by TEM.

Table VII.1 Discretization of the particle size distribution according to Schulz distribution. Volume averaged diameter is 143 nm; number averaged diameter is 132 nm.

Component	*1*	*2*	*3*
Particle diameter (nm)	102.3	136.4	177.2
n_i	0.255	0.643	0.102

The discretization using more components did not change the predicted isotropic scattering significantly.[153] Table VII.2 illustrated the isotropic scattering coefficients predicted using PY-HS model from three and five component discretization for the polystyrene latex (of the mean diameter of 143 nm and size deviation of 22 nm) at the wavelength of 687 nm and varying volume fractions.

Table VII.2 isotropic scattering coefficients predicted using PY-HS model from three and five component discretization for the polystyrene latex (of the mean diameter of 143 nm and size deviation of 22 nm) at the wavelength of 687 nm and varying volume fractions.

volume fraction		0.082	0.143	0.185	0.243	0.304
μ_s' (1/cm)	3 component	111.94	146.47	150.73	138.88	114.54
	5 components	111.54	146.05	150.45	138.89	114.88
relative difference		0.36%	0.28%	0.19%	-0.01%	-0.30%

Simulation presented in Table VII.2 showed that the differences between predicted isotropic scattering coefficients using three and five-component factorization representation are approximately 0.3% and it is less than the precision FDPM measurement.[11] Therefore, a three component discretization illustrated in the Figure VII.1 was used in the forward calculation of isotropic scattering coefficient.

In the next section, the isotropic scattering coefficient calculated from MSA-PM model prediction using 3-component discretization will be used for comparison with FDPM measurements.

VII.3. Results and discussions

VII.3.1. Isotropic scattering versus volume fraction

Figure VII.2 shows the FDPM measured isotropic scattering coefficients (symbols) [cm^{-1}] at wavelengths of 687 and 828 nm as a function of volume fraction at varying ionic strength (NaCl mM equivalents). The Debye lengths corresponding to these ionic strengths are listed in Table V.2. The scattering coefficients of all samples at 828 nm are less than those at 687 nm at the same volume fraction, as expected for the 143 nm mean size. It is evident that the isotropic scattering coefficients, at both wavelengths, first increase with the volume fraction, achieve a maximum at volume fractions around 18%, and then decrease. The plateau and the decrease of the isotropic scattering coefficients arise from the dependent scattering owing to the correlated particle positions.

Without the particle interactions, particles would scatter independently and isotropic scattering coefficient would increase linearly with volume fraction (as presented in previous chapters). The trend lines (upper line, 687 nm; lower line, 828 nm) shown in Figure VII.2 illustrated the linear relationship when particle interaction could be neglected.

The isotropic scattering coefficients shown in Figure VII.2 also increase as the ionic strength increases, or as the Debye screening length decreases. The Debye length can be calculated from the ionic strength via Eqn (3.5). When the ionic strength decreases from 5 mM to 1 mM NaCl equivalents, (correspondingly, the Debye length doubles from 4.3 to 9.6 nm), the scattering coefficient does not change significantly.

Indeed, even when the ionic strength is as low as 0.1 mM NaCl equivalents, the measured scattering coefficient does not further decrease, (shown in Figure VII.2). This suggests that the polystyrene suspension at experimental volume fraction has already been well structured at the ionic strength of 5mM, especially at the high volume fractions.

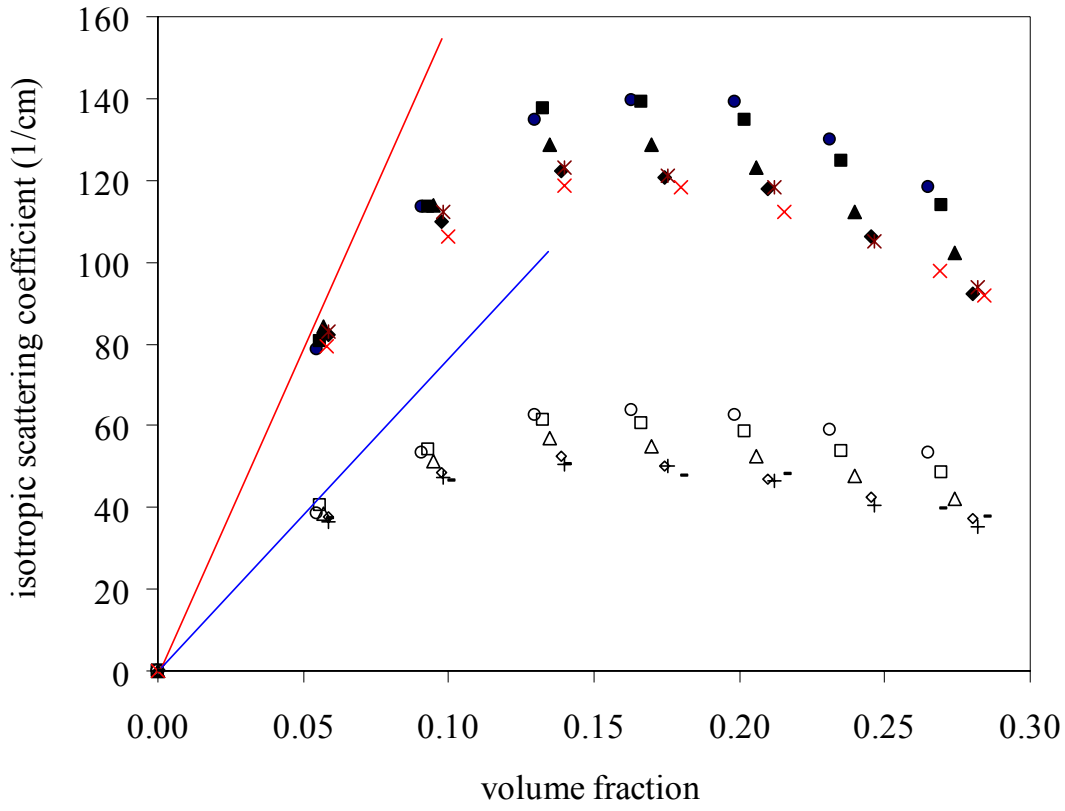

Figure VII.2 Isotropic scattering coefficients versus volume fraction obtained from FDPM measurements at two wavelengths and five ionic strengths in NaCl equivalents, (solid circle, 120 mM, 687 nm; open circle, 120 nm, 828 nm; solid square, 60 mM, 687 nm; open square, 60 mM, 828 nm; solid triangle, 25 mM, 687 nm; open triangle, 25 mM, 828 nm; solid diamond, 5 mM, 687 nm; open diamond, 5 mM, 828 nm; star, 1 mM, 687 nm; +, 1 mM, 828 nm; red cross, 0.1 mM, 687 nm; bar, 0.1 mM, 828 nm).

VII.3.2. Isotropic scattering coefficients predicted by PY model

Figure VII.3 shows the isotropic scattering coefficients obtained from FDPM measurements at 120 mM NaCl equivalents at 687 and 828 nm. Isotropic scattering coefficients calculated using Mie theory and polydisperse PY-HS model with the mean size as the only fitting parameter are also shown in the figure VII.3.

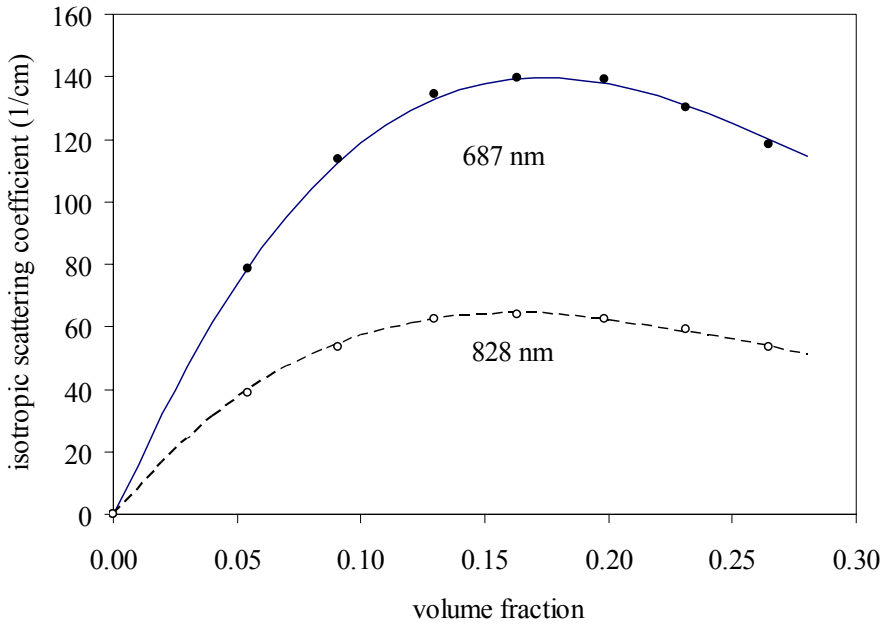

Figure VII.3 Comparison of the isotropic scattering coefficient obtained from FDPM measurements (solid circle, 687 nm; open circle, 828 nm) and predictions using Mie theory and Percus-Yevick model (solid line, 687 nm; dash line, 828 nm).

The regression is carried through by minimizing the error function:

$$\chi^2 = \sum_i ((\mu_{s,\exp t})_i - (\mu_{s,\mathrm{mod}el})_i)^2 / (error)_i^2 \qquad \text{(VII.2)}$$

where $(\mu_{s,\exp t})_i$ and $(\mu_{s,\mathrm{mod}el})_i$ are the FDPM-measured and model-predicted isotropic scattering at the i th volume fraction; and $(error)_i$ is chosen to be the standard deviation

of repeated measurement at each volume fraction. Since model prediction is based on the discretized three component mixture, the isotropic scattering coefficients $(\mu_{s,\mathrm{model}})_i$ are calculated from Eqns (III.20) and (III.24) with the particle structure factor predicted using PY-HS model. The Matlab function fminsearch.m using Nelder-Mead direct search method was used to minimize Eqn (VII.2), and convergence was achieved when the change in the error function was less than 10^{-6}.[149] The fitted mean diameter obtained from the data taken separately at each wavelength was 142 nm, and is comparable to DLS measurement of 143 nm.

VII.3.3. Isotropic scattering coefficients predicted by MSA-HSY model

Isotropic scattering coefficients as a function of volume fraction at ionic strengths of 60 mM, 25 mM, and 5 mM equivalents, are fitted using equations (II.25) and Herrera's[68] structure factor for MSA-HSY system. The polystyrene latex was assumed to be monodisperse, and the effective surface, z_{eff}, was the only fitting parameter in minimizing the error function of Eqn (VII.2). The monodisperse MSA-HSY model (Herrera *et al.*[122]) is used, and the isotropic scattering coefficient $(\mu_{s,\mathrm{model}})_i$ can be predicted from Eqn (III.25). Convergence occurred when the update of the effective surface charge was less than one electron charge and when the relative decrease in the error function, was less than 0.1. At the same ionic strength, the effective charges are similar for data evaluated at the two different wavelengths as shown in Table VII.3. The fitted effective surface charges also depend upon the wavelength used in FDPM measurements. The dependence of the fitted effective surface charge on wavelength and

ionic strength indicates that MSA-HSY model qualitatively reflects the physics behind the microstructure of charged suspension.

Table VII.3 Fitted effective average charge of MSA models.

Ionic strength NaCl equivalents		120 mM	60 mM	25 mM	5 mM	1 mM
Debye screening Length (nm)		0.88	1.24	1.93	4.31	9.63
Effective Charge MSA-HSY	687 nm	1.9	1240	836	404	137
	828nm	0	1005	1137	489	184
Effective Charge MSA-PM	687 nm	0	7	12	15	15
	828 nm	0	3	9	12	13

The isotropic scattering coefficients predicted using the regressed effective surface charges at varying ionic strength, together with FDPM measured values, are plotted associated with the corresponding experimental data as a function of the volume fraction in Figure VII.4. Herein, the monodisperse MSA-HSY model is used in the calculation. Figure VII.4 shows that the regressed curves predicted with MSA-HSY model match the FDPM experimental data well.

The fitted effective charges at each ionic strength increases from around 160 electron charges at 1 mM NaCl equivalents to 1000 electron charges at 60 mM NaCl equivalents. At 25 and 60 mM NaCl equivalents, the fitted surface charge is approximately equal to the value estimated from the zeta potential measurement (introduced in Chapter III) of 1000 electron charges. The increase in the regressed z_{eff}

with increasing ionic strength, indicates that the screening of ESI due to micro ions is not evenly estimated in Herrera's MSA-HSY model. Specifically, the screening effect at higher ionic strengths tends to be overestimated and requires an increase in z_{eff} to compensate for the overpredicted screening effects.

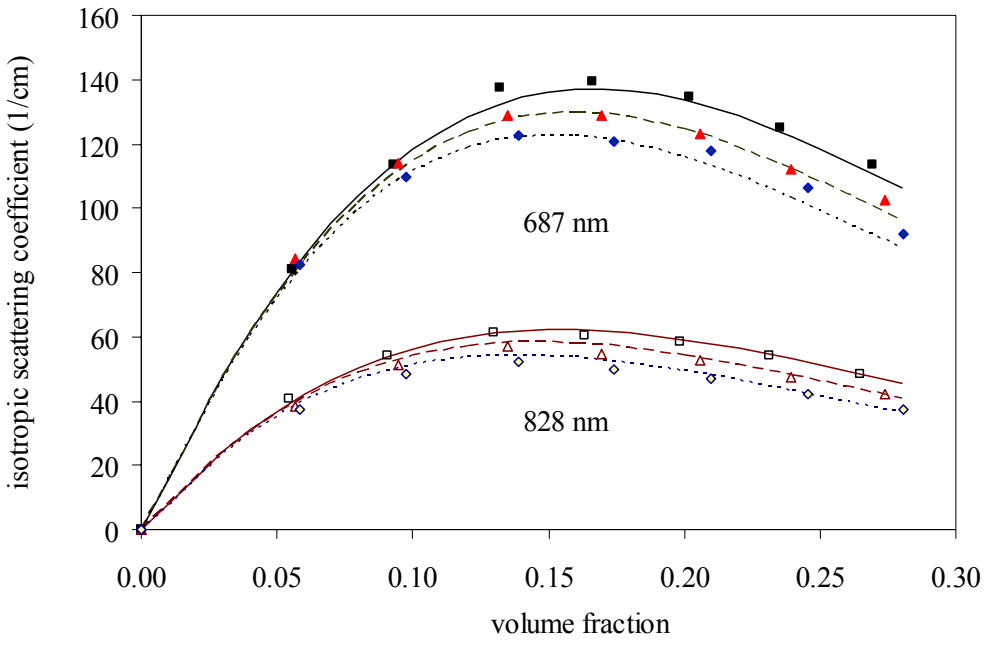

Figure VII.4 Isotropic scattering coefficients versus volume fraction obtained from FDPM measurements as a function of wave length and ionic strength in NaCl equivalents (solid square, 60 mM, 687nm; open square, 60 mM, 828 nm; solid triangle, 25 mM, 687 nm; open triangle, 25 nm, 828 nm; solid diamond, 5 mM, 687 nm; open diamond, 5 mM, 828 nm) and the corresponding MSA-HSY model predictions (solid line, 60 mM, 687nm and 828 nm; dashed line, 25 mM, 687 nm and 828 nm; dotted line, 5 mM, 687 nm and 828 nm).

To illustrate the sensitivity of MSA-HSY model predicted isotropic scattering coefficients to surface charge at each wavelength, Figure VII.5 shows the variation in

isotropic scattering coefficient with surface charge, z_{eff}, at 25 mM. Due to the strong screening effect by micro ions at higher ionic strengths, the change of isotropic scattering coefficient is less sensitive to the change in surface charges than at lower ionic strengths, where electrostatic interaction decays much slower with increasing interparticle separation distance.

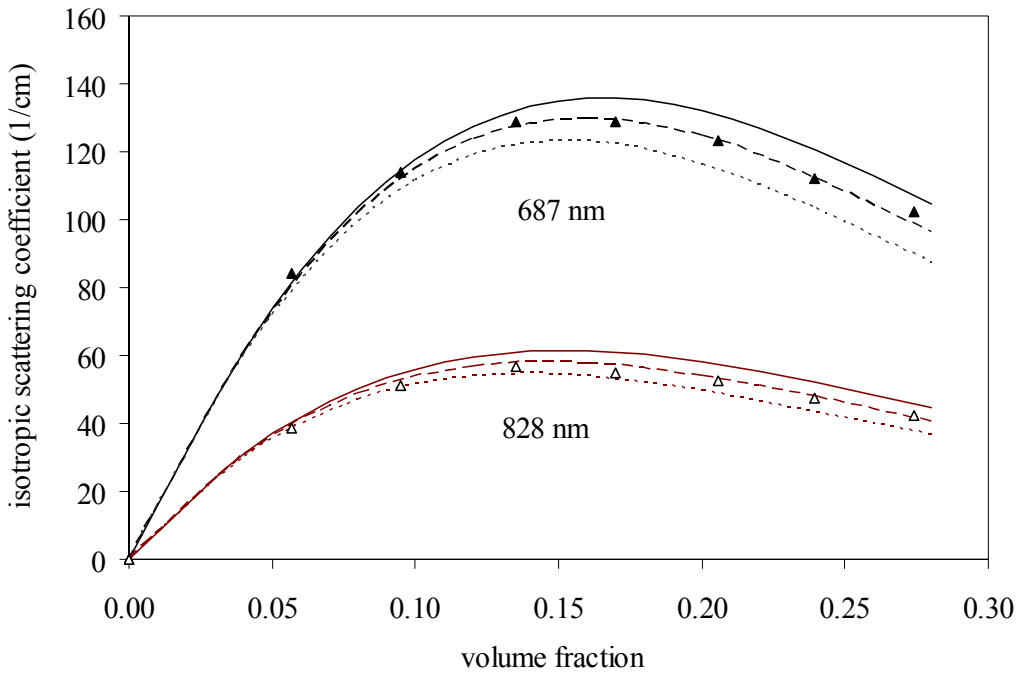

Figure VII.5 Isotropic scattering coefficients predicted from MSA-HSY versus volume fraction as a function of surface charge at 25 mM NaCl equivalents ionic strength at the wave lengths of 687 and 828 nm (solid line, z_{eff} = 400, 687 nm and 828 nm; dashed line, z_{eff} = 1000, 687 and 828 nm; dotted line, z_{eff} = 1400, 687 and 828 nm). Experimental values of isotropic scattering coefficients obtained from FDPM are represented as triangles (solid triangle, 687 nm; open triangle, 828 nm).

VII.3.4. Isotropic scattering coefficients predicted by MSA-PM model

Figure VII.6 shows experimental values (symbols) of isotropic scattering coefficients as a function of volume fraction and ionic strength as well as the fitted values (lines) using MSA-PM model describing the structure of discretized three component colloidal mixture. The only regression parameter of the MSA-PM model for the mixture is the surface charge density, which is assumed to be uniform for all the particles in the mixture. This assumption suggests that effective particle surface charge of a particle is proportional to its surface area.

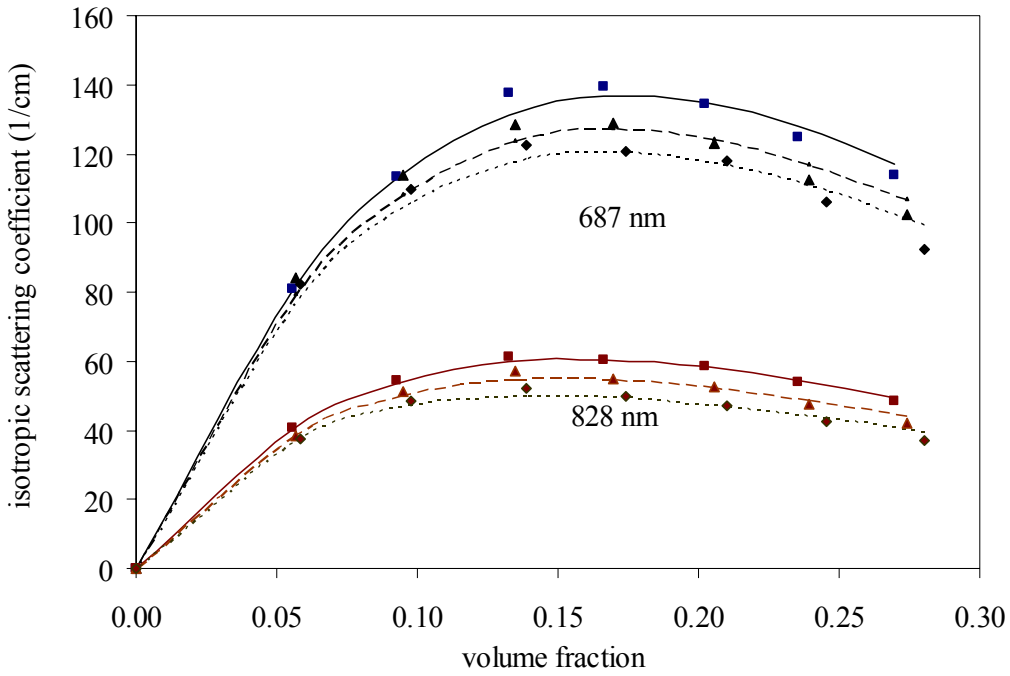

Figure VII.6 Isotropic scattering coefficients versus volume fraction obtained from FDPM measurements as a function of ionic strength in NaCl equivalents and wavelength (square, 60 mM, 687nm and 828 nm; triangle, 25 mM, 687 nm and 828 nm; diamond, 5 mM, 687 nm and 828 nm) and the MSA-PM model predictions (solid line, 60 mM, 687nm and 828 nm; dashed line, 25 mM, 687 nm and 828 nm; dotted line, 5 mM, 687 nm and 828 nm).

The number averaged charge calculated from the fitted surface charge density employing MSA-PM model are also listed in the Table VII.3.

The fitted surface charges using MSA-PM are 1~2 orders of magnitude less than those fitted using MSA-HSY. The fact that regressed z_{eff} using MSA-PM is much smaller that those using MSA-HSY is reasonable in considering that the screening effects of ESI in HSY is considered while it is neglected in PM model. The synthetic isotropic scattering coefficient using MSA-PM model does not change significantly with the change in ionic strength, in agreement with the trend of the synthetic data shown in Figure VI.3.

The surface charge density regressed using MSA-PM increases as the ionic strength decreases from 60 to 1 mM NaCl equivalent, while the average surface charge regressed using MSA-HSY decreases as the ionic strength decreases from 25 mM to 1 mM NaCl equivalents.

To illustrate the sensitivity of the MSA-PM model to surface charge, Figure VII.7 plots the predicted isotropic scattering coefficients and illustrates the predicted decrease of scattering with increasing average particle charge at the wavelength of 687 nm. Figure VII.7 also shows that at volume fractions greater than 15%, the MSA-PM model tends to overpredict the scattering coefficient.

Both the MSA-HSY and MSA-PM models predict hindered scattering with the increase in surface charge and the decrease of ionic strength. Both models can be used to regress experimental scattering data. The summation of the residue square of the

regression using MSA-HSY and MSA-PM models over different volume fraction is calculated from:

$$ResNor = \sum_i ((\mu_{s,\exp t})_i - (\mu_{s,\mathrm{mod}el})_i)^2 \qquad \text{(VII.3)}$$

The obtained summations of residue squares at various ionic strengths are listed in Table VII.4.

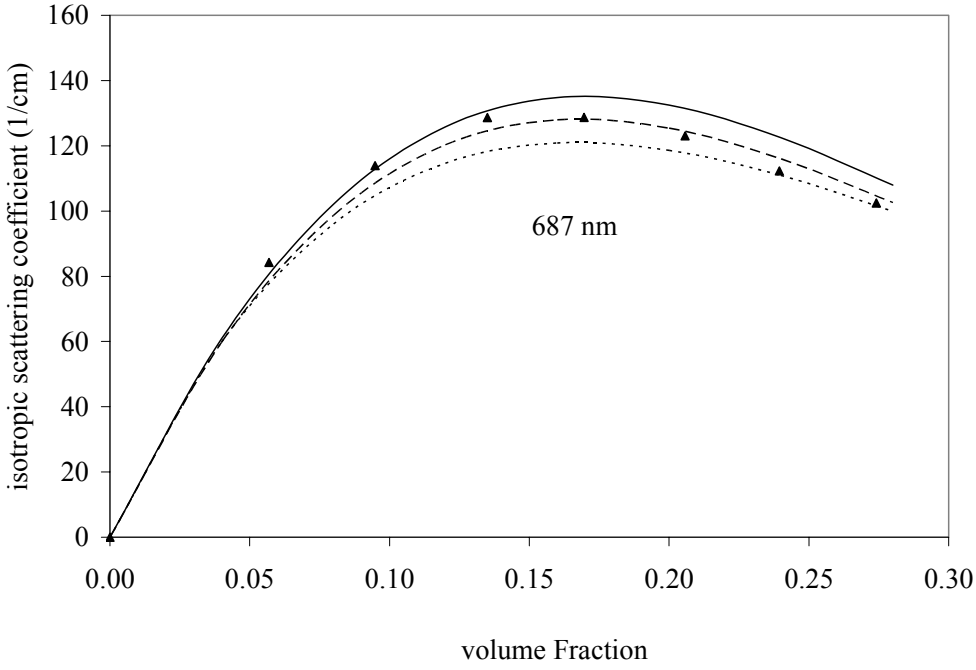

Figure VII.7 Isotropic scattering coefficients at 687 nm versus volume fraction predicted from MSA-PM at 687 nm and 25 mM NaCl equivalents (solid line, z_{eff} = 6; dashed line, z_{eff} = 10; dotted line, z_{eff} = 16) and FDPM experimental measured values at corresponding wave length and ionic strength(symbols).

Table VII.4 shows that at the highest ionic strength (except 120 mM), the summations of the residue squares obtained from MSA-HSY model fitting are less or equal to those obtained from MSA-PM model fitting.

Table VII.4 The summation of the residue square (1/cm)^2 of the regression using MSA-HSY and MSA-PM models at various ionic strengths.

ionic strength NaCl eqiv.		1 mM	5 mM	25 mM	60 mM	120 mM
λ 687 nm	MSA-HSY	27.5	28.8	38.3	28.2	94.3
	MSA-PM	118.0	106.3	126.7	63.0	10.4
λ 828 nm	MSA-HSY	21.2	13.4	7.6	5.5	59.8
	MSA-PM	21.2	13.6	11.6	4.7	8.0

At the ionic strength of 120 mM, electrostatic interaction is sufficiently quenched, and the volume exclusion effect dominates. The MSA-PM model regression provides a better fit since it considers the polydispersity in the particle size distribution, which is neglected in monodisperse MSA-HSY model. Generally, MSA-HSY prediction matches FDPM experimental data better than the prediction using MSA-PM mixture model, which does not capture the physics of screening effects due to micro ions.

Though the parameter estimation of surface charges varies with ionic strength obtained from two MSA models, MSA-HSY model qualitatively addresses the physics

behind the structure of concentrated suspension with strong electrostatic interactions for the polystyrene of 143 nm at the two experimental wavelengths.

VII.4. Summary

This work shows that the first principle models, PY-HS, MSA–HSY, or MSA-PM, can be used to explain the scattering of charged suspensions as measured by FDPM. At high ionic strength (>120 mM NaCl equivalents), even when the particles are strongly charged, the PY-HS model predicts isotropic scattering coefficient with accuracy.

When the ionic strength is less than 60 mM NaCl equivalents and the volume fraction is greater than 5%, the electrostatic interaction increases the structure of model polystyrene latex significantly, and its hindrance to scattering coefficients becomes greater than that measured at ionic strength of 120 mM NaCl equivalents or higher at the experimental wavelength for the given polystyrene latex.

The scattering coefficients at different volume fractions can be fitted with the surface charge as the single parameter estimate using MSA models. While surface charge should be independent of ionic strengths, we found that the fitted surface charge varied with the ionic strength of the suspension. At some intermediate ionic strengths, around 25~60 mM NaCl equivalent, the fitted effective charges using MSA-HSY are close to the surface charges estimated from zeta potential measurements. The fitted surface charges using MSA-PM is 1~2 orders of magnitude less than the actual charge owing to the negligence of the ionic screening effects. Prediction using MSA-PM

mixture model with three component discretization tends to overpredict the isotropic scattering coefficients.

The change in ionic strength impacts the scattering of colloidal suspensions by changing the structure of suspension. The next chapter will address the change in the colloidal structure as indicated by angular-integrated structure factor and structure factor at the zero scattering angle, due to the changing ionic strength.

CHAPTER VIII

ASSESSMENT OF SMALL ANGLE AND ANGLE-AVERAGED STRUCTURE FACTOR FROM MONITORING ELECTROSTATIC COLLOIDAL INTERACTIONS USING MULTIPLY SCATTERED LIGHT

In Chapter VII, we demonstrated that the ionic strength can significantly impact the isotropic scattering coefficients of charged colloidal suspensions and that the MSA-HSY structure factor model can qualitatively predict the dependence of the isotropic scattering coefficients on ionic strength. In this chapter, we will explore the effects of ionic strength on the colloidal structure indicated by the angle integrated structure factor <S(q)> and structure at zero scattering vector S(0). The chapter is adopted from [Y., Huang, and E.M., Sevick-Muraca, *J. Colloid Interface Sci.* **251**, 434 (2002)].[157]

VIII.1. Introduction

The correlated particle positions in a colloidal suspension can be represented through a structure factor function, *S(q)*, which has been introduced in Chapter III. A typical structure factor function for a monodisperse suspension is illustrated in the following Figure VIII.1. Generally, the higher the oscillating amplitude in the S(q) curve, the more ordering exists in the particle spatial correlation in general. The dashed line shown in Figure VIII.1 indicates a higher structure in a suspension than the continuous curve does. When particles are randomly positioned, the structure factor S(q) equals to identity.

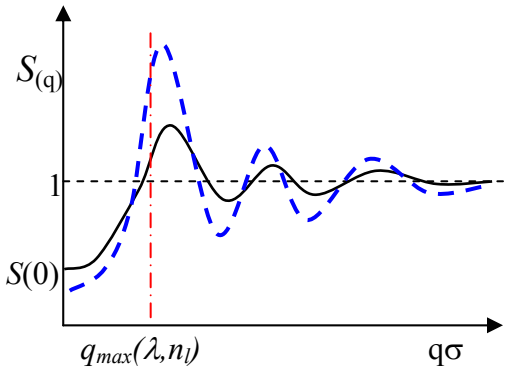

Figure VIII.1 Static structure factor S(q) versus dimensionless scattering vector q/σ, where σ is the particle diameter. Generally, the higher the oscillating amplitude in the S(q) curve, the more ordering exists in the particle spatial correlation in general.

The scattering vector q is defined as $q = \frac{4\pi n_l}{\lambda}\sin(\frac{\theta}{2})$, where θ is the scattering angle; n_l is the refractive index of the suspending fluid and λ is the wavelength in the free space. As the scattering angle increases from *0* to the maximum scattering angle π, q increases accordingly from 0 to the maximum magnitude of the scattering vector, $q_{\max} = \frac{4\pi n_l}{\lambda}$, which is limited by the incident wavelength and the refractive index of the suspending fluid. The first peak of S(q) curve shown in Figure VIII.1 usually occurs when the dimensionless wave vector $q\sigma$ is in the range from 5 to 7. At the long wavelength region ($q\sigma$<1), the effective q region determined by the wavelength and solvent refractive index, is within a small region from the origin. S(q) curve can be approximated by a quadratic function (shown in Figure VIII.1).[7]

Typically, the static structure is measured using small angle light [158-160], x-ray[35-37] or neutron scattering, [23, 27-34] but measurements have been reported using turbidity[23, 161-

[163], and videomicroscopy.[164, 165] X-ray and neutron scattering have shorter wavelengths, and the scattering techniques using X-ray and neutron can probe a wide spectrum of S(q) even at small scattering angles even for small particles with diameter less than 100 nm. Employing X-ray, neutron scattering techniques requires a synchrotron source or nuclear reactor, which are expensive and cannot be implemented in a general laboratory or in industrial environment for on line application. As written earlier in the second section of Chapter II, turbidity measurements, which account for light scattering *out of* the optical path, but not light scattering *back into* the optical path, have been used to investigate the colloidal structure.[161, 162, 166] Diffuse transmission spectroscopy (DTS) directly measures diffuse transmittance of multiply scattered light in a static manner. Though it has been tried to obtain structure factor of a colloidal suspensions,[60] we are not aware of the repeated report of its application probably owing to its incapability to separate light scattering from light absorption.

Structure factor *S(q)* as a function of scattering vector q for a multiple scattering suspension, is not trivial. Angle integrated structure factor <*S(q)*> and structure factor at zero scattering vector, are easier to obtain and can be used as a structure indicator.

VIII.1.1. Angle integrated structure factor <S(q)>

When using light scattering techniques, the detectable structure factor obtained is limited to certain range owing to its relative longer wavelength. The angle-integrated structure factor, <*S*(*q*)>, is defined as the ratio of the actual or measured scattering coefficient to that predicted from Mie theory assuming all particles in a suspension are

randomly oriented and scatter independently: $< S(q) >= \frac{\mu_{s,actual}'}{\mu_{s,Mie}'}$, where $\mu_{s,actual}'$ are the actual scattering coefficients and $\mu_{s,Mie}'$ are the isotropic scattering coefficients in assuming *independent* scattering. Therefore, angle integrated structure factor <*S(q)*>, indicates the quenching in the scattering due to the ordering of particle arrangement in a dense suspensions. In dilute colloidal suspensions (ϕ_v < 1%), particles are randomly oriented and scatter independently, and <*S*(*q*)> is equal to one.

VIII.1.2. Structure factor at zero scattering vector

The static structure factor at zero wave vector, *S*(*0*), indicates the balance of repulsive and attractive forces, and is another indicator of the structure of a colloidal suspension. In a monodisperse system, *S*(*0*) is directly related to the osmotic pressure of a colloidal suspension.

For a colloidal suspension, the particle under Brownian motion will exert a force on the wall of its container. If a solvent and a colloid suspension are separated by a semi-permeable membrane that only allows suspending fluid to pass through, then a excess pressure will be created within the colloidal suspension as shown in Figure VIII.2. The excess pressure usually denoted as Π is called colloidal osmotic pressure, and can be determined by measuring the difference in liquid height in capillary tubes connected to the two chambers as shown in Figure VIII.2.

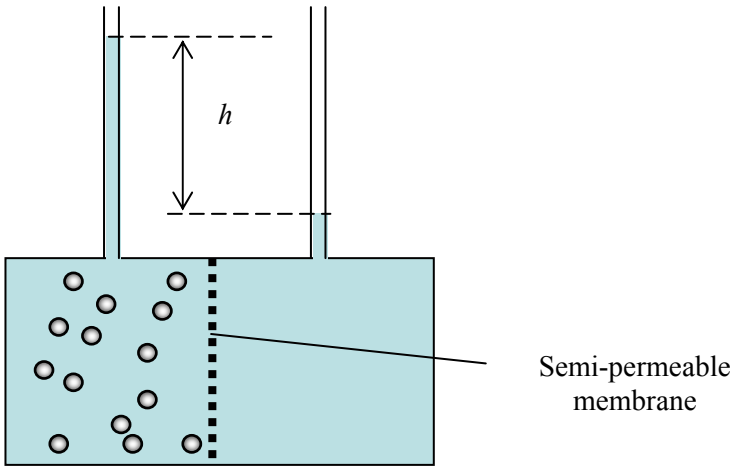

Figure VIII.2 Osmotic pressure of a colloidal suspension: the difference between the height of the capillary tubes connected to the two chambers separated by semi-permeable membrane, which only allow suspending fluid to pass through.

For a non-ideal gas, the equation of state can be written in the form of viral equation:

$$P = k_B T \cdot (\frac{n_M}{V}) \cdot [1 + B \cdot \frac{n_M}{V} + C \cdot (\frac{n_M}{V})^2 + ...]$$

where n_M moles of gas occupies a volume of V; B and C here are second and third Virial coefficients. Likewise, the osmotic pressure of a colloidal suspension, Π, can also be written in the form of virial equation:

$$\Pi = \rho k_B T \cdot [A_1 + A_2 \cdot \rho + A_3 \cdot \rho^2 + ...] \qquad \text{(VIII.1)}$$

where ρ is the concentration of colloidal particle in a suspension, and virial coefficients, A_1, A_2, and A_3, depend on the unit of particle concentration. For a monodisperse suspension, S(0) is related to the colloidal isothermal osmotic compressibility, $\chi_T = (\frac{d\partial\phi_v}{\partial\Pi})_T$, by:

$$S(0) = (\frac{6\phi_v}{\pi\sigma^3})k_B T\chi_T = (\frac{6\phi_v}{\pi\sigma^3})k_B T(\frac{d\partial\phi_v}{\partial\Pi})_T \quad \text{(VIII.2)}$$

Upon assuming the semi-empirical Carnahan–Starling equation of state for the osmotic pressure, $\Pi(\phi_v) = \rho k_B T \frac{\phi_v + \phi_v^2 + \phi_v^3 - \phi_v^4}{(1-\phi_v)^3}$, the structure factor at zero scattering angle, S(0), can be expressed as:[7]

$$S(0) = \frac{(1-\phi_v)^4}{(1+2\phi_v)^2 - \phi_v{}^3(4-\phi_v)} \quad \text{(VIII.3)}$$

The structure factor at the zero scattering angle can also be determined by light scattering measurements. Upon using static light scattering, Ottewill and Richardson[24] derived values of S(0) for diluted polystyrene suspensions (< 0.015 g/cm^3) at low ionic strength (< 5-mM NaCl equivalents) by evaluating S(q) as a function of scattering angle and extrapolating to zero wave vector. In their work, they demonstrated that S(0) decreases with decreasing ionic strength and with increasing polystyrene volume fraction.[19] In suspensions with strong multiple scattering, static light scattering will not be feasible.

Recently, Banerjee and coworkers[7] extracted *S(0)* from two-wavelength FDPM measurements of isotropic scattering coefficients as a function of volume fraction for polystyrene suspensions with dominant volume exclusion effects, where long wavelength approximation was applied. They showed that S(0) obtained using long wavelength approximation for a suspension (with the particle size of 150 nm and the solvent refractive index of 1.33) matches favorably with the true values.[7]

Upon comparing FDPM-measured isotropic scattering coefficients with the corresponding theoretical prediction using PY-HS model, Sun *et al.* investigated the microstructure and extracted the particle size information for concentrated suspensions, where volume exclusion effects dominate.[9-13]

More recently, attention has been focused on the particle interactions and resulting microstructures associated with charged colloidal systems.[31, 166-171] It was shown in the Chapter VII that alteration of electrostatic interactions due to varying ionic strength can strongly influence the isotropic scattering coefficients of a dense polystyrene latex. In the work presented in this chapter, we will be interested in how <S(q)> and S(0) vary with changing electrostatic interactions owing to changing ionic strength.

The next section will briefly review the theory for predicting angle-integrated structure factor $\langle S(q) \rangle$ and determining $S(0)$ from $\langle S(q) \rangle$ measured at two wavelengths with small particle approximation. The static structure factor at zero wave vector, $S(0)$, and angle-integrated structure factor, <S(q)>, obtained from FDPM measurements and from model fitting using MSA-HSY model will be compared.

VIII.2. Theory and methods

This section will first introduce the theory of determining <S(q)> and structure factor at zero scattering vector S(0) using the long wavelength approximation from two wavelength FDPM measurements of isotropic scattering coefficients.

VIII.2.1. Angle-integrated structure factor <$S(q)$>

The value of <$S(q)$> indicates the impact of the correlated particle positions on scattering. For a monodisperse system, <$S(q)$> can be calculated from:

$$< S(q) >= \frac{\mu_{s,actual}'}{\mu_{s,Mie}'} = \frac{\int_0^{\pi} F(q,\sigma)S(q,\sigma,\phi_v)(1-\cos\theta)\sin\theta d\theta}{\int_0^{\pi} F(q,\sigma)(1-\cos\theta)\sin\theta d\theta} \qquad \text{(VIII.4)}$$

where ϕ_v is the particle volume fraction of a suspension; σ is the particle diameter. The numerator, also the isotropic scattering coefficient, $\mu_{s,actual}'$, can be measured directly from FDPM or predicted from Eqn (3.25) with Mie theory predicting form factor, $F(q,\sigma)$, and a structure factor model, as described in Chapter III. The denominator reflecting the independent scattering arising from random particle positions can be computed directly from Mie scattering theory and particle volume fraction. The angle-integrated structure factor <$S(q)$> can be calculated from the measured and the calculated μ_s' using Eqn (VIII.4).

When the long wavelength is large in comparison to the particle diameter σ, the effective range for S(q) that can be interrogated is within a small range from origin (Figure VIII.1), where S(q) can be approximated as a quadratic function. The theory of obtaining S(0) from long wavelength approximation will be presented in the following.

VIII.2.2. Static structure factor at zero wave vector

For a monodisperse suspension, the structure factor can be calculated from the three-dimension Fourier transform of radial correlation function $g(r)$, introduced in Chapter III:[55]

$$S(q) = 1 + \frac{4\pi\rho}{q}\int_0^\infty (g(r)-1)\sin(qr)rdr \qquad \text{(VIII.5)}$$

where ρ is the number density of suspended particles and r is center-to-center particle separation distance. At large $r = r^o$, g(r) approaches the value of 1 as shown in Figure III.6, and the integration of Eqn (VIII.5) can be truncated at some $r = r^o$. Then the Eqn (VIII.5) can be written as:

$$S(q) = 1 + 4\pi\rho\int_0^{r^o} (g(r)-1)\frac{\sin(qr)}{qr}r^2 dr \qquad \text{(VIII.6)}$$

When the wavelength is long enough, such as $q_{max}r_o$ is small, one can expand $\sin(qr)$ in a Taylor series: $\sin(qr) = qr - \frac{(qr)^3}{3!} + 0((q\sigma)^5)$ about $qr = 0$, and replace $\sin(qr)$ in Eqn (VIII.4) with its Taylor expansion to obtain:

$$S(q) = 1 + 4\pi\rho\int_0^\infty (g(r)-1)r^2 dr - \frac{4\pi\rho(q\sigma)^2}{3!\sigma^2}\int_0^\infty (g(r)-1)r^4 dr + O(q\sigma)^4 \qquad \text{(VIII.7)}$$

Consequently, Eqn (VIII.7) can be as also presented as:

$$S(q) = S(0) + \alpha_o \cdot (q\sigma)^2 + O(q\sigma)^4 \qquad \text{(VIII.8)}$$

by defining:

$$S(0) = 1 + 4\pi\rho\int_0^\infty (g(r) - 1)r^2 dr \qquad \text{(VIII.9)}$$

and

$$\alpha_o = -\frac{4\pi\rho}{3!\sigma^2}\int_0^\infty (g(r) - 1)r^4 dr \qquad \text{(VIII.10)}$$

where $S(0)$ and α_o are constant to a given suspension.

Eqn. (VIII.8) actually can be equivalently considered as the Taylor expansion of $S(q)$ at $q = 0$. Therefore this method is restricted at small q regions, where wavelength is large in comparison to particle diameter in order to ensure that $S(q)$ at the range of $0<q<q_{max}$ can be reasonably approximated by a quadratic function. Banerjee and coworkers[7] showed that at the wavelength, $\lambda > \lambda_{\min} = \frac{2\pi\sigma}{n_l}$, the error of angle integrated structure factor <S(q)> predicted using long wavelength value is within 2% of true value.[7] The long wave length approximation is also termed as small $q\sigma$ approximation or small particle approximation.

Upon inserting the Eqn (VIII.8) into Eqn (VIII.4), we can obtain:

$$< S(q) >= \frac{\mu_{s,\exp t}'}{\mu_{s,Mie}'} \cong S(0) + \alpha_o \cdot k_a(q) + O(qx)^4 \qquad \text{(VIII.11)}$$

with

$$k_\alpha(q) = \frac{\int_0^\pi F(q)(qx)^2(1-\cos\theta)\sin\theta d\theta}{\int_0^\pi F(q)(1-\cos\theta)\sin\theta d\theta} \qquad \text{(VIII.12)}$$

Upon conducting measurements of $<S(q)>$ at two wavelengths satisfying ($q\sigma << 1$) and computing k_α from Eqn (VIII.11), the values of α_o and $S(0)$ can be determined by solving a set of linear equations straightforwardly. Likewise, we can expand $S(q)$ in other ways, including higher order polynomials, B-splines, etc. in order to obtain more information about $S(q)$.

It is realized that the methods used above cannot be directly applied to the multiple component suspensions, where a matrix of partial structure factor $S_{ij}(q)$ is required to completely describe the particle position correlation in a suspension. Nonetheless, the values of obtained $<S(q)>$ and $S(0)$ are still predictive of the polydisperse systems with the exception that $S(0)$ obtained cannot be related to the osmotic pressure as it does to monodisperse systems.[98] However, the change in the value of $S(0)$ still indicates the interaction and structure changes in concentrated suspensions.

Below 10%, polydispersity does not significantly influence the static structure factor.[9] For charged colloidal systems, the influence of polydispersity upon the structure factor is further quenched by the strong electrostatic interactions.[35-37] In this contribution, the static structure factor computed from the monodisperse MSA-HSY model will be used to analyze the FDPM scattering data for the polystyrene latex with the mean size of 143 nm and size deviation of 22 nm. The angle-integrated structure factor <S(q)> and structure factor at zero scattering angle determined from FDPM two wavelength measurement as a function of volume fraction will be presented in the next section.

VIII.3. Results and discussions

In order to obtain S(0), the isotropic scattering coefficients of a colloidal suspension of mean diameter of 143 nm as a function of wavelength were measured at the wavelength of 687 and 828 nm and at varying ionic strength from 1 to 120 mM NaCl equivalent. The zeta potential of the particles measured in 120mM NaCl solution is 72 mM, and average surface charge determined using conductometric titration is 26,000 electron charges. The characterization methods have been detailed in Chapter V, and the properties of polystyrene latex are summarized in Table V.4 as the entry of latex A.

The measured scattering coefficients have been presented in Figure VII.2, and will not be repeated in this Chapter. Briefly, Figure VII.2 showed that the isotropic scattering coefficients measured using FDPM depend upon both ionic strength and volume fraction of suspensions owing to the change in particle position correlation. In addition, Figure VII.4 showed the isotropic scattering coefficients predicted by Herrera's MSA-HSY model (with the regressed effective average surface charges summarized in the Table VII.3) match favorablely with FDPM measurements. The measured isotropic scattering coefficients were used to obtain angle-integrated structure factor using Eqn (VIII.4) as a function of volume fraction at varying ionic strength.

VIII.3.1. Angle-integrated structure factor as a function of volume fraction

Figures VIII.3 (a) through (d) illustrate the experimentally obtained value of angle-integrated structure factor at 687 nm (filled symbols) and 828 nm (open symbols) as a function of volume fraction at varying ionic strength. The predicted values of $\langle S(q) \rangle$ computed from Eqn (VIII.4) and from the MSA-HSY model using the parameter

estimate of the effective surface charge are also presented as solid (687 nm) and dotted (828nm) lines.

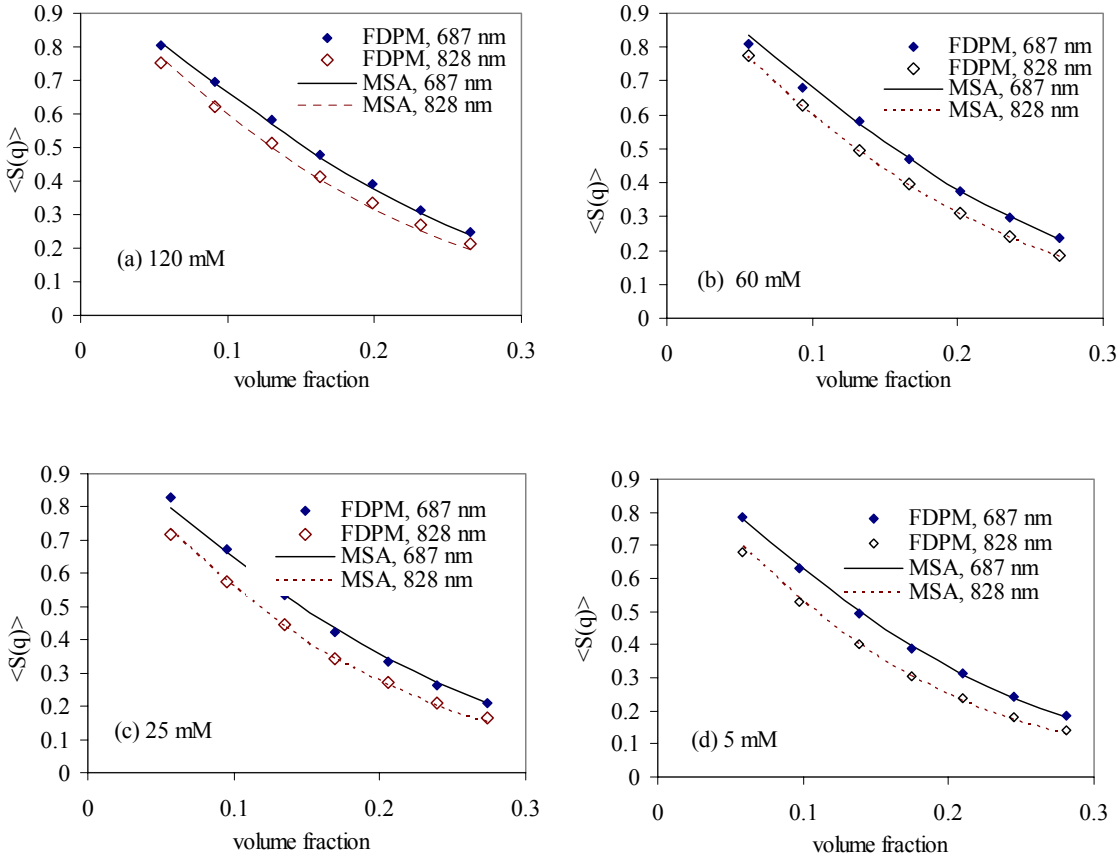

Figure VIII.3 Angle integrated structure factor versus volume fraction at four different ionic strengths for polystyrene latex with mean diameter 143 nm and size deviation 22 nm. The symbols denote FDPM-derived values at 687 (filled) and 828 (open) while the lines represent the MSA-HSY values at 687 (solid) and 828 (dashed).

Inspection of Figures VIII.4 (a) through (d) shows that <S(q)> decreases with increasing volume fraction as well as with decreasing ionic strength. With increasing volume fraction, free space in the suspension decreases, and volume exclusion effects

become more significant and result in increasing scattering hindrance. With decreasing ionic strength, the colloidal electrostatic repulsive forces become significant, and the suspension becomes more structured, further discounting scattering efficiency.

Figure VIII.4 indicates that the change in the microstructure associated with altering volume fraction and ionic strength is successfully captured by the FDPM scattering measurements. It is noteworthy that since we used the parameter estimate of effective surface charge from the scattering measurements (as shown in Figure VII.4) to predict $<S(q)>$ from theory, it is not surprising that the experimentally derived values and those predicted by the model agree. However, the fact that effective surface charge regressed does not show dependence on volume fraction suggests MSA-HSY model can be predictive in estimating colloidal properties.

The experimentally determined angle-integrated structure factor $<S(q)>$ at the wavelength of 687 and 828 nm were used to obtain $S(0)$ using the method introduced in the previous section.

VIII.3.2. S(0) as a function of volume fraction at different ionic strength

Figures VIII.4 (a) through (d) illustrate that the static structure factor at zero scattering angle, $S(0)$, obtained from dual wavelength FDPM measurements conducted at all ionic strengths (symbols) consistently decreases with volume fraction. The decrease in $S(0)$ earmarks hindered scattering and increased ordering, and provides further evidence that FDPM can probe the structure of colloidal suspensions.

Figure VIII.4 (a) also shows that the experimentally obtained values of $S(0)$ at the highest ionic strength (indicated by triangles) agree with the prediction of the hard sphere Carnahan-Starling model (indicated by diamonds). This reproduces previous work.[7]

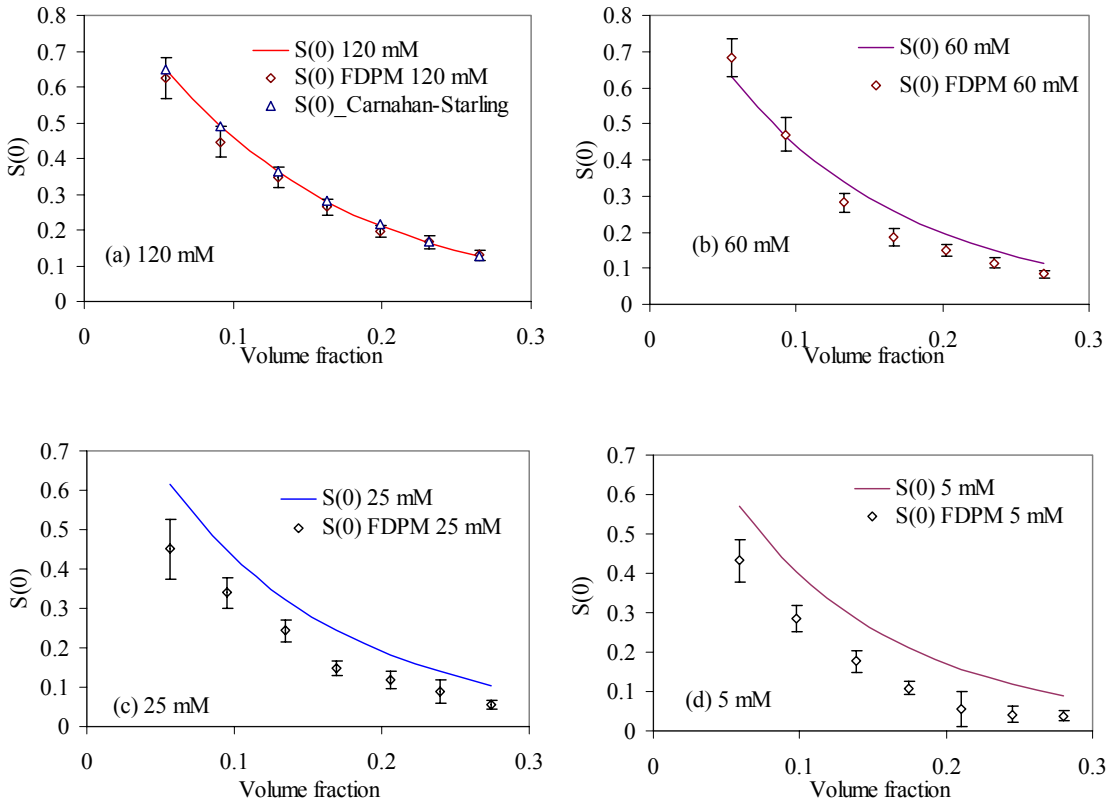

Figure VIII.4 S(0) of polystyrene latex with mean diameter of 143 nm versus volume fraction determined from FDPM measurements at the wavelength of 687 and 828 nm at differing ionic strengths of (a) 120 mM, (b) 60 mM, (c) 25 mM, and 5 mM NaCl. The symbols (open diamond) denote FDPM derived values while the lines represent the MSA-HSY prediction. In (a), the triangle symbols represent values predicted from the Carnahan-Starling equation. Propagated error bars from FDPM measurements are included.

Yet Figures VIII.4b through VIII.4d show that the values of S(0) extracted from FDPM scattering measurements deviate from than those predicted from the MSA-HSY model at ionic strengths of 60 mM, 25 mM, and 5 mM NaCl equivalent (solid lines). The difference between the experimentally derived values and the model prediction increases as the ionic strength decreases. Two possible reasons for the mismatch are 1) the potential inaccuracy of the MSA-HSY model and 2) the invalidity of the small dimensionless wave vector approximation used to extract $S(0)$ from FDPM measurements.

In the first case, it is well known that the PY approximation describes the structure of hard sphere systems more accurately than using MSA describes the HSY system. Furthermore, the MSA underestimates the structure of a suspension, since it underestimates the peaks of $S(q)$.[131, 153] In addition, the values of the predicted structure factor illustrated by the solid lines in Figures VIII.4a through VIII.4d are based upon the successful recovery of the parameter estimate of the effective surface charge. Generally, a increased in the ordering of suspensions is indicated by the decrease in the value of $S(0)$ and increase in the first peak $S(q_m)$ in the $S(q) \sim q$ curve. Since MSA-HSY underestimates structure of a suspension, it also overestimates $S(0)$ and underestimates $S(q_m)$, as shown in Figure VIII.1, where the dashed lines indicating higher ordering represent a lower value of $S(0)$ and higher value of $S(q_m)$. The overestimation of $S(0)$ using MSA-HSY model with the parameter estimates of effective surface charges at 828 nm should result in higher values(solid lines) in the predicted values of S(0) in comparison to experimental results (symbols) in Figures VIII. 4a through VIII.4d.

In the second case, since the effective q regions corresponding to the wavelengths used herein are within the small q region well before the first peak $S(q_m)$ in $S(q) \sim q$ curve, the small wave vector approximation is appropriate (Figure VIII.1). Yet, the small q contribution of $S(q)$ due to multiple scattering does not completely describe the influence of structure at all possible wave vectors.

In order to satisfy the small $q\sigma$ approximation used herein, the wavelengths need to be long enough for effective q region ($0<q<q_{max}$) to ensure that $S(q)$ in this region can be approximated with a quadratic function with reasonable accuracy (Figure VIII.1). In order to verify if the small wave vector approximation used here is responsible for the discrepancy, this method was validated through simulation using the PY-HS model. Since PY-HS is widely verified by scattering measurements and Monte Carlo simulations,[99, 101, 111] it is reasonable to consider PY-HS as true model for structure. While S(0) from PY-HS structure factor model was considered as the "true" value, the synthesized value of $S(0)$ obtained from Eqn (VIII.8) with values of $<S(q)>$ at two wavelengths computed from Eqn (VIII.4), where the numerator was calculated using Eqn (III.25) with PY-HS structure factor and denominator was calculated from Mie scattering theory. The value of $S(0)$ from synthetic scattering data was systematically less than the true values, and the difference between them decreased as the wavelength increased as shown in Table VIII.1 . The synthetic isotropic scattering coefficients were generated using PY-HS model prediction based upon a polystyrene suspension of mean diameter 143 nm and the volume fraction of 0.20.

Table VIII.1 Structure factor at zero wave vector, S(0) determined from synthetic isotropic scattering coefficients (predicted using PY-HS model) at two wavelengths using long wavelength approximation for a polystyrene suspension of the mean diameter of 143 nm and the volume fraction of 0.20. The value of model prediction using PY-HS is 0.209 and is considered as "true" value.

wavelength (nm)	687 785	687 828	785 828
S(0)	0.165	0.170	0.180
Error in S(0)	-0.044	-0.039	-0.029

Table VIII.1 shows that the synthetic value of S(0) obtained from the long wavelength approximation at 687 and 828 nm wavelengths was 0.170. This synthetic *S(0)* is less than the true value of *S(0)* computed to be 0.209 by a difference of 0.039, which is an error that is slightly greater than can be accounted for by FDPM measurement error.

Nonetheless, Figure VIII.4a shows that the values of *S(0)* derived from FDPM measurements and from the small wave vector approximation at high ionic strength (120 mM NaCl equivalents) matches the prediction by MSA-HSY and HS-PY. This suggests that the error arising from the small wave vector approximation may not be the main reason for the discrepancy between the MSA predicted and FDPM determined *S(0)*. Instead, the MSA-HSY structure factor model and the parameter estimate of the effective surface charge, z_{eff}, resulted in an overestimation of S(*0*) and an underestimation of the structure.

To minimize the influence of the small wave vector approximation, longer wavelengths should be used. However, at longer wavelengths, the scattering efficiency of individual colloidal particles decreases and relative experimental error may consequently increase. Hence at longer wavelengths, the increased accuracy of the small wave vector approximation using FDPM can be offset by reduced measurement precision.

Intuitively, *S(0)* will not have same sensitivity as the peak of the *S(q)* to the structure or particle interaction, especially when *S(0)* approach zero. Nonetheless, while a shorter wavelength may exclude a more sensitive *q*-range for assessing colloidal structure, the extraction of *S(0)* provides a simple means to assess changes in structure without solving the full ill-posed inverse problem.

VIII.3.3. Obtaining *S(q)* from multi wavelength FDPM measurement

It has been shown[7] that one can obtain information on $<S(q)>$ from two wavelength FDPM measurements at small wave number region, wherein the structure factor S(q) can be approximated by a quadratic function.[7] Theoretically, it is possible to approximate $S(q)$ using other functions, including B-spline, Legendre polynomials, etc. and the corresponding expansion coefficients can be determined from isotropic scattering coefficients as a function of wavelength. However, the inverse problem of determining$<S(q)>$ from scattering data is an ill posed Fredholm problem. It usually requires accurate experimental scattering coefficients in order to acquire reliable information of $S(q)$. In order to provide robust estimation, the measurements in isotropic scattering must be within 0.5%. Due to the limited number of wavelengths and

insufficient measurement accuracy, extracting S(q) based on B-splines methods has not let to robust estimation of S(q) about first peak in S(q), and will not be provided here. Future investigation is suggested.

VIII.4. Summary

Frequency domain photon migration can effectively probe the structural change associated with the change in electrostatic particle interaction and with change in volume fraction. For charged polystyrene lattices, the ordering of particles in a suspension increases with decreasing ionic strength and increasing volume fraction, as indicated by the decrease in $S(0)$ and the integrated structure factor <S(q)>. Using the parameter estimates of effective charge, predictions of $S(0)$ were compared with experimentally-derived values of $S(0)$. While predictions and experimental values of $S(0)$ matched at high ionic strengths, the agreement expectedly deteriorated with decreasing ionic strength and reduced screening, indicating the limitations of the MSA-HSY structure factor model applied to this charged colloidal system. Nonetheless, this research demonstrated the potential of FDPM as a method for effectively assessing particle interactions within a dense ensemble suspension for assessing first principle models of colloidal interactions.

CHAPTER IX

ASSESSMENT OF ELECTROSTATIC INTERACTION BY RHODAMINE 6G ADSORPTION ON POLYSTYRENE LATEX USING FREQUENCY DOMAIN PHOTON MIGRATION

Chapters VII and VIII assessed the electrostatic interaction of concentrated suspensions by measuring the change in isotropic scattering coefficients measured using FDPM. Since the electrostatic interactions among particles also depend upon effective surface charge, the chapter will focus on investigating the change in electrostatic interactions resulting from varying effective surface charge due to adsorption of Rhodamine 6G. This chapter is adopted from "Huang, Y., Yuwono, V., and Sevick-Muraca, E.M. *Langmuir* **18**, 9192 (2002) Copyright [2002] American Chemical Society".[172]

IX.1. Introduction

The ability to mediate colloidal particle interactions could be critical for controlling stabilities, rheology, as well as self-assembly of nano-particles. Yet the measurement of parameters that govern interactions within dense colloidal suspensions remains elusive. For the case of electrostatic interactions, the intrinsic surface charge (also called *structural* surface charge) is governed by the functional groups on the particle surface and is measured by titration. Nonetheless, titration is inconvenient for dynamically evaluating the electrostatic interaction in dense suspensions.[150, 151, 152] In

addition, the ionization equilibrium of surface groups and the ion condensation of the counter ions impact electrostatic interactions. The *effective* surface charge, which discounts the ion condensation and charge regulation, is typically used to describe electrostatic interactions.

There is no direct method for measuring either surface charge or electrostatic potential at the particle surface. The zeta potential, ζ, which is defined as the electrostatic potential at the particle shear plane (as shown in Figure V.18), is used to characterize the particle electrostatics. From the zeta potential obtained from electrophoretic measurements in diluted suspensions, the effective surface charge, $z_{eff,}$ can then be evaluated through the analytical solution of Poisson-Boltzmann equation with suitable approximation.[107] The Smoluchowski approximation can be applied when the thickness of electrical double layer κ^{-1} is thin in comparison to the particle radius R ($\kappa R > 100$); Debye-Hückel approximation assumes low surface potential and low ionic strength ($\kappa R < 0.1$). Generally, the colloidal suspension is between these two extreme cases.

Within industrial processes involving dense suspensions, such as emulsions, electrophoretic measurement is not directly applicable since dilution alters original solvent conditions, and therefore alters counter ion condensation and ionization equilibrium. Consequently, techniques have recently been developed to characterize electrostatic interactions in dense suspensions. For example, electroacoustic techniques have been applied in measuring zeta potential as well as particle size distribution of concentrated suspensions.[70, 77-79] Values of zeta potentials obtained from electroacoustic

sonic amplitude (ESA) (Figure II.16) or colloidal vibration potential (CVP) measurements (introduced in Chapter II) differ from those obtained from standard electrophoresis.[75, 92] Furthermore, these perturbative techniques require an oscillatory electric force or sonic field, which may disturb the structure of the suspension. FDPM has been demonstrated to provide a non-perturbative measurement of electrostatic interactions in dense colloidal suspensions.

Obtaining parameter estimates of the effective surface charges of dense polystyrene latex suspensions at varying ionic strengths (1-120 mM NaCl equiv.) have been shown in chapter VII, where FDPM measured isotropic scattering coefficients were fitted against MSA–HSY. This chapter demonstrates the change in the parameter estimate of effective surface charge determined using FDPM with the change in the surface charge caused by Rhodamine 6G (R6G) adsorption. While the parameter of effective surface charge is strictly dependent upon the structure factor model and may not adequately predict titratable surface charge, its variation with amounts of absorbed cationic surfactant should nonetheless reflect changing electrostatic interactions.

IX.2. Methods and materials

IX.2.1. Methods introduction

ESI among particles can be modeled either by PM model shown as Eqn (III.3) or by HSY model shown as Eqn (III.4). Ionic strength and effective surface charge determine the ESI, which quenches the scattering power of suspension through interfering microstructure. With independent knowledge of particle size, ionic strength,

isotropic scattering coefficient, as well as a structure factor model one can solve Eqn (III.25) numerically for effective surface charge, z_{eff}. Apparently, the estimated effective surface charges using this scheme depends strongly on the interaction potential model and approximation relation used in predicting structure factor, $S(\sigma,\lambda,\theta,\varphi)$, from particle interaction potentials. Based on the same scattering data, the parameter estimate of effective surface charge using MSA-PM model are about two orders of magnitude less than that obtained using MSA-HSY model, as illustrated in Table VII.3.

Figure IX.1 plots the isotropic scattering coefficient for a monodisperse suspension (with mean particle diameter of 143 nm at the ionic strength of 5 mM NaCl equivalent) predicted using PM and HSY models as functions of effective surface charge respectively.

In order to obtain comparable scattering coefficients predicted by the HSY model, the PM model requires parameters of effective surface charges to be two orders of magnitude less than those used in the HSY model. Clearly, the effective surface charges estimated from isotropic scattering data are model dependent.

Since the parameter estimate of effective surface extracted from PM model is too small to be physically realistic, we used the HSY model to describe changes in electrostatic interaction from FDPM measurement of isotropic scattering and adsorption of cationic surfactant onto the surface of well-characterized polystyrene particles.

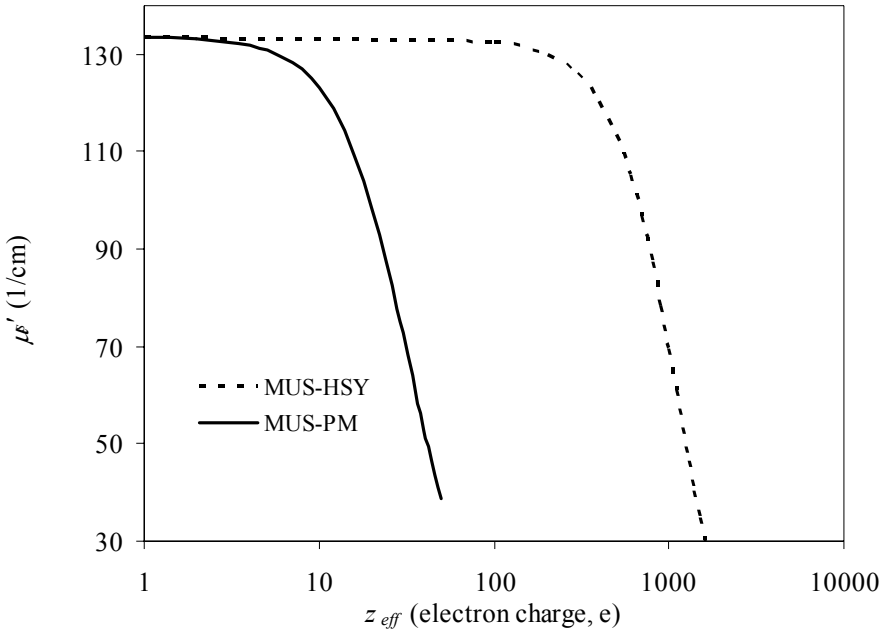

Figure IX.1 Calculated z_{eff} [e.c.] from isotropic scattering coefficient using an interaction model and MSA approximation relation (with volume fraction of 0.186, mean size 143 nm, ionic strength of 5 mM NaCl equiv.). (a) Solid line, using primary interaction potential model; (b) dashed line, using hard sphere Yukawa interaction potential model.

IX.2.2. Characterization of R6G fluorescence spectrum

Rhodamine 6G (R-4127, Sigma, St. Louis, MO) is a positively charged surfactant. The molecular structure of Rhodamine 6G in shown in Figure IX.2

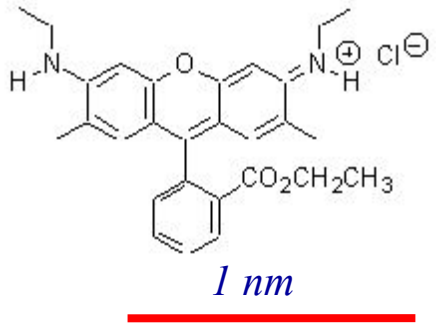

Figure IX.2 Schematic of Rhodamine 6G molecule.

Rhodamine 6G can be used to modify the surface charge by adsorbing on negatively charged polystyrene surface occurs two main mechanisms: 1) ion condensation[170, 173] owing to electrostatic interaction; 2) condensation owing to the hydrophobicity of R6G.[174, 175] At low R6G surface coverage, the electrostatic effect dominates, and at higher R6G surface coverage, hydrophobic interactions become significant.[174, 175]

Figure IX.3 below shows the R6G absorbed spectrum measured using a spectro-fluorometer (Fluorolog-2, Spex Industries Inc., Edison, NJ). The excitation spectrum is determined at the detection wavelength of 830 nm, and emission spectrum is measured with the excitation wavelength of 250 nm. R6G strongly absorbs light at the wavelength of 529 nm, fluoresces at 566 nm with high quantum efficiency (as shown in Figure IX.3). This enables measurement of R6G concentrations using fluorescence measurements. R6G does not fluoresce in the red and infrared wavelength region. Since time-dependent techniques such as FDPM effectively provide separate optical properties

of absorption and scattering of a multiple scattering medium, the evaluation of colloid scattering capacity is enabled at 687 nm without the interference from R6G absorbance or fluorescence.

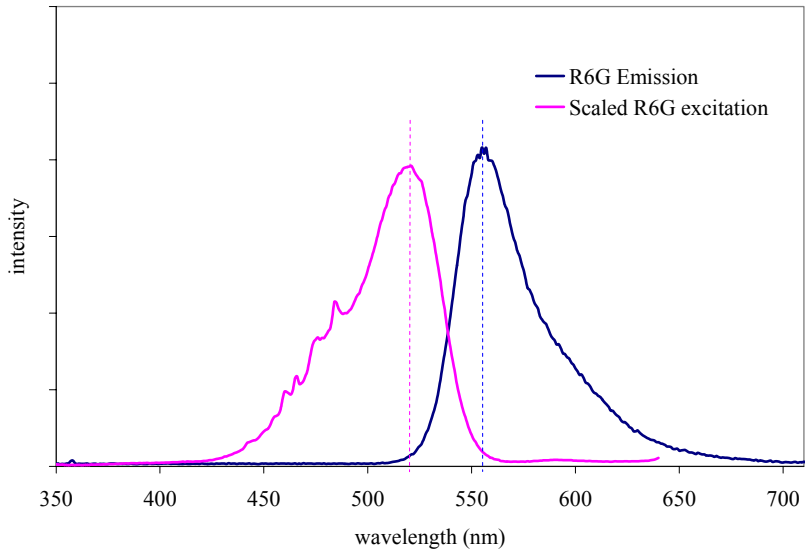

Figure IX.3 Absorption and emission spectra of Rhodamine 6G in 5 mM NaCl. The excitation spectrum is determined at the emission wavelength of 830 nm, and emission spectrum is measured with the excitation wavelength of 250 nm. The intensities of excitation and emission are not based on their absolute value.

The surface charge of negatively charged polystyrene particles, can be adjusted by adsorbing positively charged R6G[175, 176] and the changes in surface charge can be inferred by measuring changes in scattering owing to changes in electrostatic interaction.

IX.2.3. R6G adsorption isotherm

To determine the R6G adsorption isotherm, R6G was added to Latex A (with mean diameter of 143 nm and standard size deviation of 22 nm) of volume fraction 0.5% at 5 mM NaCl to achieve concentrations ranging from 0.1 to 2 mM. After equilibration

at room temperature for 24 hours, the R6G-polystyrene suspensions were centrifuged at 12,000 rpm, 25,000 g (max) (Sorvall RC-5B, GMI. Inc., Clearwater, MN) for 45 minutes and the supernatant was collected. The supernatants were then centrifuged again at 56,000 rpm, 33,000g (max) (Beckman L8-M, Miami, FL) for 45 minutes. The R6G concentrations in the final supernatant were measured in a 10 mm florescence cell using a spectrofluorometer (Fluorolog-2, Spex Industries Inc., Edison, NJ) at the excitation wavelength 529 nm, and the emission wavelength of 556 nm. A calibration curve was prepared by plotting the florescence intensity versus supernatant R6G concentration in 5 mM NaCl. The measured fluorescence intensities of final supernatants were than converted to R6G concentration using this calibration curve, and the amount of adsorbed R6G was easily calculated from R6G mass balance.

Figure IX.4 illustrates the adsorption isotherm of R6G on the latex A of mean diameter of 143 nm and size deviation of 22 nm. Gong *et al.*[151] reported that across a range of R6G concentration there are two plateaus in the adsorption isotherm of R6G on polystyrene corresponding to electrostatic and hydrophobic condensation mechanisms: the first one starts at approximate supernatant concentrations between 1 μM and 30 μM; the second one start at several hundred μM.

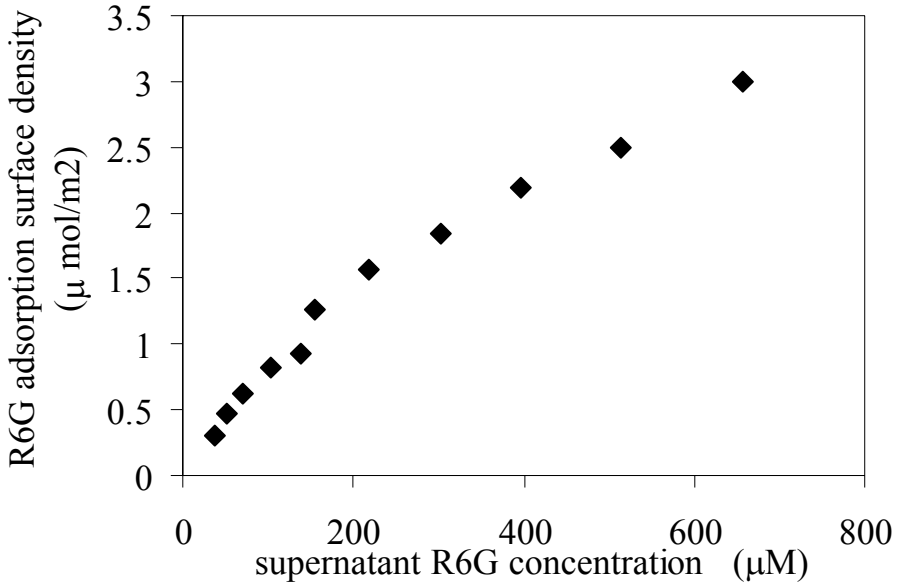

Figure IX.4 Average adsorption density of R6G [μmole/m^2] on polystyrene of mean size 143 nm and size deviation of 22 nm surface versus supernatant R6G concentration [μM] in 5 mM NaCl solution.

The experimental isotherm of this works starting at 39 μM and ending at about 700 μM, is roughly the interim region of the two plateaus in Gong *et al.*'s works.[151] It is expected that a better design of experiment would to be able to reproduce Gong *et al.*'s work. The primary purpose of preparing adsorption isotherm is to show that dominant amount of R6G in the suspension are adsorbed on polystyrene surface. From the adsorption isotherm shown in Figure IX.4, calculation shows that more than 99.9% of R6G added to the suspension was adsorbed on the polystyrene surface. The amount of free R6G in the supernatant was negligible in comparison to the amount R6G adsorbed on the polystyrene particle surface.

IX.2.4. FDPM measurements

FDPM measurements at 687 nm were conducted on approximate 100 ml of polystyrene latex of mean diameter of 143 nm (of volume fraction, $\phi = 0.186$ and 5 mM NaCl equiv.). To this sample, aliquots of the same polystyrene solutions but containing 4 mM R6G were added.[17] Aliquot amounts were weighed using a 1/10,000g resolution balance (Denver Instrument M-220D, Fisher) and added to the solution. After each addition of R6G-polystyrene aliquot sample, the solution was stirred using a sonic stirrer (F60 dismemberator, Fisher Scientific) at low power (< 4 mW), and FDPM measurement of μ_a and μ_s' was performed 30 minutes later to ensure adsorption equilibrium was achieved. Since the R6G-polystyrene aliquots had the same particle volume fraction as the solution, constant volume fraction was maintained through all measurements. The FDPM measurements were repeated three times for each sample. The FDPM measured isotropic scattering and absorption coefficients of the polystyrene latex with R6G adsorption on particle surface will be presented in the next section with discussions.

IX.3. Results and discussions

IX.3.1. Change of μ_s' and μ_a with Rhodamine 6G adsorption

Figures IX.5a and IX.5b plot the isotropic scattering and absorption coefficients as a function of surface R6G adsorption density on polystyrene particles. The isotropic scattering coefficient, μ_s', first increased with the R6G concentration, and then reached a

plateau (starting at R6G concentration adsorption density of 0.3 x 10^{-7} mole/m^2, with further addition of R6G).

The R6G surface coverage rate at the inflection point can be simply obtained by multiplying the R6G adsorption density 0.3 × 10^{-7} mol/m^2 with the area occupied by one mole of R6G molecules that lie on particle surface, where the unit surface area covered by a R6G molecules is roughly estimated from the molecular dimension of R6G (shown in Figure IX.2) to be 1.6 nm × 0.9 nm = 1.44 nm^2.

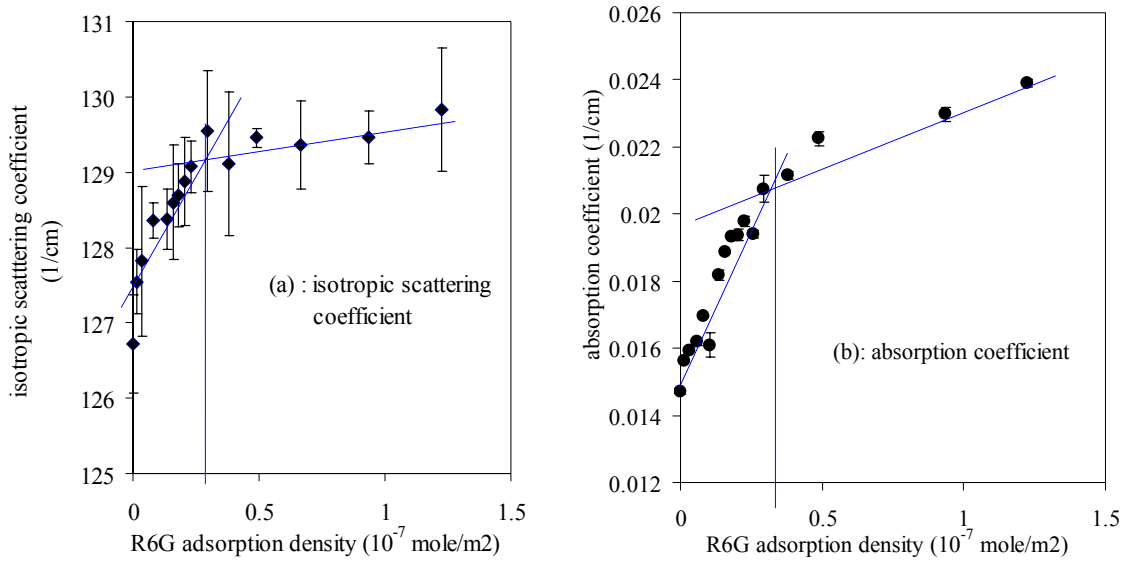

Figure IX.5 FDPM measured isotropic scattering (1/cm], and absorption coefficients (1/cm) versus total R6G concentration [mM] in polystyrene suspensions with volume fraction of 0.186 and ionic strength of 5 mM NaCl equiv.

Since the R6G surface coverage on polystyrene (as calculated from the adsorption isotherm, and the molecular size of R6G) was found to be < 10 % at the inflection point, and since only trace amount of R6G was added, the change in scattering cross section and change in ionic strength owing to R6G addition could not be

responsible for FDPM measured change in μ_s'. The change in effective surface charge owing to R6G adsorption and its impact on particle spatial ordering must be responsible for the increased scattering power.

Figure IX.5b shows a similar change in absorption coefficient owing to the adsorption of R6G. The absorption coefficient first increased with a sharper slope, and then increased with a flatter slope after the inflection point. It is noted that the inflection points in both Figures IX.5a and IX.5b occur at comparable R6G adsorption density of approximate 0.3×10^{-7} mole/m^2. In both cases of absorption and scattering, the inflection point was determined from the interception of two linear curves in the steeply rising and plateau regions. The inflection point Figure IX.5a occurs at 0.3×10^{-7} mole/m^2, well below the intrinsic surface charge density of 6.3×10^{-7} mole/m^2. This inflection point has not been reported in literature, and the change in the absorption efficiency suggests molecular configuration change.

Dimerization and subsequently fluorescence quenching of R6G have been reported in water at high R6G concentration. [174, 177] R6G surface condensation enhances the dimerization of adsorbed R6G. Because light absorption efficiency of dimerized R6G decreases relative to its molecular form.[174, 177] The reduced rate of absorption efficiency of R6G may indicate the change in molecular configuration. The existence of inflection points at both scattering and absorption curves at same "critical" R6G concentration suggests that presence of hydrophobic condensation after the inflection point and that R6G adsorbed after the inflection points does not effectively modify the surface charge of polystyrene particles as well as it does in its molecular state before

inflection point. Nonetheless, Figure IX.5 suggests that R6G condensation on negatively charged polystyrene particle surface may not be one-to-one based in this experimental condition of high volume fraction ($\varphi = 0.186$) and low R6G adsorption density.

In order to validate that change in adsorption mechanism others have reported,[151] FDPM measurement at the low volume fraction of 0.0267 were conducted at high R6G adsorption densities. Figure IX.6 illustrated the absorption coefficient versus R6G adsorption density at the volume fraction of 0.0267 measured at 650 nm. The inflection point occurred at about 5.4×10^{-7} mole/m^2, slightly less than the measured titratable surface change density. Despite the possible remaining surfactant and possible surface charge non-uniformity[178] on the polystyrene particle surface, this inflection point nonetheless corresponds to the surface charge density, agreeing with work of Gong *et al.*[151]

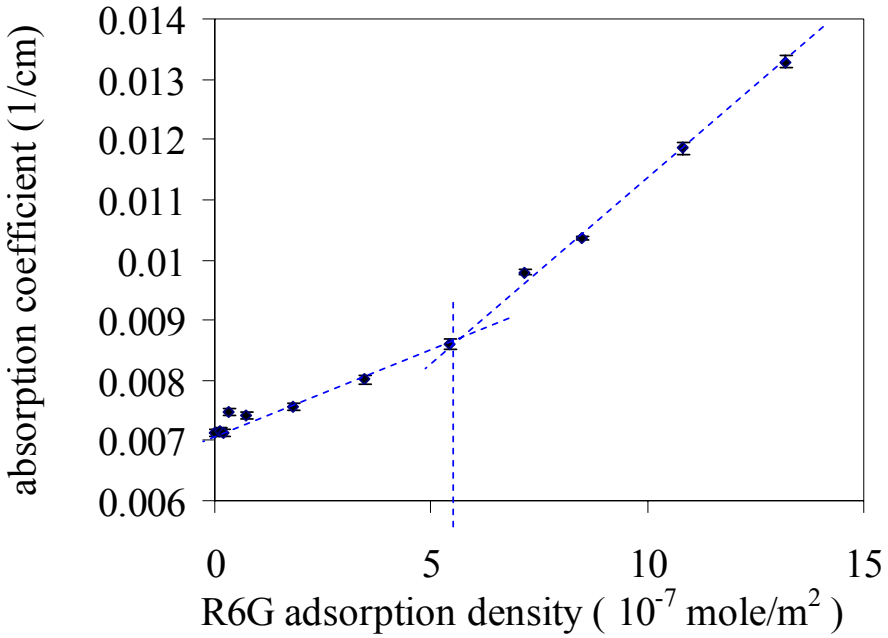

Figure IX.6 FDPM measured absorption coefficients (1/cm), versus total R6G concentration (1/cm] in polystyrene suspensions with volume fraction of 2.67% and ionic strength of 5 mM NaCl equiv. at the wavelength of 650 nm.

Consequently, FDPM measurements of light absorption may provide an indication of change in R6G adsorption mechanism at low adsorption densities not previously reported as well at high adsorption densities.

Nonetheless, FDPM measurements successfully captured the subtle changes in the optical properties of scattering and absorption owing to added trace amount of R6G.

IX.3.2. Change in effective surface charge owing to R6G adsorption

Because of the complexity of R6G adsorption on polystyrene surfaces, one cannot infer the change in surface charge of the polystyrene from adsorbed R6G by simple neutralization calculation.[151, 152, 175] Herein the effective surface charge was also obtained by regressing experimentally obtained scattering coefficients to the MSA-HSY

model prediction after each addition of R6G aliquot. At constant volume fraction and salt concentration, the isotropic scattering measured by FDPM and predicted by MSA-HSY model increases with decreasing effective surface charge associated with increasing R6G concentration. The parameter estimates of z_{eff} were obtained by least squares whereby convergence was achieved when the step size of surface charge was less than 1 electron charge and the difference between model predicted isotropic scattering coefficient and FDPM measured value was less than 0.1 $(1/cm)^{-1}$.

Figure IX.7 illustrates the estimates of effective surface charge at varying R6G surface adsorption density, showing that the effective surface change decreases as R6G concentration increases. The propagated errors in z_{eff} originated from uncertainties of FDPM measurement estimated from Figure IX.1 are about 10 electron charges. The surface charge of 300 electron charge corresponds to the surface charge density of 0.8 x 10^{-8} mole/m^2.

The parameter estimate of effective surface charge at zero R6G adsorption is about two orders in magnitude less than the surface charge obtained from titration. Assumptions in interaction potential model and approximation relations may be the major reasons for the underestimated effective surface charges, and underscore the current state of the non-qualitative description of the physics of particle ensembles. While the PM model is used to describe the interaction, the parameter estimate of effective surface charge would be less than 10, as can be estimated from Figure IX.1. Other sources of errors reside in the assumed monodispersity and independent measurement errors associated with particle size, ionic strength, and isotropic scattering

coefficients. These errors may also contribute to the underestimation in effective surface charge.

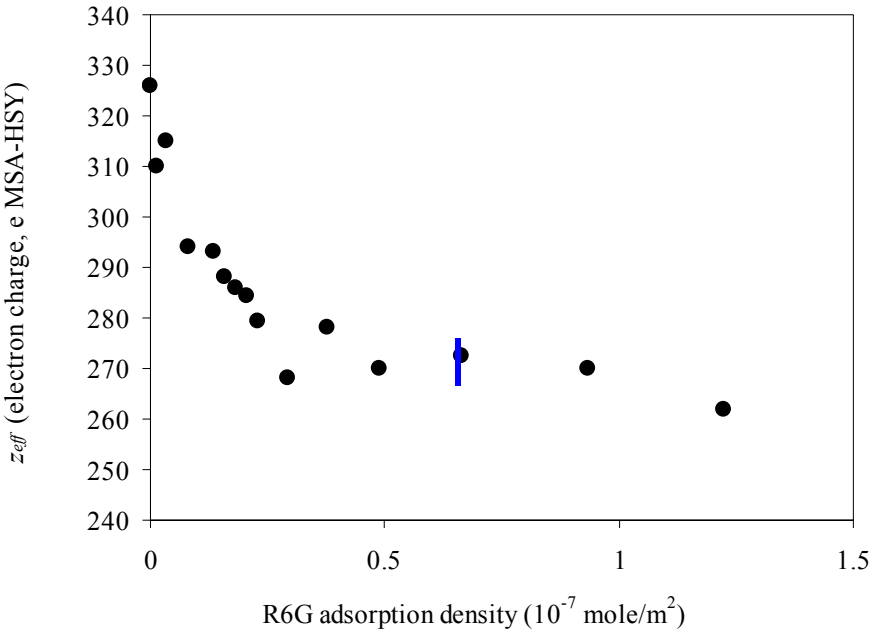

Figure IX.7 Parameter estimate of average z_{eff} [e.c.] per particle versus R6G surface adsorption density [mole/m^2] in the polystyrene suspension (with volume fraction of 0.186, mean size 143 nm, ionic, ionic strength of 5 mM NaCl equiv.). The propagated errors in z_{eff} from the uncertainties of FDPM measurement is approximately 10 electron charge.

Nonetheless, while the physics of electrostatic interaction within the ensemble may not be completely captured, the MSA-HSY model captured the physics of decreased spatial ordering with reduction of effective surface charges owing to R6G adsorption.

IX.4. Summary

FDPM sensitively and effectively captures the increase in isotropic scattering coefficient and absorption coefficients associated with changing electrostatic interaction owing to R6G adsorption on polystyrene surface. Combining FDPM and the MSA-HSY model, a parameter estimate of the effective surface charge was obtained as a function of added adsorbed R6G. As expected, the parameter estimate of surface charge decreases with measured adsorption of positively charged R6G in negatively charged polystyrene particles. FDPM, when combined with a structure model of electrostatic interaction, may provide a potential probe assessing electrostatic interactions of dense, undiluted suspension.

CHAPTER X

MULTIPLE WAVELENGTH MEASUREMENTS OF SCATTERING OF CONCENTRATED POLYSTYRENE SUSPENSIONS

Previous results in Chapter VII show that the parameter estimates of effective surface charges at 687 nm are greater than those obtained at 828 nm, and those estimated at lower ionic strengths are generally less than those obtained at a higher ionic strength. To determine the possible reasons for this and achieve a better understanding of the structure of dense suspensions, we resort to multiple wavelength measurements for more information and for further verification. In this chapter, we present FDPM measurements of isotropic scattering coefficients as a function of volume fraction at 7 wavelengths. The isotropic scattering coefficients as a function of wavelength or as a function of particle volume fraction will also be used to regress mean particle sizes.

The majority of FDPM measurements were conducted by group members Dali Singh Sarabjyot and John Rasmussen, and their contribution to this chapter is recognized.

X.1. Introduction

Using FDPM, Sun *et al.*[9, 11, 13] has previously extracted particle sizing information of concentrated suspensions from measured isotropic scattering coefficient at multiple volume fractions but at a single wavelength. However, dilution, which may change interactions and even particles size for emulsions, is not always applicable. Particle sizing using multiple wavelength FDPM measurement may provide a solution.

Monodisperse MSA-HSY model has been used along with FDPM to estimate effective surface charges in Chapter VII, and the estimated values for effective surface charges depend upon the wavelength and ionic strength. In order to further investigate MSA-HSY model and to demonstrate particle sizing using FDPM, multiple wavelength measurements of the isotropic scattering coefficient for latex A (of mean particle diameter of 143 nm) and B (of mean particle diameter of 226 nm) are conducted at 7 wavelengths and 3 ionic strengths.

In the following sections, the materials used in our FDPM measurements will be briefly summarized, and the experimental results and discussion will then be presented followed by a short summary section.

X.2. Materials and methods

Two polystyrene lattices were obtained from Dow Chemicals: Latex A has the mean particle size of 143 nm (measured using dynamic light scattering) and size standard deviation of 22 nm (obtained from analyzing TEM images); latex B has the mean particle size of 226 nm and size standard deviation of 44 nm both obtained from dynamic light scattering. Both lattices were first dialyzed using deionized-ultrafilted water, and then the ionic strength is adjusted by adding NaCl solutions. The details regarding sample preparation were presented in Chapter V, and sample properties are summarized in Table V.4.

FDPM measurements were conducted at 7 wavelengths: the light at the wavelengths of 488, 514, 568 nm are generated from Argon-Krypton laser, and the light

at the wavelengths of 650, 687, 785, 828 nm are generated from laser diode. FDPM instrumentation has been introduced in Chapter V.

Isotropic scattering coefficients were determined by averaging FDPM measurements conducted at 3 modulation frequencies 70, 80, and 90 MHz. The isotropic scattering coefficients was obtained from the phase shift (PS) and average intensity (DC) as a function of the source detector separation using the multiple distance methods introduced in Chapter V.

X.3. Results and discussions

X.3.1. Isotropic scattering coefficients measured at multiple wavelengths

The FDPM measured isotropic scattering coefficients for the latex of mean particle diameter of 143 nm an latex B of mean particle diameter of 226 nm are shown in Figures X.1 and X.2 respectively.

As illustrated in Figure X.1, FDPM measured isotropic scattering coefficients measured at all wavelengths do not increase linearly with volume fraction due to the quenched scattering arising from particle interactions. With increasing wavelength, the change in scattering coefficients versus volume fractions increasingly deviates from a linear behavior, indicating the extent of scattering hindrance increases with increasing wavelength. Figure X.1 also demonstrates increasing influence of ionic strength on scattering with increasing wavelength.

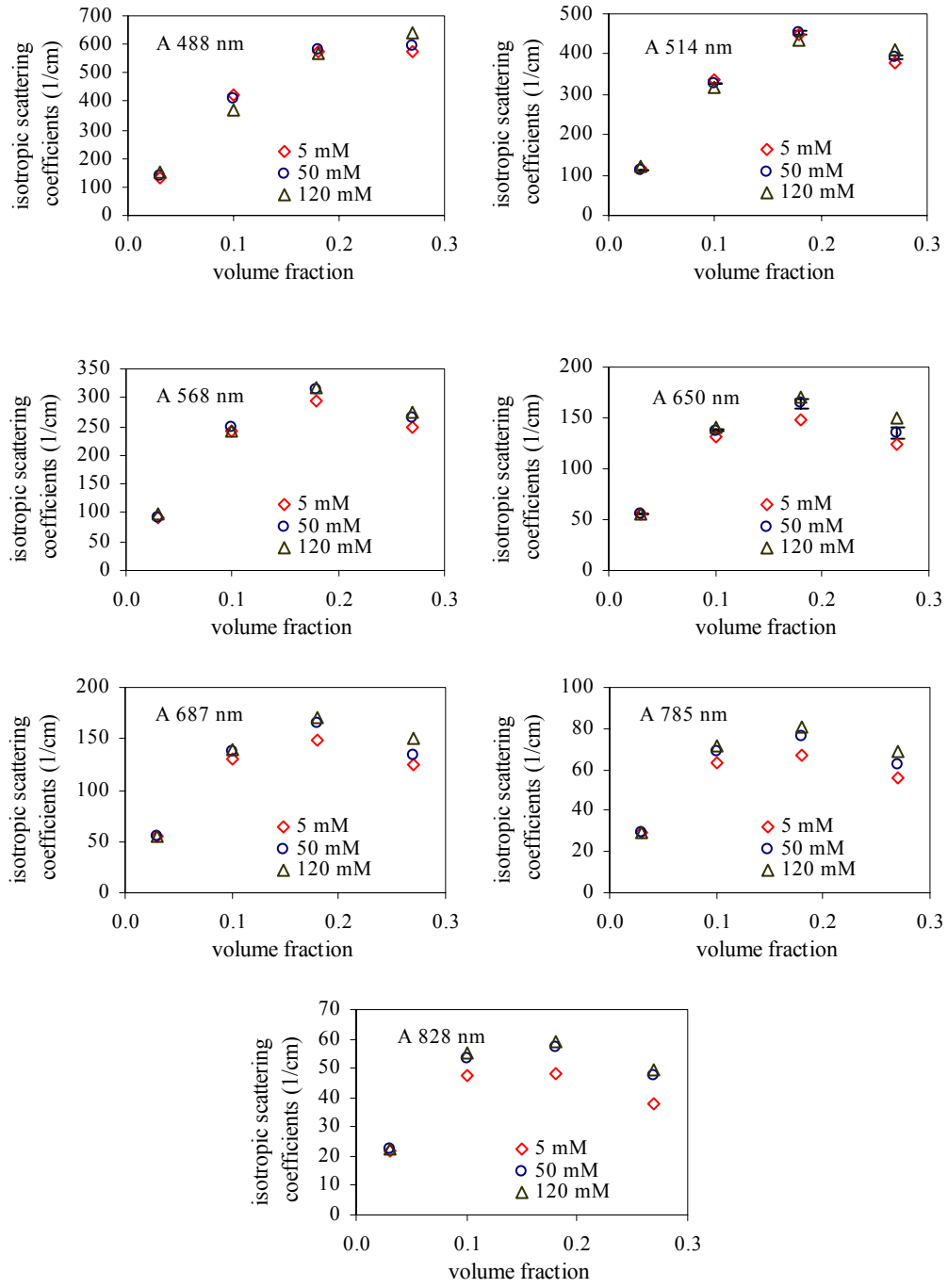

Figure X.1 Isotropic scattering coefficient (1/cm) versus volume fraction measured at seven wavelengths and 3 ionic strengths for the latex of mean diameter 143 nm . (Circle, 5 mM NaCl equivalent; diamond, 50 mM NaCl equivalent; triangle, 120 mM NaCl equivalent).

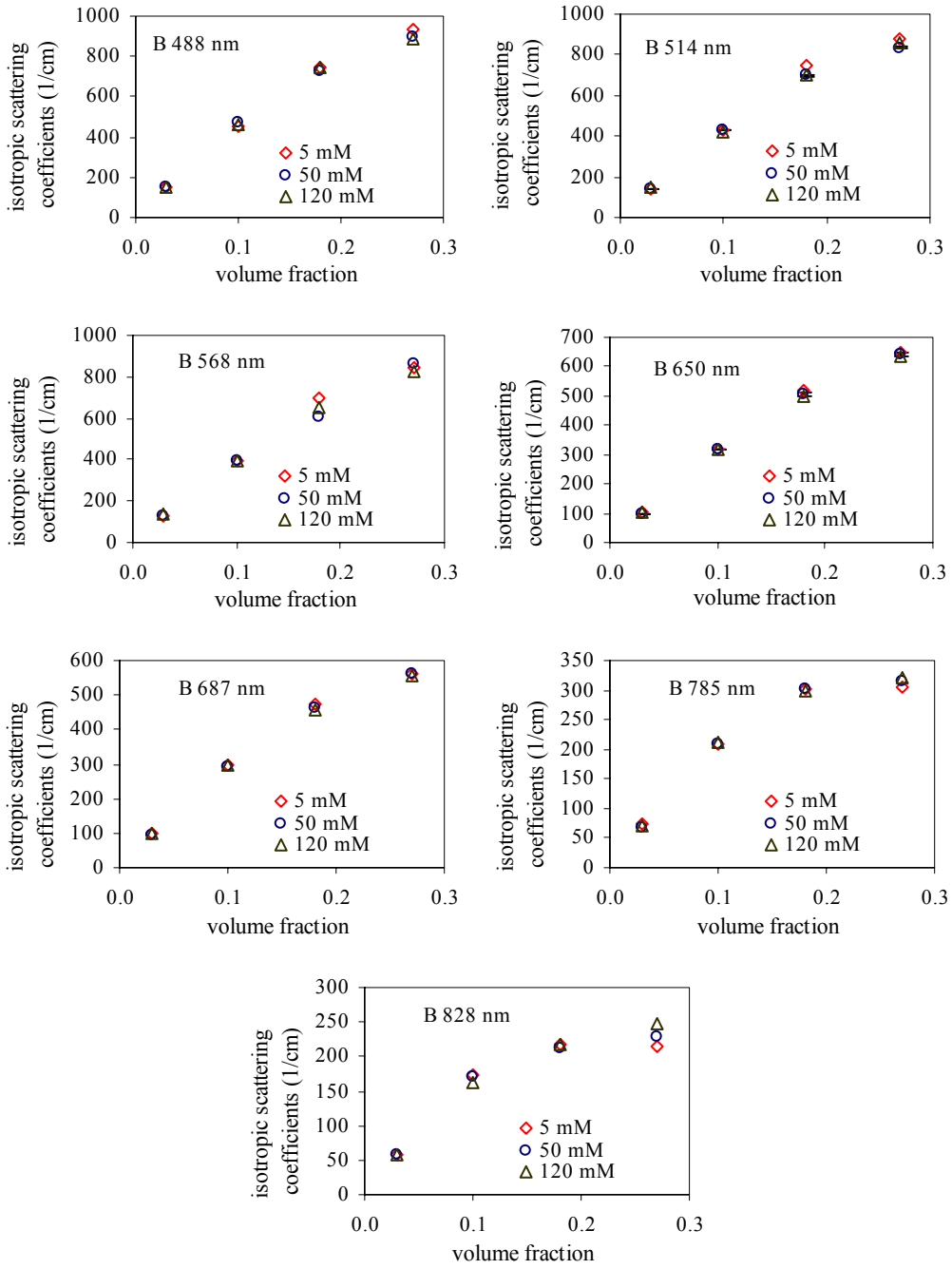

Figure X.2 Isotropic scattering coefficient (1/cm) versus volume fraction measured at seven wavelengths and 3 ionic strengths for the latex of mean diameter of 226 nm. (Circle, 5 mM NaCl equivalent; diamond, 50 mM NaCl equivalent; triangle, 120 mM NaCl equivalent).

Figure X.2 also shows increasing hindrance on scattering with increasing wavelength and with increasing volume fraction. Scattering coefficients of latex of mean diameter of 226 nm shown in Figure X.2 vary with volume fraction in a linear fashion, contrary to the results of latex of mean diameter of 143 nm (shown in Figure X.1), this indicates that the latex of mean diameter of 143 nm is more structured at the length scale of wavelength.[55] The primary reason for the reduced scattering hindrance for suspensions of larger particles is that particle center-to-center separation distance at same volume fraction increases with the particle size. Therefore at some length scale, there are more scatter centers in polystyrene latex of smaller diameter, and the extent of position correlation at the length scale of wavelength increases with scatter number density owing to the decreased mean particle separation distance.

Figure X.2 does not show the apparent dependence of FDPM measured scattering on the ionic strength except at the wavelength of 828 nm at the highest volume fraction. This can be explained by the fact that ESI effects increase with decreasing particle separations, as will be further detailed later.

X.3.2. Particle sizing using monodisperse PY-HS model

It is widely accepted that at the ionic strength above 0.10 mM NaCl equivalent, (where electrostatic interaction among charged particles are screened and dispersions force are negligible for a particle size less than a micrometer), interactions among polystyrene particles can be modeled as that of hard sphere. To obtain the mean particle size, the monodisperse hard sphere model is first used to estimate the experimental isotropic scattering coefficients measured at the ionic strength of 120 mM NaCl

equivalent for mean particle size at each volume fraction by minimizing the following equation:

$$\chi^2 = \sum_i (\mu_{s,\exp}^{'}(i) - \mu_{s,cal}^{'}(i))^2 / w(i)^2 \quad \text{(X.1)}$$

where the weight factor w(i) is chosen to be the mean deviation averaged over the deviations obtained at all of the 3 different ionic strengths at each volume fraction. This ensures that the weight factor w(i) is more representative at volume fraction. Here a varying refractive index model for polystyrene is used, since a much wider range of wavelength is used in this chapter.[179]

$$n_p = 2.4418 + {2.4668 \times 10^{-2}}/{\lambda^2} + {1.6291 \times 10^{-3}}/{\lambda^4} + 0i \quad \text{(X.2)}$$

By minimizing the error function of Eqn (X.2), with theoretical value calculated using monodisperse PY-HS model, the mean particle size is obtained as the only unknown at each volume fraction for both lattices. The regressed mean particle sizes are listed in Table X.1.

Table X.1 Mean size regressed using monodisperse PY-HS model from multiple wavelength measured isotropic scattering coefficients for lattices A(with mean diameter of 143 nm) and B (with mean diameter of 226 nm) at each volume fraction. The mean sizes for lattices A and B determined using DLS are 226 nm and 143 nm respectively.

Volume fraction		0.03	0.1	0.18	0.27
Mean size (nm)	A	140	141	141	144
	B	200	208	214	223

FDPM measured isotropic scattering coefficients for the polystyrene latex of mean particle diameter of 143 nm at ionic strength of 120 mM are plotted in the Figure X.3 as symbols, together with monodisperse PY-HS predictions using the regressed mean size at each volume fraction. The FDPM measured and calculated isotropic scattering coefficients for the polystyrene latex of mean particle diameter of 226 nm are presented in Figure X.4.

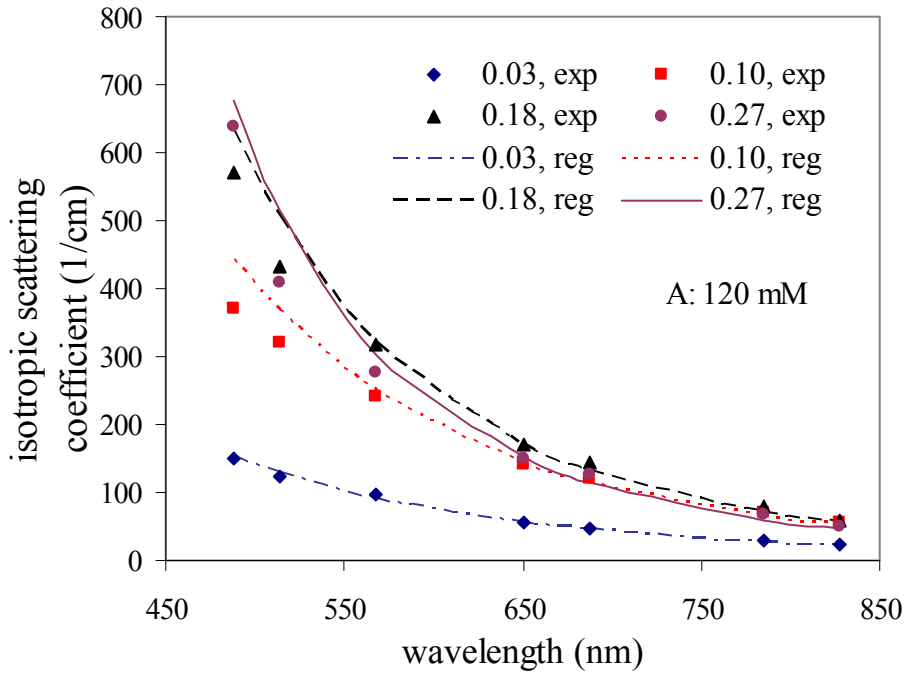

Figure X.3 Monodisperse PY-HS model fitting against FDPM measured isotropic scattering coefficient at the ionic strength of 120 mM NaCl equivalent versus wavelength for polystyrene latex of mean diameter of 143 nm at each volume fraction. (The symbols, FDPM measurements; lines, least squares regressions).

Figure X.3 shows that the regressed values for the isotropic scattering coefficients at wavelengths less than 650 nm are systematically greater than the FDPM measured values at volume fraction of 0.10 or higher, Figure X.4 in shows that the

regressed scattering coefficients are systematically greater than the corresponding experimental values at volume fraction 0.10 or higher for all wavelengths. It was verified that the regressed particle sizes shown in Table X.1 corresponds to the global minimum at each volume fraction by plotting the error function shown in Eqn (X.1) as a function of mean particle diameter.

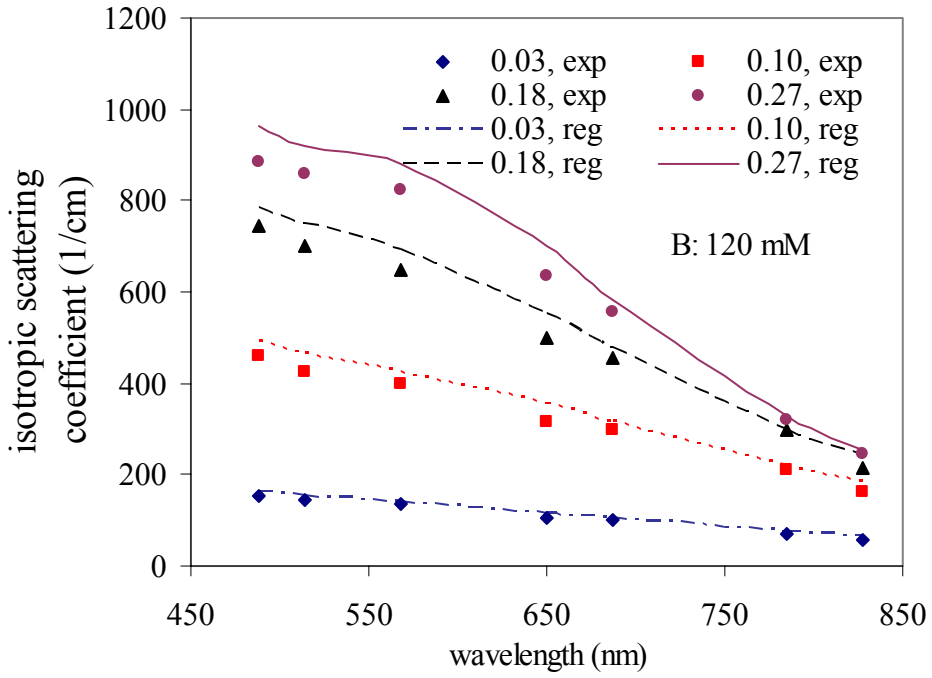

Figure X.4 Monodisperse PY-HS model fitting against FDPM measured isotropic scattering coefficient at the ionic strength of 120 mM NaCl equivalent, as a function of wavelength for polystyrene latex of mean diameter of 226 nm at each volume fraction (The symbols, FDPM measurements; lines, least squares regressions).

Nonetheless, the regressed mean sizes for both lattices are close to the mean size determined using dynamic light scattering, especially for latex A, where the difference in

mean size obtained from FDPM and DLS are within the precision limits of DLS, which is typically with 1-2% of measured values.

The systematic over-prediction shown in Figure X.3 and Figure X.4 (where volume fractions were assumed known) cannot be avoided by changing the estimated particle size, since the predicted scattering coefficient depends not only on the particle size and wavelength, but also on the structure factor model as shown by equation (3.25). The mismatch existed between experimental values (symbols) and model prediction (lines) shown in Figures X.3 and X.4 must be due to the systematic error in the structure factor model at a higher volume fraction. At the volume fraction of 0.03, PY-HS predicts only weak or negligible structure, particles scatter independently (or near independently), and therefore the model predicted scattering coefficients are close to their corresponding experimental values.

X.3.3. Regress particle size using polydisperse PY-HS model

Assuming the refractive index used is accurate, the systematic difference between experimental and model predicted data shown in Figures X.3 and X.4 suggests that using the mono-disperse PY-HS to describe the scattering is inappropriate at volume fraction higher than 0.03 even at the ionic strength of 120 NaCl equivalents. Specifically, the possible reasons for this mismatch are: 1) Influence of the polydispersity while assuming a monodisperse model; 2) inappropriate application of PY-HS model for addressing structure.

At moderate polydispersity, the monodisperse PY-HS model generally predicts isotropic scattering coefficient significantly less than the polydisperse model. Figure

V.5 shows the ratio of isotropic scattering coefficients predicted using polydisperse PY-HS model (with the mean size 143 nm and size deviation 22 nm), where a Gaussian distribution of particle size is assumed, to those predicted with the monodisperse version (with the mean size 143 nm). Figure X.5 shows that the ratio of the predicted scattering coefficient using PY-HS polydisperse model (with the mean size of 143 nm and standard size deviation of 22 nm) to that using monodisperse model (with the mean size of 143 nm) increases with increasing wavelength and with increasing volume fraction as a function of wavelength.

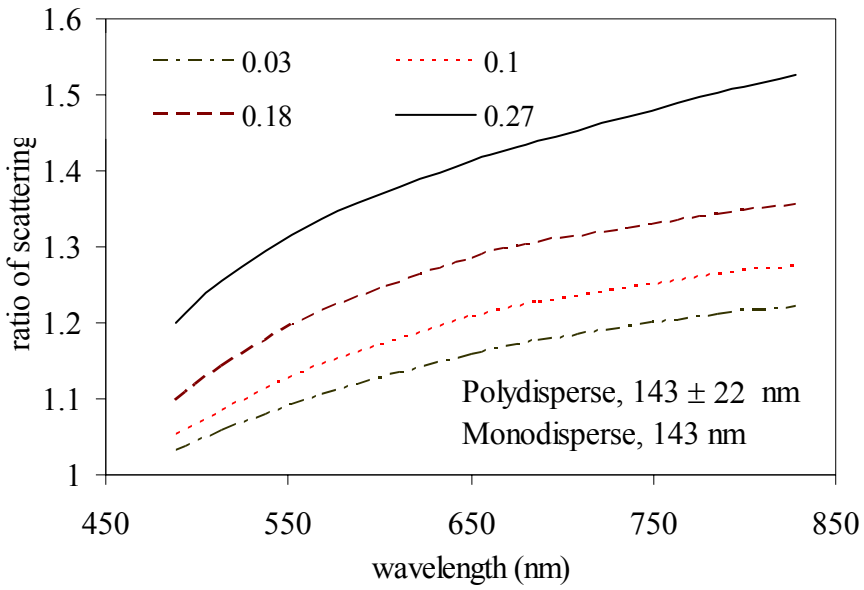

Figure X.5 The ratio of isotropic scattering coefficients predicted using polydisperse PY-HS model (mean size 143 nm, size deviation 22 nm) to those predicted using monodisperse PY-HS model (mean size 143 nm) as a function of wavelength at various volume fraction.

Due to the polydispersity of lattices, the monodisperse model cannot provide an unbiased fit of FDPM measured isotropic scattering coefficients as shown in Figures X.3

and X.4. Therefore negligence of the polydispersity must be listed as one of the reasons for the poor regression results.

The polydisperse PY-HS model can also be regressed to the data by minimizing Eqn (X.1) to find the mean size and spread of the assumed Gaussian distribution as the two unknowns. Here the convergence criteria are chosen to be that the change in norm of unknown between iterations is less than 10^{-8} $(1/cm)^2$. The obtained mean particle size and standard size deviation for both lattices are listed in Table X.2. The isotropic scattering coefficients predicted using the regressed mean size and size deviation using polydisperse PY-HS model and experimental scattering data for the polystyrene latex (latex A) of mean diameter of 143 nm are shown in the Figure X.6.

Table X.2 Mean size and standard size deviation as the two unknowns regressed using polydisperse PY-HS model from multi wavelength FDPM measured isotropic scattering coefficients at ionic strength of 120 mM NaCl at each of known volume fractions, 0.03, 0.10, 0.18, 0.27.

Samples		0.03	0.10	0.18	0.27
A	Mean Size (nm)	135.9	97.0	119.2	127.6
	Standard Deviation(nm)	19.2	43.0	29.9	22.7
B	Mean Size (nm)	209.8	208.7	213.8	229.1
	Standard Deviation(nm)	26.9	31.2	23.9	12.3

A comparison of Figures X.3 and X.6 shows that the inversion using polydisperse PY-HS model (with both particle size and size deviation as unknowns) at

each ionic strength provides a better fit. Without systematically under-or over-predicting isotropic scattering coefficients, polydisperse PY-HS model is at least more suitable in describing the measured scattering data. However, the regressed mean sizes for the polystyrene latex of the mean diameter of 143 nm using the polydisperse model are generally less than the value determined using dynamic light scattering and vary with volume fraction.

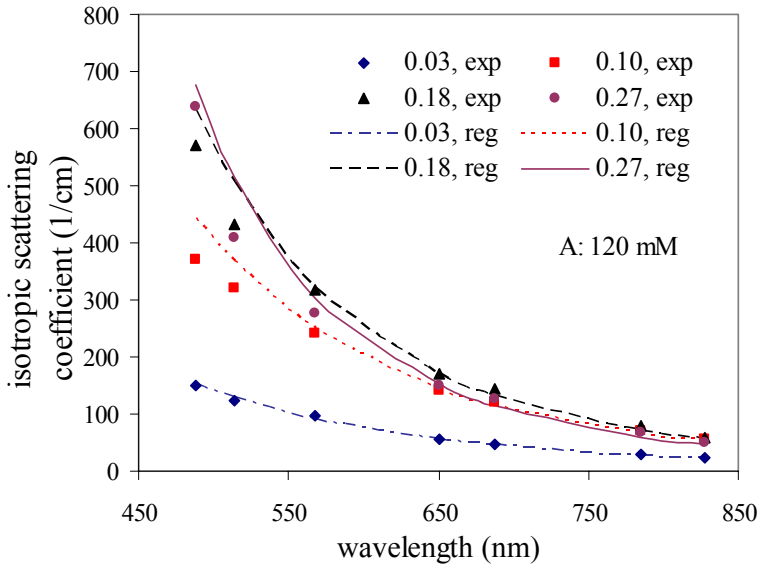

Figure X.6 Isotropic scattering coefficient versus wavelength at 4 volume fractions for the polystyrene latex (with mean size of 143 nm and deviation of 22 nm). Symbols denote FDPM measurements at ionic strength of 120 mM. Lines denote prediction using PY-HS polydisperse model with regressed mean size and size deviation.

Since the Mie theory predicts increased scattering coefficient with increasing particle size at the visible wavelengths for particles with size between 100 and 300 nm, the underestimation of size for the latex of 226 nm using polydisperse PY-HS model indicates that isotropic coefficients are overpredicted in polydisperse PY-HS model.

The corresponding model predicted data in using the latex of mean diameter 226 nm are shown in Figure X.7, which indicates that at the wavelengths of 514 nm or lower, the polydisperse PY-HS model still significantly over predicts isotropic scattering coefficients, where both regressed particle sizes and size deviations used in model prediction are smaller than DLS values. Figure X.7 also suggests that polydisperse PY-HS model overpredicts scattering coefficients with the assumed volume fraction.

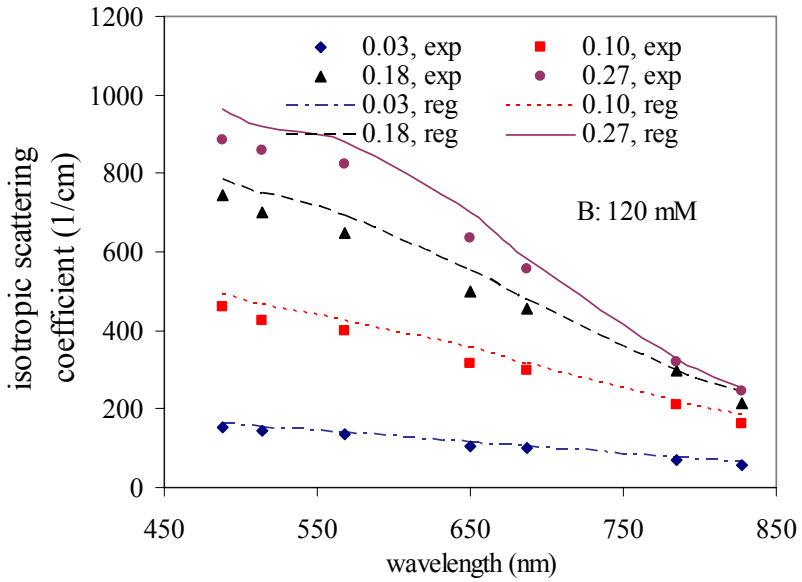

Figure X.7 Isotropic scattering coefficients versus wavelength at 4 volume fractions for Latex B (with mean size of 226 nm and deviation of 43 nm). Symbols denote FDPM measurements at ionic strength of 120 mM. Lines denote lines predicted using PY-HS polydisperse model with regressed mean size and size deviation.

The over-estimation in scattering coefficient indicates that PY underestimates the quenching effects on scattering due to particle interaction at the ionic strength of 120 mM NaCl equivalents.

We realize that modeling the particle interaction as simple hard spheres may also contribute to the ill-fit. Since the error of model predicted structure factor depends on the wavelength and on volume fraction used, the results of particles sizing using the PY-HS model may depend upon the experimental wavelengths and volume fractions.

It is noted that even though the regressed mean size for the polystyrene latex of mean diameter of 143 nm (Latex B) are closer to the DLS values at the volume fraction of 0.27, one cannot conclude that PY-HS model predictions are more accurate at higher volume fractions, since PY-HS structure factor model systematically overpredicts isotropic scattering coefficients (shown in Figures X.3 and X.4 for the monodisperse cases and in Figures X.6 and X.7 for the polydisperse cases). However, FDPM multiple wavelength measurements combined with PY-HS model can provide reasonably accurate means to estimate particle size as well as particle size distribution at increased volume fractions.

X.3.4. Estimation of z_{eff} at multiple wavelengths

Using a similar least squares regression scheme that was used to obtain mean particle size, the effective surface charges, z_{eff}, at each volume fraction and at each ionic strength have been obtained as the only unknowns by minimizing Eqn (X.1) from multiple wavelength measured scattering coefficients with MSA-HSY.[122] The mean particle diameter in the forward prediction using monodisperse MSA-HSY is chosen to be those (shown in Table X.1) regressed at each volume fraction at the ionic strength 120 mM NaCl equivalents. The parameter estimates of surface charges for polystyrene latex of mean diameter 143 nm are shown in the Table X.3, where the convergence

criteria are set to be the parameter estimate of the effective surface charge less than 0.1 or a change in the χ^2 error function less than 10^{-4}.

Table X.3 Regressed effective surface charge for the latex of mean diameter of 143 nm at 4 volume fractions and 3 ionic strengths.

Volume fraction		0.03	0.1	0.18	0.27
z_{eff}, *e. c.*	5 mM	0	518	515	491
	50 mM	0	1232	1299	1892
	120 mM	0	0	0	0

At the lower volume fraction of 0.03, particle positions are not correlated, and there is no perceivable impact of ionic strength on the FDPM measured scattering coefficients. At the ionic strength of 120 mM, the regression naturally goes to zero, since the size used in prediction is obtained from regression using PY-HS model from the scattering data measured at 120 mM ionic strength. It is well known that MSA model reduces to PY-HS when the effective surface charge vanishes.

We can see that the regressed effective surface charges obtained at the volume fractions of 0.1 and 0.18 are extremely close, and are slightly different from that obtained at the volume fraction of 0.27. It is also shown that the effective surface charges obtained at an ionic strength of 5 mM is less than those obtained at 50 mM NaCl equivalent, agreeing with the results shown in Chapter VII and affirming an uneven estimation of the screening effects at different ionic strength by MSA-HSY model.

Even though Figure X.5 shows that polydispersity can generate significant differences in the PY-HS model prediction, it is widely considered that polydispersity can be neglected at strong ESI when polydispersity index is less than 10%. Though monodisperse MSA-HSY model is used in the regression, the z_{eff} obtained are still predictive of ESI effects on the structure and scattering of a concentrated suspension.

From the scattering coefficients of the polystyrene latex of mean diameter 226 nm (Figure X.2), one can conclude that ionic strength does not impact the measured scattering significantly. The corresponding regressed effective surface charges do not change appreciably with ionic strength and therefore are not presented here.

The possible reasons for the diminution of electrostatic effects on the scattering of the latex with mean diameter of 226 nm (Latex B) are: 1) the electrostatic interaction in the mean diameter of 226 nm is relatively weaker than that in the latex of 143 nm; and 2) the mean particle separation distances for the latex of 226 nm are larger at *constant* volume fraction (resulting from reduced number of particle in a unit volume), which greatly reduces the particle electrostatic forces predicted using Eqn (III.3). Assuming the surface charge density is proportional to zeta potential and considering that the latex of mean diameter of 143 nm has a higher zeta potential (72 mV) than the latex with mean particle size of 226 nm (and with mean zeta potential of 48 mV), the magnitude of electrostatic repulsive force between contacting particles for 143 nm diameter latex is about 60% of that the latex of 226 nm (as estimated from Eqn (III.3)).

For the second reason, at constant volume fraction, an increase in particle size will increase the particle separation distance due to decreased particle number density.

Furthermore, an increase in particle size will decrease the electrostatic force between particles by a factor of $\frac{1}{r\exp(\kappa r)}$ owing to the increasing particle center to center distance, r, as shown in Eqn (III.3). How sharply the ESI diminishes with increasing r depends on the value of κ^{-1}, which indicates thickness of electric double layers. As the particle surface separation distances become greater than twice of the value of κ^{-1}, the ESI between the particles can be considered negligible and interaction between particles can be considered as that between hard spheres.

At the same volume fraction and ionic strength, particle electrostatic interactions tend to be less important for determining particle structure.

Another reason is due to the fact that isotropic scattering coefficients predicted using Eqn (X.3) for the latex of 226 nm measured at visible wavelengths are not sensitive to the change in structure due to q range determined by the particle and wavelength (shown in Figure X.8).

$$\mu_s'(\lambda) = \frac{6\phi_v}{(2\pi m/\lambda)^2 \sigma^3} \int_0^\pi F(q) \cdot S(q) \cdot \sin\theta \cdot (1-\cos\theta) d\theta \qquad \text{(X.3)}$$

The sensitivity of the scattering coefficient predicted from Eqn (X.3) to the structure factor depends on the effective q range, $0<q<q_{max}$ with $q_{\max}\sigma = \frac{4\pi n_l \sigma}{\lambda}$. The maximum q ranges interrogated by wavelength λ_1 and λ_2 are $0<q\sigma<q_{1,max}\sigma$ and $0<q\sigma<q_{2,max}\sigma$ respectively. As the ordering in particle position of a monodisperse suspension increases due to increased particle repulsive force, the structure factor represented by continuous curve (shown in Figure X.8) shifts to that represented by the

dashed curve, which has a smaller value in S(0) and a higher value of the first peak in S(q). At the wavelength of λ_1, Eqn (X.3) predicts a smaller isotropic scattering coefficients indicating a more structured suspension, since the all the values of S(q) represented by the dashed curve (indicating higher ordering) are smaller that those represented by the continuous line in the effective q range of $0<q\sigma<q_{1,max}\sigma$.

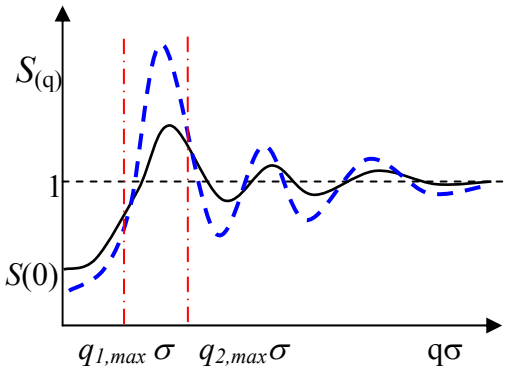

Figure X.8 Structure factor curve S(q) and effective dimensionless q range indicated by $q_{max}\sigma$. The maximum dimensionless scattering vector $q_{max}\sigma$ increases proportionally with the particle diameter in a suspension and decreases with the wavelength. The angle–integrated structure factor is the structure factor averaged over t he interval [0, $q_{max}\sigma$]. The dashed line represents a higher structure than the solid line does.

However, at the wavelength of λ_2 and at an effective q range of $0<q\sigma<q_{2,max}\sigma$ (shown in Figure X.8), the solid line and the dashed line crosses. The values of S(q) represented by dashed curve are less that those represented by the continuous line for the q between the origin and the crossing point, while the value represented by the dashed curve are greater than that represented by the continuous curve for the q value between the crossing point and $q_{2,max}\sigma$. Therefore, the angle-integrated structure factor <S(q)> over the effective dimensionless q range of [0, $q_{2,max}\sigma$], for the S(q) represented by both

solid and dashed lines may be close, and the isotropic scattering coefficient predicted from both S(q) curve with the effective q range [0, $q_{2,max}\sigma$] are similar. Consequently, the sensitivity of the isotropic scattering coefficient to the structure changes depends on the dimensionless *q* range determined by the wavelength and the particle diameter.

The dimensionless q range for the particles of diameter 143 nm appears at the right hand side of the first S(q) peak (Figure X.3) even at,488 nm, which is the smallest wavelength used in the work of this thesis. At longer wavelengths, such as 687 and 828 nm, the effective q range is sufficiently close to the origin and the S(q) in the range can be approximated using long wavelength approximation (as shown in Chapter VIII). For the latex of mean particle diameter of 226 nm, the $q_{max}\sigma$ is beyond the first peak in the $S(q)$ curve at the wavelength of the 488 nm, and the FDPM measured scattering coefficient does not show change with the changing ionic strength.

In summary, the decreased repulsive electrostatic force (due to increased particle separation distance) and decreased sensitivity of isotropic scattering to the change in structure (due to increased dimensionless q) together cause the smaller dependence of the FDPM measured isotropic scattering on ionic strength.

X.3.5. Estimation of z_{eff} at multiple volume fractions

In the previous section, we obtained z_{eff} from isotropic scattering coefficients measured from multiple wavelengths at a single volume fraction. In this section, z_{eff} are regressed from scattering data at each wavelength and at each ionic strength but at varying volume fractions by minimizing the error function.

$$\chi^2 = \sum_i (\mu_{s,\exp}^{'}(\phi_{v,i}) - \mu_{s,cal}^{'}(\phi_{v,i}))^2 / w(i)^2 \quad \text{(X.4)}$$

where $\mu_{s,\exp}^{'}(\phi_{v,i})$ and $\mu_{s,cal}^{'}(\phi_{v,i})$ represent measured and predicted (Eqn (X.4)) isotropic scattering coefficients at the volume fraction of $\phi_{v,i}$. To illustrate how MSA-HSY treats the impact of the ionic strength on the scattering at different wavelengths, we regressed effective surface charges at different ionic strengths at each wavelength, where the mean particle size used at each wavelength were chosen to be that regressed using PY-HS model from $\mu_{s,\exp}^{'}(\phi_{v,i})$ measured at 120 mM at all four volume fraction at the wavelength. The effective particle size and the obtained effective surface charges, z_{eff}, for each wavelength are shown in the Table X.4.

Table X.4 Parameter estimates of effective surface charge regressed from FDPM measured isotropic scattering coefficients at four volume fractions for the latex of mean diameter of 143 nm at each wavelength. The mean size is chosen to be that regressed at four volume fractions at ionic strength of 120 mM using monodisperse PY-HS model.

Wavelength (nm)		488	514	568	650	687	785	828
effective size (nm)		137	136	143	145	149	150	147
z_{eff}, e	5 mM	0	216	408	482	541	512	598
	50 mM	0	438	1136	1731	1859	1559	1330
	120 mM	0	2	2	2	2	2	2

The parameter estimates of effective surface charges depend upon the wavelength and the ionic strength of their suspension. The regressed effective surface charge increases with wavelength when the wavelength is 650 nm or lower.

In addition, the parameter estimate of effective surface charge at the ionic strength of 5 mM is significantly less than that obtained at 50 mM. These results suggest that MSA-HSY overestimated the electrostatic interactions among particles at lower ionic strength, since MSA-HSY model requires a smaller effective surface charge to predict the hindered scattering due to electrostatic interaction. These results affirm that the screening effects are relatively overestimated in the MSA-HSY model at higher ionic strengths.

Since the ionic strength does not show significant impact on the scattering coefficients of latex of 226 nm diameter, the regressed effective surface charges are close to zero due to the fact that FDPM measured isotropic scattering coefficients of the latex do not evidently depend on the ionic strength.

X.4. Summary

Polydispersity can have a significant impact on the measured isotropic scattering coefficient at the ionic strength of 120 mM, which can be sensitively detected using FDPM. A least squares regression using PY-HS model can provide mean particle size and size deviation with reasonable accuracy. From multiple wavelength measurement of scattering coefficients, the parameter estimates of effective surface charges at 5 mM NaCl equivalents are less than those at 50 mM NaCl equivalents, indicating that MSA-

HSY unevenly predicted screening effects at different ionic strengths. The estimated parameter representing surface charge depends on the wavelength.

The parameter estimates of particle size information using PY-HS model and effective surface charges using MSA-HSY model are summarized in Tables X.5, X.6, and X.7.

Table X.5 Parameter estimation of particle size information using both polydisperse and monodisperse PY-HS model from multiple wavelength FDPM measurements at the ionic strength of 120 mM NaCl equivalent at various volume fractions. Where the mean particle size and standard size deviation for latex A are 143 and 22 nm, and the mean particle size and standard size deviation for latex B are 266 and 44 nm.

.

Volume fraction			0.03	0.10	0.18	0.27
Polydisperse PY-HS model regression	A	Mean size (nm)	135.9	97.0	119.2	127.6
		Standard deviation(nm)	19.2	43.0	29.9	22.7
	B	Mean size (nm)	209.8	208.7	213.8	229.1
		Standard deviation(nm)	26.9	31.2	23.9	12.3
Monodisperse PY-HS model regression	A	Mean size (nm)	140	141	141	144
	B	Mean size (nm)	200	208	214	223

Table X.6 Regressed effective surface charge for the latex of mean diameter of 143 nm at 4 volume fractions and 3 ionic strengths using monodisperse MSA-HSY model, the effective particle diameter used in the model prediction are those regressed using PY-HS model regression from multiple wavelength FDPM measured isotropic scattering coefficients measured at the ionic strength of 120 mM NaCl equivalent.

Volume fraction		0.03	0.1	0.18	0.27
Effective size (nm)		140	141	141	144
z_{eff}, e	5 mM	0	518	515	491
	50 mM	0	1232	1299	1892
	120 mM	0	0	0	0

Table X.7 Parameter estimates of effective surface charge regressed from FDPM measured isotropic scattering coefficients at four volume fractions for the latex of mean diameter of 143 nm at each wavelength. The mean size is chosen to be that regressed at four volume fractions at each wavelength at ionic strength of 120 mM using monodisperse PY-HS model.

Wavelength (nm)		488	514	568	650	687	785	828
Effective size (nm)		137	136	143	145	149	150	147
z_{eff}, e	5 mM	0	216	408	482	541	512	598
	50 mM	0	438	1136	1731	1859	1559	1330
	120 mM	0	2	2	2	2	2	2

CHAPTER XI

LIGHT ABSORPTION AND INTERFERENCE APPROXIMATION

In the previous chapters, isotropic scattering coefficients predicted using Eqn (III.25) are based upon the interference approximation introduced in Chapter II, where a form factor describing angle-dependent scattering intensity is associated with a structure factor model (introduced in Chapter III) addressing dependent scattering in order to predict isotropic scattering coefficient in a dense suspension. We have presented in the Chapter II that particle light absorption is intrinsically related to the particle light scattering. Light scattering outward from the particle is referred as particle scattering, while light scattering toward particle center causes particle light absorption. FDPM enables simultaneous determination of light scattering and light absorption properties of a concentrated suspension. The absorption coefficient measured using FDPM provides us a chance to measure particle absorption efficiency and to examine interference from the perspective of light absorption. The chapter will present the validation for methodology of determining particle absorption efficiency and attests interference approximation from measured particle absorption efficiency as a function of volume fraction.

The chapter is adopted from a manuscript (with manuscript number, OT18921) submitted to "Applied Optics" with the title "Validating the assumption to the interference approximation using measurements of absorption efficiency and hindered

scattering in dense suspensions" prepared by Yingqing Huang and Eva M. Sevick-Muraca, and accepted for publication.

XI.1. Introduction

Light scattering and absorption are critical performance properties and lend commercial value to many dense dispersion products, such as paints, pigments, foods and cosmetics. Yet, closely positioned particles do not scatter light independently as they do when isolated as individual particles[17, 18] or contained within an ensemble of particles in a diluted suspension.[16] Spatial correlation of particles, or microstructure, arises owing to particle interactions.[55] The non-random or preferred particle orientation creates an interference pattern in the far field that reduces the scattering power of dense suspensions.

The interference approximation[20, 21, 180] assumes that the incident or scattered electromagnetic wave from each individual particle within a dense suspension is not influenced by its nearest neighboring particles. Instead, the scattered wave fronts from each particle are assumed to destructively or constructively interfere in the far field in a manner that reduces or enhances scattering power. From the interference approximation and measurement of scattered radiation, the particle correlation function has been inferred and used to obtain inter-particle interaction potentials.[181, 182] Salgi and Rajagopalan reviewed the implication of structure factor and inter-particle interactions upon scattering from generalized polydisperse colloidal suspensions.[111]

Besides scattering, the measurement of the particle absorption efficiency offers an alternative method to observe the validity of the interference approximation. Since

the interference approximation assumes that a uniform incident electromagnetic field on a particle is undisturbed by other nearby particles, the attenuation of incident field owing to particle absorption should be linearly related to particle volume fraction of a suspension.

Using time-dependent light propagation in dense suspensions, we seek to confirm the validity of the assumption of uniform, undisturbed incident electromagnetic field assumed by the interference approximation through measurement of absorption in dense suspensions. In addition, we seek to simultaneously confirm the validity of far field interference through measurement of isotropic scattering.

The concept of light absorption from particle suspensions within the context of radiative transfer theory (RTE) has been detailed in Chapter IV, and will be briefly summarized in the following. We will also briefly review the assumption of the interference approximation, which impacts the diffuse light propagation in multiply scattering medium.

XI.2. Background and theory

The absorption power of a particle suspension can be described by the absorption coefficient μ_a (1/cm) and, for diffusely scattered light in a multiply scattering medium, the scattering power can be indicated by the isotropic scattering coefficient, μ_s' (1/cm). For a multiple scattering, monodisperse suspension, in which scattering particles are randomly oriented (< 1% in volume for most non-metal oxide suspensions), the

scattering coefficient varies linearly with particle number density, ρ, and scattering cross section, C_{sca}:

$$\mu_s' = \rho C_{sca}(1-g) \tag{XI.1}$$

here g is the scattering anisotropy, indicating the distribution of angularly scattered light intensity, and the scattering cross section, C_{sca}, can be calculated from Mie theory by $C_{sca} = \int_0^{\pi} F(\theta, x, n_p, n_l) d\theta$, where $F(\theta, x, n_p, n_l)$ is form factor predicting the angle-dependent scattering intensity from particles; θ is scattering angle; x is termed particle size parameter, which can be derived from the particle diameter d and wavelength, λ, by $x=\pi d/\lambda$; n_p is the refractive index of the particles; and n_l is the refractive indices for the suspending medium.

For a concentrated suspension, Eqn (XI.1) overpredicts experimental values of the isotropic scattering coefficients since the correlated position of particles arising primarily from volume exclusion is not accounted. The light scattered from closely positioned particles are partially phase-correlated due to their correlated particle position, and the correlated wave-fronts scattered from closely neighboring particles interfere destructively or constructively. Upon using statistical mechanics and liquid theory arguments to address hindered scattering owing to correlated particle position, Vrij *et al.*[20] proposed that the isotropic scattering coefficient can be predicted by:

$$\mu_s'(\lambda) = \frac{6\phi_v}{(2\pi n_l/\lambda)^2 \sigma^3} \int_0^{\pi} F(q) S(q) \sin\theta (1-\cos\theta) d\theta \tag{XI.2}$$

where ϕ_v is the volume fraction of particles; $q = (4\pi n_l/\lambda)\sin(\theta/2)$ is the scattering vector; $F(q)$ is the form factor describing the angle-dependent scattered intensity from particles; and $S(q)$ is the structure factor, which can be obtained from the Fourier transformation of the pair correlation function introduced in Chapter III. It is implicitly assumed in Eqn (XI.2) that: 1) the incident light field is scattered by individual particles independently; 2) hindered scattering results from the interference of light scattered from different particles in the far field; and 3) the interference effect can be corrected using a structure factor, which can be predicted from particle position correlation. These assumptions comprise the interference approximation. Dik and Ivanov[22] have investigated the upper applicable limit of particle concentration in which the interference approximation remains valid, and pointed out that the interference approximation is only suitable for small particles at a relatively low refractive index. For example, at the relative refractive index $n_p/n_l = 1.8$, the interference approximation is applicable when particle size is $x < 1.5$. A decrease in real particle refractive index increases the upper limit of applicable particle size.

To date, the interference approximation has been examined and demonstrated by measurements of light scattering.[9, 20-22, 96, 162, 180, 183, 184] Yet another consequence of the interference approximation is an unhindered absorption efficiency of individual particles. Since the electric field incident on a particle is not impacted by light scattered from nearest particle neighbors, then the absorption cross section of a particle, C_{abs}, should remain constant even with the existence of correlated particle position. The

absorption cross section, C_{abs}, can be obtained by subtracting the scattering cross section C_{sca} from the total extinction cross section, C_{ext}, which can be calculated from the scattering amplitude in forward direction using scattering theory. Based on this argument, the absorption owing to particles can be fully determined from its scattering pattern. To date, there has been no simultaneous validation of the interference approximation using both absorption and scattering measurements.

The absorption of the suspending fluid is proportional to the absorption efficiency of the fluid, α and the local radiance, $\varphi(r,\hat{\Omega},t)$, which represents the radiation energy passing through a unit area within a unit time at the position *r*, solid angle, $\hat{\Omega}$, and time *t*. For a homogeneous fluid, α is related to the imaginary refractive index of the medium, n_l" and the wavelength, λ, by $\alpha = \frac{4\pi n_l''}{\lambda}$. In a suspension of total volume *V*, radiance loss due to absorption from the suspending fluid can be written as: $\int_V \varphi(r,\hat{\Omega},t)(1-\phi_v)\alpha dV$, where a factor of (*1*-ϕ_v) is inserted into the integrand to exclude the volume occupied by the particles. The term ϕ represents the volume fraction of the particles in the suspension. In the same manner, the absorption loss due to the suspended particles can be described by: $\int_V \varphi(r,\hat{\Omega},t)\phi_v\mu_{a,p}dV$, where volume based absorption efficiency of particles, $\mu_{a,p}$, (which is not necessarily equivalent to the corresponding bulk properties of same materials,) can be calculated from $\mu_{a,p} = \rho C_{abs}$ for a monodisperse suspension. Therefore, the total radiance absorption loss in volume

V due to both particles and suspending fluid is $\int_V \varphi(r,\hat{\Omega},t)[(1-\phi_v)\alpha+\phi_v\mu_{a,p}]dV$. Consequently, the linear summation of absorption efficiencies of particles and suspending fluid each weighted by their volume fraction is simply the absorption coefficient of the suspension:

$$\mu_a = \phi\mu_{a,p} + (1-\phi_v)\alpha \,. \tag{XI.3}$$

As a result, the propagation of multiply scattered light within a dense suspension can be inferred from optical properties of scattering and absorption predicted from Eqns (XI.2) and (XI.3) that are consistent with interference approximation. Here we use simultaneously determined μ_a and $\mu_s^{'}$ from frequency domain photon migration (FDPM) measurements fitted to the diffusion equation in order to justify the assumptions made in interference approximation.

XI.3. Materials and methods

Frequency domain photon migration (FDPM) provides a time-dependent measurement of light propagation within multiple scattering media. The details of FDPM instrumentation and data analysis has been provided in Chapter V. Briefly, FDPM involves launching intensity-modulated light into a suspension using fiber optics and detecting the amplitude and phase delay of the propagated "photon intensity wave" collected at a known distance away from the point of incident illumination.[145, 185] From the corresponding solution of photon diffusion equation, one can obtain the intensity attenuation and relative phase shift a function of μ_a, μ_s' and two different source-detector separation distances, r and r_o.[148]

$$\ln\left(\frac{rAC(r)}{r_0 AC(r_0)}\right) = -(r - r_0)\sqrt{\frac{3}{2}\mu_a(\mu_a + \mu_s')}\left(\sqrt{1 + \left(\frac{\omega}{c\mu_a}\right)^2} + 1\right)^{1/2} \quad \text{(XI.4)}$$

$$PS(r) - PS(r_0) = (r - r_0)\sqrt{\frac{3}{2}\mu_a(\mu_a + \mu_s')}\left(\sqrt{1 + \left(\frac{\omega}{c\mu_a}\right)^2} - 1\right)^{1/2} \quad \text{(XI.5)}$$

where ω is the modulation frequency, and c is the speed of light in the medium. The amplitude of photon density wave, AC, and the phase shift, PS, are detected upon collecting light at positions r_o and r away from the optical source using a fiber to deliver the light to a detector. The left hand sides of the above Eqns (XI.4) and (XI.5) can be experimentally determined and are proportional to the relative source-detector fiber separation distance ($r - r_o$). The proportionality ratio, can be determined by linear regression of left hand sides against ($r - r_o$), and used to determine μ_a and μ_s' with both high precision and accuracy.[10] In this contribution, we measured isotropic scattering and absorption coefficients of polystyrene lattices at volume fractions up to 0.30.

FDPM measurements of AC and PS for each sample were conducted at 6 modulation frequencies between 60 and 100 MHz at increments of 10 MHz. The source-detector fiber separation distances were chosen within the range of 5 ~ 13 mm with increments of 0.5 mm. Typically, measurements were made at 11 different source-detector fiber separation distances. The source-detector fiber separation distances were accurately controlled by a computer controlled motion system (ESP 300, Newport Cor. CA).

The preparation and characterization of polystyrene latex samples have been provided in Chapter V. Particle size distributions of Polystyrene (PS) lattices (Dow

Chemical Corp. Midland, MI) were determined using dynamic light scattering (Malvern Zetasizer 3000HS, Worcestershire, UK) for two lattices: which have mean diameters of 226 and 143 nm respectively. To remove ions and the surfactant used to stabilize the suspensions, both lattices were first dialyzed (Spectra/Pro: MWCO 6-8,000, Spectrum Laboratories Inc., Rancho Dominguez, CA) in deionized-ultra-filtered water until the conductivity of the dialyzing water was less than 6 ppm NaCl equivalents, as measured using a titration controller (Accumet Model 150, Fisher). The ionic strength was adjusted by adding a sodium chloride solution (S1240, Spectrum Chemical Mfg. Corp., Gardena, CA). The sample information for these two polystyrene lattices was summarized in Table V.4.

XI.4. Results and discussions

XI.4.1. FDPM measurement of AC and PS

Figures V.1a and V.1b illustrate the typical FDPM-measured AC and PS for latex A (at the volume fraction of 0.16 and ionic strength of 120 mM NaCl equivalent) as a function of relative source detector fiber separation distance at 6 modulation frequencies ranging from 50 to 100 MHz. The standard deviations for the AC measurement are typically about 0.1% of the measured AC amplitudes. The standard deviations for PS measurement are generally within 0.5% of the PS measurements. The error bars presented in Figure XI.1a and XI.1b are smaller than the symbols representing the data. Figure XI.1c illustrates the distance dependent logarithm of the relative AC, which corresponds to the left hand side of Eqn (XI.4). Figure XI.1b and XI.1c show that

both the logarithm of the relative AC and the relative PS vary linearly with relative source-detector fiber separation distance, agreeing with Eqns (XI.4) and (XI.5).

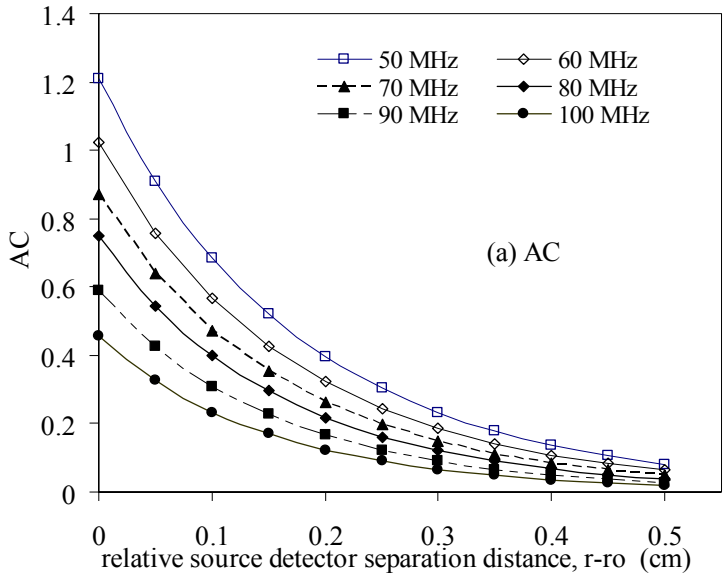

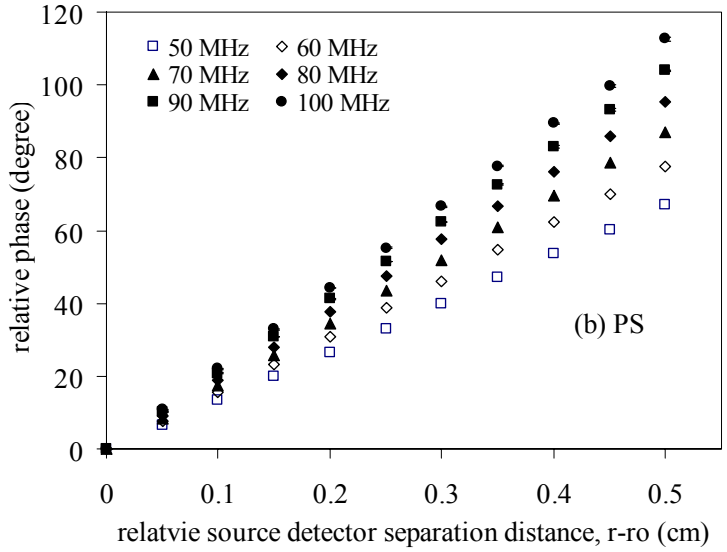

(Figure XI.1 continued on the next page)

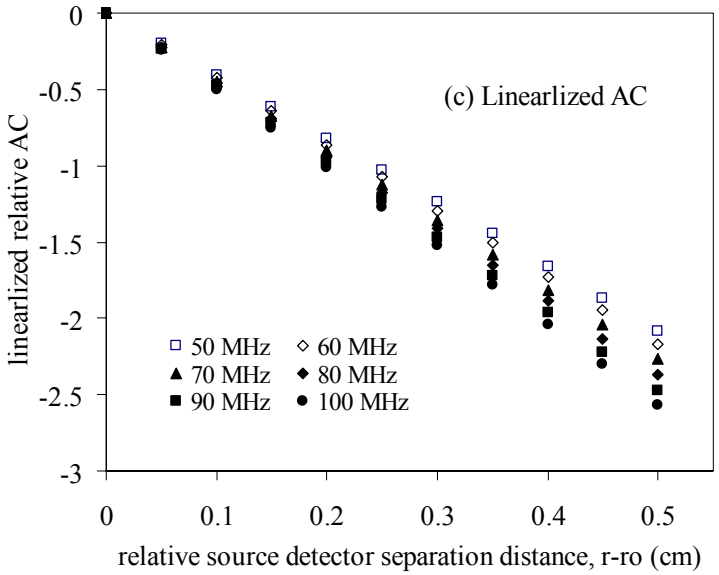

Figure XI.1 FDPM measurements of AC (a), PS (b), and logarithm of relative AC (c) for 143 nm latex (at the volume fraction of 0.16 and ionic strength of 120 mM NaCl equivalent) as a function of source-detector fiber separation distance at 6 modulation frequencies.

XI.4.2. Absorption and scattering properties of dense suspensions

Figure XI.2 shows the FDPM measured isotropic scattering coefficients versus volume fraction for the latex of mean diameter 226 nm at three wavelengths and three ionic strengths. The isotropic scattering coefficients do not vary linearly with the volume fraction, owing to microstructure resulting from the inter-particle volume exclusion and electrostatic interactions. Increasing electrostatic interaction due to the decreasing ionic strength increases the ordering of particle spatial correlation and decreases scattering power when the particle volume fraction $\phi > 0.05$.

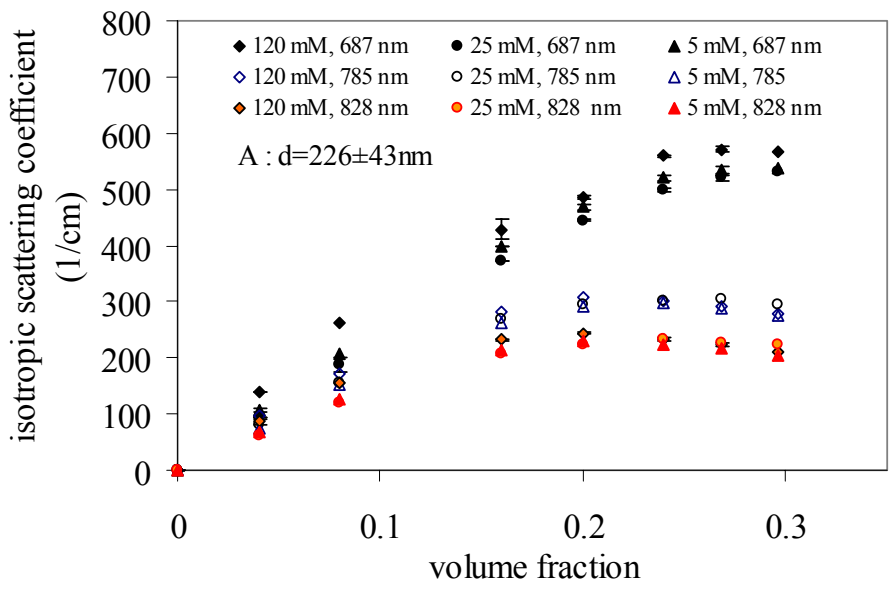

Figure XI.2 Isotropic scattering coefficients (1/cm) versus volume fraction for latex of mean diameter of 226 nm at wavelengths of 687, 785, and 828 nm and at ionic strengths of 120, 25 and 5 mM NaCl equiv.

The corresponding data for the 143 nm latex at the wavelength of 828 and 687 nm are similar and are shown in Figure XI.3. Details regarding data analysis via Percus-Yevick model with hard sphere interaction and mean spherical approximation with hard sphere Yukawa interaction have been provided in Chapter VII.

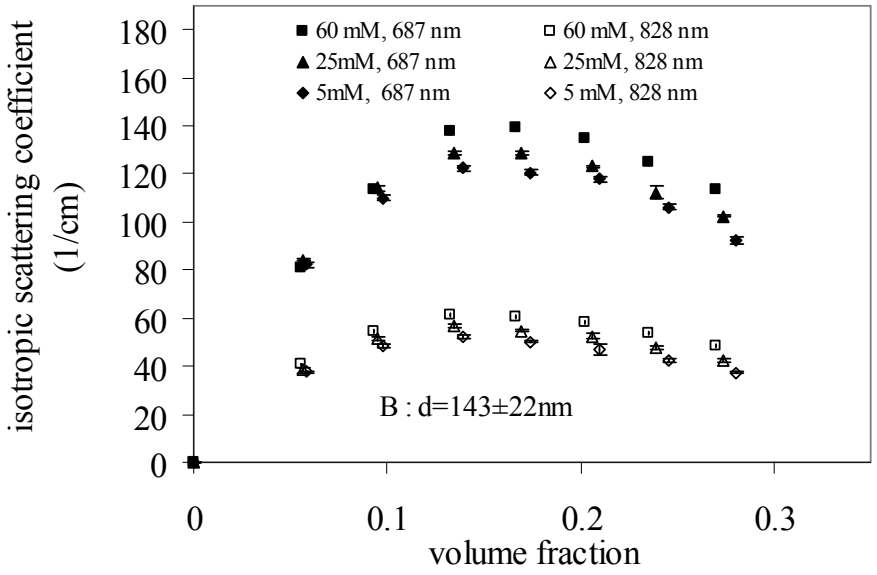

Figure XI.3 Isotropic scattering coefficients (1/cm) versus volume fraction for 143 nm latex at wavelengths of 687 and 828 nm and at ionic strengths of 120, 25 and 5 mM NaCl equiv.

Figures XI.4 and XI.5 show the absorption coefficient versus volume fraction at three wavelengths and ionic strengths for lattices of diameters 226 and 143 nm respectively. The linear relationship between absorption coefficient and the volume fraction shown in both figures affirms the interference approximation. While ionic strength impacts the microstructure and scattering power of concentrated charged suspensions as shown in Figures XI.2 and XI.3, the absorption power owing to the particles does not vary with ionic strength. In contrast to the non-linear dependence of isotropic scattering coefficient, the absorption coefficient remains linear across the range of volume fractions measured in strong support for assumptions made in the interference approximation.

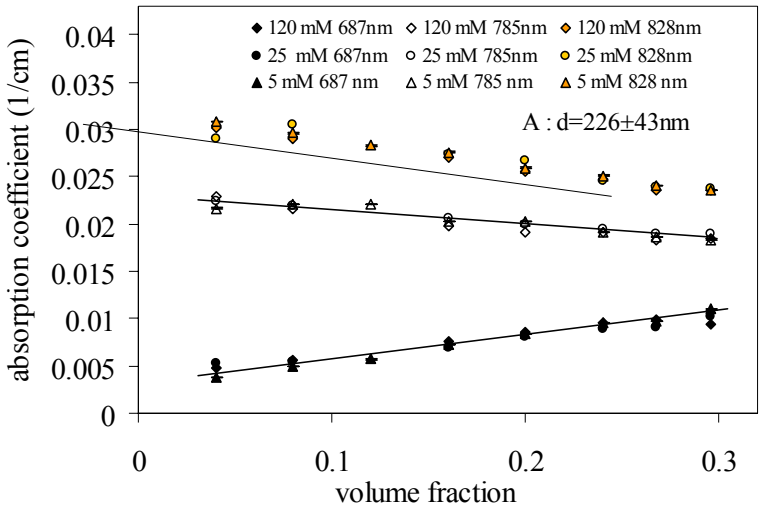

Figure XI.4 Absorption coefficients (1/cm) versus volume fraction for latex of diameter of 226 nm at wavelengths of 687 and 828 nm and at ionic strengths of 120, 25, and 5 mM NaCl equiv.

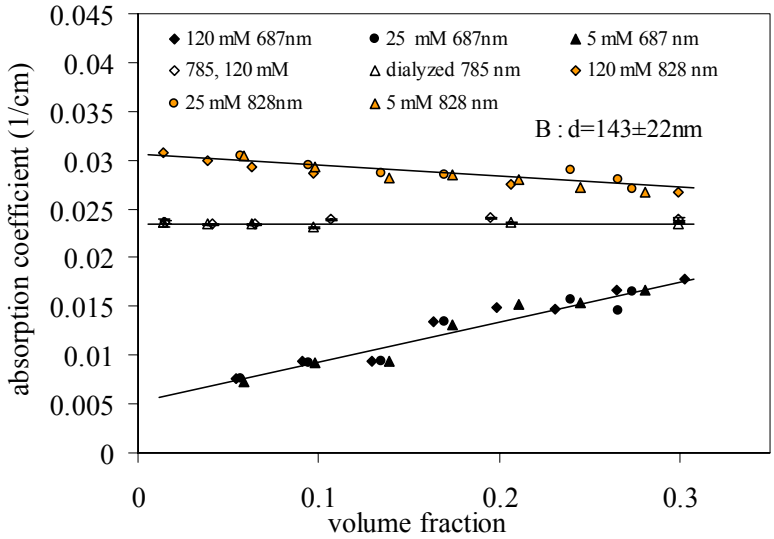

Figure XI.5 Absorption coefficients (1/cm) versus volume fraction for latex of diameter 143 nm at the wavelengths of 687, 785, and 828 nm and at ionic strengths of 120, 25, and 5 mM NaCl equiv.

XI.4.3. Suspending fluid absorption

From Eqn (XI.3), one can see that the y-intercept at $\phi_v = 0$ corresponds to the absorption efficiency of the suspending fluid, while at $\phi_v = 1$, the summation of intercept and slope represents the volume-based absorption efficiency of the latex particles. Since the polystyrene lattices were dialyzed and only trace amounts of non-absorbing NaCl were added to adjust ionic strength, the absorption coefficient of the suspending fluid can be considered to be that of water. The intercepts from least squares regression of data taken at the different ionic strengths for both lattices were employed to determine the wavelength-dependent absorption coefficient of suspending fluid. The absorption coefficients for the suspending fluid for both lattices, as well as those reported in the literature[186] are listed in the Table XI.1. The consistency between our results with the measured transmission spectrum in the literature further affirms that Eqn (XI.3) is suitable to describe the absorption of suspending fluid in suspension. When the ratio of refractive indices of the particles to the suspending fluids, *m,* is less then 1.3, then the upper applicable particle size predicted from the criteria provided by Dikand Ivanov is about $d_{\max} < \frac{\lambda}{(m-1)\pi}$.[22] Therefore, the experimental conditions in this work are well below the upper applicable limit valid for interference approximation. Furthermore, the calculation of the imaginary refractive index of suspending fluid n_l'' is straight forward by using relation $n_l'' = \lambda\alpha/4\pi$ where λ is the free space wavelength. The calculated imaginary refractive indices for the suspending fluid are also listed in Table XI.1.

Table XI.1 Absorption efficiencies of water α (1/cm) from references[186, 187] as well as from FDPM measurement of absorption coefficients for dense suspensions of lattices A&B. The imaginary refractive indices of water determined from FDPM measured absorption coefficients of lattices A&B are also provided.

Mean diameter (nm)		226	143	226	143
λ	α (cm^{-1}) Ref [186, 187]	α(cm^{-1})	α, (cm^{-1})	n_{water}" x10^7	n_{water}" x10^7
687 nm	0.005250	0.0036 ± 0.0008	0.0051 ± 0.0004	0.20 ± 0.05	0.277 ± .024
785 nm	0.025933	0.0230 ± 0.0001	0.0234 ± 0.0001	1.44 ± 0.01	1.46 ± 0.04
828 nm	0.029139	0.0315 ± 0.0004	0.0307 ± 0.0003	2.07 ± 0.03	2.02 ± .02

XI.4.4. Particle absorption

The particle absorption efficiencies for both lattices were obtained from least squares linear regression results and are listed Table XI.2 for rough comparison. While the real refractive index of a particle can be measured from light scattering or diffraction measurement, the imaginary refractive index of nanoparticles remains an elusive measurement.

Table XI.2 Volume based particle absorption efficiency and imaginary refractive indices determined from FDPM measurement of absorption coefficients for both lattices of diameter 226 nm and 143 nm respectively.

	$\mu_{a,p}$ (cm^{-1})		n_p" x10^7	
λ	226 nm latex	143 nm	226 nm	143 nm
687 nm	0.0262 + 0.0038	0.0475 ± 0.002	1.30 + 0.19	2.52 + 0.12
785 nm	0.0073 + 0.0014	0.0247 ± 0.001	0.420 + 0.08	1.53 + 0.07
828 nm	0.0043 + 0.0011	0.0175 ± 0.002	0.613 + 0.07	1.15 + 0.14

The scattering cross section and absorption cross section for a spherical particle of known diameter can be calculated from the refractive indices of particle and its surrounding at a given wavelength using Mie theory algorithm. When the particle size, real refractive index of the particles, and refractive index of suspending liquid are known, the particle absorption cross section only depends on the imaginary part of particle refraction index. The Mie scattering theory shows that for a 100 ~ 500 nm diameter particle with a real part of refractive index equivalent to 1.59 surrounded by a solvent of refractive index 1.33, the absorption efficiency is approximately a linear function of the imaginary particle refractive index when the magnitude of the imaginary particle refractive index is less then 0.1. Figure XI.6 plots particle absorption efficiency (the ratio of absorption cross section to the cross section of particle) predicted using Mie theory versus imaginary refractive index for particle of size 226 nm at three different real refractive indices. Figure XI.6 with both axes in logarithm reveals the absorption efficiency is proportional to the imaginary refractive index and the proportional constant depends on the real part of particle refractive index. Consequently, one can determine the imaginary particle refractive index from the measured absorption efficiency if the real refractive index is available.

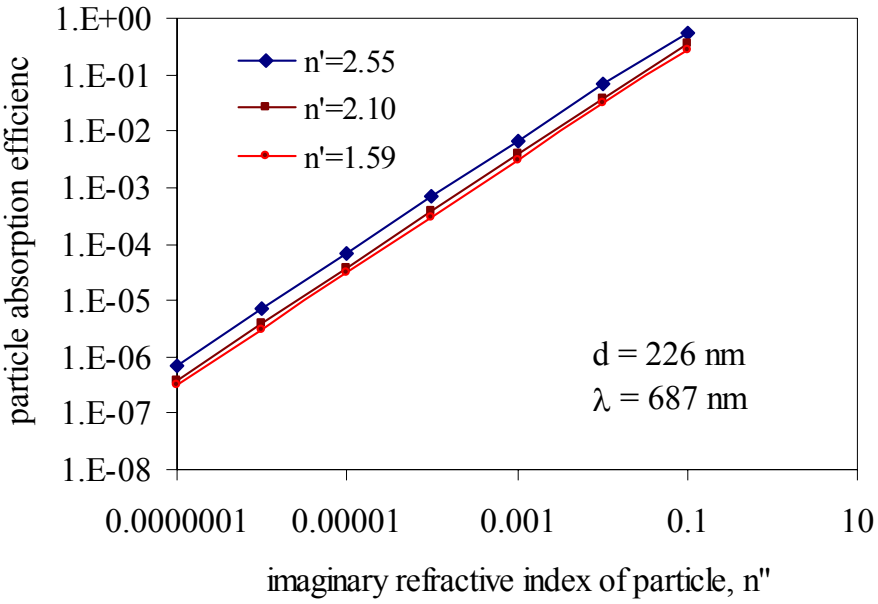

Figure XI.6 Mie theory prediction of absorption efficiency versus imaginary refractive index for particle of size 226 nm at three different real refractive indices, where the refractive index for the surrounding is selected to be 1.33.

In this work, the mean absorption cross sections for polystyrene particles were calculated by dividing volume based absorption efficiency obtained from FDPM measurements by mean particle volume. The optimization Matlab function fzero.m (MathWorks, Natick, MA) was used to estimate the imaginary particle refractive index from the measured particle absorption cross section using Mie theory as the prediction model. Assuming the refractive index for polystyrene to be 1.59,[*14] and refractive index of water as 1.33, the imaginary refractive indices for both lattices of diameters of 226 and 143 nm respectively were obtained and are listed in Table XI.2. The differences in the numerical values of the imaginary refractive indices between the two lattices may lie

with the different polymerization recipes, since different recipes are typically required to produce emulsions of differing sizes.

The light absorption efficiencies of a typical commercial bulk polystyrene (STYRON polystyrene resins) at wavelengths of 600, 700, 800, and 900 nm are 0.05, 0.05, 0.05 and 0.04 respectively, and are comparable to the results obtained from FDPM. Considering that the light absorption efficiency for bulk polystyrene at the wavelengths used herein is weak and on the same order of magnitude with water absorption at the wavelengths of 785 and 828 nm, trace amounts of light-absorbing components in the recipe may change absorption efficiencies of polystyrene nano-particles significantly. Nonetheless the absorption efficiencies for both lattices are of the same order of magnitude with those of bulk polystyrene at comparable wavelengths. We are not aware of any other method capable of distinguishing particle absorption in dense suspensions in the presence of overwhelming scattering.

Finally, it is noteworthy that the absorption efficiency of particles is invariant to the microstructure of suspension that reduces scattering power (Figures XI.4 and XI.5). A simulation using Mie theory shows that the volume-based absorption efficiency increases significantly with particle size. Figure XI.7 shows the relative volume based absorption efficiency increases with the particle diameter, where the particle of diameter 50 nm is chosen as the reference with real refractive index of particle chosen to be 1.59 (representing the value of polystyrene) and solvent refractive index selected to be 1.33 (representing the value of water).

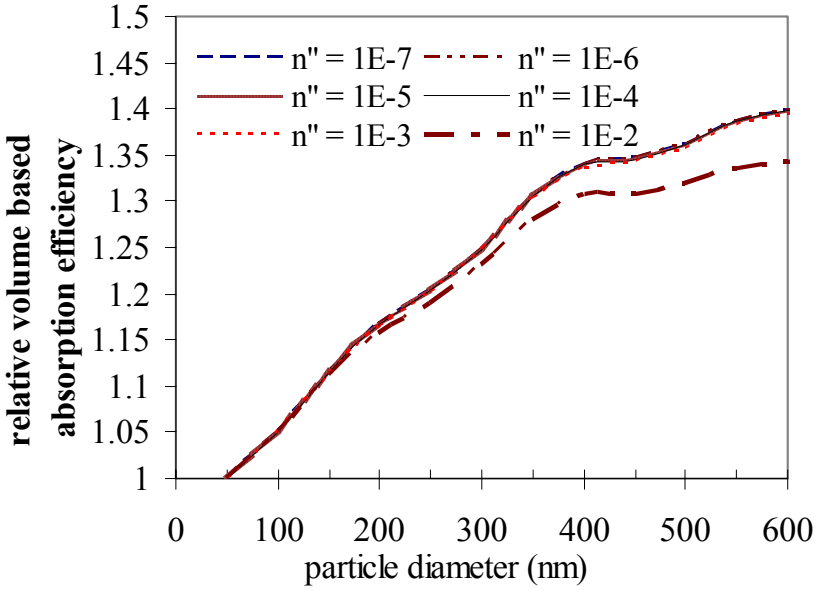

Figure XI.7 Relative volume based particle light absorption efficiency (relative to the particle of diameter 50 nm) as a function of particle diameter predicted from the Mie theory for particles of real refractive index of 1.59 surrounded by solvent with refractive index of 1.33.

Figure XI.7 the relative volume based absorption efficiency varies in a similar manner and follows a "Master" curve when the particle imaginary refractive index falls bellow 10^{-3}. The sensitivity of volume based absorption efficiency to particle size shown in Figure XI.7 may be sufficient for monitoring particle size with FDPM absorption when the particle size is less than 500 nm. Without the consideration of particle interactions that govern microstructure, the measured particle absorption efficiencies may be valuable for obtaining particle size and volume fraction information.

XI.5. Summary

In summary, the absorption coefficients of dense suspensions are a linear function of particle volume fraction and, consistent with the interference approximation, do not depend on the microstructure as does the scattering coefficient. With FDPM measurements of absorption and scattering coefficients, the light absorption efficiencies of particle and suspending fluid can be obtained simultaneously, and measured absorption efficiencies can be used to obtain imaginary refractive index of suspending particles.

This chapter demonstrated the capability of FDPM of measuring particle absorption efficiencies. The next chapter will illustrate an application of determining pigment absorption efficiency using FDPM.

CHAPTER XII

CHARACTERIZATION OF PIGMENTS ABSORPTION EFFICIENCIES

This chapter will display a new application of using FDPM to characterize pigment and paint particles. In Chapter VI, we demonstrated that the absorption coefficient of a colloidal suspension varies linearly with its particle concentration. Upon measuring the absorption coefficient as a function of volume fraction using FDPM, we have obtained the absorption efficiencies of the both suspended polystyrene particles and suspending fluids as shown in Chapter VI. Polystyrene particles weakly absorb light in the visible and near infrared region, and the light absorption efficiency of polystyrene particles can be determined by the method presented in the previous chapter. However, pigment particles strongly absorb light and light propagation in dense pigment dispersions may not be modeled as a diffusion process as introduced in Chapter III. This chapter presents a way of measuring pigment absorption efficiencies through diluting trace amounts of pigment particles in a polystyrene dispersion and subsequently measuring the absorption coefficient of the polystyrene dispersions.

This chapter is adopted with permission from [Yingqing Huang, Eva, M. Sevick-Muraca, "Characterization of pigment absorption efficiency using frequency domain photon migration," Anal. Chem. **75**, 6958-6962, (2003).

XII.1. Introduction

Gloss and color are important product attributes in the textile and automobile industries and are key performance properties for printing ink, cosmetics, hair dyes, and many other products. Pigments, which refer to insoluble colorants, determine the color of paints and numerous plastic products through their optical properties of scattering and absorption. Light scattered outwardly from the particle changes the direction of light propagation, whereas light scattered inward into the particle can result in light absorption. The color of coatings is mainly determined by the wavelength-dependent light absorption efficiency of pigments, while the gloss of coating is typically related to scattering properties. Color matching, which guarantees agreement of color feature with the designed pattern of products and ensures uniformity among products in massive production, requires accurate measurements of absorption and scattering properties of pigments.

An understanding of light interaction with pigment particles is paramount in the coatings industry and is conventionally described through the phenomenological Kubelka-Munk (K-M) theory.[93] In K-M theory, the scattering coefficient, $S(\lambda)$, and absorption coefficient, $K(\lambda)$, which are used to describe optical properties of coating layers, reflect the percentage loss of the forwardly propagated radiation per unit distance due to media scattering and absorption, respectively. Since K-M theory treats dispersions as continuous uniform media, $K(\lambda)$ and $S(\lambda)$ cannot be related through first principles to the physical properties of pigment particles and their dispersing vehicles. The “dispersion vehicle” is a widely accepted nomenclature in pigments and paints

industry. It refers to a dilution medium, usually a polymer dispersion, in which a suitable amount of pigment and other additives are added and homogenized in formulating paints and pigments products. The formulated dispersion containing pigments and other additives is then applied to substrate to form a coating layer for testing pigments. Since the dilution dispersion is the medium that delivers pigments to a coating application, it is called the "vehicle." In order to determine the absorption and scattering properties from pigments using conventional K-M theory, one needs to first disperse pigments in suitable dispersing vehicles, and then coat the dispersions on standard substrates. The value of $K(\lambda)$ and $S(\lambda)$ can then be evaluated from measured reflectance with suitable empirical correction[188, 189] and measurements repeated as a function of pigment concentration enable distinction of the pigment scattering and absorption from that arising from the dispersing vehicle. While the measurements of diffuse reflectance can be easily reproduced within the same laboratory, one cannot guarantee reproducibility from one laboratory to another.[94] Consequently, comparison of optical properties of pigments between laboratories usually requires a third commonly-accepted pigment as reference.

Previous work has been accomplished to obtain pigment physical properties though measured phenomenological scattering and absorption data in order to improve efficiencies in paints formulation. Billmeyer *et al.* reported an approach to estimate the complex refractive index of pigment.[190] They measured angle-dependent (14°-166°) scattering intensity of dilute pigment dispersions in order to obtain scattering phase function $P(\theta)$, which when fitted against Mie theory prediction provided the complex

refractive index of pigment particles. The time consuming method requires extrapolation of scattering intensity in forward and backward directions in dilute pigment suspensions (10^{-4}% by volume). Vargas and Niklasson[191] reported a method based on four-flux theory in order to extract complex refractive index and mass density of pigments from reflectance and transmittance measurements of pigment coatings layers. Unfortunately, since they neglected interference effects owing to correlated particle positions that impact scattering efficiency, their approach may result in a mis-prediction of particle absorption efficiency.

Frequency domain photon migration (FDPM) techniques enable accurate determination of the optical properties of a multiple scattering medium. The details of FDPM instrumentation and data analysis have been presented in Chapter V. Briefly, FDPM involves launching intensity modulated light through a fiber optic into a multiply scattering medium. The amplitude of the "photon density wave" will attenuate, and will be phase-shifted as the wave travels within the medium away from its source. Another fiber optic is used to collect the photon density wave and direct it to a detector. In this study, the distance of collecting fiber from the source fiber was adjusted using a computer controller motion device (ESP 300 Motion Controller, NewPort, CA). Upon detecting the phase shift and amplitude attenuation as a function of distance away from the source and upon fitting the measured data to the diffusion equation describing the propagation of multiply scattered light, accurate measurement of the isotropic scattering coefficient, μ_s', and absorption coefficient, μ_a, can be simultaneously obtained.

With the assumption of isotropic scatterers, the first principle properties, μ_s' and μ_a have been related to the corresponding phenomenological optical properties $K(\lambda)$ and $S(\lambda)$ by:[192, 193]

$$S = \mu_a / 2 \tag{XII.1}$$

$$K / S = (8/3) \cdot (\mu_a / \mu_s^{'}) \tag{XII.2}$$

The total absorption of a scattering medium is attributable to both the particles as well as the suspending fluid. Upon using interference approximation, it is derived in the Chapter IV and verified in the Chapter VI that the absorption efficiency of a suspension, μ_a (1/cm) varies linearly with its particle volume fraction. ϕ_v:

$$\mu_a = \phi_v \cdot \mu_{a,p} + (1 - \phi_v) \cdot \alpha \tag{XII.3}$$

Chapter VI demonstrates that by measuring μ_a as a function of particle concentration, the absorption efficiencies of both particles and suspending fluid can be obtained via least squares linear regression of measured absorption coefficients against Eqn (XI.3).

The diffusion approximation (introduced in Chapter IV) presumes that the absorption coefficient is much smaller than the scattering coefficient ($\mu_s^{'} > 100\ \mu_a$). For the pigment dispersions with strong absorption, diffusion approximation fails and FDPM cannot be directly applied. However, one can dilute a suitable amount of pigments into a multiple scattering medium with minimal absorption as vehicle to ensure the validity of the diffusion approximation. The pigment absorption efficiency can be evaluated from their contribution to the overall absorptions of the coating layer. For strongly absorbing

pigments, only a few PPM in weight of pigment concentration is enough to change absorption coefficient for accurate FDPM measurement.

In this work, we demonstrate measurement of particle absorption efficiencies of three different pigments dispersed in multiply scattered polystyrene latex using FDPM measurement of absorption. In the following section, the materials and investigation method are briefly induced before the discussion of the experimental results.

XII.2. Material and methods

XII.2.1. Sample preparation

Three different water-dispersed pigments: Phthalo Green (CI# 74260), AAA Diarylide Yellow (CI# 21090) and Naphthol Red (CI# 12315), were obtained from the Riotech Corporation (Reading, PA). The pigments concentrations were used as received [approximately 45% (in weight)] and diluted in water. Polystyrene latex of size 226 ± 43 nm (measured by Zetasizer 3000 HS, Malvern Instrument, UK) was obtained from Dow Chemical (Midland, IL) and used as a dispersing vehicle for the pigments. To remove surfactant and salt, the polystyrene latex was dialyzed (Spectra/Pro: MWCO 6-8,000, Spectrum Laboratories Inc., Rancho Dominguez, CA) using ultrafilted-deionized water until the conductivity of equivalent dialyzing water was less than 6 PPM NaCl equivalent measured using a titration controller (Accumet Model 150, Fisher). The dialyzed polystyrene latex was then conditioned to the NaCl concentration of 120 mM by adding 2 M NaCl solution (S1240, Spectrum Chemical Mfg. Corp., Gardena, CA). The conditioned polystyrene latex was then diluted using 120 mM NaCl solution to the

desired particle volume fraction. The particle volume fraction was measured using the evaporation method, which simply involved weighting polystyrene sample using a 1/10,000 g resolution balance (Denver Instrument M-220D, Fisher) before and after drying in an oven at 90°C for 8 hours.

Seven wavelengths were used for FDPM measurements of absorption and isotropic scattering coefficients of each dispersion. An Argon-Krypton gas discharge laser (643 R-AR-A01, Melles-Griot Laser Group, Carlsbad, CA) provided light at wavelengths of 488, 514, and 568 nm, and laser diodes (Thorlabs, CA) provided light at the wavelengths of 650, 687, 785, 828 nm. At each of the wavelengths at 650 nm or lower, a corresponding band pass filter, which only allows the light within a narrow region (± 3-10 nm) about the light source to pass through, was positioned at the photon detector to remove potential fluorescence from the polystyrene particles.

For each dispersion, FDPM measurements were conducted 3 times at the modulation frequencies of 70, 80, and 90 MHz. The FDPM measurements of relative phase and amplitude at each of these 3 frequencies were then averaged and fitted to the diffusion equation to obtain the final isotropic scattering and absorption coefficients.

The isotropic scattering and absorption coefficients were measured as a function of pigment concentrations, while maintaining polystyrene PVC constant. Aliquot dispersions of pigments with concentrations of about 1% by weight were first prepared by diluting commercial pigment dispersions in 120 mM NaCl solution. After each addition of pigment aliquot to the polystyrene vehicle, the dispersion was homogenized using a sonic stirrer (Dismembrator, Model 60, Fisher) for approximately 10 minutes at

the power of 4 W. One hundred ml of the polystyrene dispersion of 5% by volume were used as the vehicle for assessment of pigment absorption by FDPM measurement. FDPM measurements were conducted 30 minutes after sonication to ensure equilibrium conditions.

XII.2.2. Experimental design

The isotropic scattering and absorption coefficients were measured as functions of pigment concentrations, while maintaining polystyrene volume fraction constant. Aliquot dispersions of pigments with concentrations of about 1% by weight were first prepared by diluting commercial pigment dispersions in 120 mM NaCl solution. After each addition of pigment aliquot to the polystyrene vehicle, the dispersion was homogenized using a sonic stirrer (Dismembrator, Model 60, Fisher) for approximately 10 minutes at the power of 4 W. One hundred ml of the polystyrene dispersion of 5% by volume were used as the vehicle for assessment of pigments absorption by FDPM measurement. FDPM measurements were conducted 30 minutes after to ensure complete dispersion of pigments in vehicle.

XII.3. Results and discussions

XII.3.1. Determination of pigment absorption efficiency

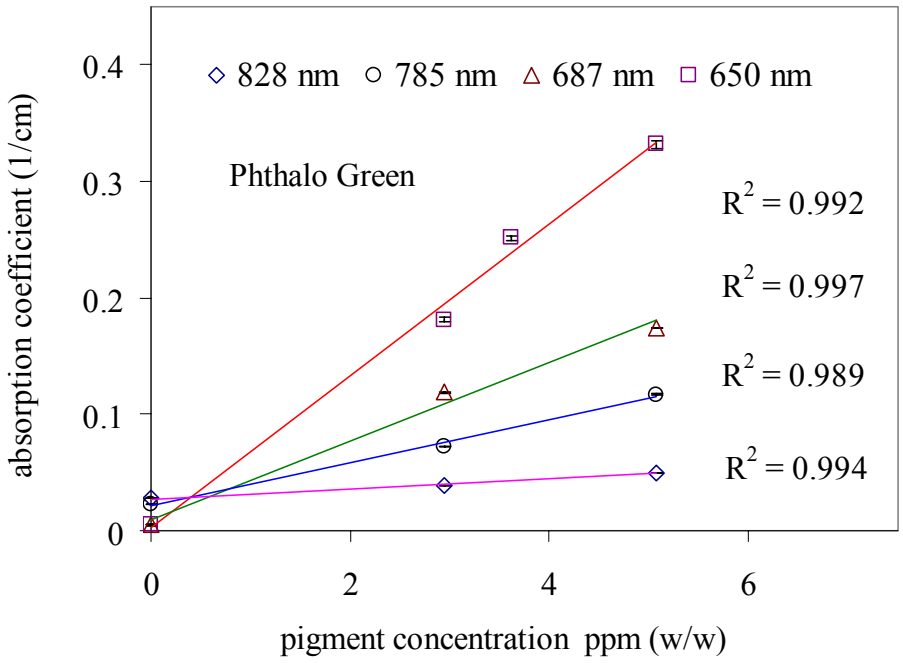

Figure XII.1 Absorption coefficient (cm^{-1}) versus phthalo green pigment concentration (ppm, w/w) in the polystyrene latex with the 5% PVC at the wavelengths of 828, 785, 687, and 650 nm. (Symbols denote FDPM measurement; lines denote least squares regression).

The symbols in Figure XII.1 indicate the measured absorption coefficients plotted as a function of pigment concentration in the polystyrene latex as measured at four wavelengths, 650, 687, 785, and 828 nm. The unit for the pigments concentration is weight-based part per million (ppm). The measured absorption coefficient increases linearly with the concentration of pigments as indicated by the least squares regression lines. Since the total amount of pigment aliquot (<0.5 ml) added to the dispersion vehicle was much smaller than the total amount of the vehicle (approximately 100 ml),

the change in the total volume could be neglected. Therefore, Eqn. (XII.3) describing the measured absorption efficiencies for the dispersions can be converted to reflect weight-based absorption efficiencies of pigment particles:

$$\mu_a = \mu_{a,PSL} + \varepsilon_{pigments} \cdot \mu_{a,pigments}^{*} \qquad \text{(XII.4)}$$

where $\mu_{a,PSL}$, $\mu_{a,pigments}^{*}$, and $\varepsilon_{pigments}$, are the absorption coefficient of background polystyrene vehicle, the weight-based absorption efficiencies of pigment particle, and the weight concentration of pigments in dispersions, respectively. From Eqn. (XII.4), one can see that the regressed intercept in the Figure XII.1 represents the absorption coefficient of the dispersing polystyrene latex, and the slope represents the weight-based absorption efficiencies of pigments, $\mu_{a,pigments}^{*}$ (1/cm ppm), which is defined as the contribution to the absorption coefficient (1/cm) owing to a unit increase of the pigment concentration (in weight-based ppm). We note that only trace amount of pigment was added here, and the error in measuring the amount of added pigment may determine the accuracy of the final measured pigment absorption efficiency. The corresponding absorption data at other wavelengths for the yellow and red pigments are alike and are not presented for brevity.

XII.3.2. Pigment absorption at different polystyrene volume fractions

To examine the potential impact of the volume fraction of dispersion vehicle on measured absorption efficiencies of the pigments, we also measured absorption coefficient as a function of pigment concentration at varying volume fraction of polystyrene vehicles. We prepared dispersions at 5 different polystyrene volume

fractions (with range from 0.064 to 0.318), and measured the absorption coefficients of these pigment-free dispersions. We then added the same amount of red pigment aliquot (60 μL) to the each dispersion and conducted FDPM measurement of isotropic scattering and absorption coefficients after the pigments were well dispersed. The above process was repeated twice using the red pigment aliquot, and then using the green pigments as aliquot for another three sequential additions. Here only one wavelength of 568 nm is presented for illustration of the results. The measured absorption coefficients at varying polystyrene volume fractions as a function of pigment concentration at 568 nm are shown in Figure XII.2.

Figure XII.2a shows that the measured absorption coefficients increase linearly as a function of red pigment concentration added step-wise at 5 different PVCs of polystyrene latex vehicle. The measured absorption efficiencies also increase with PVC owing to particle absorption associated with the particulate dispersing vehicles. The regressed slopes in Figure XII.2a represent the weight based absorption efficiencies for the red pigments and are presented in Table XII.1. Figure XII.2b shows that the absorption coefficients increase with the sequential addition of green pigment in the dispersions, which already contains 1.88 ppm of red pigment. The symbols on the y-axis at zero concentration of *green* pigment in Figure XII.2b correspond to the dispersions with the greatest concentration of *red* pigment added as shown in Figure XII.2a.

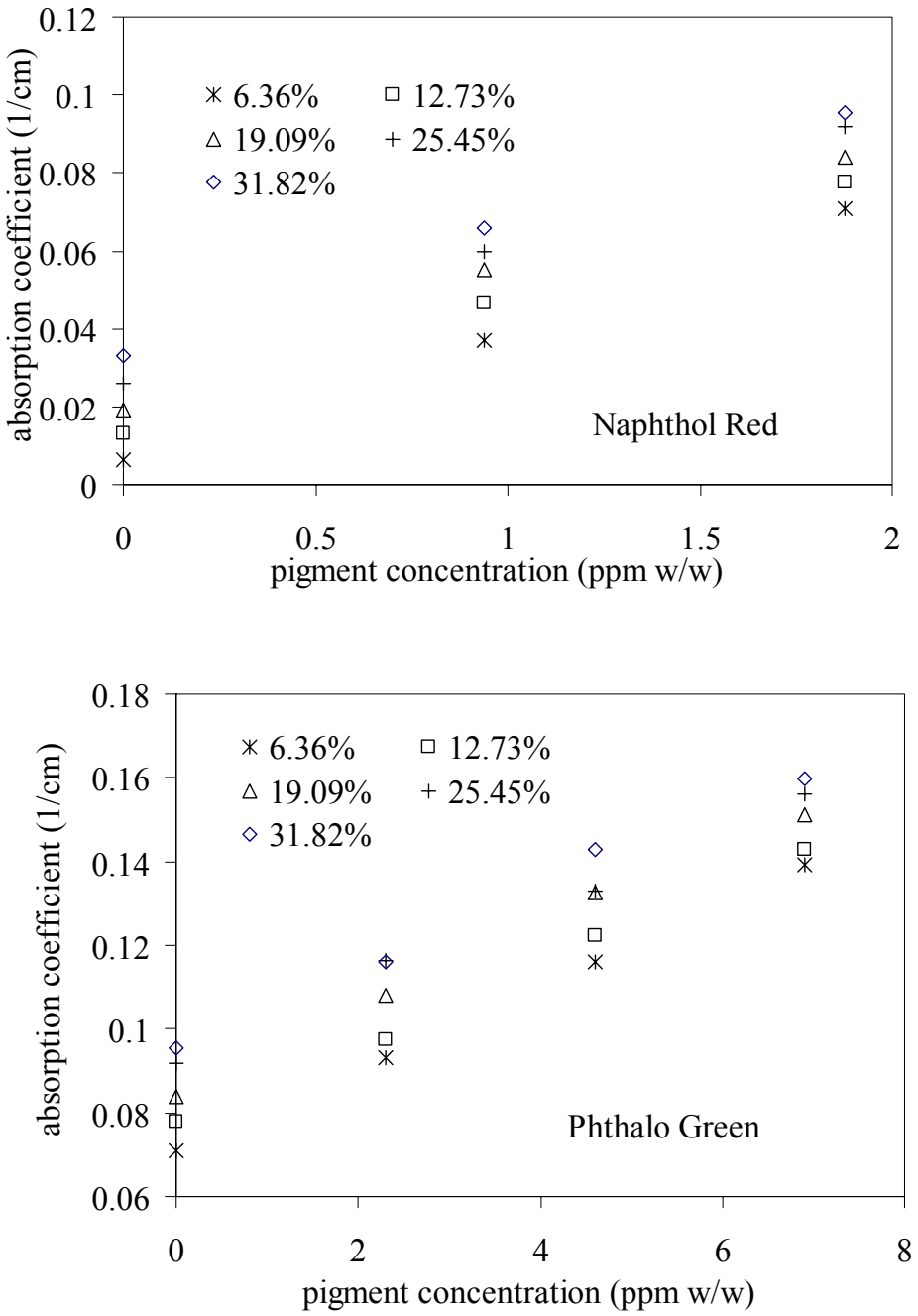

Figure XII.2 Absorption coefficient (cm^{-1}) versus (a) naphthol red (b) phthalo green pigment concentration (ppm, w/w) at five different PVCs of polystyrene lattices at the wavelength of 568 nm. (Symbols denote FDPM measurements).

Both Figures XII.2a and XII.2b show a linear relationship between the absorption coefficient and pigment concentration, confirming Eqn. (XII.4). The absorption

efficiencies for the green pigment were obtained from regression of the data in Figure XII.2b and are shown in Table XII.1.

Table XII.1 Weight based absorption efficiencies of red and green pigments measured at varying volume fractions of polystyrene vehicle at the wavelength of 568 nm

Volume fraction	0.064	0.127	0.191	0.255	0.318
Red (1/cm ppm)	0.0344	0.0344	0.0344	0.0351	0.0348
Green(1/cm ppm)	0.00986	0.00957	0.00984	0.00908	0.00954

A statistical analysis indicates that there is no significant difference at the confidence level of 90% between absorption efficiencies for the pigment particles measured at varying volume fractions. The constant pigment absorption efficiencies for both green and red pigments at varying volume fractions of dispersion vehicle suggests that the absorption efficiencies of pigments do not depend on the particle volume concentrations of dispersion vehicles. The absorption efficiencies shown in Figure XII.2b increase linearly with the concentration of green pigment, indicating that the green and red pigments absorb light independently of each other. Figure XII.2 validates the method for measuring the absorption efficiencies of pigment particles. The error in determining the added pigment amount may contribute the greatest error in the final measured pigment absorption efficiency.

Since the total volume of the pigment aliquot, (in which pigment concentration is only a few percent in weight) added to the dispersion vehicles were less than 0.5% of

that for a vehicle, they are negligible in comparison to the volume of dispersion vehicles. Therefore, the contributions of the pigment scattering should be negligible in comparison to the overall scattering dominated by the particles of dispersion vehicle. FDPM measured scattering coefficients do not change appreciably with the addition of pigment aliquots at all of 5 vehicle particle volume fraction, and only increase with the volume fraction of dispersing vehicle within the range from 200 to 900 1/cm. The data for the scattering is presented in the following subsection.

XII.3.3. Isotropic scattering coefficients

While Figures XII.2 showed the absorption coefficients at the sequential addition of pigments at different volume fraction of polystyrene suspension vehicle, the corresponding isotropic scattering coefficients measured using FDPM are shown in Table XII.2.

The influence of particle size, particle volume fraction in dense suspensions,[9, 11, 13] and particle interactions owing to depletion force[6] and electrostatic forces (Chapters VII and VIII) has been reported extensively. Herein, as we add a small volume of pigment aliquot, the absorption coefficients changed dramatically, but (assuming no change in particle interaction, particle size, and particle volume fraction) there should be little or no change on the FDPM measured scattering coefficients.

Indeed, the complimentary scattering data associated with added pigments at varying volume fraction of dispersing vehicles as shown in Figure XII.2, tend to support this assumption.

Table XII.2 lists the FDPM measurements of isotropic scattering coefficient measured at 568 nm for the polystyrene dispersions (226±43 nm diameter) at varying weight based pigment concentrations of green and red pigments.

Table XII.2 FDPM measurements of isotropic scattering coefficients (cm^{-1})and standard deviations (mean ± standard deviation 1/cm) for polystyrene dispersion (226 ± 43 nm) vehicles at 5 PVC's and at varying weight-based concentrations for green and red pigments.

Red Pigment (ppm)		0	0.94	1.88	1.88	1.88	1.88
Green Pigment (ppm)		0	0	0	2.30	4.61	6.91
Volume Fraction	0.064	252±3	259±18	245±9	259±1	254±2	255±5
	0.127	466±3	457±12	454±2	444±4	464±5	464±3
	0.191	625±5	604±4	614±18	598±21	607±4	622±5
	0.255	774±5	708±11	718±6	688±16	716±7	755±5
	0.318	864±6	805±3	798±14	851±28	830±4	864±7

At the lower volume fractions of 0.064 and 0.127, the isotropic scattering coefficient at 568 nm does not change significantly as red and green pigments were added. An F-test[194] of variances in the measured scattering coefficients rejects that there are significant differences among measured isotropic scattering coefficients with added concentrations of red and green pigments at the confidence interval of 0.10. This is contrast to the linear increase in absorption coefficient with increasing pigment concentration shown in Figure XII.2. On the other hand, at higher volume fractions of

0.151 and 0.255, isotropic scattering coefficients do slightly change as one might expect owing to the sensitivity of altered ensemble structure which could take place with the adding of dissimilar particle suspension on a dense suspension (as shown in Chapters VII and VIII).

Figures XII.3 through XII.5 confirm that while absorption coefficients measured at 687, 785, and 828 nm depend upon the concentration and color of pigment added (as shown in Figure XII.2), the isotropic scattering coefficients remains relatively constant in the 0.05 volume fraction PVC dispersion vehicles.

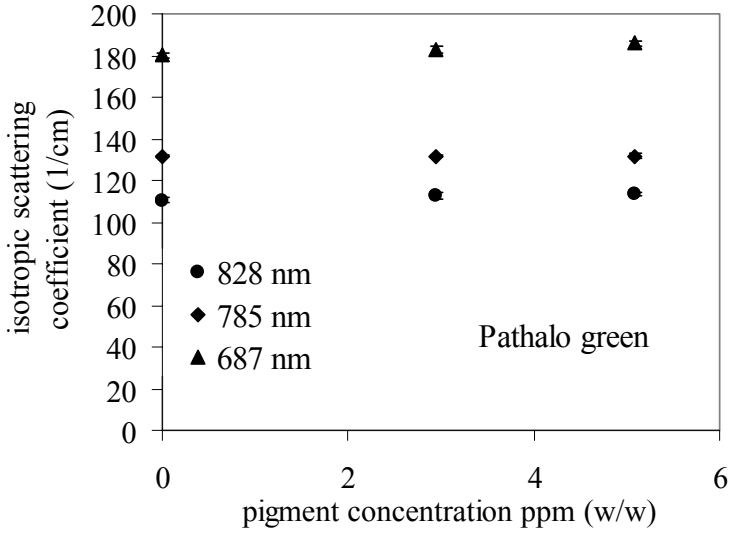

Figure XII.3 Isotropic scattering coefficient for polystyrene dispersion vehicle (226±43 nm) of 5% PVC as a function of weight based ppm concentration for Phthalo green pigment.

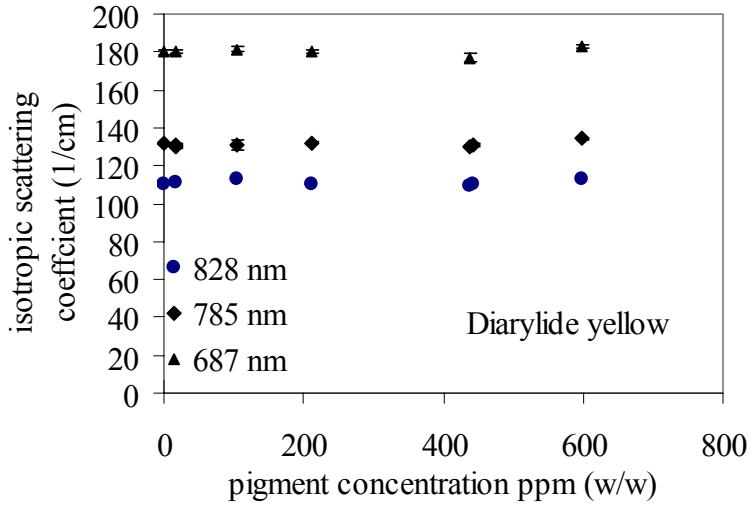

Figure XII.4 Isotropic scattering coefficient for polystyrene dispersion vehicle (226±43 nm) of 5% PVC as a function of weight based ppm concentration for diarylide yellow pigment.

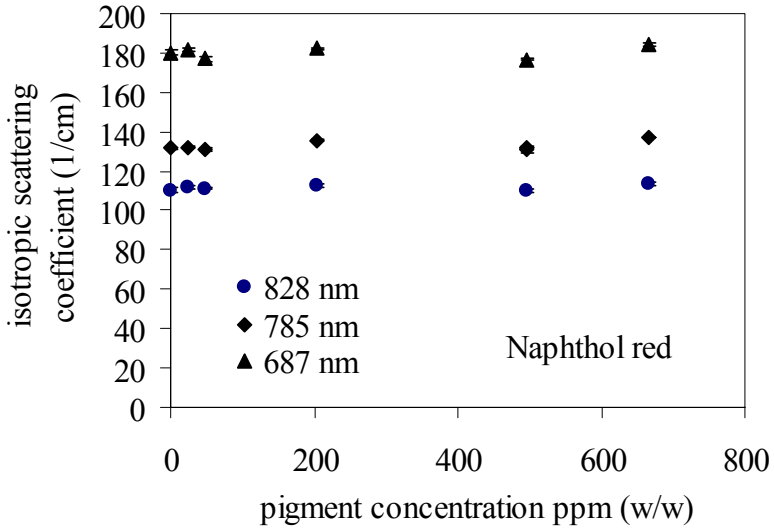

Figure XII.5 Isotropic scattering coefficient for polystyrene dispersion vehicle (226±43 nm) of 5% PVC as a function of weight based ppm concentration for naphthol red pigment.

A stringent statistic analysis of variance (ANOVA) was conducted to determine the statistical likeness of the isotropic scattering coefficients shown in Figures XII.3 through XII.5 at each wavelength. An F-test of variances in the measured scattering coefficients rejects the hypothesis that there are significant changes in scattering with added diarylide yellow. However, there are trends of slight increases in isotropic scattering coefficient for the other two colors of pigments, which disable similar conclusions of independent scattering change for green and red pigments.

The addition of dispersions of pigment aliquot to the dispersions vehicle may indeed slightly change the scattering coefficients by contributing to the overall scattering efficiency and alternating microstructure of the dispersion vehicle. Alternatively and more likely, the slight changes in scattering may also be due to the error associated with assuming no change in total particle volume (whether in the size or total number) with the addition of pigment.

Table XII.3 lists the values of isotropic scattering for data shown in Figures XII.3 through XII.5. Clearly, the scattering coefficient changes are with the expected 1% error and confirm that the FDPM measurements independent of absorption and scattering.

Table XII.3 FDPM measurements of isotropic scattering coefficients (cm^{-1}) and standard deviations (mean ± standard deviation 1/cm) for polystyrene dispersion (226 ± 43 nm) at varying weight-based concentrations for the dyes as shown in Figures XII.3 through XII.5. The mean of the isotropic scattering coefficients is also provided across samples of varying pigment concentrations.

Green Pigment (ppm)	0.0	5.1	2.9				Mean
828 nm	110±2	114±1	113±2				112±2
785 nm	132±1	132±2	132±1				131.7
687 nm	180±2	186±1	183±1				183±3

Yellow Pigment (ppm)	0.0	15.9	105.4	211.9	438.4	597.6	Mean
828 nm	111±2	111±1	113±1	110±1	110±1	113±1	111±2
785 nm	132±1	131±1	131±3	132±1	130±1	134±1	132±2
687 nm	180±2	180±1	182±1	180±1	177±2	183±1	180±2

Red Pigment (ppm)	0.0	24.2	47.6	495.4	204.5	666.1	Mean
828 nm	111±2	112±1	111±1	110±1	112±1	114±1	112±2
785 nm	132±1	132±1	131±1	132±1	136±1	137±1	133±3
687 nm	180±2	181±1	177±1	177±1	182±1	184±1	180±3

XII.3.4. Absorption spectra of pigments

Figure XII.6a shows the absorption spectra of three pigments at seven wavelengths determined from FDPM measurement. The error bar indicates the standard deviation of the FDPM measurement at the three modulation frequencies.

The measured absorption efficiencies span five orders of magnitudes, if plotted using a logarithm scale as shown in Figure XII.6b. Currently, we are not aware of any other methods capable of measuring particle absorption efficiencies comparable to FDPM and unable to provide comparison for verification of FDPM results. Nonetheless, we can qualitatively examine FDPM measured spectrum based on complementary color principles. For example, we know that green and red colors are a pair of complementary colors, and yellow and violet colors are another pair of complementary colors. The measured spectrum for red pigment has the maximum absorption efficiency at the wavelength of about 500 nm, which is in the green region; the measured spectrum for green pigments has the maximum absorption efficiency at the wavelength of 650 nm in red region. Also, the measured spectrum for yellow pigment has the minimum absorption from green through red region, but has the trend of increasing absorption while the wavelength shifts from blue toward violet. These observations are consistent with complementary color principles enabling us to state that on a qualitative basis, FDPM measured pigments absorption spectrum reflects the physics of the appearance of color. The supporting material provides the scattering data of measurements at 687, 785, and 828 nm.

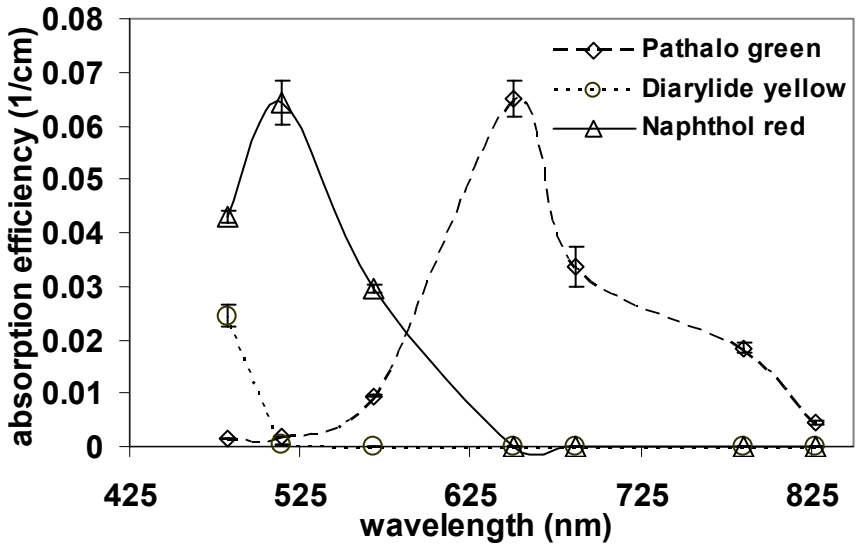

(a)

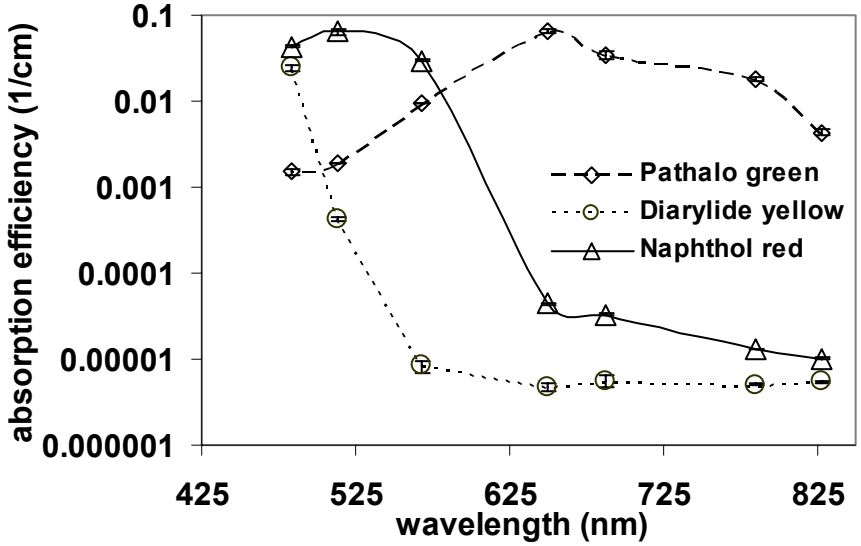

(b)

Figure XII.6 Absorption efficiency (cm^{-1}) of pigments shown in (a) linear and (b) logarithmic scales as a function of wavelength (diamond, phthalo green; circle, diarylide yellow; triangle, naphthol red).

The FDPM measured pigment absorption efficiency may also be valuable in obtaining complex refractive index of pigments. It has been introduced in Chapter II that the light absorption and scattering cross section of spherical pigment particles can be theoretically calculated from particle size, complex refractive index of the pigment particles and suspending fluid using the Mie theory:

$$C_{abs} = f_1(n_p', n_p'', n_l, \lambda, \sigma) \tag{XII.5}$$

$$C_{sca} = f_2(n_p', n_p'', n_l, \lambda, \sigma) \tag{XII.6}$$

where, n_p' and n_p'' are the real and imaginary parts of complex particle refractive index; n_l is the refractive index of suspending fluid; λ is the wavelength in free space; and σ is the particle diameter. Alternatively, the particle size and the refractive index of suspending fluid can be independently characterized, and the complex refractive indices of a particle can be determined from measured absorption and scattering cross section of particles, C_{abs} and C_{sca} by inverting Mie theory of Eqns (XII.5) and (XII.6) numerically.

$$n_p' = f_1^{-1}(C_{abs}, C_{sca}, n_l, \lambda, \sigma) \tag{XII.7}$$

$$n_p'' = f_2^{-1}(C_{abs}, C_{sca}, n_l, \lambda, \sigma) \tag{XII.8}$$

Chapter VI has demonstrated the possibility of determining imaginary refractive index of nanoparticles from FDPM measured absorption cross section, C_{abs}.

Upon assuming independent scattering (introduced in Chapter II), the scattering cross section can be related to the measured isotropic scattering coefficient by:

$$C_{sca} = \frac{\mu_s'}{\rho(1 - g(n_p, n_l))} \tag{XII.9}$$

where g is the scattering isotropy and can be calculated from Mie theory. For suspensions such as titanium dioxide and polystyrene with minimal absorption, where diffusion approximation applies, absorption coefficients measured by FDPM can be used to determine absorption cross section of particle C_{abs} using the method introduced in Chapter XI. The complex refractive indices of these weak absorbing particles such as titanium dioxide and polystyrene can be determined from solving coupled Eqns (XII.7) through (XII.9).

For concentrated strong absorbing pigments, the absorption cross section can be determined through diluting the pigments into suitable vehicles and subsequently measuring absorption coefficients of vehicles as demonstrated in this chapter. The scattering cross section, C_{sca} can be inferred by subtracting absorption efficiency, C_{abs}, from the total extinction efficiency, C_{ext}, which can be routinely measured from standard turbidity measurement. Therefore, the complex refractive index of strong absorbing pigments may also be determined by using the inverted Mie theory of Eqns (XII.7) and (XII.8) from FDPM measured absorption, associated with the total extinction determined by turbidity measurement.

XII.4. Conclusions

The absorption coefficients of dense dispersions vary linearly with the concentration of pigments in dispersions. Using FDPM, we have successfully measured pure absorption spectra of three pigments independent of scattering. FDPM measured absorption spectra may provide an efficient way to characterize pigment absorption

efficiencies for color prediction and offer new opportunities to obtain physical properties of pigments in R&D and product quality control.

CHAPTER XIII

SUMMARY AND CONCLUSIONS

In this work, we have successfully demonstrated FDPM measurements are sensitive not only to the strong volume exclusion interactions, but also to the more elusive electrostatic interactions. Under the context of the interference approximation, we derived photon diffusion equation based specially on a colloidal suspension and affirmed interference approximation addressing dependent scattering. In addition, we validated FDPM as an effective tool to measure pigment absorption efficiency. Specifically, we have addressed following several issues:

The FDPM data analysis methods have been systematically examined for precisely and accurately determining isotropic scattering coefficient. The most suitable data analysis scheme has been identified and used throughout the later experimental investigation.

In this dissertation, we have demonstrated that the sensitivity of FDPM measured scattering coefficients to changing electrostatic interactions among charged suspended particles. We have showed that increase in the ESI owing to decreasing ionic strength can increase the ordering of suspended particles. By comparing S(0) obtained from the MSA-HSY model prediction and that extracted from two wavelength FDPM measurements, we showed that the MSA-HSY model overestimates the value for S(0), and underestimates structure of suspensions with strong electrostatic interactions.

We have used MSA-HSY and MSA-PM structure factor models in addressing FDPM measured scattering data. The effective surface charges obtained by regressing the model predicted scattering data against FDPM measurement, have been compared with those obtained from zeta potential measurement and from conductometric titration. The MSA-HSY model is superior over the MSA-PM model in that MSA-HSY not only provided a better fit in regression but also estimated more physical meaning surface charges owing to its consideration of screening effects to Coulombic interaction by micro ions in suspending liquid. We have also demonstrated that FDPM has the potential to obtain a parameter estimate of effective surface charge of concentrated colloidal particles.

Using multiple wavelength measurement, we have demonstrated that FDPM can be used to obtain particle size information based on the simply least squares method. We have shown that the biased residuals of regression using monodisperse PY-HS model indicates that polydispersity cannot be neglected. A simulation shows these biased residues can be avoided if the polydisperse PY-HS model is used to describe light scattering of dense suspensions. From multiple wavelength FDPM measurements, we demonstrated that the sensitivity of scattering upon the electrostatic interactions depends upon the particle size in suspensions. FDPM measured scattering coefficient does not vary significantly with changing ionic strength for a polystyrene latex of the mean diameter of 226 nm at volume fraction less than 18% for visible wavelengths.

We have further verified that the linear relation between absorption coefficient and particle volume fraction from FDPM measurement affirms the assumptions in

interference approximation, which ascribe dependent scattering to the interference of light scattered from the different particle independently scattering light. We have also shown that FDPM measurements of absorption coefficient as a function of volume fraction can simultaneously determine volume based absorption efficiencies of suspended particles and suspending fluid, which can be used to extract imaginary refractive indices of both particles and suspending media.

Upon applying the linear relation between measured absorption coefficient and pigment concentration, we have determined, for the first time, the absolute pigment absorption spectra for three sample pigments at seven wavelengths. In doing so, we demonstrated the potential of FDPM as a standard pigment characterizing tool in pigments and paints industry.

In summary, the works presented in this thesis have advanced the understanding of the electrostatic interaction and their impact on the structure of charged concentrated colloidal suspensions. Upon deriving photon diffusion in colloidal suspensions, this thesis developed and verified a linear relation between absorber concentrations and absorption coefficient for the suspensions. This linear relationship has enabled us to determine pure absorption of suspended particles.

It is suggested the following works to be addressed in the future.

1. Investigate depletion interaction among colloidal suspensions. Beside electrostatic interactions, depletion forces due to the entropy effects of added polymer is critical to the formation of 3-D nano particle assembly, and gains significant application in new photonic device,

colloidal crystals, and new functional materials based on assembled protein.

2. Extend FDPM to multiple wavelength capability. FDPM demonstrated the potential in particle sizing of the concentrated suspensions, and in determining absorption spectrum for pigments. In order to move FDPM for online particle sizing and for characterizing pigment absorption efficiencies in the whole visible region spectrum, multiply wavelength measurements capacity must be enabled. The white light emission diode (LED), which may be modulated by superimposing a RF component on the direct driving current, may provide as a potential light source in future multiple wavelength FDPM instrumentation.
3. Monitoring industry particulate process using both absorption and scattering data. Previous group members have been focused on the characterization of concentrated suspension using only scattering data so far. With the additional information of particle light absorption efficiencies, which are also sensitive to particle size and particle concentration, FDPM can be more effective and more robust in characterizing industrial particulate streams, such as online monitoring emulsion polymerization or crystallization processes.

REFERENCES

1. A. M. Kulkarni and C. F. Zukoski, "Nanoparticle crystal nucleation: Influence of solution conditions," Langmuir **18**(8), 3090-3099 (2002).
2. J. H. Holtz and S. A. Asher, "Polymerized colloidal crystal hydrogel films as intelligent chemical sensing materials," Nature **389**(6653), 829-832 (1997).
3. J. H. Holtz, J. S. W. Holtz, C. H. Munro, and S. A. Asher, "Intelligent polymerized crystalline colloidal arrays: Novel chemical sensor materials," Analytical Chemistry **70**(4), 780-791 (1998).
4. D. H. Napper, *Polymeric stabilization of colloidal dispersions* (Academic Press, London, 1983).
5. S. M. Richter, R. R. Shinde, G. V. Balgi, and E. M. Sevick-Muraca, "Particle sizing using frequency domain photon migration," Particle & Particle Systems Characterization **15**(1), 9-15 (1998).
6. R. Shinde, G. Balgi, S. Richter, S. Banerjee, J. Reynolds, J. Pierce, and E. Sevick-Muraca, "Investigation of static structure factor in dense suspensions by use of multiply scattered light," Applied Optics **38**(1), 197-204 (1999).
7. S. Banerjee, R. Shinde, and E. M. Sevick-Muraca, "Assessment of $S(0,\phi)$ from multiply scattered light," Journal of Chemical Physics **111**(20), 9133-9136 (1999).

8. S. Banerjee, R. Shinde, and E. M. Sevick-Muraca, "Probing static structure of colloid-polymer suspensions with multiply scattered light," Journal of Colloid and Interface Science **209**(1), 142-153 (1999).

9. Z. G. Sun, C. D. Tomlin, and E. M. Sevick-Muraca, "Investigation of particle interactions in concentrated colloidal suspensions using frequency domain photon migration: Monodisperse systems," Journal of Colloid and Interface Science **245**(2), 281-291 (2002).

10. Z. G. Sun, Y. Q. Huang, and E. M. Sevick-Muraca, "Precise analysis of frequency domain photon migration measurement for characterization of concentrated colloidal suspensions," Review of Scientific Instruments **73**(2), 383-393 (2002).

11. Z. G. Sun and E. M. Sevick-Muraca, "Investigation of particle interactions in dense colloidal suspensions using frequency domain photon migration: Bidisperse systems," Langmuir **18**(4), 1091-1097 (2002).

12. Z. G. Sun and E. M. Sevick-Muraca, "Inversion algorithms for particle sizing with photon migration measurement," AICHE Journal **47**(7), 1487-1498 (2001).

13. Z. G. Sun, C. D. Tomlin, and E. M. Sevick-Muraca, "Approach for particle sizing in dense polydisperse colloidal suspension using multiple scattered light," Langmuir **17**(20), 6142-6147 (2001).

14. C. F. Bohren and D. R. Huffman, *Absorption and scattering of light by small particles* (Wiley, New York, 1983).

15. H. C. van der Hulst, *Light scattering by small particles* (Dover, New York, 1981).

16. S. Fraden and G. Maret, "Multiple light-scattering from concentrated, interacting suspensions," Physical Review Letters **65**(4), 512-515 (1990).

17. L. E. McNeil, A. R. Hanuska, and R. H. French, "Orientation dependence in near-field scattering from TiO2 particles," Applied Optics **40**(22), 3726-3736 (2001).

18. L. E. McNeil, A. R. Hanuska, and R. H. French, "Near-field scattering from red pigment particles: Absorption and spectral dependence," Journal of Applied Physics **89**(3), 1898-1906 (2001).

19. Y. L. Xu, "Electromagnetic scattering by an aggregate of spheres," Applied Optics **34**(21), 4573-4588 (1995).

20. A. Vrij, E. A. Nieuwenhuis, H. M. Fijnaut, and W. G. M. Agterof, "Application of modern concepts in liquid-state theory to concentrated particle dispersions," Faraday Discussions (65), 101-113 (1978).

21. V. P. Dik and A. P. Ivanov, "Extinction of light in dispersive media with high particle concentrations: applicability limits of the interference approximation," Journal of the Optical Society of America A-Optics Image Science and Vision **16(5)**, 1034 (1999).

22. V. P. Dik and A. P. Ivanov, "Limits of applicability of the interference approximation for description of extinction of light in disperse media with high concentration of particles," Optics and Spectroscopy **86**(6), 909-913 (1999).

23. M. H. G. M. Penders and A. Vrij, "A small-angle neutron-scattering study on polydisperse silica spheres coated with polyisobutene," Colloid and Polymer Science **268**(9), 823-831 (1990).

24. R. H. Ottewill and R. A. Richardson, "Studies of particle-particle interactions using polystyrene lattices and time-average light-scattering," Colloid and Polymer Science **260**(7), 708-719 (1982).

25. R. H. Ottewill, S. J. Cole, and J. A. Waters, "Characterization of particle morphology by scattering techniques," Macromolecular Symposia **92**, 97-107 (1995).

26. M. J. Grimson, "Small-angle scattering from colloidal suspensions," Journal of the Chemical Society-Faraday Transactions **79**, 817 (1983).

27. J. A. H. M. Moonen, C. G. Dekruif, A. Vrij, and S. Bantle, "Small-angle neutron-scattering of colloidal silica dispersions in a non-polar solvent," Colloid and Polymer Science **266**(9), 836-848 (1988).

28. M. H. G. Duits, R. P. May, A. Vrij, and C. G. Dekruif, "Small-angle neutron-scattering of concentrated adhesive-hard-sphere dispersions," Langmuir **7**(1), 62-68 (1991).

29. S. Ashdown, I. Markovic, R. H. Ottewill, P. Lindner, R. C. Oberthur, and A. R. Rennie, "Small-angle neutron-scattering studies on ordered polymer colloid dispersions," Langmuir **6**(2), 303-307 (1990).

30. K. Alexander, D. J. Cebula, J. W. Goodwin, R. H. Ottewill, and A. Parentich, "Small-angle neutron-scattering studies on an ion-exchanged polystyrene latex," Colloids and Surfaces **7**(3), 233-242 (1983).

31. R. H. Ottewill, H. J. M. Hanley, A. R. Rennie, and G. C. Straty, "Small-angle neutron-scattering studies on binary-mixtures of charged-particles," Langmuir **11**(10), 3757-3765 (1995).

32. R. H. Ottewill, "Small-angle neutron-scattering from colloidal dispersions," Journal of Applied Crystallography **24**, 436-443 (1991).

33. R. H. Ottewill, E. Sinagra, I. P. Macdonald, J. F. Marsh, and R. K. Heenan, "Small-angle neutron-scattering studies on nonaqueous dispersions .5. Magnesium carbonate dispersions in hydrocarbon media," Colloid and Polymer Science **270**(6), 602-608 (1992).

34. M. Kotlarchyk and S. H. Chen, "Analysis of small-angle neutron-scattering spectra from polydisperse interacting colloids," Journal of Chemical Physics **79**(5), 2461-2469 (1983).

35. R. Grunder, Y. S. Kim, M. Ballauff, D. Kranz, and H. G. Muller, "Analysis of polymer lattices by small-angle x-ray-scattering," Angewandte Chemie-International Edition in English **30**(12), 1650-1652 (1991).

36. J. Moonen, C. Pathmamanoharan, and A. Vrij, "Small-angle x-ray-scattering of silica dispersions at low particle concentrations," Journal of Colloid and Interface Science **131**(2), 349-365 (1989).

37. J. Moonen, C. Dekruif, and A. Vrij, "Determination of the structure factor for concentrated silica dispersions using small-angle s-ray-scattering .1. Simulation," Colloid and Polymer Science **266**(11), 1068-1076 (1988).

38. B. J. Berne and R. Pecora, *Dynamic light scattering: With applications to chemistry, biology, and physics* (Wiley, New York, 1976).

39. R. Pecora, *Dynamic light scattering: Applications of photon correlation spectroscopy* (Plenum Press, New York, 1985).

40. A. Moussaid and P. N. Pusey, "Multiple scattering suppression in static light scattering by cross-correlation spectroscopy," Physical Review E **60**(5), 5670-5676 (1999).

41. P. N. Pusey, "Suppression of multiple scattering by photon cross-correlation techniques," Current Opinion in Colloid & Interface Science **4**(3), 177-185 (1999).

42. V. Viasnoff, F. Lequeux, and D. J. Pine, "Multispeckle diffusing-wave spectroscopy: A tool to study slow relaxation and time-dependent dynamics," Review of Scientific Instruments **73**(6), 2336-2344 (2002).

43. D. J. Pine, D. A. Weitz, J. X. Zhu, D. J. Durian, A. Yodh, and M. Kao, "Diffusing-wave spectroscopy and interferometry," Macromolecular Symposia **79**, 31-44 (1994).

44. D. A. Weitz, J. X. Zhu, D. J. Durian, H. Gang, and D. J. Pine, "Diffusing-wave spectroscopy - the technique and some applications," Physica Scripta **T49B**, 610-621 (1993).

45. P. D. Kaplan, M. H. Kao, A. G. Yodh, and D. J. Pine, "Geometric constraints for the design of diffusing-wave spectroscopy experiments," Applied Optics **32**(21), 3828-3836 (1993).

46. A. G. Yodh, P. D. Kaplan, and D. J. Pine, "Pulsed diffusing-wave spectroscopy - high-resolution through nonlinear optical gating," Physical Review B **42**(7), 4744-4747 (1990).

47. D. J. Pine, D. A. Weitz, J. X. Zhu, and E. Herbolzheimer, "Diffusing-wave spectroscopy - dynamic light-scattering in the multiple-scattering limit," Journal De Physique **51**(18), 2101-2127 (1990).

48. X. L. Wu, D. J. Pine, P. M. Chaikin, J. S. Huang, and D. A. Weitz, "Diffusing-wave spectroscopy in a shear-flow," Journal of the Optical Society of America B-Optical Physics **7**(1), 15-20 (1990).

49. D. A. Weitz, D. J. Pine, P. N. Pusey, and R. J. A. Tough, "Nondiffusive Brownian-motion studied by diffusing-wave spectroscopy," Physical Review Letters **63**(16), 1747-1750 (1989).

50. D. J. Pine, D. A. Weitz, P. M. Chaikin, and E. Herbolzheimer, "Diffusing-wave spectroscopy," Physical Review Letters **60**(12), 1134-1137 (1988).

51. D. S. Horne and C. M. Davidson, "Application of diffusing-wave spectroscopy to particle sizing in concentrated dispersions," Colloids and Surfaces a-Physicochemical and Engineering Aspects **77**(1), 1-8 (1993).

52. D. J. Durian, "Accuracy of diffusing-wave spectroscopy theories," Physical Review E **51**(4), 3350-3358 (1995).

53. D. J. Durian, "Penetration depth for diffusing-wave spectroscopy," Applied Optics **34**(30), 7100-7105 (1995).

54. F. Scheffold, "Particle sizing with diffusing wave, spectroscopy," Journal of Dispersion Science and Technology **23**(5), 591-599 (2002).

55. J. P. Hansen and I. R. McDonald, *Theory of simple liquids,* 2nd ed. (Academic Press, London, 1986).

56. H. Gang, A. H. Krall, and D. A. Weitz, "Thermal fluctuations of the shapes of droplets in dense and compressed emulsions," Physical Review E **52**(6), 6289-6302 (1995).

57. H. Gang, A. H. Krall, and D. A. Weitz, "Shape fluctuations of interacting fluid droplets," Physical Review Letters **73**(25), 3435-3438 (1994).

58. S. Chandresekar, *Radiative transfer* (Oxford University Press, New York, 1960).

59. A. Ishimaru, *Wave propagation and scattering in random media*, IEEE/OUP series on electromagnetic wave theory (IEEE Press; Oxford University Press, New York, 1997).

60. P. D. Kaplan, A. D. Dinsmore, A. G. Yodh, and D. J. Pine, "Diffuse transmission spectroscopy - a structural probe of opaque colloidal mixtures," Physical Review E **50**(6), 4827-4835 (1994).

61. B. C. Wilson, E. M. Sevick, M. S. Patterson, and B. Chance, "Time-dependent optical spectroscopy and imaging for biomedical applications," Proceedings of the IEEE **80**(6), 918-930 (1992).

62. Z. G. Sun, S. Torrance, F. K. McNeil-Watson, and E. M. Sevick-Muraca, "Application of frequency domain photon migration to particle size analysis and monitoring of pharmaceutical powders," Analytical Chemistry **75**(7), 1720-1725 (2003).

63. H. Jiang, J. Pierce, J. Kao, and E. M. Sevick-Muraca, "Measurement of particle size distribution and volume fraction in concentrated suspensions with photon migration techniques," Applied Optics **36**, 3310 (1997).

64. A. K. Holmes, R. E. Challis, and D. J. Wedlock, "A wide bandwidth study of ultrasound velocity and attenuation in suspensions - comparison of theory with experimental measurements," Journal of Colloid and Interface Science **156**(2), 261-268 (1993).

65. A. K. Holmes, R. E. Challis, and D. J. Wedlock, "A wide-bandwidth ultrasonic study of suspensions - the variation of velocity and attenuation with particle-size," Journal of Colloid and Interface Science **168**(2), 339-348 (1994).

66. A. S. Dukhin and P. J. Goetz, "Characterization of concentrated dispersions with several dispersed phases by means of acoustic spectroscopy," Langmuir **16**(20), 7597-7604 (2000).

67. A. S. Dukhin and P. J. Goetz, "Acoustic and electroacoustic spectroscopy characterizing concentrated dispersions emulsions," Advances in Colloid and Interface Science **92**(1-3), 73-132 (2001).

68. A. Dukhin and P. Goetz, "Acoustic and electroacoustic spectroscopy.," Abstracts of Papers of the American Chemical Society **223**, U434-U434 (2002).

69. R. W. O'Brien, D. W. Cannon, and W. N. Rowlands, "Electroacoustics online," Abstracts of Papers of the American Chemical Society **216**, U596-U596 (1998).

70. R. W. OBrien, R. A. Wade, M. L. Carasso, R. J. Hunter, W. N. Rowlands, and J. K. Beattie, "Electroacoustic determination of droplet size and zeta potential in concentrated emulsions.," Abstracts of Papers of the American Chemical Society **212**, 39-Pmse (1996).

71. A. S. Dukhin, P. J. Goetz, T. H. Wines, and P. Somasundaran, "Acoustic and electroacoustic spectroscopy," Colloids and Surfaces A-Physicochemical and Engineering Aspects **173**(1-3), 127-158 (2000).

72. A. S. Dukhin, P. J. Goetz, and C. W. Hamlet, "Acoustic spectroscopy for concentrated polydisperse colloids with low density contrast," Langmuir **12**(21), 4998-5003 (1996).

73. A. S. Dukhin and P. J. Goetz, "Acoustic and electroacoustic spectroscopy," Langmuir **12**(18), 4336-4344 (1996).

74. A. S. Dukhin and P. J. Goetz, "Characterization of chemical polishing materials (monomodal and bimodal) by means of acoustic spectroscopy," Colloids and Surfaces A-Physicochemical and Engineering Aspects **158**(3), 343-354 (1999).

75. A. J. Babchin, R. S. Chow, and R. P. Sawatzky, "Electrokinetic measurements by electroacoustical Methods," Advances in Colloid and Interface Science **30**(1-2), 111-151 (1989).

76. R. W. O'Brien, "The electroacoustic equations for a colloidal suspensions," Journal of Fluid Mechanics **212**, 81 (1990).

77. R. W. Obrien, M. James, and R. J. Hunter, "Electroacoustic measurements of the zeta potential of kaolinite particles in non-dilute suspensions," Abstracts of Papers of the American Chemical Society **201**, 16-Coll (1991).

78. M. James, R. J. Hunter, and R. W. Obrien, "Effect of particle-size distribution and aggregation on electroacoustic measurements of zeta potential," Langmuir **8**(2), 420-423 (1992).

79. M. L. Carasso, W. N. Rowlands, and R. A. Kennedy, "Electroacoustic determination of droplet size and zeta-potential in concentrated intravenous fat emulsions," Journal of Colloid and Interface Science **174**(2), 405-413 (1995).

80. R. J. Hunter and R. W. OBrien, "Electroacoustic characterization of colloids with unusual particle properties," Colloids and Surfaces A-Physicochemical and Engineering Aspects **126**(2-3), 123-128 (1997).

81. R. J. Hunter, "Recent developments in the electroacoustic characterization of colloidal suspensions and emulsions," Colloids and Surfaces A-Physicochemical and Engineering Aspects **141**(1), 37-66 (1998).

82. A. S. Dukhin, V. N. Shilov, H. Ohshima, and P. J. Goetz, "Electroacoustic phenomena in concentrated dispersions: New theory and CVI experiment," Langmuir **15**(20), 6692-6706 (1999).

83. A. S. Dukhin, H. Ohshima, V. N. Shilov, and P. J. Goetz, "Electroacoustics for concentrated dispersions," Langmuir **15**(10), 3445-3451 (1999).

84. R. O'Brien, "Comments on "Electroacoustic phenomena in concentrated dispersions: New theory and CVI experiment" by A. S. Dukhin et al.," Langmuir **17**(4), 1314-1314 (2001).

85. A. S. Dukhin and P. J. Goetz, *Ultrasound for characterizing colloids: Particle sizing, zeta potential, rheology,* 1st ed., Studies in interface science, v. 15 (Elsevier, Amsterdam, 2002).

86. F. Babick, F. Hinze, and S. Ripperger, "Dependence of ultrasonic attenuation on the material properties," Colloids and Surfaces A-Physicochemical and Engineering Aspects **172**(1-3), 33-46 (2000).

87. R. Zana and E. B. Yeager, "Ultrasonic vibration potentials," Modern Aspects of Electrochemistry (14), 1-60 (1982).

88. E. Yeager and R. Zana, "Ionic solvation numbers from compressibilities and ionic vibration potentials measurements - comment," Journal of Physical Chemistry **79**(12), 1228-1230 (1975).

89. R. W. Obrien, P. Garside, and R. J. Hunter, "The electroacoustic reciprocal relation," Langmuir **10**(3), 931-935 (1994).

90. A. S. Dukhin and P. J. Goetz, "Characterization of aggregation phenomena by means of acoustic and electroacoustic spectroscopy," Colloids and Surfaces A-Physicochemical and Engineering Aspects **144**(1-3), 49-58 (1998).

91. R. J. Hunter, *Zeta potential in colloid science: principles and applications* (Academic Press, London, 1981).

92. R. J. Goetz and M. S. Elaasser, "Effects of dispersion concentration on the electroacoustic potentials of O/W miniemulsions," Journal of Colloid and Interface Science **150**(2), 436-452 (1992).

93. P. Kubelka and F. Munk, "Ein beitrag zur optic der farbanstriche," Z. Tech. Phys. **12**, 593 (1931).

94. H. G. Völz, *Industrial color testing: fundamentals and techniques,* 2nd, completely rev. ed. (Wiley-VCH, Weinheim ; New York, 2001).

95. A. Vrij, "Mixtures of hard-spheres in the Percus-Yevick approximation - light-scattering at finite angles," Journal of Chemical Physics **71**(8), 3267-3270 (1979).

96. A. Vrij, "Concentrated, polydisperse solutions of colloidal particles - light-scattering and sedimentation of hard-sphere mixtures," Journal of Colloid and Interface Science **90**(1), 110-116 (1982).

97. C. G. Dekruif, E. M. F. Vanlersel, A. Vrij, and W. B. Russel, "Hard-sphere colloidal dispersions - viscosity as a function of shear rate and volume fraction," Journal of Chemical Physics **83**(9), 4717-4725 (1985).

98. C. G. Dekruif, P. W. Rouw, J. W. Jansen, and A. Vrij, "Hard-sphere properties and crystalline packing of lyophilic silica colloids," Journal De Physique **46**(C3), 295-308 (1985).

99. D. Frenkel, R. J. Vos, C. G. Dekruif, and A. Vrij, "Structure factors of polydisperse systems of hard-spheres - a comparison of Monte-Carlo simulations

and Percus-Yevick theory," Journal of Chemical Physics **84**(8), 4625-4630 (1986).

100. J. Mellema, C. G. Dekruif, C. Blom, and A. Vrij, "Hard-sphere colloidal dispersions - mechanical relaxation pertaining to thermodynamic forces," Rheologica Acta **26**(1), 40-44 (1987).

101. C. G. Dekruif, W. J. Briels, R. P. May, and A. Vrij, "Hard-sphere colloidal silica dispersions - the structure factor determined with SANS," Langmuir **4**(3), 668-676 (1988).

102. R. J. Baxter, "Percus-Yevick equation for hard spheres with surface adhesion," Journal of Chemical Physics **49**(6), 2770-& (1968).

103. P. W. Rouw, A. Vrij, and C. G. Dekruif, "Adhesive hard-sphere colloidal dispersions .3. Stickiness in N-dodecane and benzene," Colloids and Surfaces **31**, 299-309 (1988).

104. C. G. Dekruif, P. W. Rouw, W. J. Briels, M. H. G. Duits, A. Vrij, and R. P. May, "Adhesive hard-sphere colloidal dispersions - a small-angle neutron-scattering study of stickiness and the structure factor," Langmuir **5**(2), 422-428 (1989).

105. M. Yasutomi and M. Ginoza, "Analytical solution of Ornstein-Zernike equation for adhesive-hard-sphere Yukawa fluids," Molecular Physics **89**(6), 1755-1764 (1996).

106. R. J. Hunter, *Foundations of colloid science,* 2nd ed. (Oxford University Press, Oxford, 2001).

107. P. C. Hiemenz and R. Rajagopalan, *Principles of colloid and surface chemistry,* 3rd ed. (Marcel Dekker, New York, 1997).

108. T. Yukawa, "Interaction between identical nuclei," Physical Review C **8**(5), 1593-1605 (1973).

109. J. S. Hoye and L. Blum, "Solution of Yukawa closure of Ornstein-Zernike equation," Journal of Statistical Physics **16**(5), 399-413 (1977).

110. C. A. Miller and P. Neogi, *Interfacial phenomena: Equilibrium and dynamic effects*, Surfactant science series ; v. 17 (M. Dekker, New York, 1985).

111. P. Salgi and R. Rajagopalan, "Polydispersity in colloids - implications to static structure and scattering," Advances in Colloid and Interface Science **43**(2-3), 169-288 (1993).

112. B. Larsen, "Studies in statistical-mechanics of Coulombic systems .3. Numerical-solutions of Hnc and Rhnc equations for restricted primitive model," Journal of Chemical Physics **68**(10), 4511-4523 (1978).

113. G. M. Abernethy and M. J. Gillan, "New method of solving the Hnc equation for ionic liquids," Molecular Physics **39**(4), 839-847 (1980).

114. P. J. Rossky and H. L. Friedman, "Accurate solutions to integral-equations describing weakly screened ionic systems," Journal of Chemical Physics **72**(10), 5694-5700 (1980).

115. H. Arandaespinoza, M. Medinanoyola, and J. L. Arauzlara, "Static structure of the 2-dimensional hard-disk plus Yukawa fluid," Journal of Chemical Physics **99**(7), 5462-5466 (1993).

116. M. S. Wertheim, "Exact solution of Percus-Yevick integral equation for hard spheres," Phys. Rev. Lett. **10**, 321 (1963).

117. E. Thiele, "Equation of state for hard spheres," J. Chem. Phys. **39**, 474 (1963).

118. J. P. Badiali, L. Blum, and M. L. Rosinberg, "Localized adsorption at solid liquid interfaces - the sticky site hard-wall model," Chemical Physics Letters **129**(2), 149-154 (1986).

119. F. J. Rogers and D. A. Young, "New, thermodynamically consistent, integral-equation for simple fluids," Physical Review A **30**(2), 999-1007 (1984).

120. L. Blum, "Mean spherical model for asymmetric electrolytes .1. Method of solution," Molecular Physics **30**(5), 1529-1535 (1975).

121. L. Blum and J. S. Hoye, "Solution of the Ornstein-Zernike equation with Yukawa closure for a mixture," Journal of Statistical Physics **19**(4), 317-324 (1978).

122. J. N. Herrera, P. T. Cummings, and H. Ruiz-Estrada, "Static structure factor for simple liquid metals," Molecular Physics **96**(5), 835-847 (1999).

123. M. Ginoza and M. Yasutomi, "Analytical structure factors for colloidal fluids with size and interaction polydispersities," Physical Review E **58**(3), 3329-3333 (1998).

124. M. Ginoza and M. Yasutomi, "Analytical model of the static structure factor of a colloidal dispersion: interaction polydispersity effect," Molecular Physics **93**(3), 399-404 (1998).

125. M. Ginoza and M. Yasutomi, "Static structure factor for a colloidal dispersion with size and "charge" polydispersities: Mean spherical approximation model in hard-sphere Yukawa fluids," Physical Review E **59**(2), 2060-2066 (1999).

126. D. Gazzillo and A. Giacometti, "Structure factors for the simplest solvable model of polydisperse colloidal fluids with surface adhesion," Journal of Chemical Physics **113**(21), 9837-9848 (2000).

127. H. Ruiz-Estrada, M. Medina-Noyola, and G. Nagele, "Rescaled mean spherical approximation for colloidal mixtures," Physica A **168**, 919 (1990).

128. K. Hiroike, "Supplement to Blums theory for asymmetric electrolytes," Molecular Physics **33**(4), 1195-1198 (1977).

129. K. Hiroike, "Ornstein-Zernike relation for a fluid mixture with direct correlation functions of finite range," Journal of the Physical Society of Japan **27**(6), 1415-& (1969).

130. L. Blum and J. S. Hoye, "Mean spherical model for asymmetric electrolytes .2. Thermodynamic properties and pair correlation-function," Journal of Physical Chemistry **81**(13), 1311-1317 (1977).

131. J. M. Mendezalcaraz, M. Chavezpaez, B. Daguanno, and R. G. Klein, "Structural properties of colloidal suspensions" Physica A **220**, 173 (1995).

132. S. Zumer, A. Golemme, and J. W. Doane, "Light extinction in a dispersion of small nematic droplets," Journal of the Optical Society of America A-Optics Image Science and Vision **6**(3), 403-411 (1989).

133. M. Lax, "Multiple scattering of waves. II. The effective field in dense systems," Physical Review A **85(4)**, 621 (1952).

134. R. West, D. Gibbs, L. Tsang, and A. K. Fung, "Comparison of optical-scattering experiments and the quasi-crystalline approximation for dense media," Journal of the Optical Society of America A-Optics Image Science and Vision **11**(6), 1854-1858 (1994).

135. L. Blum and G. Stell, "Polydisperse systems .1. Scattering function for polydisperse fluids of hard or permeable spheres," Journal of Chemical Physics **71**(1), 42-46 (1979).

136. P. M. Saulnier, M. P. Zinkin, and G. H. Watson, "Scatterer correlation-effects on photon transport in dense random-media," Physical Review B **42**(4), 2621-2623 (1990).

137. B. Chance, M. Cope, E. Gratton, N. Ramanujam, and B. Tromberg, "Phase measurement of light absorption and scatter in human tissue," Review of Scientific Instruments **69**(10), 3457-3481 (1998).

138. J. J. Duderstadt and L. J. Hamilton, *Nuclear reactor analysis* (John Wiley & Sons, New York, 1976).

139. I. Livsey and R. H. Ottewill, "Light-scattering by concentric sphere particles," Advances in Colloid and Interface Science **36**, 173-184 (1991).

140. A. J. Welch and M. E. van Gemert, *Optical thermal response of laser irradiated tissue* (Plenum Press, New York, 1995).

141. L. V. Wang and S. L. Jacques, "Source of error in calculation of optical diffuse reflectance from turbid media using diffusion theory," Computer Methods and Programs in Biomedicine **61**(3), 163-170 (2000).

142. J. B. Fishkin and E. Gratton, "Propagation of photon-density waves in strongly scattering media containing an absorbing semiinfinite plane bounded by a straight edge," Journal of the Optical Society of America A-Optics Image Science and Vision **10**(1), 127-140 (1993).

143. S. Fantini, M. A. Franceschini, and E. Gratton, "Semi-infinite-geometry boundary-problem for light migration in highly scattering media - a frequency-domain study in the diffusion-approximation," Journal of the Optical Society of America B-Optical Physics **11**(10), 2128-2138 (1994).

144. B. Chance, J. S. Leigh, H. Miyake, D. S. Smith, S. Nioka, R. Greenfeld, M. Finander, K. Kaufmann, W. Levy, M. Young, P. Cohen, H. Yoshioka, and R. Boretsky, "Comparison of time-resolved and time-unresolved measurements of deoxyhemoglobin in brain," Proceedings of the National Academy of Sciences of the United States of America **85**(14), 4971-4975 (1988).

145. E. M. Sevick, B. Chance, J. Leigh, S. Nioka, and M. Maris, "Quantitation of time-resolved and frequency-resolved optical-spectra for the determination of tissue oxygenation," Analytical Biochemistry **195**(2), 330-351 (1991).

146. S. M. Richter, "Frequency domain photon migration for the characterization of concentrated suspensions," Ph.D. Dissertation (Purdue University, 2000).

147. E. M. Sevick-Muraca, E. Kuwana, A. Godavarty, J. P. Houston, A. B. Thompson, and R. Roy "Near-infrared fluorescence imaging and spectroscopy in random media and tissues", in *Biomedical photonics handbook,* T. Vo-Dinh, editor-in-chief. (CRC press, Boca Raton, 2002), Chapter 33.

148. J. B. Fishkin, P. T. C. So, A. E. Cerussi, S. Fantini, M. A. Franceschini, and E. Gratton, "Frequency-domain method for measuring spectral properties in multiple-scattering media - methemoglobin absorption-spectrum in a tissuelike phantom," Applied Optics **34**(7), 1143-1155 (1995).

149. J. C. Lagarias, J. A. Reeds, M. H. Wright, and P. E. Wright, "Convergence properties of the Nelder-Mead simplex method in low dimensions," Siam Journal on Optimization **9**(1), 112-147 (1998).

150. K. Ito, N. Ise, and T. Okubo, "Determination of the number of effective charges of colloidal particles by transference measurements," Journal of Chemical Physics **82**(12), 5732-5736 (1985).

151. Y. K. Gong, K. Nakashima, and R. L. Xu, "Characterization of polystyrene latex surfaces by conductometric titration, rhodamine 6G adsorption, and electrophoresis measurements," Langmuir **16**(22), 8546-8548 (2000).

152. Y. K. Gong, K. Nakashima, and R. L. Xu, "A novel method to determine effective charge of polystyrene latex particles in aqueous dispersion," Langmuir **17**(9), 2889-2892 (2001).

153. G. Nagele, "On the dynamics and structure of charge-stabilized suspensions," Physics Reports-Review Section of Physics Letters **272**(5-6), 216-372 (1996).

154. J. B. Hayter and J. Penfold, "An analytic structure factor for macroion solutions," Molecular Physics **42**(1), 109-118 (1981).

155. Y. A. Vlasov, X. Z. Bo, J. C. Sturm, and D. J. Norris, "On-chip natural assembly of silicon photonic bandgap crystals," Nature **414**(6861), 289-293 (2001).

156. S. R. Kline and E. W. Kaler, "Interactions in colloidal mixtures: Partial structure factors in mixtures of colloidal silica and an anionic oil-in-water microemulsion," Journal of Colloid and Interface Science **203**(2), 392-401 (1998).

157. Y. Q. Huang and E. M. Sevick-Muraca, "Assessment of small-angle and angle-averaged structure factor for monitoring electrostatic colloidal interactions using multiply scattered light," Journal of Colloid and Interface Science **251**(2), 434-442 (2002).

158. M. Quesada-Perez, J. Callejas-Fernandez, and R. Hidalgo-Alvarez, "Structural effects of the solvent composition in colloidal liquids," Journal of Chemical Physics **110**(12), 6025-6031 (1999).

159. T. Gisler, S. F. Schulz, M. Borkovec, H. Sticher, P. Schurtenberger, B. Daguanno, and R. Klein, "Understanding colloidal charge renormalization from surface-chemistry - experiment and theory," Journal of Chemical Physics **101**(11), 9924-9936 (1994).

160. W. Hartl and H. Versmold, "Liquid-like ordered colloidal suspensions - the influence of the particle concentration," Journal of Chemical Physics **88**(11), 7157-7161 (1988).

161. U. Apfel, K. D. Horner, and M. Ballauff, "Precise analysis of the turbidity spectra of a concentrated latex," Langmuir **11**(9), 3401-3407 (1995).

162. U. Apfel, R. Grunder, and M. Ballauff, "A turbidity study of particle interaction in latex suspensions," Colloid and Polymer Science **272**(7), 820-829 (1994).

163. J. W. Jansen, C. G. Dekruif, and A. Vrij, "Attractions in sterically stabilized silica dispersions .3. 2nd Virial-coefficient as a function of temperature, as measured by means of turbidity," Journal of Colloid and Interface Science **114**(2), 492-500 (1986).

164. J. C. Crocker and D. G. Grier, "When like charges attract: The effects of geometrical confinement on long-range colloidal interactions," Physical Review Letters **77**(9), 1897-1900 (1996).

165. M. D. CarbajalTinoco, F. CastroRoman, and J. L. ArauzLara, "Static properties of confined colloidal suspensions," Physical Review E **53**(4), 3745-3749 (1996).

166. M. Quesada-Perez, J. Callejas-Fernandez, and R. Hidalgo-Alvarez, "Probing electrostatic forces in colloidal suspensions through turbidity data," Journal of Colloid and Interface Science **217**(1), 177-185 (1999).

167. J. Chang, P. Lesieur, M. Delsanti, L. Belloni, C. Bonnetgonnet, and B. Cabane, "Structural and Thermodynamic Properties of Charged Silica Dispersions," Journal of Physical Chemistry **99**(43), 15993-16001 (1995).

168. R. Krause, B. Daguanno, J. M. Mendezalcaraz, G. Nagele, R. Klein, and R. Weber, "Static structure factors of binary suspensions of charged polystyrene

spheres - experiment against theory and computer-simulation," Journal of Physics-Condensed Matter **3**(24), 4459-4475 (1991).

169. B. Daguanno and R. Klein, "Structural effects of polydispersity in charged colloidal dispersions," Journal of the Chemical Society-Faraday Transactions **87**(3), 379-390 (1991).

170. M. Quesada-Perez, J. Callejas-Fernandez, and R. Hidalgo-Alvarez, "Ionic condensation theories and the liquidlike structures observed in colloidal dispersions," Physical Review E **61**(1), 574-582 (2000).

171. M. Quesada-Perez, J. Callejas-Fernandez, and R. Hidalgo-Alvarez, "Renormalization processes in the charge density of polymer colloids," Colloids and Surfaces A-Physicochemical and Engineering Aspects **159**(2-3), 239-252 `(1999).

172. Y. Q. Huang, V. Yuwono, and E. M. Sevick-Muraca, "Modification of electrostatic interaction by rhodamine 6G adsorption on polystyrene latex as assessed by frequency domain photon migration," Langmuir **18**(24), 9192-9197 (2002).

173. L. Belloni, "Ionic condensation and charge renormalization in colloidal suspensions," Colloids and Surfaces a-Physicochemical and Engineering Aspects **140**(1-3), 227-243 (1998).

174. M. T. Charreyre, P. Zhang, M. A. Winnik, C. Pichot, and C. Graillat, "Adsorption of rhodamine-60 onto polystyrene latex-particles with sulfate groups at the surface," Journal of Colloid and Interface Science **170**(2), 374-382 (1995).

175. E. Mubarekyan and M. Santore, "Characterization of polystyrene latex surfaces by the adsorption of rhodamine 6G," Langmuir **14**(7), 1597-1603 (1998).

176. J. P. S. Farinha, M. T. Charreyre, J. M. G. Martinho, M. A. Winnik, and C. Pichot, "Picosecond fluorescence studies of the surface morphology of charged polystyrene latex particles," Langmuir **17**(9), 2617-2623 (2001).

177. K. Nakashima, Y. S. Liu, P. Zhang, J. Duhamel, J. R. Feng, and M. A. Winnik, "Picosecond fluorescence studies of energy-transfer on the surface of poly(butyl methacrylate) latex-particles," Langmuir **9**(11), 2825-2831 (1993).

178. J. D. Feick and D. Velegol, "Measurements of charge nonuniformity on polystyrene latex particles," Langmuir **18**(9), 3454-3458 (2002).

179. R. H. Boundy and R. R. e. Boxer, *Styrene, its polymers, copolymers, and derivatives* (Reinhold Publishing Corp., New York, 1952).

180. Y. Kuga and A. Ishimaru, "Retroreflectance from a dense distribution of spherical-particles," Journal of the Optical Society of America A-Optics Image Science and Vision **1**(8), 831-835 (1984).

181. R. Rajagopalan, "Probing interaction forces in colloidal fluids through static structural data - the inverse problem," Langmuir **8**(12), 2898-2906 (1992).

182. R. Rajagopalan, "Interaction forces from static structure factors of colloidal dispersions: The inverse problem." Abstracts of Papers of the American Chemical Society **211**, 2 (1996).

183. A. Vrij, "Light-scattering by dispersions of model colloids," Advances in Colloid and Interface Science **16**(JUL), 139-141 (1982).

184. R. Garg, R. K. Prud'homme, I. A. Aksay, F. Liu, and R. R. Alfano, "Optical transmission in highly concentrated dispersions," Journal of the Optical Society of America A-Optics Image Science and Vision **15**(4), 932-935 (1998).

185. B. J. Tromberg, L. O. Svaasand, T. T. Tsay, and R. C. Haskell, "Properties of photon density waves in multiple-scattering media," Applied Optics **32**(4), 607-616 (1993).

186. L. H. Kou, D. Labrie, and P. Chylek, "Refractive-indexes of water and ice in the 0.65-μM to 2.5-μM spectral range," Applied Optics **32**(19), 3531-3540 (1993).

187. R. M. Pope and E. S. Fry, "Absorption spectrum (380-700 nm) of pure water .2. Integrating cavity measurements," Applied Optics **36**(33), 8710-8723 (1997).

188. R. T. Marcus and P. E. Pierce, "An analysis of the 1st surface correction for the color matching of organic coatings from the viewpoint of radiative-transfer theory," Progress in Organic Coatings **23**(3), 239-264 (1994).

189. J. L. Saunderson, "Calculation of the color of pigmented plastics," J. Opt. Soc. Am. A **32**, 727 (1942).

190. F. W. Billmeyer, P. G. Chassaigne, and J. F. Dubois, "Determining pigment optical-properties for use in the Mie and many-flux theories," Color Research and Application **5**(2), 108-112 (1980).

191. W. E. Vargas and G. A. Niklasson, "Pigment mass density and refractive index determination from optical measurements," Journal of Physics-Condensed Matter **9**(7), 1661-1670 (1997).

192. P. S. Mudgett and L. W. Richards, "Multiple scattering calculations for technology," Applied Optics **10**(7), 1485 (1971).

193. T. Burger, J. Kuhn, R. Caps, and J. Fricke, "Quantitative determination of the scattering and absorption coefficients from diffuse reflectance and transmittance measurements: Application to pharmaceutical powders," Applied Spectroscopy **51**(3), 309-317 (1997).

194. D. L. Massart, *Chemometrics : a textbook*, Data handling in science and technology ; v. 2 (Elsevier Science Pub. Co., Amsterdam, 1988).

APPENDIX A

LITERATURE REVIEWS PERTAINING TO DEPENDENT SCATTERING

A. 1 Introduction

Particle separated far apart, such as those immersed in a dilute suspensions scatter independently. The scattering power of a dilute suspension is proportional to its particle number density. "*If particles are spatially position together, as in agglomerated coatings or concentrated suspensions, interactions between the radiation fields of adjacent particles can lead to variations in the magnitude and spatial arrangement of scattering light in the near and far field,"* reported by McNeil *et al.*[1] The classical approximation of independent scattering fails at an increased particle volume fraction (> 5%). The phenomena of dependent scattering have been experimentally observed and theoretically proved by solving governing Maxwell equations.

A.2 Experimental observation of dependent scattering

In concentrated particle suspensions, the scattering power indicated by the inverse mean free path (MFP) does not increase with particle concentration due to electromagnetic interactions at higher volume fraction (> 5%). It is found that coherent backscattering from colloidal suspension, arising from photon self-interference effect, leads to an enhance intensity cone in the backward scattering.[2-5] Fraden and Maret

correlated MFP for propagating light to short time self-diffusion constant of particles, which depends on inter-particle interactions restraining particle motion.[6]

At a volume fraction higher than 45%, photon localization may occur.[7,8] Researchers are also considering developing photonic material from structured colloidal precursors.[9] Beside the quenched scattering efficiencies determined using FDPM showed in previous chapters, *Garg et al.*[10] also reported that isotropic scattering coefficients measured using pulsed laser decreases with particle concentration when it is greater than a critical value, while dependent scattering always predicts that scattering coefficient is proportional to particle concentration.

In pigments and paints industrials, it is found that the hiding power, which represents how effective a coating layer can shield the appearance of covered substrate, fails to increase linearly with the increasing pigment concentration as it does at a dilute dispersion.

These experiments have unequivocally demonstrated the dependence on the scattering pattern and scattering intensity on the particle spatial arrangement.

A. 3 Theoretical treatment of multiple scattering

Theoretical treatment of light scattering from a concentrated suspension can be classified in two categories: one uses interference approximation (IA), as discussed in the previous chapters; another one through the solution of governing multiple scattering Maxwell equations using T-Matrix methods.[11] Since the interference approach has been extensive discussed in the previous chapters, only T-Matrix based theories will be discussed in this appendix. Before addressing light scattering from colloidal ensemble

containing numerous particles, small particle systems with a few particles will be discussed first.

A.3.1 Small particle systems

For small particle systems containing a few particles, rigorous treatment is possible from solving the governing Maxwell equation either numerically or analytically. Mie theory, which calculates angular dependent light scattering amplitude from a single spherical particle, involves expanding the planar incident and scattering fields in vector spherical harmonics and determining expansion coefficients for the scattering field in terms of those for the incident field through the boundary condition of the Maxwell equation. The scattered field distribution can be reconstructed by multiplying the determined expansion coefficients with corresponding harmonics and summing up to obtain scattering field profile. In this thesis, an algorithm for Mie's calculation provided by Bohren and Huffman was applied in calculating particle scattering form factor.[12]

However, the classical Mie theory just deals with light scattering from a single isolated spherical particle. Using similar series expansion as Mie theory, Xu *et al.*[13]analytically obtained the scattering field distribution from an agglomerate of identical particles, where particles are positioned in lines and these lines cross at centers. These "snow-flake" arrangements of particles can offer simplified treatment due to their symmetry. Their solution indicates that the scattering field from the particle agglomerate differs significantly from the simple summation of scattering fields of same number of isolated particles.[13]

To investigate the relative position on the scattering pattern of a system containing only a few particles, McNeil *et al.*[1, 14] solved the Maxwell equation using finite elements methods to obtain the light scattering pattern by a few closely position particles. They reported that:

> *"Depending on the orientation of the particles with respect to the incident light, these interactions can either* ***increase*** *or* ***decrease*** *the scattering efficiency, the isotropy of the scattering, and the magnitude of electric field strength within the matrix of particles. In the mid-visible range, two particles in line increase the back scattering fraction by 28%, and attenuating strength by 38% over that of a single particles, whereas if the particles are in the diagonal configuration the backscattering fraction and scattering strength are actually reduced by addition of the second particle. If the particles are separated by* ***distances comparable with their diameter****, as in the case for high particle concentrations or agglomerated systems, the near field interactions between the radiation fields of the particles can strongly influence the resulting far-field electric field distribution and thus the appearance and the hiding power of a coating*."

In a system with more than one closely positioned particles, each particle is immersed in the secondary fields scattered by other particles. Calculating light scattering field of arbitrarily positioned particle using this method is not trivial.

A.3.2 T-Matrix methods

To expand the limitation of Mie theory, Waterman and coworkers[11] developed T-Matrix method which offers a more general approach for addressing light scattering from a system containing arbitrary number of particles. In T-Matrix method, both incident electromagnetic filed, $E_i(r)$, and scattering electric fields, $E_s(r)$, are expanded in series of vector spherical harmonics:

$$E_i(r) = \sum_{n=1}^{\infty} \sum_{m=-n}^{n} [a_{mn} RgM_{mn}(kr) + b_{mn} RgN_{mn}(kr)] \tag{A.1}$$

$$E_s(r) = \sum_{n=1}^{\infty} \sum_{m=-n}^{n} [p_{mn} M_{mn}(kr) + q_{mn} N_{mn}(kr)] \tag{A.2}$$

where RgM_{mn} and RgN_{mn} are regular vector harmonics that are regular at origin; M_{mn} and N_{mn} are vector spherical harmonics vanishing at infinite. The expansion coefficients for the scattering field $\mathbf{p} = [p_{mn}\ q_{mn}]$, can be related to the expansion coefficient for the incident field $\mathbf{a} = [a_{mn}\ b_{mn}]$ by a transformation:

$$p_{mn} == \sum_{n'=1}^{\infty} \sum_{m'=-n'}^{n'} [T^{11}_{mm'nn'} a_{mn} + T^{12}_{mm'nn'} b_{mn}] \tag{A.3}$$

$$q_{mn} == \sum_{n'=1}^{\infty} \sum_{m'=-n'}^{n'} [T^{21}_{mm'nn'} a_{mn} + T^{22}_{mm'nn'} b_{mn}] \tag{A.4}$$

The above equation can be denoted in a compact Matrix notation, and the method is so called T-Matrix method:

$$\mathbf{p=T \cdot a} \tag{A.5}$$

The transformation matrix showed in Eqn (A.5) depends only on the particle size, shape, physical properties, and orientation, but not on the incident field. For a

single spherical particle, T-Matrix is diagonal, with $T^{11}_{mm'nn'} = -\delta_{mm'}\delta nn' b_n$, and $T^{22}_{mm'nn'} = -\delta_{mm'}\delta nn' a_n$, and reduces to Mie theory for spherical scatter. T-matrix method is more complex, and it allows one to study the scattering of systems containing spheroid particles, or cylindrical particles. Using T-Matrix approach, Mischenko[15] proposed a method for calculating light scattering from randomly oriented particle systems. The methodology of T-Matrix will be briefly introduced here.

For a multiple-particle system, each particle is immersed in the incident field, and is also under the secondary electromagnetic field scattered from all other particles. The overall scattered electric field for the particle system is the summation of the scattering effects due to both primary and second fields.

In spherical expansion of the scattered electromagnetic field from a single scatter entity, the usual practice chooses the coordinate origin for harmonic expansion as the particle symmetric center, and both the incident and scattered fields are expanded with regard to this origin. However, to apply the boundary condition for addressing secondary fields of light scattering of a particle, and in order to use the orthogonal properties of the harmonics, one needs to employ vector harmonic addition theory in which a harmonic about an origin can be re-expanded in harmonics about another origin. For example, the harmonics with regarding the center of particle j as origin, $M_{mn}(kr^j)$ and $N_{mn}(kr^j)$, need be expanded in the harmonics with regarding the center of another particle i, $RgM_{kl}(kr^i)$, $RgN_{kl}(kr^i)$ $M_{kl}(kr^i)$, $N_{kl}(kr^i)$ to address light scattering of particle i to the secondary field scattered by particle j.

$$M_{mn}(kr^j) = \sum_{l=1}^{\infty}\sum_{k=-1}^{l}[A_{kl}^{mn}(kr^{ji})RgM_{kl}(kr^i) + B_{kl}^{mn}(kr^{ji})RgN_{kl}(kr^i)] \quad (A.6)$$

$$N_{mn}(kr^j) = \sum_{l=1}^{\infty}\sum_{k=-1}^{l}[A_{kl}^{mn}(kr^{ji})RgN_{kl}(kr^i) + B_{kl}^{mn}(kr^{ji})RgM_{kl}(kr^i)] \quad (A.7)$$

where $r^{ji}=r^j-r^i$. The explicit expression for the coefficients, A_{kl}^{mn} and B_{kl}^{mn} in the above two equations have been provided by Mackowski.[16] Using above process, one can derive a linear relation for the scattered filed expansion coefficients for particle *j*:

$$\mathrm{p}^j = T^j(a^j + \sum_{i\neq j} H^{ji}\,\mathrm{p}^i) \quad (A.8)$$

where T^j represent the standard Loren-Mie scattering for each isolated sphere and is only a function of sphere size parameter and refractive indices , with $p^j=T^j\,\boldsymbol{a}$ holds if particle *j* is position isolated. The matrix H^{ji}, whose elements are the coefficients of [A_{kl}^{mn} , B_{kl}^{mn}], accounts for electromagnetic interaction or electromagnetic coupling between particle *i* particle *j*, depends on the particle spatial arrangement.[16] The first term at the right hand of Eqn (A.8) represents the primary incident field, and the second term is corresponding to the secondary field scattered by other particles. Eqn (A.8) states that the scattered light field by the particle *j* can be obtained from the transition using T matrix from both primary and secondary incident fields. A manipulation of the equation (A.8) can leads to the sphere-centered transition matrices that transform the expansion coefficients of the incident field into expansion coefficients of the individual scattered fields.[15]

$$p^j = \sum_i T^{ji} p^i \quad (A.9)$$

where the transformation matrix T^{ij}, defined in with the scatterer symmetry center as the origin, depends on the particle orientation. The harmonic expansions of scattered field from the individual scatterer center will be transformed into an expansion based on a common origin for the whole particle system by applying the addition theorem for vector harmonics, in order to be able to summarize the scattering field from all scatterers to obtain the overall scattering pattern for the system. One can find the expansion coefficients based on a single system origin as:

$$\mathbf{p} = \sum_j J^j p^j = \sum_j \sum_i J^j T^{ji} a^i = \sum_j \sum_i J^j T^{ji} J^i \mathbf{a} \qquad \text{(A.10)}$$

where **p, a**, are vectors of expansion coefficients for overall scattering of incident fields based on the common origin; the transform matrix J^j, similar in the form as H matrices in Eqn (A.8), is plugged in to transform the expansion coefficients originated at particle *j* to those based on the common system coordinate origin. Eqn A.10 can be denoted using compact Matrix notation as:

$$\mathbf{p} = \mathbf{T} \cdot \mathbf{a} \qquad \text{(A11)}$$

Where the transition matrix **T** defined in the eqn (A.11) can be used to directly compute the expansion coefficients for the incident field with the harmonic expansion coefficients contained in the vector **a**, based on a common system coordinate.

Using this approach, Mishchenko and Machowski[17] calculated light scattering from two randomly position spheres and showed that scattering coefficient of the two particle system depends on particle alignment and separation distance.

Quirantes *et al.*[18] calculated light scattering by a particle pair as a function of separation distance and particle size, and reported a upper volume fraction limit for

independent scattering. They reported that at the $\frac{4\pi\sigma}{\lambda} = 0.1$, the particle with volume fraction of 10^{-5} will cause a 2~2.5% difference in the scattering in comparison to infinite dilution system, where the refractive index for particle is assumed 1.2 times of that of suspending fluid. The Quirantes's calculation also showed that impact of the volume fraction on the scattering efficiency decreases with the increase in the particle size parameter, $k\sigma$.[18]

Based on T-Matrix methods, modern computer power can afford the memory and enough speed for calculating the scattered fields for a system containing particle as many as 1 million. A typical colloidal system contains Billions of particles per c.c., and particles are under continuous motion while keeping position correlated, calculations of optical properties using T-Matrix distribution for such as system have not been a routine process.

Actually, it is not necessary, and it is also impossible to determine the position of all particles in a colloidal suspension for calculating the scattering. Instead, one can take T-Matrix method with a reduced statistically representative system, or using various approximation methods. Here the Monte Carlo simulation and the quasi crystalline approximation (QCA) will be briefly summarized.

A.3.3 Monte Carlo simulation

Monte Carlo simulation approach introduces a "box" containing a number of particles to represent a colloidal suspension, and a "snapshot" of particle arrangement, or called a realization, for all particles in a "box" is generated randomly using Monte Carlo simulation according the ensemble thermodynamic properties of suspensions.[19, 20] By

using Foldy-Lax multiple scattering equation,[21] Maxwell equation for discrete scatterers in a homogeneous background can be expressed in the Matrix notation as:

$$p^m = \sum_{m=1, m\neq n}^{N} T^m H^{mn} p^n + \exp(ik_{inc} \cdot r^m) T^m a_{inc}{}^m \qquad \text{(A.12)}$$

where p^m is again the vector of expansion coefficients for spherical harmonics for particle m; vector $a_{inc}{}^m$ contains the harmonic coefficients for incident wave expanded with regard to particle m; k_{inc} is the wave number of the incident wave; N is the number of spheres in the "box"; The matrix of H^{mn} is the vector spherical wave transformation matrix; T^m is again the Lorenz-Mie transformation matrix for particle m with its own center as the harmonic expansion origin. The multiple scattering Maxwell equation of Eqn (A.12) for each realization of particle arrangement can be solved (usually by iteration methods), and the overall scattering field profile E_s for all N particles at an observation point r can be calculated. The component of H^{mn} depends on particle arrangement, may not be same at each realization. The computed results are averaged over all realizations to obtain the final results representing the colloidal suspension. Tsang *et al.*[22, 23] solved multiple scattering Maxwell's equations iteratively for each realization of particles in a cubic box that contains 4000 dielectric particles and corresponds 25% by volume. They reported that the coherent wave nature is preserved by incorporating a Percus-Yevick hard sphere structure factor model. Iteration need for solve the equation (A.12) was reported to be 9 times before achieving convergence. They also showed that the calculated extinction rate for the light wave does not change significantly when the number of realization is above 20.[22]

Using Monte Carlo simulation, Tsang *et al.* also calculated light scattering from systems of spheroidal particle.[24]

Monte Carlo simulation is generally timing consuming and computationally intensive. Various approximation theories have been created to addressing the light scattering from the random scatters. These multiple scattering theory includes Quasi-crystalline approximation (QCA),[25] and interference approximation detailed in the previous chapters. Instead of calculating scattering by averaging over many simulated realizations to obtain representative properties, these approximations solve the multiple scattering Maxwell equation only once over a representative system configuration where particle arrangement can be represented by pair correlation function (PCF), $g(r)$.

A.3.4 Quasi-crystalline approximation

Quasi crystalline approximation (QCA) have been developed to approximately calculate the propagation constant for coherent electromagnetic wave propagation in media, where a pair distribution function are used to addressing the position correlation.[26] Under the QCA, the integral equation for the configuration average of exciting field $< \overline{E}^{E}(r \mid r^{1}) >$ at field point r acting on a scatterer at r^{1} can be written as:

$$< E_E(r \mid r^1) >= \overline{E}_i(r^1) + n_0 \int dr^2 g(r^2 - r^1) \cdot T(r^2) \cdot < E_E(r \mid r^2) > \qquad \text{(A.13)}$$

where a pair correlation function $g(r)$, calculated form the integral equation approach described by models such as PY-HS model or MSA-HSY, is included to account the microstructure. $T(r^2) \cdot < E_E(r \mid r^2) >$ is the field scattered by a single scatterer at r^2 when excited by $< E^E(r \mid r^2) >$. Where $\overline{E}_i(r)$ is the incident field at position r. Similar

to Eqn. (A.8), Eqn (A.13) states that the field at $r = r^1$ is due to the incident field plus the field scattered form the all other particles. Whereas the ensemble average of particle position correlation is represented in PDF $g(r)$, and the orientation-dependent electrostatic interaction are encrypted in the transformation matrix, $T(r^2)$, depending on the coordinate of r^2 with regard to the origin at r^2. Eqn (A.13) can be solved by a numerical approach or by analytical approach at some special cases. Analytical solution requires using the translation addition theory for spherical vector harmonics to convert the series expansion of $T(r^2)\cdot < E_E(r \mid r^2) >$ (which is naturally expanded with the origin r^2) to the origin located at r^1. From the solution, the parameter governing the electromagnetic wave propagation can be calculated.

Using PY-HS model in addressing microstructure of the suspensions, QCA also predicts the quenched scattering with the increasing volume fraction and QCA solutions agree well with Monte Carlo simulation[22, 23] and controlled experiments.[27] A simplified approximation based on the QCA by setting g(r) as $g(r) = \begin{cases} 0 & r < \sigma \\ 1 & r > \sigma \end{cases}$ is commonly used and is called hole correction.[11] This approximation only is suitable for dilute suspensions.

A.3.5 Quasi-crystalline approximation with coherent potential

By using method of coherent potential to the study of multiple scattering of electromagnetic wave from random distributed scatterers, Tsang and Kong provided so called quasi crystalline approximation with constant potential (QCA-CP).[28] By identify the electromagnetic potential operator, the problem of electromagnetic scattering was

treated entirely within the framework of quantum-mechanical potential scattering. Where, T-Matrix is used as dyad transition operator in the scattering problem, and a PDF was also included to addressing the particle position correlation. By using QCA-CP, the effective dielectric constant and the scattering coefficient for a colloidal system can be derived. The details about QCA-CP have been given by Tsang and Kong.[28]

It is shown that both QCA and QCA-CP can address depending scattering with good accuracy. However at higher volume fraction, QCA-CP predictions match experimental results better than QCA approach.[28]

Dik and Invanov[29] compared extinction coefficients predicted using both QCA and IA, and concluded that at lower volume fraction and small particle size, QCA and IA agree well, but the agreement deteriorates with the increasing volume faction and increasing particle size parameter.

A.4 Summary

This appendix reviewed the theory addressing multiple scattering from randomly distributed scatters using T-Matrix approach. Theoretically, T-Matrix can offer rigorous treatment of multiple light scattering for a particle system with arbitrary particle arrangement.

Similar to the IA detailed in the previous chapters, both QCA and QCA-CP can predict quenched light scattering efficiencies at increased volume fraction, and model prediction using QCA-CP matches with experimental data better than that using QCA does.

In comparison to QCA or QCA-CP, IA, which requires minimized computer powers can provides predations match with the experimental data and with QCA-CP and QCA for most industry colloidal system of practical importance.

A.5 References

1. L. E. McNeil, A. R. Hanuska, and R. H. French, "Orientation dependence in near-field scattering from TiO2 particles," Applied Optics **40**(22), 3726-3736 (2001).
2. Y. Kuga and A. Ishimaru, "Retroreflectance from a dense distribution of spherical-particles," Journal of the Optical Society of America A-Optics Image Science and Vision **1**(8), 831-835 (1984).
3. A. Ishimaru and Y. Kuga, "Attenuation constant of a coherent field in a dense distribution of particles," Journal of the Optical Society of America **72**(10), 1317-1320 (1982).
4. P. E. Wolf, G. Maret, E. Akkermans, and R. Maynard, "Optical coherent backscattering by random-media - an experimental-study," Journal De Physique **49**(1), 63-75 (1988).
5. E. Akkermans, P. E. Wolf, R. Maynard, and G. Maret, "Theoretical-study of the coherent backscattering of light by disordered media," Journal De Physique **49**(1), 77-98 (1988).
6. S. Fraden and G. Maret, "Multiple light-scattering from concentrated, interacting suspensions," Physical Review Letters **65**(4), 512-515 (1990).
7. S. John, "Localization of light," Physics Today **44**(5), 32-40 (1991).

8. P. E. Wolf and G. Maret, "Weak localization and coherent backscattering of photons in disordered media," Physical Review Letters **55**(24), 2696-2699 (1985).

9. Y. A. Vlasov, X. Z. Bo, J. C. Sturm, and D. J. Norris, "On-chip natural assembly of silicon photonic bandgap crystals," Nature **414**(6861), 289-293 (2001).

10. R. Garg, R. K. Prud'homme, I. A. Aksay, F. Liu, and R. R. Alfano, "Optical transmission in highly concentrated dispersions," Journal of the Optical Society of America A-Optics Image Science and Vision **15**(4), 932-935 (1998).

11. J. G. Fikioris, "Multiple Scattering from Inhomogeneous Media," IEEE Transactions on Antennas and Propagation **AP14**(2), 202-& (1966).

12. C. F. Bohren and D. R. Huffman, *Absorption and scattering of light by small particles* (Wiley, New York, 1983), pp. xiv, 530 p.

13. Y. L. Xu, "Electromagnetic scattering by an aggregate of spheres," Applied Optics **34**(21), 4573-4588 (1995).

14. L. E. McNeil, A. R. Hanuska, and R. H. French, "Near-field scattering from red pigment particles: Absorption and spectral dependence," Journal of Applied Physics **89**(3), 1898-1906 (2001).

15. M. I. Mishchenko, "Light-scattering by randomly oriented axially symmetrical particles," Journal of the Optical Society of America A-Optics Image Science and Vision **8**(6), 871-882 (1991).

16. D. W. Mackowski, "Analysis of radiative scattering for multiple sphere configurations," Proceedings of the Royal Society of London Series A-Mathematical Physical and Engineering Sciences **433**(1889), 599-614 (1991).

17. M. I. Mishchenko and D. W. Mackowski, "Light-scattering by randomly oriented bispheres," Optics Letters **19**(20), 1604-1606 (1994).

18. A. Quirantes, F. Arroyo, and J. Quirantes-Ros, "Multiple light scattering by spherical particle systems and its dependence on concentration: A T-matrix study," Journal of Colloid and Interface Science **240**(1), 78-82 (2001).

19. K. H. Ding, L. Tsang, and S. E. Shih, "Monte Carlo simulations of particle positions for densely packed multispecies sticky particles," Microwave and Optical Technology Letters **30**(3), 187-192 (2001).

20. K. H. Ding, C. E. Mandt, L. Tsang, and J. A. Kong, "Monte-Carlo simulations of pair distribution-functions of dense discrete random-media with multiple sizes of particles," Journal of Electromagnetic Waves and Applications **6**(8), 1015-1030 (1992).

21. L. Tsang, J. A. Kong, and R. T. Shin, *Theory of microwave remote sensing*, Wiley series in remote sensing (Wiley, New York, 1985).

22. L. Tsang, C. E. Mandt, and K. H. Ding, "Monte-Carlo simulations of the extinction rate of dense media with randomly distributed dielectric spheres based on solution of Maxwells equations," Optics Letters **17**(5), 314-316 (1992).

23. L. M. Zurk, L. Tsang, K. H. Ding, and D. P. Winebrenner, "Monte-Carlo simulations of the extinction rate of densely packed spheres with clustered and

nonclustered geometries," Journal of the Optical Society of America A-Optics Image Science and Vision **12**(8), 1772-1781 (1995).

24. L. Tsang, K. H. Ding, S. E. Shih, and J. A. Kong, "Scattering of electromagnetic waves from dense distributions of spheroidal particles based on Monte Carlo simulations," Journal of the Optical Society of America A-Optics Image Science and Vision **15**(10), 2660-2669 (1998).

25. M. Lax, "Multiple scattering of waves. II. The effective field in dense systems," Physical Review A **85(4)**, 621 (1952).

26. L. Tsang and J. A. Kong, "Effective propagation constants for coherent electromagnetic-wave propagation in media embedded with dielectric scatters," Journal of Applied Physics **53**(11), 7162-7173 (1982).

27. R. West, D. Gibbs, L. Tsang, and A. K. Fung, "Comparison of optical-scattering experiments and the quasi-crystalline approximation for dense media," Journal of the Optical Society of America A-Optics Image Science and Vision **11**(6), 1854-1858 (1994).

28. L. Tsang and J. A. Kong, "Multiple-scattering of electromagnetic-waves by random distributions of discrete scatterers with coherent potential and quantum-mechanical formulism," Journal of Applied Physics **51**(7), 3465-3485 (1980).

29. V. P. Dik and A. P. Ivanov, "Limits of applicability of the interference approximation for description of extinction of light in disperse media with high concentration of particles," Optics and Spectroscopy **86**(6), 909-913 (1999).

APPENDIX B

MSA-HSY MODEL (HERRERA ET AL.)

Herrera *et al.* presented a structure factor model for monodisperse colloidal systems using mean spherical approximation (MSA), where particles interact through hard spherical Yukawa (HSY) interactions.

There are typographical errors in the equation presented for calculating structure factor in the original publication. The correct equations used in the calculating structure factor in the previous chapters are presented as following.

B.1 Parameter definition

e_o = 1.60 x 10^{-19} (Coulumb) //electron charge

k_B = 1.38 x 10^{-23} (Jole/K) //Boltzmann constant

N_A= 6.02 x 10^{23} (/mole) //Avogadro number

ε = 8.85 x10^{-12} (C^2/Jm) electric permittivity for vacuum

ε_r =78.54 //dielectric constant

T (K) //temperature

κ //inverse Debye length

σ //mean particle size

z_{eff} //effective surface charge

θ //scattering angle

η //volume fraction

λ //wavelength

m //refractive index of suspending fluid

B.2 Calculation of structure factor S(k)

$$L_B = \frac{e_o^{\,2}}{4\pi \cdot \varepsilon \cdot \varepsilon_r \cdot k_B T}$$

$$\varepsilon_o = \frac{z_{eff}^{\,2} \cdot L_B}{\sigma \cdot (1 + z/2)^2}$$ //dimensionless coupling energy

$$q = \frac{m}{4\pi\lambda} \sin(\theta/2)$$ //scattering vector

$$k = q \cdot \sigma$$ //dimensionless scattering vector

$$z = \kappa \cdot \sigma$$

$$\eta_1 = 1 - \eta$$

$$\eta_2 = 1 + 2\eta$$

$$\eta_3 = \eta_2 / \eta_1$$

$$\eta_4 = 2 + \eta$$

$$\eta_5 = 3\eta$$

$$\eta_6 = 6\eta$$

$$\varphi_o = \frac{1 - \exp(-z)}{2}$$

$$\varphi_1 = \frac{1}{z^3} \cdot [1 - \frac{z}{2} - (1 + \frac{z}{2}) \cdot \exp(-z)]$$

$$\xi_o = z - (2 + z) \cdot \varphi_o + \xi_1 \cdot (\eta_3 + \frac{z}{2}) \cdot \frac{1}{z}$$

$$\xi_1 = 2z \cdot \varphi_o - {12\eta \cdot \varphi_1 \cdot z^2}\Big/{\eta_1}$$

$$\xi = \xi_1 \cdot \gamma + \xi_o$$

Find the roots for the following equation to obtain the value of parameter γ.

$$\gamma \cdot (\gamma + 1) = \frac{\eta_6 \cdot \varepsilon}{\xi^2}$$

The only positive root to the equation about is corresponding to the root of physical meanings, and can be easily identified. Here, the parameter ε indicates the interaction potential at contact.

$$\alpha_o = \eta_6 \cdot \frac{2 + z}{\eta_1 \cdot z^2}$$

$$\alpha_1 = \eta_6 \cdot \frac{2\eta_2 + z \cdot \eta_4}{(\eta_1 \cdot z)^2}$$

$$A = \frac{1}{\eta_1} \cdot [\eta_3 \cdot (1 + 2\gamma) + 2z \cdot \gamma \cdot (\gamma + 1)]$$

$$B = \frac{1}{\eta_1} \cdot [1 - 2\gamma \cdot (1 + 2\gamma + 2\frac{\eta_3}{z})]$$

$$C = \frac{1}{\eta_5} \cdot [-\gamma \cdot \exp(z) \cdot (\xi_1 \cdot \gamma + \xi_o)]$$

$$D = \frac{\gamma}{\eta_5} \cdot (-\alpha_o + z \cdot \alpha_1 \cdot \gamma - z \cdot \gamma) - C$$

$$R_1 = k \cdot \cos k + k - 2\sin k$$

$$R_2 = \cos k - 1$$

$$R_3 = \frac{k \cdot \cos k + z \cdot \sin k}{z^2 + k^2}$$

$$R_4 = \frac{z}{z^2 + k^2}$$

$$R = 1 - \eta_6 \cdot [\frac{A \cdot R_1}{k^3} + \frac{B \cdot R_2}{k^2} - \frac{R_3 \cdot z \cdot D \cdot \exp(-z)}{k} + (D + C) \cdot R_4]$$

$$T_1 = k \cdot \sin k - 2 + k - 2.0 \sin k$$

$$T_2 = \sin k - k$$

$$T_3 = \frac{z \cdot \cos k - k \cdot \sin k}{z^2 + k^2} - \frac{1}{z}$$

$$T_4 = \frac{k}{z^2 + k^2}$$

$$T = -\eta_6 \cdot [\frac{A \cdot T_1}{k^3} + \frac{B \cdot T_2}{k^2} + \frac{T_3 \cdot z \cdot D \cdot \exp(-z)}{k} + (D + C) \cdot T_4]$$

$$S(k) = \frac{1}{R^2 + T^2}$$

Where S(k) is the structure factor at the dimensionless scattering vector $k = q \cdot \sigma$.

B. 3 Calculation of S(0) form MSA-HSY model.

When scattering angle vanishes, the calculation for S(0) can be simplified. The structure factor at zero scattering vector, S(0) can be calculated from:

$$CC = 6 \cdot (C + D)$$
$$DD = 6 \cdot D \cdot \exp(-z) \cdot (1 + z)$$
$$S(0) = \frac{z^2}{[\eta \cdot (A \cdot z + 3B \cdot z - cc + DD + z/\eta]^2}$$

Reference: J. N. Herrera, P. T. Cummings, and H. Ruiz-Estrada, "Static structure factor for simple liquid metals," Molecular Physics **96**(5), 835-847 (1999).

APPENDIX C

PEER-REVIEWED PUBLICATION GENERATED FROM RESEARCH

1. **Huang, Y.**, and Sevick-Muraca, E.M. "Characterization of pigment absorption efficiency using frequency domain photon migration," *Anal. Chem.* **75**, 6958 (2003).

2. **Huang, Y.**, and Sevick-Muraca, E.M. "Validating the assumption to the interference approximation using measurements of absorption efficiency and hindered scattering in dense suspensions," Accepted for publication in *Appl. Opt.*

3. **Huang, Y.**, Yuwono, V., and Sevick-Muraca, E.M. "Assessment of electrostatic interaction by Rhodamine 6G adsorption on polystyrene latex using frequency domain photon migration," *Langmuir* **18**, 9192 (2002).

4. **Huang, Y.**, and Sevick-Muraca, E.M. "Assessment of angle-averaged structure factor and S(0) using multiply scattered light to monitor electrostatic colloidal interactions," *J. Colloid Interface Sci.* **251**, 434 (2002).

5. **Huang, Y.**, Sun, Z., and Sevick-Muraca, E. M. "Assessment of electrostatic interactions in dense colloidal suspensions with multiply scattered light," *Langmuir*, 8, 2048 (2002).

6. Sun, Z., **Huang, Y.**, and Sevick-Muraca, E.M. "Precise analysis of frequency domain photon migration measurement for characterization of concentrated colloidal suspensions," *Rev. Sci. Instrum*. **7**, 383 (2002).

7. Dali, S. S., Rasmussen, J., Huang, Y., Roy, R., and Sevick-Muraca, E. M. "Determination of Particle Size in Dense Suspensions Using Multi-wavelength Frequency Domain Photon Migration Measurements, *Submitted to AICHE J.*

APPENDIX D

CONFERENCE PRESENTATIONS

(*Presenter)

1. Dali, S. S.*, Rasmussen, J., **Huang, Y**., and Sevick-Muraca, E. M. "Determination of Particle Size in Dense Suspensions Using Multi-wavelength Frequency Domain Photon Migration Measurements," AICHE Annual Meeting. November 2003, San Francisco, California.

2. **Huang, Y**., and Sevick-Muraca, E. M.* "Characterization of Dense Particulate Suspensions Using Multiply Scattered Light," AICHE Annual Meeting. November 2003, San Francisco, California.

3. **Huang, Y.***, and Sevick-Muraca, E. M. "Characterization of Pigment Particle Absorption Efficiencies Using Frequency Domain Photon Migration," AICHE Annual Meeting. November 2003, San Francisco, California.

4. **Huang, Y.** * "A novel method for the determination of the light absorption spectra of pigment particles using multiply scattered light," *ISCC Annual Meeting.* April 2003, Chicago, Illinois.

5. **Huang, Y.**, Sun, Z., and Sevick-Muraca, E. M. * "Assessment of electrostatic interaction in dense colloidal suspensions with multiply scattered light using frequency domain photon migration," *Chemistry at Interface Gordon Conference.* July 2002, New London, Connecticut.

6. **Huang, Y.***, Yuwano, V., and Sevick-Muraca, E. M. "Assessment of changing electrostatic interaction using multiply scattered light," *223rd ACS National Meeting*. April 2002, Orlando, Florida.

7. **Huang, Y.***, Sun, Z., and Sevick-Muraca, E. M. "Frequency-domain photon migration assessment of static structure factor of colloidal suspensions at varying volume fraction and ionic strength," *Advances in Optics for Biotechnology, Medicine and Surgery.* June 2001, Banff, Canada.

8. **Huang, Y.**, Sun, Z., and Sevick-Muraca, E. M.* "Information of static structure factor from frequency-domain photon migration measurements of multiply scattered light in colloidal suspension of varying volume fraction and ionic strength," *The 75th ACS Colloid and Surface Science Symposium*. June 2001, Pittsburgh, PA.

9. **Huang, Y.***, Sun, Z., and Sevick-Muraca, E. M. "Comparison of average isotropic light scattering coefficients and averages structure factors of polystyrene lattices at two Debye lengths," *Particle 2001*. February 2001, Orlando, FL.

APPENDIX E

NOMENCLATURE

Abbreviations

AC	amplitude
CVP	chemical vibration potential
DC	average intensity
DLS	dynamic light scattering
DWS	diffusing wave spectroscopy
ESA	electroacoustic sonic amplitude
ESI	electrostatic interaction
FDPM	frequency domain photon migration
HNC	Hypernetted-chain
HSY	hard spherical interaction
K-M	Kubelka-Munk
MSA	mean spherical approximation
MSA-HSY	mean spherical approximation with hard sphere Yukawa interaction
MSA-PM	mean spherical approximation with primary model interaction
OCM	one component system
O-Z	Ornstein-Zernike
PCF	pair correlation function
PDW	photon density wave
PM	primary model

PS	phase shift
PY	Percus-Yevick
QCA	quasi-crystalline approximation
QCA-CP	quasi-crystalline approximation with coherent potential
R6G	Rhodamine 6G
RDF	radial distribution function
RTE	radiative transport equation
RY	Rogers-Young
SANS	small angle light scattering
SAXS	small angle x-ray scattering
SLS	static light scattering
TCF	total correlation function
UVP	ultrasonic vibration potential

List of Symbols

English symbols

AC_{rel}	relative amplitude
C_{abs}	particle absorption cross section
C_{sca}	particle scattering cross section
C_{ext}	particle total extinction cross section
c	speed of light in medium
$c(r)$	direct correlation function

$c_{i,j}(r)$	direct correlation function between component i and j
D	photon diffusion coefficient
D_p	Particle self diffusion coefficient
DC_{rel}	relative average intensity
e	electron charge
$f(r)$	mixing function in closure relation to O-Z equation
$f(x)$	particle size distribution function
$f_A(x)$	particle area-based size distribution function
$f_m(x)$	particle mass-based size distribution function
$F(\theta)$	form factor
F_{eff}	effective form factor
$F_{i,j}$	binary form factor of particles i and j
g	scattering anisotropy
$g(r)$	redial distribution function
$g_{i,j}(r)$	radial distribution function between component i and j
$h(r)$	total correlation function
$h_{i,j}(r)$	total correlation function between component i and j
$H_{i,j}(r)$	3D Fourier transform of $h_{ij}(r)$
$\vec{j}$	specific current density; angular current density
$\bar{J}$	current density
k_B	Boltzmann constant
$K(\lambda)$	Kubelka-Munk absorption coefficient

$K(\omega)$	acoustic extinction coefficient
$K(\omega,x)$	acoustic extinction efficiency for particle of diameter x
m	the ratio of refractive index of particle to that of solvent in a suspension
n_l	refractive index of the medium
PS_{rel}	relative phase shift
q	scattering vector
q_{max}	maximum scattering structure factor in a medium
r	center to center distance between particles
r	position vector
s	optical path length
S_{AC}	amplitude of optical source
S_{DC}	average intensity of optical source
$s(r,t)$	intensity of optical source
$S_1(r, \hat{\Omega}, t)$	current density of optical source at position r and time t
$S(0)$	structure factor at the zero scattering vector
$S(q)$	structure factor at the scattering vector q
$<S(q)>$	Angle-integrated structure factor
S_r	strength of optical source
$S_{i,j}$	partial structure factor of component i and j
$S(\lambda)$	Kubelka-Munk scattering coefficient
t	time
x	particle diameter

U_d	electrophoretic mobility of a particle
$< U_d >$	effective electrophoretic mobility for different particles
v	speed of particle
V	volume
z_{eff}	effective particle surface charge
z_i	effective particle surface charge of component i

Greek symbols

ρ_i	number density of the component i in the colloidal mixture
ε_0	electric permittivity of vacuum
ε_r	dielectric constant of the suspending medium
σ	particle diameter
σ_i	particle diameter of component i
κ	inverse Debye screening length.
κ^{-1}	Debye screening length
θ	scattering angle
λ	wavelength of light
μ_o	cosine of scattering angle
μ_a	absorption coefficient of light
μ_s'	isotropic scattering coefficient
$\mu_{a,pigments}$	volume based absorption efficiency for pigment

$\mu_{a,pigments}$	weight based absorption efficiency for pigment
μ_s'	isotropic scattering coefficient
ϕ	flux; flux rate
φ	angular flux; specific intensity; radiance
ε	particle volume fraction
ϕ_o	phase shift of optical source
ω	modulation frequency
ζ	zeta potential of particles
Π	colloidal osmotic pressure
Σ_{tr}	macroscopic transport cross section; inverse mean transport free path

VITA

Yingqing Huang received his B.S. in chemical engineering from Tsinghua University in Beijing, China in 1992. After that, his career progressed in industry first as a process engineer, downstream section manager, and later as a technical manager in Asian Pacific Amino Acids Corporation.

In 1997, Yingqing Huang attended University of Missouri-Rolla (UMR) and received an M.S. degree in chemical engineering in 1999. At Texas A&M University, Yingqing Huang received the Celanese Award for his achievement in academic development, where he has been working on his Ph.D. since 1999. Yingqing Huang received his Ph.D. in 2004.

He can be reached via: Photon Migration Laboratories, Department of Chemical Engineering, MS 3122, Texas A&M University, College Station, TX 77843-3122.